EPFL

Natural slicks on Lake Geneva: From small-scale effects to large-scale formation and distribution

Mehrshad FOROUGHAN

École
polytechnique
fédérale
de Lausanne

2023

Acknowledgment

My PhD and the present dissertation, like many other endeavors, relied on the invaluable help, guidance, and companionship of numerous individuals who have walked alongside me throughout this journey, either in its entirety or during specific phases. The PhD journey is an extraordinary experience, a mission that cannot be abandoned midway. Despite its persistent challenges and occasional frustrations, this journey has catalyzed a profound and unexpected transformation within me, both in direct and indirect ways. I am, therefore, sincerely grateful for the presence and teachings of all the people who have played a role in shaping my growth.

First and foremost, I want to express my sincere thanks to my PhD advisor, **David Andrew Barry**. It was his curiosity that planted the seed for my chosen research topic, which I passionately pursued over the past five years. In addition to the valuable scientific discussions we had during this time, I am especially grateful for his guidance when it came to making key decisions about my priorities throughout my PhD. His advice played a key role in ensuring a relatively smooth completion of my thesis in the last few months. I am also thankful for the freedom he gave me to explore my own study path. Though I encountered numerous failures and frustrations, this autonomy fostered my growth as an independent researcher.

Next, I would like to express my gratitude to my "unofficial" co-advisor, **Ulrich Lemmin**, for his guidance, valuable insights, and particularly his invaluable assistance with writing manuscripts. He patiently took us under his wing, guiding us through the process of revising scientific work and teaching us how to responsibly refine our presentations for the scientific community. His enduring dedication and passion for the job he loves, even long after his retirement, serve as a remarkable role model for me. His lifelong commitment to his career is truly inspiring and wholehearted.

My research heavily relies on direct observations conducted at Lake Geneva, and I am profoundly grateful to all those who supported me in both preparing the instrumentation and during the field campaign itself. I want to give a special shout-out to **Htet Kyi Wynn**, **Benjamin Graf**, and **Valentin Kindschi** for their invaluable contributions. Htetkyi not only taught me how to

plan and prepare for field campaigns but was also my constant companion during measurements. His sense of responsibility and well-organized style made campaigns run smoothly, allowing me to focus on collecting scientific data. Benjamin and Valentine, talented engineers in our lab, spent a lot of time designing and maintaining instruments/sensors and finding creative solutions when faced with challenges. They were true lifesavers when things didn't go as planned during our time on the lake. Plus, their company always made the experience more enjoyable.

I want to give a big thanks to **Marie Sudki** and **Rima Bermuda** for their help, especially with all the administrative work that would have given me a massive headache if I had to do it on my own. I'll never forget the excitement in Marie's voice whenever we talked, and she always went out of her way to provide me with as many options as possible for any request I had. What meant a lot to me was that we became really good friends, and seeing her always warms my heart. Rima also helped me a lot in the final phase of my PhD and with setting up my defense. Her smile and calmness were always reassuring, especially when things didn't go as planned.

I also want to express my gratitude to all my colleagues and friends at ECOL. I spent the majority of my time at EPFL with them, and I feel incredibly fortunate to have their support in facing both academic and non-academic challenges. **Mahmood Ziabari** is near and dear to me as we shared the same proposal and went through the demanding journey of completing our PhDs together. We spent countless hours discussing a wide range of topics, both scientific and non-scientific, and took many walks together, which made the difficult times during this journey more bearable. I also want to acknowledge **Rafael Reiss**, my funny, responsible, and kind friend. He not only offered his help in the best possible way but also had the ability to brighten my day with his fantastic personality and, of course, the great coffee we shared!

I have learned a great deal and enjoyed spending time with **Abolfazl Rahaghi**, as my project was a continuation of his PhD and he acted as my mentor at the beginning. Another colleague, **Mohsen Cheraghi**, also holds a special place in my memories. We shared some wonderful moments together, and he was the one who joined me for a nice first lunch at EPFL. I want to extend my thanks to **Frédéric Soulignac** for being a fantastic and fun office mate during the early stages of my PhD. **Amir Razmi**, despite his short appearance in our lab, always brightened the atmosphere with his warm laughter. Gratitude is also owed to **Qihao Jiang**, my kindhearted friend with a beautiful and inquisitive mind.

I am deeply grateful for the presence and contributions of two office mates, **Haoran Shi** and **Zhaoyang Luo**, who each made different stages of my journey memorable through their positive attitudes and engaging small talk. I would also like to thank **Yuhong Shuai**, **Shiyu Yan**, **Qiaoli Wang**, and **Congrong Yu**, whose presence added brightness and joy to the lab, creating cherished moments. **Naifu Peng**'s calm and friendly attitude left a lasting impression, and **François Mettra**, with whom I shared memorable campaigns on the lake, was always willing to help and engage in discussions on topics of shared interest. Lastly, I want to thank **Violaine Piton**, whose wonderful personality always lightened the mood. With her kind heart, being around her feels like being with an old friend.

During my PhD at ECOL, I also had the chance to work with some talented master's students and interns on different topics. I want to thank **Aloys Cretegny**, **Vianney Roux**, and **Sylvia Zhang** for all that I learned from them. Their smart solutions and bright minds constantly amazed me as we faced challenges together. I also want to thank the civil service members in our lab, especially **Florian Reinhard**, **Didier Ansermet**, **Sébastien Peiris**, and **Baptiste Thiévent**. They were a tremendous help in preparing the instruments and carrying out the field campaigns. I want to thank also **Auguste Bertholet** for the engaging discussions and new perspective he brought to our lab.

I would like to express my gratitude to **Rob Uittenbogaard**, who served as an excellent mentor during the early stages of my PhD. Through our meetings and discussions, I learned a great deal from him. His passion for science and positive attitude were truly inspiring. I also want to thank his wife, **Akke**, who kindly hosted us on several occasions, preparing unforgettable meals that created wonderful memories.

I am immensely thankful to **Johny Wüest**, a remarkable professor with whom I had the privilege of assisting in his limnology course. Working alongside him, I gained extensive knowledge about the fundamentals of this captivating research field. Observing his teaching style, which aimed to actively engage students and encourage them to develop their own original ideas, was a valuable learning experience. Furthermore, I want to express my appreciation to the other APHYS/Limnology Center members who supported me in setting up test instruments on the LéXPLORE platform. Special thanks go to **Sébastien Lavanchy**, **Natacha Pasche**, and **Damien Bouffard** for their valuable assistance.

I also had the pleasure of making many friends and collaborators at the environmental engineering building (GR), and I am deeply grateful for their presence. In particular, I want to thank

here in Switzerland. Mahshid has always provided me with the warmth and sense of family that I cherish deeply. I also want to acknowledge the parallel journey I have had with Pasha, whose fellowship has brought about significant changes in me, coinciding with my PhD path.

To my parents and sister, **Giti**, in Iran, I send my deepest love. Their presence in my heart has been a constant source of energy, propelling me forward during challenging times. I am forever grateful for their dedicated support and the love that binds us together.

Last but not least, I want to express my profound gratitude for having my best friend by my side throughout this journey. Your love, patience, and encouragement have meant the world to me. I am eagerly looking forward to setting out on future journeys together. To my beloved, **Shiva**, thank you from the bottom of my heart.

Abstract

Low wind speeds (< 4 m s^{-1}) are ubiquitous in many water bodies, yet the physical processes occurring at the air-water interface in this range are poorly understood. A notable example is smooth patches on the water surface, known as natural slicks, formed when biogenic surfactants dampen short wind waves. This thesis investigates natural slicks in Lake Geneva from two perspectives: (i) Their small-scale effects on surface and near-surface temperature dynamics and their impact on air-water exchanges, and (ii) the formation and distribution of slicks in the lake, dominated mainly by underlying large-scale currents. Furthermore, the thesis examines a range of interrelated physical processes in the low wind regime, including calm-to-wind-wave transitions, near-surface stratification, and the development of multiscale temperature fronts. For that, in situ observations were combined with airborne, shore-based and satellite remote-sensing data, and 3D hydrodynamic modeling. Surface water sampling campaigns also confirmed the association between smooth patchiness and natural slicks.

Natural slicks affect physical processes at the air-water interface by damping short waves. A notable example occurred when strong shortwave solar radiation induced significant temperature gradients in a thin near-surface layer while wind speeds fluctuated around a 1.5 m s^{-1} surface wave generation threshold. While intense near-surface stratification was maintained within slicks, enhanced wave-induced mixing in non-slick areas was observed. As a result, sharp surface temperature gradients developed closely aligned with slick/non-slick boundaries. In contrast to previous studies carried out in oceans, warmer slicks were found under the studied environmental conditions. These results highlight the importance of wave-induced mixing under low wind conditions and underscore the potential role of slicks in air-water exchanges. However, determining the effect of slicks on surface fluxes using direct measurements is challenging due to their small spatial extent and the inherent wind variability at low wind speeds. To address this challenge, a series of field campaigns incorporating flux measurements were conducted, combined with wavelet analysis for evaluating short-term fluxes and dynamic flux footprint analysis. The results unveil how spatiotemporal flux variability under low wind conditions is affected by slicks, surface and near-surface temperature fluctuations, and short wind wave generation. This study is the first to use flux measurements on a moving platform with short-term flux estimations, offering a tool to address flux variability related to spatiotemporal heterogeneities.

In addition to small-scale processes, strong winds can trigger gyres, eddies, and coastal upwelling in lakes. These processes can lead to the formation of fronts and filaments, which in turn create zones of intense convergence and downwelling where floating materials like surfactants concentrate when the wind subsides. This thesis investigates a striking ~10-km long "frontal slick" in Lake Geneva, developing on the warm side of a surface temperature front. Numerical modeling, supported by satellite data, showed that large eddies interact with density gradients associated with coastal upwelling, creating a strong convergent front. In lakes, these dynamics are common and considered a primary mechanism for large-scale slick formation, as well as highly efficient at transporting surface materials.

This thesis improves our understanding of physical processes under low wind conditions, focusing on natural slicks, which are overlooked in physical limnology. However, the findings are not limited to the specific characteristics of Lake Geneva but contribute to the expanding knowledge of surfactant-enriched water surfaces and their role in modulating air-water exchange across marine and aquatic environments.

Keywords

Zusammenfassung

Niedrige Windgeschwindigkeiten (< 4 m s^{-1}) sind in vielen Gewässern allgegenwärtig, doch die damit einhergehenden physikalischen Prozesse an der Luft-Wasser-Grenzfläche sind nur wenig untersucht. Ein eindrückliches Beispiel sind Bereiche mit glatter Wasseroberfläche, bekannt als natürliche Oberflächenfilme (englisch: Slicks), welche sich bilden, wenn biogene Tenside windinduzierte Kapillarwellen dämpfen. Diese Dissertation untersucht verschiedene Aspekte von natürlichen Slicks im Genfersee: 1) die kleinskaligen Auswirkungen auf die oberflächennahe Temperaturdynamik und den Luft-Wasser-Austausch, und 2) die Entstehung und Verteilung von Slicks im See. Des Weiteren untersucht diese Arbeit verschiedene miteinander verbundene physikalische Prozesse unter niedrigen Windgeschwindigkeiten, einschliesslich des Übergangs von Windstille zu windinduzierten Kapillarwellen, der oberflächennahen Temperaturschichtung und der Entwicklung von multiskaligen Temperaturfronten. Zu diesem Zweck wurden In-situ Messungen und Oberflächenwasserproben mit luft-, küsten- und satellitengestützten Fernerkundungsdaten sowie 3D hydrodynamischer Modellierung kombiniert.

Natürliche Slicks beeinflussen physikalische Prozesse an der Luft-Wasser-Grenzfläche, indem sie Kapillarwellen dämpfen. Diese Dissertation untersucht ein besonders bemerkenswertes Fallbeispiel, hervorgerufen durch sonneneinstrahlungsbedingte Temperaturgradienten in einer dünnen oberflächennahen Schicht und Windgeschwindigkeiten, welche um 1,5 m s^{-1} (Schwellwert für die Entstehung von Kapillarwellen) schwankten. Innerhalb des Slicks war eine starke oberflächennahe Schichtung sichtbar, während eine verstärkte welleninduzierte Durchmischung in Bereichen ohne Slicks beobachtet wurde. Infolgedessen entwickelten sich zwischen Slick- und Nicht-Slick-Bereichen scharfe Oberflächentemperaturgradienten. Diese Ergebnisse verdeutlichen die Bedeutung von welleninduzierter Durchmischung unter niedrigen Windgeschwindigkeiten und unterstreichen die potenzielle Bedeutung von Slicks im Luft-Wasser-Austausch. Aufgrund der geringen räumlichen Ausdehnung der Slicks und der inhärenten Variabilität niedriger Windgeschwindigkeiten, war es nicht möglich, die Auswirkungen auf Oberflächenflüsse durch direkte Messungen zu bestimmen. Daher wurde eine Reihe von Feldkampagnen mit Flussmessungen durchgeführt, kombiniert mit einer

Wavelet-Analyse zur Bewertung kurzfristiger Flüsse und einer dynamischen Analyse des Fluss-Fussabdrucks. Die Ergebnisse verdeutlichen, wie die räumlich-zeitliche Flussvariabilität unter niedrigen Windgeschwindigkeiten durch Slicks, oberflächennahe Temperaturschwankungen sowie Kapillarwellen beeinflusst wird. Diese Studie hat erstmals Flussmessungen von einer bewegten Plattform mit kurzfristigen Flussschätzungen kombiniert und damit ein Instrument zur Untersuchung der Flussvariabilität durch räumlich-zeitliche Heterogenitäten aufgezeigt.

Starke Winde können Wirbel und Küstenauftrieb in Seen hervorrufen, welche wiederum zur Bildung von Fronten und Filamenten führen. Dadurch entstehen Zonen starker Konvergenz und des Abtriebs, in denen sich schwimmende Materialien wie Tenside anhäufen, sobald der Wind nachlässt. Diese Dissertation untersucht einen markanten ~10 km langen frontartigen Oberflächenfilm im Genfersee, der sich auf der warmen Seite einer Oberflächentemperaturfront bildete. Numerische Simulationen und Satellitenbilder zeigten, dass grossskalige Wirbel mit küstenauftriebsbedingten Dichtegradienten interagierten und so eine starke konvergente Front erzeugten. In Seen ist diese Dynamik weit verbreitet und gilt als Hauptmechanismus für die Erzeugung von grossräumigen Oberflächenfilmen sowie den äusserst effizienten Transport von Oberflächenmaterial.

In dieser Arbeit wurden physikalische Prozesse an der Luft-Wasser-Grenzfläche unter niedrigen Windgeschwindigkeiten untersucht, mit einem Fokus auf natürliche Slicks, welche in der physikalischen Limnologie nur spärlich erforscht sind. Die Ergebnisse sind jedoch nicht von den spezifischen Merkmalen des Genfersees abhängig, sondern tragen generell zu einem besseren Verständnis über mit Tensiden angereicherte Wasseroberflächen und deren Rolle bei der Steuerung des Luft-Wasser-Austauschs in marinen und aquatischen Umgebungen bei.

Stichwörter

Natürliche Oberflächenfilme, Tenside, niedrige Windgeschwindigkeiten, direkte Flussmessungen, Genfersee, Oberflächentemperatur, Kapillarwellen, frontartige Oberflächenfilme, submesoskalige Strömungen

Contents

Chapter 1   Introduction

"Man, a ship with sail unfurled, waits
    for wind master's breath to change his fates."

Rumi, 13th century

"The wind is a very subtle and nimble thing, Polycrates, and oil is sticky, greasy, and shiny. So the wind, because of the polished effect of the sea, slides over the surface, and cannot gather up waves upon the waters."

Theophylact Simocatta, 7th century

Lakes have long captivated people with their serene beauty and tranquil aura, especially during calm weather with a gentle breeze and a bright sun. While it is commonly assumed that the interaction between lakes or other water bodies and the atmosphere is less active during periods of low wind forcing than high wind and troubled waters, this assumption overlooks another critical factor: time. Fortunately, some inland lakes, like Lake Geneva, provide us with long periods of low wind and placid conditions throughout the year, offering ample opportunities for recreation and relaxation. While intense wind events can cause significant mixing and exchanges, as illustrated in Aesop's fable of the sun and the wind, gentle yet persistent low-wind processes also exert considerable influence over time. One of the most captivating features of this low-wind regime is the patchiness that appears on the surface of the water, intriguing artists, scientists, and curious onlookers alike. This study aims to explore this fascinating process using a scientific lens, shedding light on its characteristics at different scales and in interaction with other coexisting processes.

1.1   Natural slicks: A brief history

Under weak wind forcing, the air-water interface exhibits significant spatiotemporal variability. One such variability that is readily distinguishable is the heterogeneous surface roughness/color typically observed in lakes and coastal waters. Surface roughness gradients are usually caused by organized or random-like smooth patches. Under some conditions, these smooth patches are referred to as Natural Slicks, drawing an analogy to anthropogenic oil slicks. Similarly, scholarly research into natural slicks can be traced back to the problem of oil slick wave damping, which has been known since ancient times. Pouring oil on troubled waters to calm waves was a practical consideration commonly used by sailors, and its footprint in literature dates back to Aristotle's time (Scott, 1978). Over the course of more than two millennia, this phenomenon continued to be studied by thinkers and natural philosophers, with some of the earliest modern scholarly explorations being conducted by Benjamin Franklin in the 18th

century (Hühnerfuss, 2006b). In the early to mid-twentieth century, scientific inquiry into natural slicks emerged as a branch of research that built upon this historical foundation. However, people living by water bodies, including artists who portray them, were obviously aware of this phenomenon outside of the academic circles (Figure 1-1).
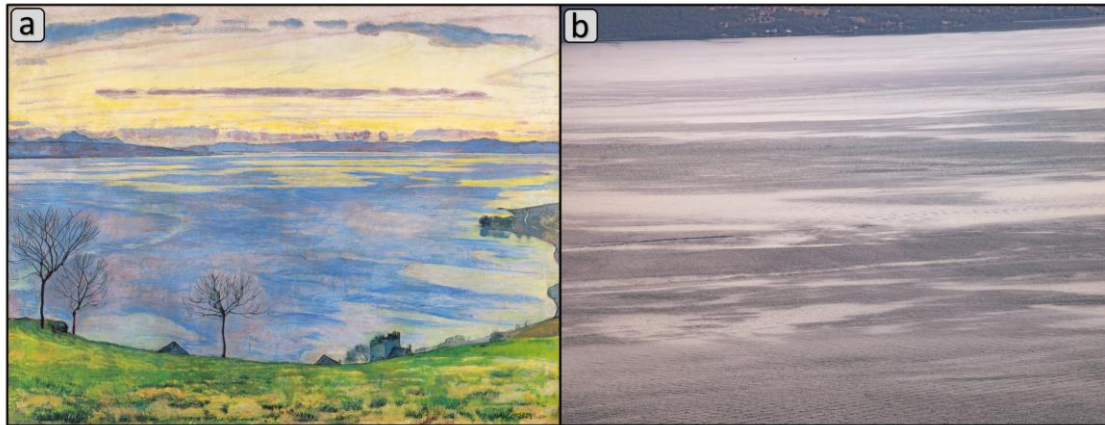
Figure 1-1. a) The painting, "Genfersee am Abend von Chexbres aus," created in 1895 by Ferdinand Hodler, is an example of how artists have portrayed Lake Geneva with its surface patches. b) An image of the lake's surface water captured by a remote camera package installed near Chexbres, almost 130 years after Ferdinand Hodler's painting. The lightly shaded patches seen in the image are examples of natural slicks currently under study in Lake Geneva.

In the 19th century, Marangoni's research on surface tension laid the groundwork for current models of wave damping by surface films. This led to a discussion of the relationship between wave damping and variations in surface tension caused by oil introduction to the surface, resulting in the development of models exploring the impact of surface-active chemical compounds on fluid motion. The significance of surface elasticity induced by surface films in wave damping was further emphasized by the works of Reynolds, Rayleigh, and Agnes Pockels in the late 19th century (Hühnerfuss, 2006b). Lamb (1895) published the first hydrodynamic theory for water wave damping by elastic surface films. Later on, Levich (1962) provided a more comprehensive treatment of the hydrodynamic theory of surface waves, including the effect of surface dilational elasticity due to soluble surfactants (surface-active agents).

These studies have expanded the focus of the research community from visible slicks to invisible surface films, which may cover much larger areas of water bodies. As scientists began to recognize the potential role of these interfacial phenomena in air-water exchanges, particularly in terms of their resistance to evaporation (Mer, 1962), there was growing concern about global warming in the late 20th century. This highlighted the need for more accurate models to explain

air-water exchange, particularly the transfer of CO_2 between the atmosphere and the ocean. The potential roles of slicks and surfactants in modulating these fluxes have fueled research in this field to the present day. Despite this shift in focus, the problem of oil pouring was not completely abandoned, as evidenced by recent examples in the literature (Cox *et al.*, 2017).

In closing this historical note, I would like to highlight three contemporary collections of articles that have made significant contributions to the study of natural slicks. These works (Gade *et al.*, 2006; Herr and Williams, 1986; Liss and Duce, 1997) have been valuable resources for the present thesis, either through direct reference or by providing useful background information.

1.2   Slicks, biogenic surfactants and surface microlayer

Surfactant distribution and natural slick formation take place on a substrate known as the Surface Microlayer (SML). The SML can be roughly defined as the top 1 micrometer to 1 millimeter of surface water, with various processes occurring over gradients of varying thickness (Hunter and Liss, 1981). The SML is the interface through which air and water exchange material, heat, and momentum. Slicks are defined as visibly surfactant-enriched surfaces due to their wave-damping property, whereas natural surfactants are also often enriched in the SML compared to sub-surface bulk water outside of slicked regions (Liss and Duce, 1997). In other words, slicks form when the concentration of surface-active materials exceeds a certain threshold, which can be associated with surface pressure. Surface pressure relates to the reduction of surface tension due to the introduction of surfactants to the surface compared to clean water (Levich, 1962; Pogorzelski *et al.*, 2006). Nonetheless, it is still an open question whether slicks are simply a special case of SML high surfactant enrichment and should be treated in the spectrum of surfactant distribution or whether their formation leads to the emergence of a new phenomenon with its own characteristics (Engel *et al.*, 2017).

The SML contains biogenic materials, including surfactants, derived from a wide variety of sources, both autochthonous and allochthonous. A sufficient concentration of dissolved organic matter can enrich the surface, even in oligotrophic waters or in periods of low biological productivity (Wurl *et al.*, 2011). Phytoplankton activities and byproducts have long been associated with natural surfactants concentration on the surface (Dietz and Lafond, 1950; Frew *et al.*, 1990; Žutić *et al.*, 1981a). Additionally, the surface-dwelling organisms inhabiting the SML also contribute to the enrichment of surface-active material (Kurata *et al.*, 2016a; Parks *et al.*, 2020;

Voskuhl and Rahlff, 2022; Zaitsev, 1997). Terrestrial organic materials can also enter the SML through wet or dry deposition when transported by atmospheric flows or directly from river inputs (Lim *et al.*, 2007; Milinković *et al.*, 2022; Penezić *et al.*, 2022). Sediment resuspension can also be a source of organic material in shallow environments (García-Flor *et al.*, 2005). Moreover, anthropogenic sources such as industrial processes, agricultural runoff, or municipal wastewater discharges can be highly enriched in surfactants (Wurl and Obbard, 2004). Surfactants can be soluble or insoluble, with the latter assumed to be a significant component of surfactants within slicks. The SML surfactant pool includes transparent exopolymer particles (Wurl and Holmes, 2008), polysaccharides (Hunter and Liss, 1981), amino acids (Kuznetsova *et al.*, 2004), and chromophoric dissolved organic matter (Tilstone *et al.*, 2010). However, the composition of the surface microlayer and the relative importance of these sources are still open fields of investigation. Short-term and seasonal variations in surfactant amounts and chemical composition further complicate the issue (Bai *et al.*, 2019; Frka *et al.*, 2009).

The SML is a highly active ecosystem that supports a diverse range of life forms (Engel *et al.*, 2017). Organisms in the SML are collectively called "neuston." Recent research reveals that the diversity and concentration of bacterioneuston communities differ from those found in the underlying water column (Howe, 2017; Obernosterer *et al.*, 2008; Stolle *et al.*, 2010). Phytoneuston represents another major biological component of SML ecosystems (Taylor and Cunliffe, 2014). Neustonic fungi also fulfill various ecosystem functions within the surface layer (Taylor and Cunliffe, 2016). In regions where slicks occur on the water's surface, they serve as hotspots for diverse life forms, despite their relatively fleeting and short-lived nature (Gove *et al.*, 2019a). Slicks offer a nurturing environment for various marine larvae and host high concentrations of neustonic zooplankton (Gallardo *et al.*, 2021; Kingsford and Choat, 1986; Whitney *et al.*, 2021). This enrichment seemingly draws predators to slicks as well. Juvenile fish actively seek out these slicks for feeding purposes (Ory *et al.*, 2018). Similarly, seabirds appear to be attracted to slicks as a rich source of prey (Lieber *et al.*, 2023). These observations indicate that slicks have a substantial ecological impact, serving as food reservoirs and contributing to the accumulation of diverse organisms. While the contribution mentioned above may not solely be attributed to a cause-and-effect relationship, but rather the passive manifestation of strong convergence zones by slicks, there is evidence suggesting that slicks also play an active role in surface material accumulations. This is evident in the biofilm-like composition of slicks (Wurl and Holmes, 2008) and the observed behavioral feedback effects exhibited by swimming organisms inside slicks (Genin *et al.*, 2005; Kingsford and Choat, 1986; Weidberg *et al.*, 2014).

The knowledge of SML and their biochemical compositions has been derived from extensive surface water sampling over the progression of this study area. Zhang et al. (1998, 2003) observed a distinct change at a depth of 50 ± 10 μm in a range of physicochemical parameters, including surface tension, pH, chlorophyll-a, organic matter, dissolved nutrients, and trace metals, utilizing both laboratory and field measurements. Contemporary samplers, such as mesh screens and glass plates, can achieve resolutions ranging from 20 to 400 μm (Cunliffe *et al.*, 2013a; Falkowska, 1999). More recently developed rotating drum samplers are capable of sampling the upper 50 μm. These devices have also been integrated into mobile platforms, enabling continuous SML sampling (Frew and Nelson, 1999; Ribas-Ribas *et al.*, 2017; Wei and Wu, 1992).

Once samples are collected, they can be examined in the field or laboratory. Some sampling efforts aim to compare the enrichment and composition of materials in slick and non-slick regions (Garabetian *et al.*, 1993; Kurata *et al.*, 2016a; Wurl *et al.*, 2016), while others target surfactant distribution mapping across more extensive water surface regions (Bai *et al.*, 2019; Sabbaghzadeh *et al.*, 2017; Wurl *et al.*, 2011). The viscoelastic modulus appears to be the key parameter for characterizing surfactants' ability to modulate air-water exchange processes. This parameter links stress and strain at the air-water interface in response to a small expansion and compression of a surface area (Watson *et al.*, 1997). However, viscoelasticity is not usually quantified directly; instead, surfactant concentration and slick/non-slick variability are typically characterized by total Surfactant Activity (SA) (Rickard *et al.*, 2019) or through the enrichment of proxy materials (Sabbaghzadeh, 2018). Fluorescent Dissolved Organic Matter (FDOM) serves as one such proxy that can be measured in situ using a fluorometer (Frew and Nelson, 1999; Ribas-Ribas *et al.*, 2017) or through fluorescence spectroscopy in laboratory settings (Bai *et al.*, 2019; Kowalczuk *et al.*, 2013; Salter, 2010). This technique was applied in this thesis to compare slick and non-slick areas based on multiple sampling campaigns. On a larger scale, surfactants can also be correlated with remotely sensed parameters, such as chlorophyll-a (Torres *et al.*, 2020; Tsai and Liu, 2003) or Colored Dissolved Organic Matter (CDOM) (Aurin *et al.*, 2018).

1.3   Effects of slicks on air-water interfacial processes

Surfactants are amphiphilic molecules, having both hydrophilic and hydrophobic parts. They tend to adsorb onto surfaces to minimize energetically unfavorable interactions. For example, at the air-water interface, the hydrophobic tails of the surfactants are directed outward

from the water phase. Surfactants can be both soluble and insoluble, depending on their chemical structure. The solubility of surfactants in subsurface water can be explained by an increase in entropy when they move into the bulk region, with higher degrees of freedom, at the expense of a decrease in enthalpy caused by the dissolution of their hydrophobic heads (Manikantan and Squires, 2020). Surfactants play a crucial role in modulating interfacial exchanges, both through static and dynamic processes. The static process involves creating a barrier-like effect at the interface, but this effect is typically only observed with condensed solid-type surfactants that rarely form in natural environments, so it is often neglected (Liss, 1983a). On the other hand, the introduction of non-zero viscoelasticity can have a significant impact on near-surface hydrodynamics by reducing the length and velocity scales of near-surface turbulence, suppressing wave growth, and amplifying wave energy dissipation (damping) (Frew, 1997). This viscoelasticity arises from the reduction of surface tension due to the presence of surfactants at the interface, which, as mentioned, also known as surface pressure. Surface pressure is related to viscoelasticity as follows:

$$\varepsilon' = -d\pi/d\ln A_e \qquad \qquad 1\text{-}1$$

where $\pi = \gamma_{clean} - \gamma_{surfactants}$ is surface pressure, A_e is surface area element and γ is surface tension. In general, slicks are typically associated with insoluble surfactants, whereas soluble surfactants tend to be more widely distributed on the surface (Elliott *et al.*, 2018; Wurl *et al.*, 2011).

The impact of surfactants on interfacial physical processes can largely be understood through two key aspects: their effects on the surface wave field and on near-surface turbulence (Frew, 1997). The former, being a more established area of study, has received greater attention. Current theories on wave-damping mechanisms in natural slicks revolve around the stimulation of Marangoni waves and the amplification of near-surface viscous dissipation, both resulting from the introduction of surfactants to the surface. As waves propagate or turbulent structures approach the interface, they create a surface tension gradient by imposing a non-uniform distribution of surfactants. This surface tension gradient serves as an additional restoring force, similar to gravity and surface tension for gravity-capillary waves, leading to the excitation of Marangoni waves (Alpers and Hühnerfuss, 1989). However, unlike gravity and capillary waves, Marangoni waves are longitudinal and undergo significant damping due to heightened viscous

dissipation within the surface boundary layer, which makes their detection considerably more challenging (Lucassen, 1968a).

While the elevated dissipation due to the presence of surfactants contributes moderately to the increased damping of gravity-capillary waves (Carlson, 1987), the primary cause of damping is due to the resonance between these two transversal and longitudinal wave types (Lucassen, 1968b; Manikantan and Squires, 2020). When the two waves resonate, the energy of gravity-capillary waves channels into enhanced viscous dissipation in the surface boundary layer. Furthermore, as a result of nonlinear wave-wave interactions, the energy of larger waves can also be dissipated through the sink induced by Marangoni waves (Alpers and Hühnerfuss, 1989). Interestingly, despite the historical reference mentioned earlier regarding the origin of natural slick wave damping, this proposed mechanism does not apply to newly spilled oil slicks; instead, their damping results from the high viscosity of their relatively thick layer on the water surface (Hühnerfuss, 2006a). As surfactants' solubility increases, their damping effect reduces (Manikantan and Squires, 2020).

The absence of waves can also suppress small-scale Langmuir circulations that contribute to near-surface turbulent transport (Veron and Melville, 2001). Additionally, besides the surface waves effect, the increased viscous dissipation due to surfactants attenuates both horizontal and vertical turbulent motions, reducing turbulent kinetic energy (Flack *et al.*, 2001; Khakpour *et al.*, 2011; Tsai, 1996a). This effect is caused by a closed-loop phenomenon, where surface divergent/convergent motions from upwelling and downwelling cause changes in surfactant concentration, creating surface tension gradients that counteract fluid motion and thicken the viscous sublayer (Davies, 1966; Matt *et al.*, 2011; Sarpkaya, 1996; Tsai and Yue, 1995). The presence of surfactants also suppresses hairpin vortices, which are a typical coherent motion in the turbulent boundary layer (Adrian, 2013) and contribute to splats (upwelling). This, in turn, reduces upward scalar transport and surface flux (Goldman *et al.*, 1988; Handler *et al.*, 2003; Shen *et al.*, 2004). Additionally, the presence of surfactants makes the surface behave more like a solid wall locally, due to the constraint of surface tension gradients on surface diverging/converging motions, compared to the clean-surface case (Khakpour, 2012; McKenna and McGillis, 2004).

The impact of slicks and surfactants on interfacial physical processes and near-surface hydrodynamics provides a basis for studies investigating their effects on air-water exchange dynam-

ics. One such effect relates to the influence of surfactant enrichment in the sea surface micro-layer on surface temperature. In a laboratory experiment conducted by Jarvis (1962a), it was observed that the impact of artificial surfactants on water surface temperature could vary depending on the type of surfactant used. The surface temperature increases when surfactant inhibits surface evaporation and decreases the cooling rate. On the other hand, a decrease in surface temperature occurs when surfactant suppresses near-surface convective motion, hindering the exchange of the cooled surface layer with the warmer bulk water. It is worth noting that the former effect, which results in an increase in surface temperature, is typically associated with compacted monolayers not commonly found in natural environments (Liss, 1983a). In a study by Saylor *et al.* (2001), marked changes in surface temperature patterns due to surfactants were observed, but no significant effect on surface temperature was found when compared to clean water under the same heat flux conditions. Nevertheless, in subsequent field studies, Frew *et al*. (2004a) and Marmorino and Smith (2006a) reported that ocean slicks are slightly colder than the surrounding non-slick water. These findings were based on in situ surface temperature measurements and remote sensing, respectively, and were also associated with reduced near-surface convective motions inside slicks.

Beyond surfactant-induced surface temperature variations, researchers explored the role of near-surface hydrodynamic modifications in air-water exchanges, particularly CO_2 exchanges. When discussing surfactants' effect on air-water exchanges, it is better to distinguish between natural slicks and non-visible (soluble) surfactant-enriched regions. While the latter seems to have a regional or seasonal impact on fluxes, natural slicks are more local and short-lived processes. In a pivotal oceanic campaign examining slicks and surfactants in air-water exchanges, researchers used shipboard eddy covariance and surface microlayer sampling (Frew *et al.*, 2004a). The authors found that surfactant enrichment correlated with reduced mean wave slope, heat, and gas transfer velocity, especially within a slick. Salter *et al.* (2011) observed suppression of CO_2 transfer velocities within an artificial slick patch in comparison to a controlled environment in the North Atlantic. Schmidt and Schneider's (2011) laboratory experiments on coastal waters demonstrated seasonal variations in surface pressure measurements, reflected in the range of transfer velocity reduction. At the ocean basin scale, Pereira *et al.* (2018a) found a reduction in CO_2 exchange relative to surfactant-free water. Mustaffa *et al.* (2020) used gas chamber measurements to demonstrate a reduction in CO_2 transfer velocity with surfactants and slicks in the Western Pacific and North Atlantic, with an almost threefold increase in suppression within slicks. Recently, Yang *et al.* (2021) identified uncertainties related to the spatial

variability of surfactants in air-water gas exchange in the Southern Ocean through a direct flux measurement campaign.

Compared to gas exchange, studies on the role of slicks and surfactants in heat and momentum exchange variability are very limited. The benchmark field campaign conducted by Frew *et al.* (2004a) is the only example of investigating heat flux variations due to surfactant enrichments and slick presence in the field. While the turbulent heat exchange, particularly sensible heat flux, is more air-side controlled than influenced by water-side turbulence, especially when compared to sparingly soluble gases like CO_2 (Kurose *et al.*, 2016), surfactants can still impact air-water turbulent heat exchange due to their effects on wave fields and surface temperature. There is still evidence that latent heat flux can depend on water-side turbulence (Komori *et al.*, 2011). Moreover, evaporation rates within slicks can be influenced by the gel-like matrix associated with slicks (Wurl *et al.*, 2016) and the reduction of the effective area caused by wave damping (Garrett, 1971). Compared to heat fluxes, the potential impact of slick-induced variations in surface roughness on momentum exchange is more readily foreseeable. Even so, such an effect has yet to be thoroughly investigated. The impact of oil slicks on reducing drag coefficients and wind-induced stress on the water surface has been studied (Benetazzo *et al.*, 2019; Shen *et al.*, 2019). Furthermore, Wu *et al.* (2019) demonstrated in a laboratory experiment that the biogenic scum layer and associated surfactants on the water surface significantly suppress air-water momentum exchange.

In concluding this section, it is important to recognize that biogenic surfactants may influence air-water interfacial processes and exchange beyond hydrodynamic modifications of surface and near-surface water. Enhanced biological activity, for example, could serve as a secondary effect, altering the air-water interface's physics. Research has demonstrated that bacterioneuston can directly influence air-sea gas exchange by consuming and producing trace gases (Nakajima *et al.*, 2013; Upstill-Goddard *et al.*, 2003). Additionally, during an oceanic slick observation, cyanobacteria-enriched slicks were found to be warmer than the surrounding water, while non-cyanobacterial slicks exhibited the expected slight reduction in surface temperature. This dual behavior was partly attributed to heat generation from biological activities (Wurl *et al.*, 2018a).

1.4 Slicks as large-scale flow visualization tools

Thus far, the introduction has primarily focused on the small-scale effects of natural slicks and their surfactant components. As mentioned earlier, a slick is a visible phenomenon that can be observed on the surface of most water bodies. The shapes and morphologies of slicks can sometimes appear random, but they can also be organized and structured. This is typically due to the interaction between two primary forces: wind stress and the underlying near-surface currents (Ermakov *et al.*, 1992). The morphology and kinematics of slicks often arise from the competing influences of these forces. Specifically, more organized slick patterns seem to be driven by large-scale convergent surface currents (D'Asaro *et al.*, 2018). As wind speed increases, the intermittent forcing by the wind can disintegrate the coherence of such large-scale slick patterns. The disintegration phase often leads to the formation of small-scale, streak-like features, which may be attributed to the development of the Langmuir Circulation or other wind-induced processes (Ermakov *et al.*, 2018b; Marmorino *et al.*, 2008a). Increased wind speed can also affect slick coverage on the surface, resulting in smaller patches as wind speed rises (Romano, 1996; Romano and Garabetian, 1996). This section, however, focuses on the role of large-scale underlying hydrodynamics in slick formation and the implications for remote sensing-based studies of surface currents.

The wave-damping properties of slicks and their modification of surface roughness serve as the primary basis for remote observations of this phenomenon. Surface roughness can be remotely observed through various methods, with the most easily accessible approach involving specular reflection of sunlight. While sun-glitter observations have their limitations (Robinson, 1997), slick patterns can still be identified within them. Scully-Power (1986) photographs taken from the US Space Shuttle offer valuable examples of slick observations in forms such as Langmuir circulations or eddies. Although deriving quantitative measurements from sun-glitter images is challenging, they can serve as a useful complement to in situ observations of the SML by illustrating the occurrence and spatial distribution of slicks. This methodology greatly assisted us in our study of slicks in Lake Geneva. Active microwave sensors, such as radars, enable more systematic measurements of sea surface roughness. Imaging radars, particularly Synthetic Aperture Radar (SAR), are most relevant for studying microlayer processes and are extensively used in oceanography.

For over four decades, slicks have been captured in radar imagery using satellite or airborne platforms (Garrett, 1986). Espedal *et al.* (1996) carried out concurrent SML sampling inside a

slick that was anticipated to be detected by an SAR satellite. This provided one of the earliest verifications of SAR-detected slicks. Gade *et al.* (1998) complemented this research by releasing artificial slicks on ocean surfaces and evaluating the performance of another spaceborne SAR imagery system. In general, later remote observations of slicks primarily served as a visualization method for various underlying surface currents rather than directly addressing the processes within the SML. These processes encompass internal waves (Alpers, 1985; Whitney *et al.*, 2021), Langmuir circulation (Marmorino *et al.*, 2007), coastal upwelling (Dabuleviciene *et al.*, 2018) and, most commonly, mesoscale (10 km to 100 km) and submesoscale (100 m to 10 km) surface currents (Ermakov *et al.*, 2011; Johannessen *et al.*, 1996; Karimova, 2012; Karimova and Gade, 2016; Marmorino *et al.*, 2010; McKinney *et al.*, 2012; Schuler and Lee, 2006).

Strong wind forcing, especially in large thermally stratified water bodies subject to the Coriolis force, can frequently trigger the formation of basin-scale gyres or mesoscale eddies, which often shape the large-scale skeleton of flow patterns in the surface layers. Submesoscale currents are frequently observed in the surface mixed layer of oceans as vortices, density fronts, filaments, and topographic wakes, with a typical timescale of hours to days (McWilliams, 2019). These currents act as a bridge between large- and small-scale processes by transferring energy from geostrophic flows to turbulent dissipation (McWilliams, 2016). The dynamics of submesoscale filaments are governed by frontogenesis, i.e., sharpening the preexisting horizontal density gradients (McWilliams, 2021). This process is critical to disrupting the geostrophic balance through a horizontal confluent deformation flow, triggering a secondary circulation with the same mechanism involved in filamentogenesis (Gula *et al.*, 2014) or the intensification of filaments (McWilliams *et al.*, 2009).

Consequently, submesoscale currents are often associated with strong convergence and significant vertical velocities, where lateral divergence ($\delta = \partial u/\partial x + \partial v/\partial y$) and vertical vorticity ($\zeta = \partial v/\partial x - \partial u/\partial y$) have larger magnitudes than the Coriolis frequency, f, i.e., $|\delta/f| \geq 1$ and $|\zeta/f| \geq 1$ (Mahadevan and Tandon, 2006). In particular, submesoscale currents are typically characterized by Rossby, $Ro = U/fL$, and Richardson numbers, $Ri_b = N^2 H^2/U^2$, of $O(1)$, with U being a characteristic speed, H and L vertical and horizontal length scales of the velocity field, respectively. Since $\zeta \sim U/L$, the Rossby number can be also defined as $Ro = \zeta/f$.

The strong convergence associated with submesoscale currents facilitates the efficient accumulation of surface materials, such as biogenic surfactants, often resulting in the formation of

slicks (D'Asaro *et al.*, 2018). As a result, slicks are widely used as passive tracers that reveal surface currents in oceans and lakes. However, slicks can also play an active role in hosting higher concentrations of various materials due to their biochemical properties and creating a gel-like matrix in the SML (Wurl and Holmes, 2008), and behavioral positive feedback effects where concentrations of prey and organic matter attract larger, swimming larval and juvenile fish (Weidberg *et al.*, 2014; Whitney *et al.*, 2021).

1.5   Other processes under low wind conditions interacting with slicks

Natural slicks are the most distinctive interfacial phenomenon of low wind conditions manifesting as smooth surfaces on water bodies. Nevertheless, in a natural environment, there are some coexisting processes that potentially interact with slicks at low wind speeds. One such process is the formation of a relatively thin warm layer during the day caused by strong short-wave solar radiation that penetrates the uppermost layer of the water column. This layer, known as the diurnal warm layer, is characterized by intense near-surface stratification, which isolates the uppermost water layer from the rest of the water column (Ward, 2006). The depth of the near-surface layer depends on several factors, including time of day (the integrated effect of solar radiation) and wind speed (Fairall *et al.*, 1996a). During the day, solar radiation heats up the near-surface layer, thus making it shallower. At night, the layer deepens as it loses heat. Wind speed also plays a role – as wind speed increases, it can mix the near-surface layer with deeper, colder water, resulting in a thicker layer and reducing stratification intensity (Gentemann and Minnett, 2008; Hughes *et al.*, 2020a). During calm conditions, the diurnal thermocline (as described by Imberger, 1985) can reach the surface.

Low wind speed conditions often exhibit intermittency in both wind magnitude and direction, leading to short-term wave growth and decay in duration- and fetch-limited scenarios, particularly in inland waters (Hwang and Wang, 2004). While transient wind speeds can occur in all wind ranges, the low wind condition is unique because the wave field can undergo significant changes when wind speed drops below or exceeds a certain threshold. On lakes, one commonly observes continuous transitions between calm surface water and the generation of young gravity-capillary waves. If no swells or waves generated by boat tracks are present on the surface, calm surface water typically appears glassy and reflects light specularly. Thus, by damping short waves, natural slicks resemble the surface state during calm periods. This wind speed threshold has been determined in the laboratory setting to be in the range of 1.6 to 1.8 m s^{-1} (Donelan and Plant, 2009). However, the threshold can depend on wind gustiness, fetch, air-

side stability, water temperature, and surface film concentration. Gentemann and Minnett (2008) reported that diurnal warm layer development in the ocean significantly changes when wind speed exceeds 1.5 m s^{-1}, potentially due to the appearance of waves. Additionally, the gustiness of the wind is another feature, particularly during unstable atmospheric conditions, that arises from random convective motion near the surface and can influence air-water exchanges in this wind regime (Grachev *et al.*, 1998; Guseva *et al.*, 2023).

Finally, submesoscale currents, as described in the previous section, can cause significant variations in surface temperature and the distribution of natural surfactants on a large scale. While these coherent motions are typically triggered during high wind episodes, they have relaxation and dissipation periods that extend beyond such events. In Lake Geneva, as low wind speeds dominated, much of the spatial variations created by these currents were detected and measured during these conditions (Hamze-Ziabari *et al.*, 2022b, 2022a). Therefore, the variations created by these currents often serve as the background for the small-scale heterogeneities mentioned earlier.

1.6   Natural slicks on Lake Geneva?

The question mark in this subsection title signifies the absence of previous studies that have specifically investigated natural slicks or surfactant-induced surface microlayers in Lake Geneva, despite the visual appeal that these smooth patches may have to common observers and artists (Figure 1-1). Even across physical limnology scientific studies, there is a remarkable absence of research that specifically addresses natural slicks in aquatic environments. While the results and implications of this dissertation are not limited to the characteristics of Lake Geneva (except perhaps in Chapter 4), this lake serves as the study site for this research. Therefore, a brief overview of the lake and its characteristics are discussed here.

1.6.1   General overview

Lake Geneva, locally known as Lac Léman, is a warm oligomictic lake that lies on the border between Switzerland and France. It has a surface area of 580 km^2 and a volume of 89 km^3, making it the largest lake in Western Europe. It is of significant regional socioeconomic and ecological importance, serving as a source of drinking water for over 900,000 people (CIPEL, 2019). The lake is comprised of two basins, stretching a total of 73 km in length (Figure 1-2). The larger eastern basin, known as Grand Lac, has a maximum width of 14 km and a depth of 309 m. The smaller western basin, known as Petit Lac, has a maximum width of 5 km and a
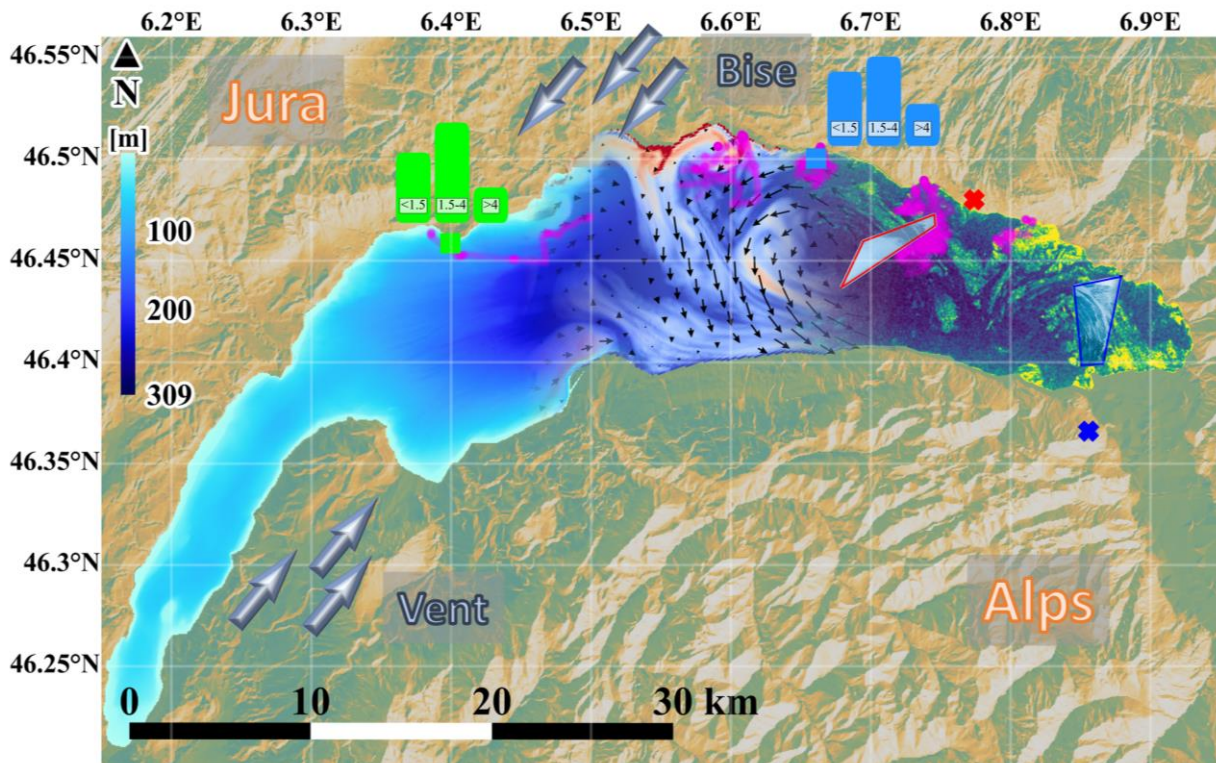
Figure 1-2. Bathymetric map of Lake Geneva with the surrounding topography (Alps and Jura) and the two primary large-scale wind patterns – the Vent originating from the southwest and the *Bise* coming from the northeast. This map includes examples of multiple datasets that complement the in situ field campaign data, which was the primary source used for analyses in this thesis. These datasets include 1) the Sentinel 1 SAR product taken on August 20th, 2020, which covers the eastern part of the lake. In the SAR image, areas with high surface roughness appear yellowish, while slick bands and smooth regions are seen as dark areas. 2) Two time-lapse images of the lake surface water were placed on top of the SAR imagery, taken almost at the same time. These images are from camera packages, referred to as TLB 1 (marked with a blue cross and outline) and TLB2 (marked with a red cross and outline), and show similar surface roughness patterns as the SAR image. 3) The central part of the lake displays a numerical simulation result obtained using the MITgcm model with a horizontal grid spacing of approximately 110 meters at the same time as the SAR and TLB images. This simulation includes surface temperature patterns and surface currents, which are shown qualitatively using black arrows. The model simulation shows a cyclonic eddy in the eastern part of the lake, whose extension can be faintly identified in the SAR product. Additionally, a southward jet is visible in the center of the lake. The magenta scattered points on the map represent one-minute GPS coordinates collected by the autonomous catamaran used in this thesis. Most of the campaign locations were chosen to be within the field of view of TLB2, a multi-pan-angle camera that provides a broad view of slicks and surface roughness, as shown on the map. The map also displays the locations of LéXPLORE and Buchillon platforms as blue and light green squares, respectively. These platforms provide long-term air-side and water-side data, which have been occasionally used in the present dissertation. The histograms, color-coded to correspond with stations, illustrate the distribution of wind speeds based on three-year data, highlighting the predominance of low-wind conditions. The lake bathymetry, which reveals relatively shallow sections in Petit Lac and Western Grand Lac according to the colorbar on the left, serves as the base layer for all data overlaid on this map.

depth of 75 m. The Rhône River is the primary inflow and outflow of the lake, entering at the eastern end and exiting through a weir at the western end, which regulates the water level. The theoretical residence time of the lake is approximately 11 years (CIPEL, 2019). During summer, Lake Geneva experiences strong stratification, with a thermocline forming at approximately 20 m depth. As fall and winter arrive, convective cooling gradually breaks down the stable thermal structure. However, the deep main basin, due to its considerable depth and mild climate, remains stratified for most of the year. Typically, the maximum mixing depth of 100 to 150 m is reached at the end of February or the beginning of March. Full-depth convective overturning occurs only during exceptionally cold winters (CIPEL, 2019).

1.6.2   Wind patterns over the lake

Lake Geneva is bordered by the Alps and the Jura Mountains (Figure 1-2). The surrounding topography creates a corridor that channels two dominant, large-scale winds, namely the *Bise* from the northeast and the Vent from the southwest. Both winds are approximately aligned with the primary axis of the western half of Lake Geneva and are characterized by high wind speeds (5 - 15 m s^{-1}) that persist for several days, generating most of the large-scale circulation in the lake (e.g., Lemmin and D'Adamo 1996; Reiss *et al.* 2020; Hamze-Ziabari *et al.* 2022). Nonetheless, despite the influence of these large-scale winds, Lake Geneva experiences a predominantly low-wind regime. During the stratification period (May to October), light winds (< 4 m s^{-1}) prevail 80-90% of the time (Lemmin and D'Adamo, 1996a). An examination of the in situ meteorological stations also indicates the prevalence of low-wind conditions in the lake (Figure 1-2).

1.6.3   Surface temperature, heat exchange, and climate change in Lake Geneva

Natural slicks strongly interact with the dynamics of Lake Surface Water Temperature (LSWT) and near-surface temperature gradients, actively influencing small-scale spatial variations of LSWT (Chapter 2) or passively manifesting through the formation of meso- to sub-meso-scale thermal structures (Chapter 4). The present study was partly motivated by a former PhD project conducted in the same laboratory, which investigated spatial patterns of surface temperature and their potential impact on air-water heat exchange. In a series of publications, Rahaghi (2018) (i) explored the long-term heat budget of the lake by calibrating, optimizing, and comparing a collection of bulk models based on two-point measurements (Rahaghi *et al.*, 2018), (ii) investigated the major meteorological factors controlling the dominant heat flux terms that determine spatial thermal patterns (Rahaghi *et al.*, 2018), and (iii) developed high-

resolution LSWT maps to obtain small-scale surface heat flux variations induced by surface temperature heterogeneity (Rahaghi *et al.*, 2019a, 2019c).

These works significantly contribute to the current understanding of spatiotemporal LSWT variability and its corresponding surface heat fluxes. Previous studies have examined the spatial variability of LSWT over Lake Geneva (Oesch *et al.*, 2008, 2005), as well as the impact of small-scale turbulence on over-lake water vapor and vertical energy balance (Vercauteren *et al.*, 2008, 2009, 2011). The latter studies utilized measurements collected from a fixed station located 100 m from the northern shore close to Buchillon (Figure 1-2). Sensible and latent heat fluxes were obtained using the direct eddy covariance method. The present dissertation aims to contribute further to the understanding of surface and near-surface thermal structures in the lake by emphasizing the role of natural slicks.

Global warming's effects on Lake Geneva's thermal structure are evident. Gillet and QuéTin (Gillet and QuéTin, 2006) reported a warming rate of ~0.065 °Cyr^{-1} for the near-surface water temperature of Lake Geneva using 28-year daily recorded data at 2 m on the south bank of the lake. Lemmin and Amouroux (2013) provided a summary of how global warming had impacted Lake Geneva's microclimate and temperature from 1970 to 2010. Their analysis showed a warming trend in the Lake Geneva region, which was most significant in night-time air temperatures, resulting in reduced convective cooling. A similar warming trend (although with considerable interannual variability) was observed in the upper 100 m of the water column, suggesting that this depth range was directly affected by global warming-induced changes to atmospheric forcing. Additionally, a recent study by Lemmin (2020) revealed that although the climate change-induced long-term warming trend seen in the upper layers of the lake was not detected in the deep hypolimnion, interannual climate change-induced variability strongly affected the deep hypolimnion. The present thesis aims to contribute to a better understanding of the lake's response under such changing environmental conditions, especially heat transport at the air-water interface and the near-surface layer, and the crucial role of the surface microlayer in modulating those exchanges.

1.7   Research objectives and approach

With its frequent presence of natural slicks and prevalent low-wind conditions, Lake Geneva presents an optimal site for investigating the effects of surfactant-enriched surfaces on

small-scale interfacial hydrodynamics and exchanges and the large-scale formation and distribution of slicks. This thesis is the first scientific documentation of this intriguing phenomenon on Lake Geneva. It aims to enhance understanding of the following: (i) the role of natural slicks in creating LSWT spatiotemporal variability, (ii) the impact of slicks and other low wind processes on the short-term variability of air-water fluxes, and (iii) the large-scale formation and distribution of slicks in response to underlying meso- to submeso-scale currents in Lake Geneva. Figure 1-3 visually depicts the conceptual relationship between the three chapters, highlighting the small- and large-scale perspectives on slick studies discussed in Sections 1.3 and 1.4. It is important to note that the field campaigns for this thesis were mainly conducted during stratification seasons, with relatively high surface temperatures recorded during the campaigns.
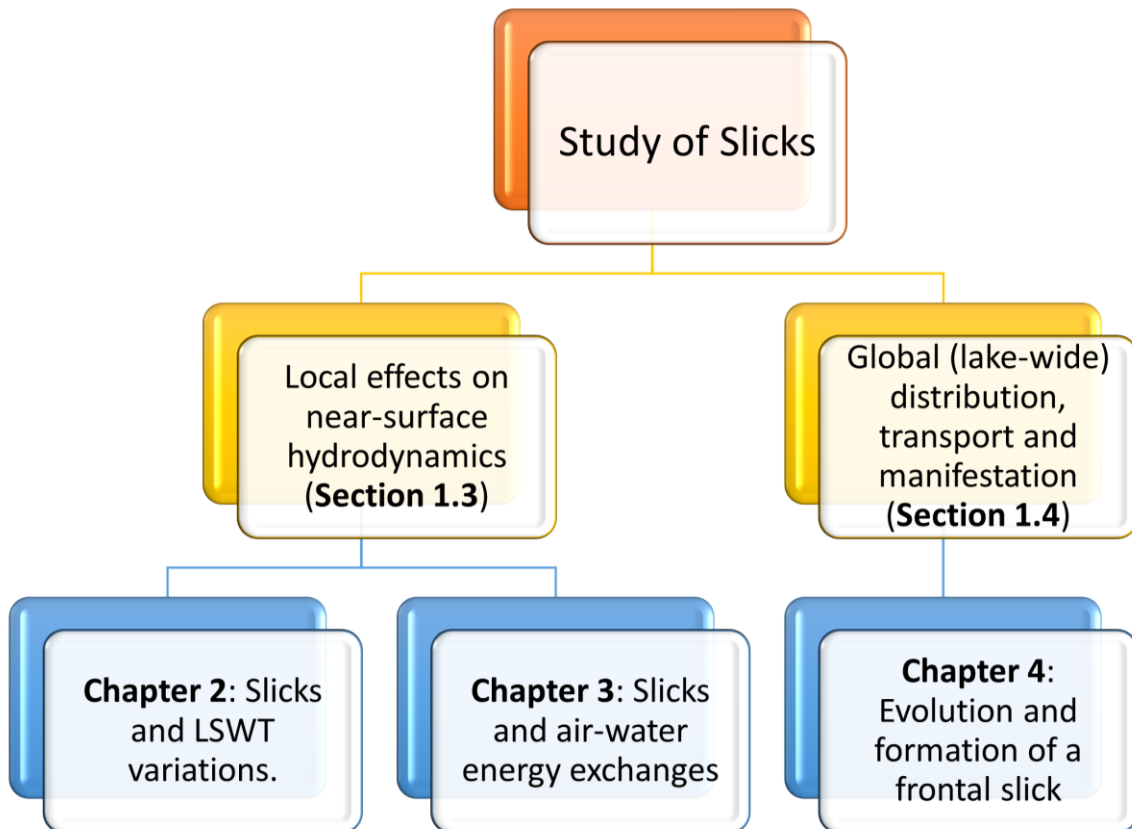
Figure 1-3. The graphic illustration presents an overview of the dissertation. Chapter 2 and Chapter 3 focus on studying slicks in Lake Geneva from a small-scale perspective, examining the local effects of natural slicks on the surface and near-surface temperature and exchanges occurring at the air-water interface. In Chapter 4, the formation and transport of natural slicks on a large scale are explored, offering an explanation for the physical origins of the observed slicks discussed in the preceding chapters.

Below, the measurements and platforms used for the results presented in the following chapters are briefly detailed in the order of their contribution to our analyses.

- An autonomous catamaran called ZiviCat measures near-surface water temperatures (down to 1.5 m) and near-surface currents (0.5 to 1 m depth) on the water-side. On the air-side, ZiviCat is equipped with a meteorological station for wind speed and humidity, as well as a direct flux measurement setup for momentum, sensible and latent heat. Internal measurement units were also used to account for catamaran motion. Additionally, a forward-facing RGB camera recorded images of surface water roughness. All ZiviCat data could be visualized in real-time from the accompanying boat, *Elodea*.

- Several campaigns were conducted to collect SML samples either concurrently with other measurements or individually. To determine surfactant concentrations, smooth patches and the rippled water around the frontal slick were sampled. The uppermost 20-150 µm of the surface was sampled using the glass-plate method, while bulk water (20 cm below the surface) was collected through hand-dipping following standard procedures (Cunliffe and Wurl, 2014). A fluorescence spectrometer was used to analyze the samples later in the laboratory.

- Air-borne and shore-based remote sensing including (i) BLIMP, a helium-filled balloon tethered to the boat, carrying an imaging package that recorded RGB and infrared (IR) images to examine the spatial variability of the Lake Surface Water Temperature (LSWT); and (ii) TLB2, an imaging system installed 192 m above the lake surface on the lake's steeply rising northern shore (Figure 1-2), which captured (angled-view) RGB and IR images that enabled surface slick detection across most of the lake's width. TLB2 also featured remotely controllable tilt and pan angles.

- The lake hydrodynamics during the field measurement campaign were detailed through 3D numerical modeling (MITgcm) of Lake Geneva (Chapter 4), based on the validated model setup of Cimatoribus *et al.* (2018).

- Satellite remote sensing, including (1) AVHRR satellite data with a 1-km grid resolution, was used to obtain whole-lake LSWT images (Riffler *et al.*, 2015), and (2) Sentinel-1 SAR product, although not directly utilized in the thesis, provided background knowledge on the distribution of slicks and their relation to the underlying hydrodynamics (Hamze-Ziabari *et al.*, 2022c).
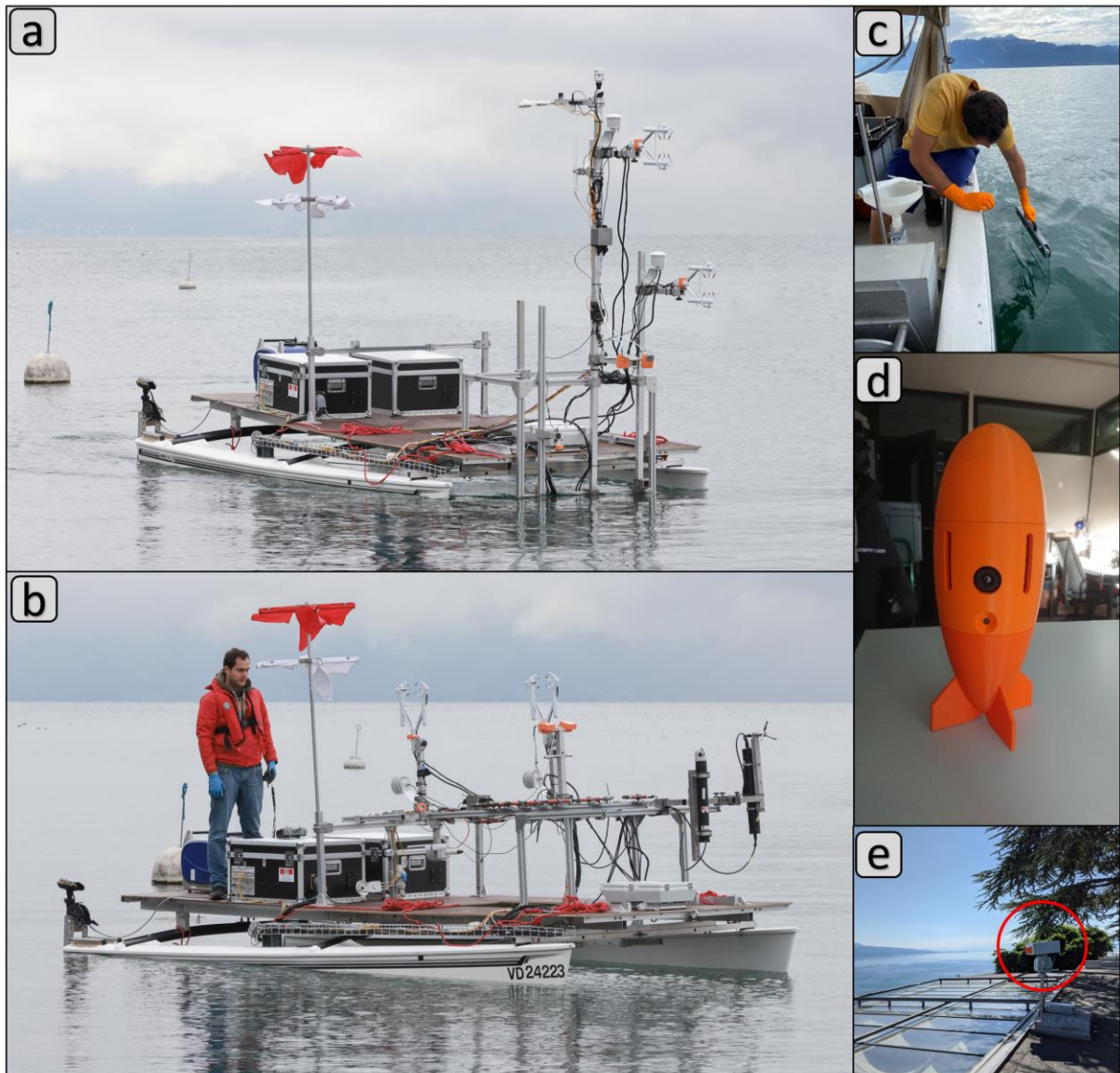
Figure 1-4. In situ and remote sensing measurement tools employed in this dissertation. The left panels show the autonomous catamaran, ZiviCat, used as the primary measurement platform for the studies presented in the following chapters. (a) The air-side sensors include a meteorological station, two sonic anemometers equipped with open-path gas analyzers, and a forward-facing RGB camera. (b) The water-side sensors comprise a near-surface water temperature mast (measuring down to 1.5 m) and near-surface currents assessed through measurements via an Acoustic Doppler Velocimeter (ADV) and a short-range Acoustic Doppler Current Profiler (ADCP). (c) Surface microlayer sampling using a glass plate from the accompanying boat (*Elodea*). (d) BLIMP imaging package. During measurements, this package is attached to a helium-filled balloon. (e) Time-lapse box (indicated by the red circle) used for taking slanted-view images from lake surface water primarily for slick/non-slick detection.

This dissertation is structured as follows:

Chapter 2 examines the potential role of natural slicks in generating small-scale, heterogeneous surface temperature patterns. Using combined ZiviCat-BLIMP measurements in a field campaign in early spring, distinct lateral surface temperature gradients were observed that aligned with slick and non-slick patterns visible on the surface. The study found that these strong temperature gradients are the result of the interplay between three factors: (i) the formation of intense near-surface stratification, (ii) the transition of the surface wave field from calm to the presence of gravity-capillary waves around a wind speed threshold of 1.5m s^{-1}, and (iii) the ability of natural surfactants to damp and inhibit wave growth. These findings differ from previous research on oceanic processes, and the underlying physical mechanisms responsible for this difference are explored in detail.

In **Chapter 3**, a novel approach utilizing underway direct flux measurement is introduced, which enables short-term air-lake exchange variability. Four transects were selected to cover different variations in environmental state variables, primarily under unstable atmospheric stability conditions. The flux measurement was conducted underway on the ZiviCat during these transects, and a shore-based remote imagery system was simultaneously used to monitor the flux footprint on a large scale. Short-term (one-minute) flux variability was analyzed in relation to the presence of slicks, surface and near-surface temperature variations, and wind-wave generation when wind speed oscillates around the 1.5 m s^{-1} threshold. The impact of each environmental factor on air-water energy exchanges is discussed extensively.

In **Chapter 4**, the focus shifts from small-scale patterns to a unique observation of a 10-km frontal slick formation that spans almost the entire width of the lake. Using the ZiviCat-BLIMP measurement platform, the evolution of this large-scale natural slick and its coinciding sharp surface temperature front (0.7 °C in ~10 m) is investigated in the field of view of a shore-based camera package. In situ measurements, numerical simulation results, and a satellite image of surface water temperature are combined to explore the horizontal and vertical large-scale currents that led to the formation of the observed frontal slicks. The interplay of different physical mechanisms, creating strong convergent flows, is examined in light of their implications for the large-scale slick formation and surface material transport.

Finally, **Chapter 5** brings together the key findings of this dissertation and outlines possible research questions to be addressed in the future.

Chapters 2 to 4 are based on manuscripts that have been published in (Chapter 2 and 4) or will be submitted (Chapter 3) to peer-reviewed journals. Therefore, the content of the chapters may be in part repetitive.

Chapter 2   Effects of natural surfactants on the spatial variability of surface water temperature under intermittent light winds on Lake Geneva

Mehrshad Foroughan, Ulrich Lemmin, and David Andrew Barry

Ecological Engineering Laboratory (ECOL), Institue of Environmental Engineering (IIE), Faculty of Architecture, Civil and Environmental Engineering (ENAC), Ecole Polytechnique Fédérale de Lausanne (EPFL), Lausanne, Switzerland

Abstract

The spatial variability of Lake Surface Water Temperature (LSWT) between smooth and rough surface areas and its potential association with the natural surfactant distribution in the surface microlayer were investigated for the first time in a lake. In spring 2019, two different field campaigns were carried out in Lake Geneva to measure: (i) the enrichment factor of Fluorescent Dissolved Organic Matter (FDOM) as a proxy for biogenic surfactants, and (ii) LSWT and near-surface water temperature profiles while simultaneously monitoring water surface roughness in both cases. Results indicate that, under intense incoming short-wave radiation and intermittent light wind conditions, the Atmospheric Boundary Layer (ABL) was stable and the accumulation of heat due to short-wave radiation in near-surface waters was greater than heat losses by surface cooling, thus creating a diurnal warm layer with strong thermal stratification in the water near-surface layer. A threshold wind speed of 1.5 m s^{-1} was determined as a transition between different dynamic regimes. For winds just above 1.5 m s^{-1}, the lake surface became patchy, and smooth surface areas (slicks) were more enriched with FDOM than rough areas (non-slick) covered with Gravity-Capillary Waves (GCW). Sharp thermal boundaries appeared between smooth and rough areas. LSWT in smooth slicks was found to be more than 1.5°C warmer than in rough non-slick areas, which differs from previous observations in oceans that reported a slight temperature reduction inside slicks. Upon the formation of GCW in non-slick areas, the near-surface stratification was destroyed and the surface temperature was reduced. Furthermore, winds above 1.5 m s^{-1} continuously fragmented slicks causing a rapid spatial redistribution of LSWT patterns mainly aligned with the wind. For wind speeds below 1.5 m s^{-1} the surface was smooth, no well-developed GCW were observed, LSWT differences were small, and strong near-surface stratification was established. These results contribute to the understanding and the quantification of air-water exchange processes, which are presently lacking for stable ABL conditions in lakes.

2.1 Introduction

In lakes and oceans, surface water temperature is a key parameter controlling the air-water exchange of heat, momentum, and mass. Surface water temperature and these exchanges are not only influenced by turbulence and waves mainly forced by wind (e.g., Garbe *et al.*, 2004; MacIntyre *et al.*, 2021b), but also by surface surfactant layers (e.g., Frew *et al.*, 2004b; Pereira *et al.*, 2018b). These processes generally show strong spatial variations, manifested by nonuniform surface water temperature patterns, which can affect flux estimates at the air-water interface (Hughes *et al.*, 2012; Rahaghi *et al.*, 2019d), and therefore should be taken into account when addressing climate warming scenarios (Calamita *et al.*, 2021). Although wind-induced surface water temperature dynamics have been investigated (Kawai and Wada, 2007; Zappa *et al.*, 2019), the effect of surfactants on surface water temperature is less documented in oceanic studies (Marmorino and Smith, 2006b), and apparently has never been investigated in lakes.

Surfactants are surface-active substances that can originate from phytoplankton metabolic by-products (Ẑutić *et al.*, 1981b), marine bacterial activities (Kurata *et al.*, 2016b), zooplankton grazing (Kujawinski *et al.*, 2002a) and, in particular for lakes, from terrestrial sources (Hunter and Liss, 1981) introduced by rivers when the riverine inflow reaches the near-surface layer (Masse and Murthy, 1990; Soulignac *et al.*, 2021). The accumulation of natural surfactants in the water surface microlayer attenuates small waves, thus creating smooth surface areas referred to as natural slicks (Gade *et al.*, 2006; Liss and Duce, 1997). Slicks are significantly more enriched with particles and dissolved material compared to surrounding non-slick (rough) surfaces (Garabetian *et al.*, 1993; Wurl *et al.*, 2016). Previous slick vs. non-slick area comparisons in oceans reported higher concentrations of surfactant-associated bacteria (Kurata *et al.*, 2016b), larval fish and microplastics (Gove *et al.*, 2019b) inside the smooth surface layers. Chlorophyll has also been used as a surfactant proxy in estimates of surfactant activity (Tsai and Liu, 2003) and its spatial distribution (De Santi *et al.*, 2019). Under light to moderate wind conditions (< 6 m s^{-1}, McKinney *et al.*, 2012), smooth surfactant-rich slicks and rough/rippled areas with low surfactant concentrations form distinct patches (Figure 2-1) and are distributed on most water bodies (Engel *et al.*, 2017; Romano, 1996).

When surfactants exceed a critical concentration, they alter the surface boundary conditions by introducing non-zero dilational viscoelasticity to the uppermost layer of the water (Frew, 1997). Dilational viscoelasticity links stress and strain at the air-water interface in response to a small

expansion and compression of a surface area (Watson *et al.*, 1997). This affects near-surface hydrodynamics by thickening the water-side viscous sublayer (Tsai, 1996b) and dampening Gravity Capillary Waves (GCW) (Alpers and Hühnerfuss, 1989), which can, in turn, modulate air-water exchanges. Since slick surfaces are smooth compared to those of rough non-slick areas, they can be observed visually (Figure 2-1), or by Synthetic Aperture Radar (SAR) inside convergent zones produced by internal waves (Alpers, 1985; Whitney *et al.*, 2021), Langmuir circulation (Marmorino *et al.*, 2007), mesoscale and submesoscale eddies (Karimova, 2012; McKinney *et al.*, 2012; Schuler and Lee, 2006), and coastal upwelling and filaments (Dabule-viciene *et al.*, 2018; Hamze-Ziabari *et al.*, 2022b). These underlying hydrodynamic processes, along with the direct effect of wind, contribute to the formation, distribution, and disintegration of slick patterns. Such dynamics, however, have not been documented in lakes.

The effect of biogenic surfactants on near-surface hydrodynamics can also result in surface water temperature heterogeneity. In a laboratory experiment, Jarvis (1962b) observed changes in surface temperature by adding artificial surfactants to the water. The temperature shift was either caused by the barrier effect of the surfactant monolayer, preventing evaporation, or by the suppression of near-surface turbulence (Bower and Saylor, 2011a). The latter effect is predominant in natural environments, and biogenic surfactants typically do not show barrier-like behavior (Liss, 1983b). Frew et al. (2004b) and Marmorino and Smith (2006b) reported that slicks are slightly colder than the surrounding non-slick water in the ocean under unstable ABL conditions and surface cooling. Under strong solar radiation and low wind conditions, a thin warm near-surface layer develops in the water when solar heating exceeds heat loss from the water surface, and as a result, a Diurnal Warm Layer (DWL) (Price et al., 1986) or a diur-nal thermocline (Imberger, 1985) is formed. Past slick field studies compared the surface wa-ter temperature to the bulk temperature (assumed constant), measured well below the water surface (Marmorino and Smith, 2006b). However, DWL formation and temperature gradients in the near-surface layer were not considered in their analyses.

Figure 2-1. a) Aerial view of slick and non-slick areas on the surface of Lake Geneva (for location, see Figure 2-2) recorded in April 2021 by a remotely-operated camera system (RGB) installed 195 m above the lake surface water and ~440 m away from the shore. This is a typical example of surface patterns frequently observed anywhere on the lake under stable atmospheric boundary layer conditions and low wind (solid-line arrows indicate direction and speed). Smooth slick and rough/rippled non-slick areas are easily distinguishable due to differences in the surface reflection; smooth slicks are more visible because of their increased specular light reflection. b) and c) Slick distribution under higher wind speed conditions (taken in March 2021). With increasing wind speed, slick areas decrease and eventually transform into streaks parallel to the wind. Dashed-line double arrows give length scales. Analysis of surface water samples during those two days showed higher organic matter enrichment inside slicks (data not shown).

The effect of biogenic surfactants on near-surface hydrodynamics can also result in surface water temperature heterogeneity. In a laboratory experiment, Jarvis (1962b) observed changes in surface temperature by adding artificial surfactants to the water. The temperature shift was either caused by the barrier effect of the surfactant monolayer, preventing evaporation, or by the suppression of near-surface turbulence (Bower and Saylor, 2011a). The latter effect is pre-dominant in natural environments, and biogenic surfactants typically do not show barrier-like behavior (Liss, 1983b). Frew *et al.* (2004b) and Marmorino and Smith (2006b) reported that slicks are slightly colder than the surrounding non-slick water in the ocean under unstable ABL

conditions and surface cooling. Under strong solar radiation and low wind conditions, a thin warm near-surface layer develops in the water when solar heating exceeds heat loss from the water surface, and as a result, a Diurnal Warm Layer (DWL) (Price *et al.*, 1986) or a diurnal thermocline (Imberger, 1985) is formed. Past slick field studies compared the surface water temperature to the bulk temperature (assumed constant), measured well below the water surface (Marmorino and Smith, 2006b). However, DWL formation and temperature gradients in the near-surface layer were not considered in their analyses.

Air-water exchange dynamics are different under stable and unstable Atmospheric Boundary layer (ABL) (Kara *et al.*, 2005; Mahrt and Hristov, 2017). Although near surface dynamics under stable ABL conditions have been studied in lakes during events (e.g., Yusup and Liu, 2016; Rahaghi *et al.*, 2019b), their potential differences in slick and non-slick areas under stable ABL and light wind conditions during DWL formation have not yet been reported. However, these differences can strongly affect air-water exchange. In Lake Geneva, it was shown that winds are light (< 4 m s^{-1}) 80 - 90% of the time during the stratification period (May to October; (Lemmin and D'Adamo, 1996a). Stable ABL conditions have been observed to last for several months in spring and early summer (Lemmin, 2020; Rahaghi *et al.*, 2019e), thus indicating that stable ABL, low wind conditions are important in the annual air-water exchange cycle.

The present study, carried out in Lake Geneva, will therefore, for the first time in a lake, explore the effect of light wind and surfactants on the spatial variability of Lake Surface Water Temperature (LSWT) under stable ABL conditions. In a novel approach, high-resolution near-surface water temperature profiles were combined with surface temperature measurements and real-time monitoring of water surface roughness. The following questions are addressed:

- Can the ability of surfactants to form slicks and affect wind wave development influence the near-surface thermal structure? If so, under what conditions?
- What is the potential relationship between LSWT variability and natural surfactants in the surface microlayer as a function of wind speed? Is there a wind speed threshold?
- What is the LSWT difference between smooth slicks and rough surface areas during DWL formation? What causes this difference?

2.2   Materials and methods

2.2.1   Study site

In 2019, two field measurement campaigns were performed on Lake Geneva (Local name: Lac Léman), a warm oligomictic perialpine lake situated between Switzerland and France at a mean altitude of 372 m. It is Western Europe's largest lake with a length of 70 km, a maximum width of 14 km, a surface area of 582 km^2, a volume of 89 km^3, and a maximum depth of 309 m (Figure 2-2a). The surrounding mountainous topography strongly affects the wind field and, as a result, the shear stress distribution over the lake (Rahaghi *et al.*, 2019d; Razmi *et al.*, 2018). In addition to the two strong dominant winds called *Bise* and *Vent*, fishermen have identified over 20 local wind fields that often have low wind speeds and only act on parts of the lake surface.

2.2.2   Measurement platforms for physical parameters

Measurements were taken from a mobile, two-platform system consisting of: (i) a 7-m long autonomous catamaran (called ZiviCat), and (ii) a 9-m^3 balloon (called BLIMP) carrying an imaging package beneath it (Figure 2-3). The ZiviCat is equipped with a set of in situ near-surface (down to 1.5 m) water temperature sensors (RBRsolo, accuracy: 0.002°C, 1 Hz), a weather station (Airmar 200WX IPX7) installed at 3-m height, with motion-corrected outputs for wind speed, wind direction, and air temperature (0.66 Hz), a relative humidity sensor at 2.8-m height (1 Hz), and an RGB Raspberry Pi camera at 1.2-m height that captures images of the lake surface in front of the ZiviCat for a qualitative measure of surface roughness. The sensor spar is located well forward of the catamaran to avoid hull disturbances. The ZiviCat also has positioning (RTK-GPS), stability (IMU), data recording, and communication systems, which allow for real-time data control, correction and analysis on the accompanying boat (Barry *et al.*, 2019).
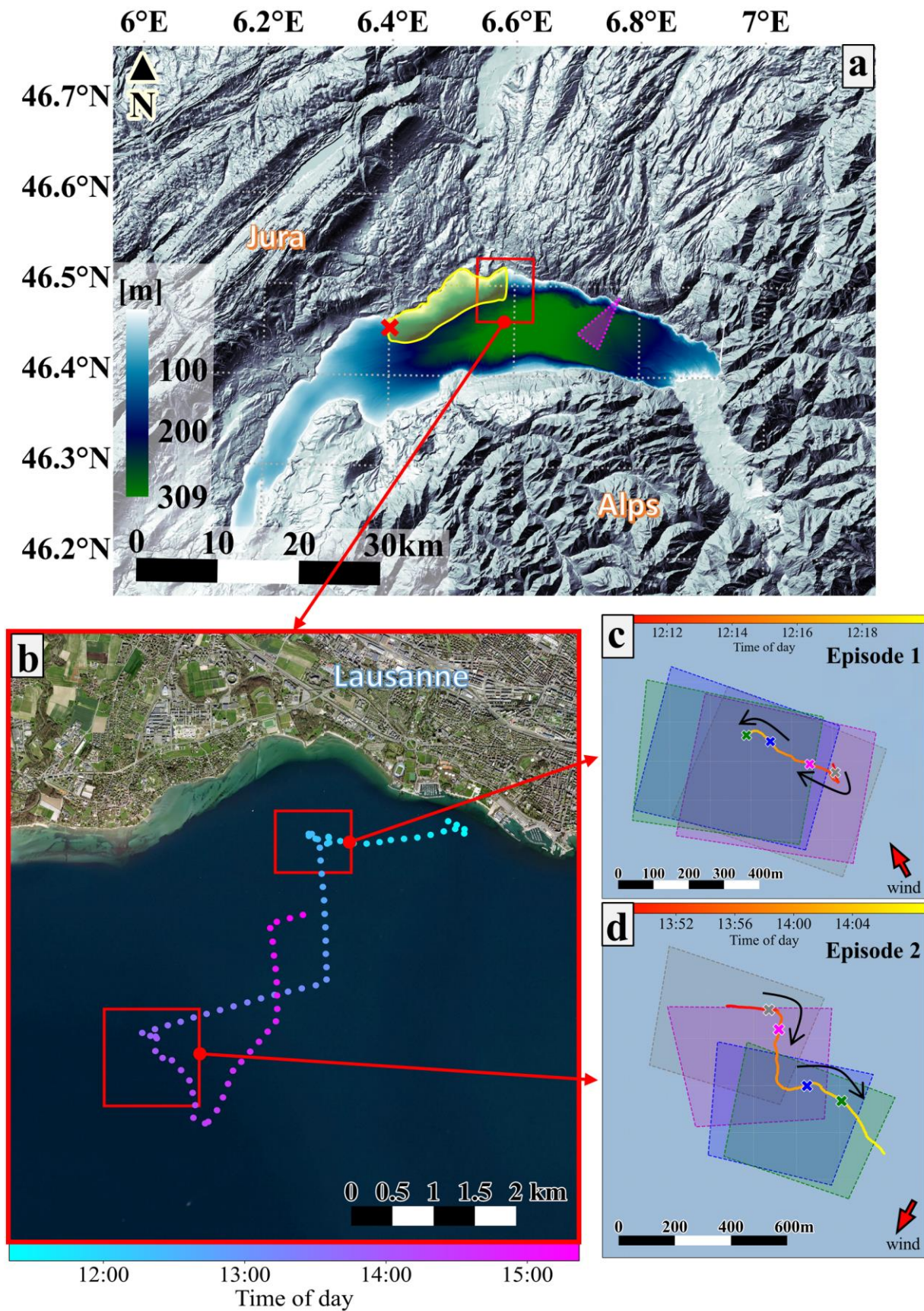
Figure 2-2. a) Location and bathymetry of Lake Geneva, and the topography of the mountain ranges surrounding the lake, i.e., the Alps to the southeast and the Jura to the northwest. The magenta triangle shows the approximate field of view of the camera system in Figure 2-1. The yellowish region along the lake's northern shore represents the area where water sampling campaigns were conducted. The red square delimits the study area. The red X marks the meteorological station Buchillon. b) Zoom of red square in (a) showing the catamaran ZiviCat track in the northern part of Lake Geneva near Lausanne on 18 April 2019. The red squares indicate the sites of the two episodes. c) and d) Zooms of the study sites in b). The four colored rectangles illustrate the geo-referenced spatial extent of the thermal snapshots in Figure 2-6 and Figure 2-7. The gray, magenta, blue, and green areas and the symbols along the tracks correspond, respectively, to panels c, d, e, and f of those figures. In all panels, colorbars indicate the time along the catamaran tracks. Black arrows in c) and d) show the direction of the catamaran movement. Red arrows give the mean wind direction during the episodes.
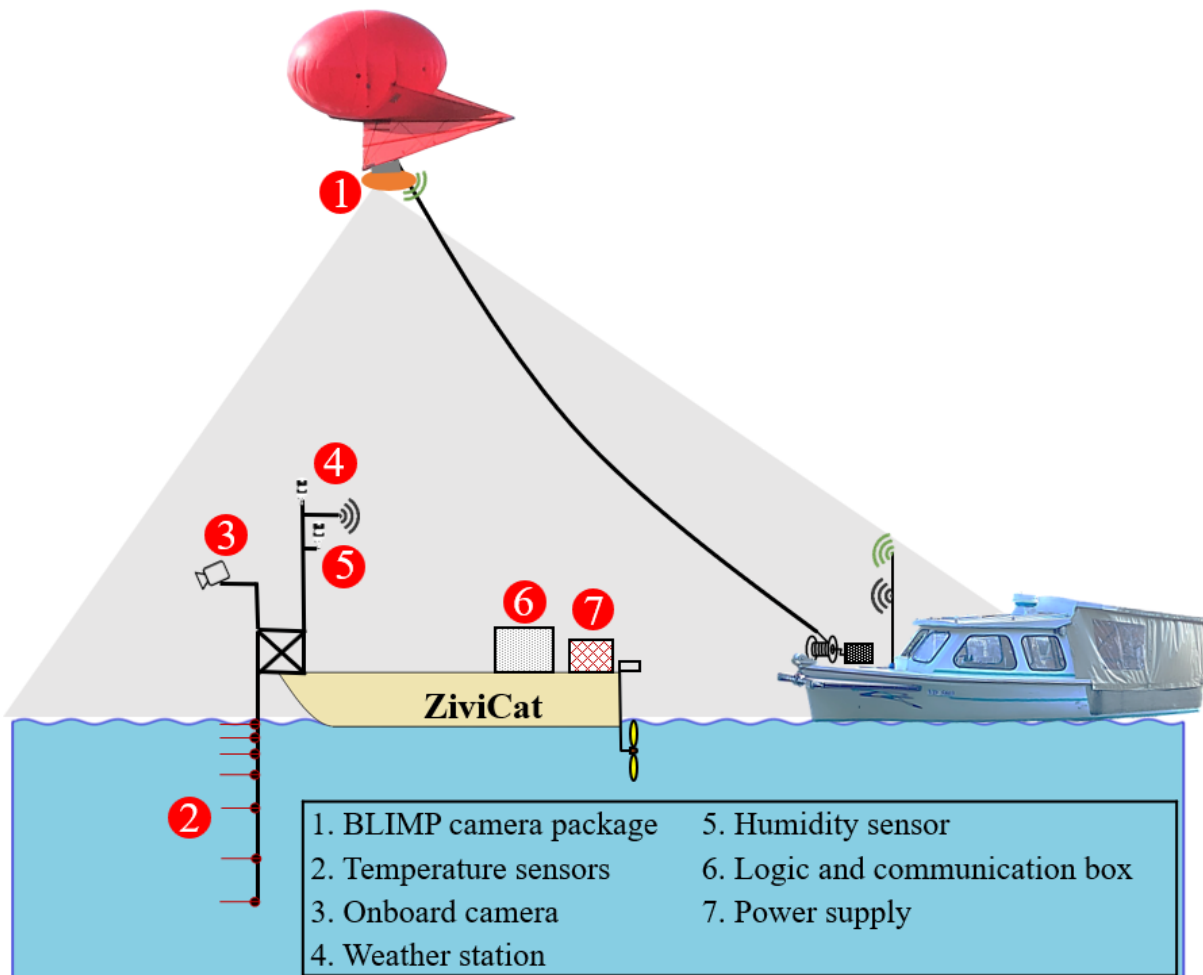
Figure 2-3. Schematic of the mobile two-platform measurement system consisting of the 9-m³ balloon called BLIMP and the remotely operated catamaran called ZiviCat. Data collected by the BLIMP and ZiviCat were transmitted to the accompanying boat, the *Elodea*, where they could be visualized in real time. The legend identifies the different sensors on the BLIMP and the ZiviCat.

The BLIMP is tethered to a winch on the accompanying boat (Figure 2-3). For the measurement campaign, the balloon was positioned approximately 500 m above the lake surface, which resulted in a surface spatial resolution of 0.8 m and an image width of about 400 m. The imaging package includes a FLIR Tau 2 Long-wave Infrared (IR) camera (7.5-13.5 µm spectral range, 640×512 pixel resolution, 14-bit digital output) and an RGB Raspberry Pi camera for visual inspection, as well as equipment for positioning (GPS), orientation, tilt angles, and communication with the boat (Liardon and Barry, 2017a). BLIMP images were corrected for nonuniformity, i.e., spatial noise caused by different detector responses in the focal plane array (the core of an uncooled IR sensor), following a two-point calibrated-based method (Rahaghi *et al.*, 2019a), as well as temporal drift. The pretreated images were then radiometrically calibrated using the temperature measurements taken at 5-cm depth by the ZiviCat. Despite the correction, some residual errors can remain in the thermal images' upper left and lower right corners (Figure 2-6 and Figure 2-7; (Rahaghi *et al.*, 2019a). Therefore, those regions should be interpreted with caution. The uncertainty associated with emissivity variation due to surface roughness modulations is negligible with a low bias, since the incident angle ($< 10°$) for image acquisition of the BLIMP package is low (Cheng *et al.*, 2019; Zappa *et al.*, 2019). The mobile ZiviCat-BLIMP system allowed following water mass parcels in real time as they transformed from smooth slicks areas to rough/rippled areas and vice versa.

2.2.3   Field Campaign 1: Surface water sampling and surfactant analysis

In situ measurement of the viscoelastic modulus provides the most direct evidence for determining the slick's ability to modulate wind-wave development and air-water exchanges (Watson *et al.*, 1997). However, in previous ocean studies, slick and non-slick regions were usually classified by measuring a proxy for surfactant concentration in water samples. Simultaneous water sampling during the ZiviCat/BLIMP measurements was not possible due to the different strategies required for each campaign. Therefore, in order to establish a reliable database on surfactant dynamics, separate water sampling field missions were conducted from 10:00 to 14:00 (local time) on 22 January, 15 February, 21 March, and 17 July 2019 in an area off the lake's northern shore (Figure 2-2a). A meteorological station (Buchillon mast; red X in Figure 2-2a) near the sampling sites recorded no clouds and the following wind speeds on these four days: 1.53 ± 0.45, 1.3 ± 0.35, 3 ± 0.55, 1.8 ± 0.35 m s^{-1}, respectively. The maximum solar radiation increased from 480 W m^{-2} in January to 980 W m^{-2} in July, while atmospheric

stability changed from unstable to stable. Surface water samples were taken from visually-identified areas of smooth and surrounding rippled water. Such surface roughness patterns are typically generated in Lake Geneva under low wind conditions (e.g., Figure 2-1), and can form anywhere on the lake. The glass-plate method was used to collect the uppermost 20-150 µm of the surface (Cunliffe *et al.*, 2013b) as well as hand-dipping to sample bulk water (20 cm below the surface) following standard procedures (Cunliffe and Wurl, 2014). The samples were brought back to the laboratory for further analysis, usually performed on the same day.

The enrichment of Fluorescent Dissolved Organic Matter (FDOM) was chosen as a proxy for biogenic surfactants (Frew *et al.*, 2002; Salter, 2010). Samples were analyzed in a Fluorescence Spectrometer (Perkin Elmer) that provided an Excitation Emission Matrix (EEM) for each sample (Figure 2-4a). The EEM was constructed by assembling emission spectra (250-600 nm) within a range of excitation wavelengths (250-550 nm). Since different organic materials fluoresce differently, one or several peaks (components) can appear in the EEM. To determine the location of peaks (emission/excitation wavelength) and the contribution of each sample to that peak, parallel factor analysis was applied (PARAFAC, see Stedmon and Bro, 2008) to the EEMs of all samples (Figure 2-4b).

Following Frew *et al.* (2002), the component close to 450 nm (emission) was selected to compute the Enrichment Factor (EF) for each sample set (surface and bulk). However, other peaks (components) appeared in the EEMs. The EF is calculated as the ratio of surface fluorescence intensity to the bulk values, which is proportional to the EF of surfactant activity (Salter, 2010). A permutation test was performed to compare the samples from slick and non-slick areas (Gove *et al.*, 2019b) in order to estimate the probability that the mean enrichment factor of FDOM inside a slick (EFi) is larger than that in the ambient water (EFo), i.e., P(EFi > EFo). To compute this probability, we first permutated the labels (slick or non-slick) randomly for all samples, then recalculated the test statistic (EFi - EFo). After sufficient permutations (e.g., 10,000), an approximate distribution of the test statistic can be obtained. The p-value was then calculated, which is the probability of getting a larger difference of mean EFs than the difference in the original data.
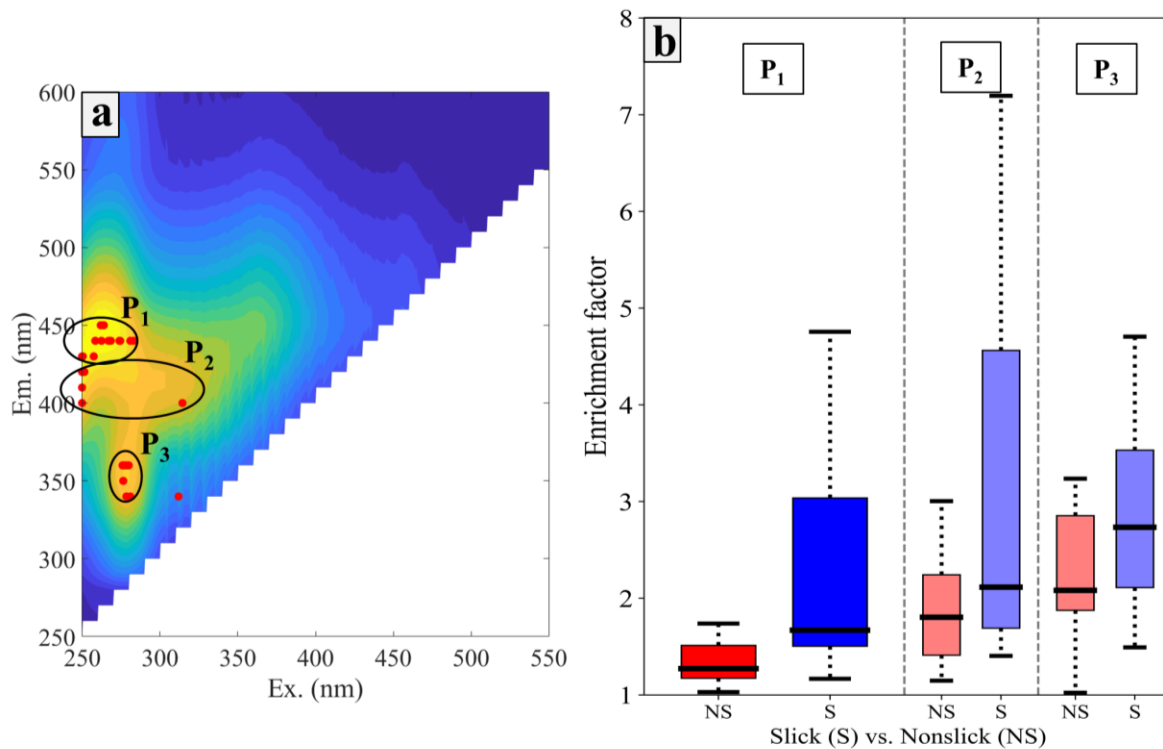
Figure 2-4. a) The integration of the three components (peaks) P1, P2, and P3 identified with PARAFAC analysis. On the plot, the dominant peaks in each sample (obtained prior to PARAFAC analysis) are displayed as red dots, with black ellipses grouping them into three categories based on Murphy *et al.* (2008). b) Box plot of the FDOM enrichment factor for components P1, P2, and P3 observed in the EEM matrix. Red/blue boxes show the interquartile range (25-75%) for Non-slick (NS) and Slick (S) areas, respectively, and tails (dashed lines) indicate the 1-99 percentile range. Heavy black lines in the boxes are the medians.

2.2.4 Field Campaign 2: LSWT patterns and near-surface stratification

The ZiviCat/BLIMP measurements were made on 18 April 2019 in the daytime under high solar radiation (maximum above 700 W m^{-2}) and low-wind conditions (< 2.5 m s^{-1}) during the early stages of the seasonal stratification period. Vigorous biological activity occurs (CIPEL, 2019), and high solar radiation creates a warm layer below the air-water interface (Fairall *et al.*, 1996b). Measurements were taken more than 1.5 km from the northern shore of the lake (Figure 2-2b). During the measurement period, there were several short (20 min) and very short (2 min) events when the wind speed exceeded 1.5 m s^{-1}. The BLIMP imaging package simultaneously captured the corresponding development of thermal water surface patterns on a larger scale.

The transient and random nature of the contrast between smooth slicks and rippled surface areas was captured by the contrast in the BLIMP images. During the measurement campaigns, we

located potentially interesting measurement areas using the infrared imagery from the BLIMP and RBG images from the ZiviCat, as well as by direct visual inspection of the state of the water surface from the accompanying boat. The ZiviCat was moved to these areas via remote control. The irregular ZiviCat tracks observed in the images (Figure 2-2b, Figure 2-6, Figure 2-7) reflect this strategy.

2.3 Results

2.3.1 Surfactants in the surface microlayer

Twenty-eight water sample sets were selected (surface and bulk) and separated into two groups: those coming from slick areas and those from non-slick areas. The enrichment factor was usually > 1 for the smooth slicks and rippled non-slick areas (Figure 2-4b, Salter, 2010). The p-value associated with the permutation test, which corresponds to the Excitation Emission Matrix (EEM) component close to 450 nm, was 0.022. This maximum, labeled P1 in Figure 2-4, corresponds to classic "A" peak regions identified by Coble (1996), representing terrestrial humic substances (Murphy *et al.*, 2008). Similar results were obtained by analyzing the remaining Fluorescent Dissolved Organic Matter (FDOM) peaks (P2, P3; Figure 2-4). Note that the dominant peak can be different for each sample set. For P1, the boxes for the slick and non-slick areas are clearly separate (higher p-value), whereas at P2 and P3 they overlap, and median values are no longer distinct. From the results, a systematic spatial variability of FDOM between smooth slicks and rough non-slick areas is evident, with wider scatter in the slicks (Figure 2-4b). For all three peaks, the interquartile range of the slick areas is significantly larger than that of the non-slick areas.

2.3.2 Air-water boundary layer

On 18 April 2019, incoming solar radiation, measured by a radiometer on the stationary platform LéXPLORE (Wüest *et al.*, 2021), located ~6 km away from our study site, increased steadily throughout the morning (Figure 2-5a). To calculate the heat budget, surface heat flux terms were determined based on the in situ ZiviCat data and the measured incoming solar radiation. The heat budget in Figure 2-5a is composed of solar short-wave radiation ($Q_{sw\downarrow}$) and surface cooling which is calculated as:
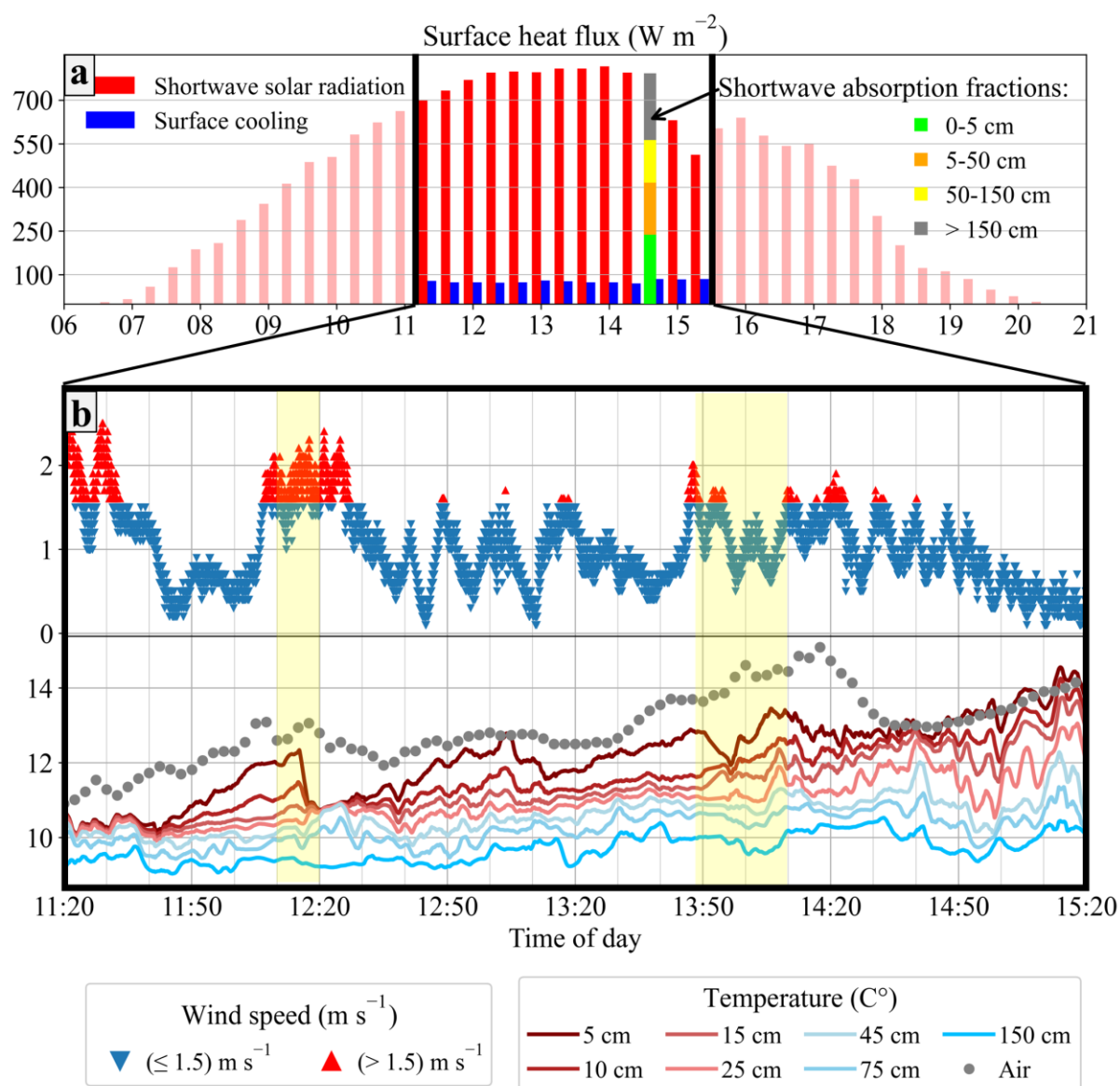
Figure 2-5. Surface energy budget and observed in situ parameters on 18 April 2019. a) Incoming short-wave radiation (red) is compared to surface cooling (blue) due to long-wave radiation, sensible and latent heat fluxes. The diurnal variation in short-wave radiation was measured, whereas the cooling terms were calculated based on the observed parameters from 11:20 to 15:20 (local time). Outside this observation period, shortwave radiation is shown in light red. The absorption fractions of incoming short-wave radiation for different layers in the water are given at 14:30; the legend indicates the depth ranges. b) Time series of wind speed (top panel; m s^{-1}) and air temperature and near-surface water temperature (bottom panel; °C) from 11:20 to 15:20. The temperature data were smoothed using a 2-min moving average. Yellow shaded bands mark Episodes 1 and 2, respectively. Wind speeds above and below 1.5 m s^{-1} are indicated in red and blue, respectively. The legend for temperature gives the water depth of the sensor.

$$Q_{cooling} = Q_{lw\uparrow} - Q_{lw\downarrow} + Q_{lat} + Q_{sen} \qquad 2\text{-}1$$

where $Q_{lw\uparrow}$ is outgoing long-wave radiation, $Q_{lw\downarrow}$ is incoming long-wave radiation, Q_{lat} is latent heat flux and Q_{sen} is sensible heat flux. We selected bulk models for the heat budget analysis (Table 2-1) based on a multi-annual two-point calibration for Lake Geneva (Rahaghi *et al.*, 2018). For roughness lengths and incoming long-wave radiation calculations, calibrated values for Lake Geneva were applied (Rahaghi *et al.*, 2018). For incoming radiation, the cloud cover fraction (C) was determined as C = 1 – s, where s is the ratio of the measured short-wave radiation to clear-sky short-wave radiation, which was calculated following Crawford and Duchon (1999) based on the methods of Meyers and Dale (1983). The latent and sensible heat fluxes were calculated using the Monin-Obukhov similarity theory and empirical relationships by estimating turbulent stability functions and roughness lengths for wind, temperature and humidity (Rahaghi *et al.*, 2018; Zeng *et al.*, 1998). The atmospheric stability parameter was calculated as $\zeta = z/L_{MO} = 0.93$, where z is the measurement height for wind speed, and L_{MO} is the air-side Monin-Obukhov length obtained from averaged values during the entire measurement period; the Monin-Obukhov length will be discussed in the Discussion section. During the measurement period, short-wave radiation clearly dominated the surface heat budget, with surface cooling having a negligible effect under such low-wind conditions. Water surface temperatures were clearly below the air temperature (Figure 2-5b). Due to the resulting downward heat flux, the near-surface water temperature increased (Figure 2-5b) at all levels in the near-surface water column during the measurement period. The absorption profile of the incoming shortwave radiation in the water was estimated as:

$$f(z) = \sum_{i=1}^{n} F_i\left[1 - \exp\left(-k_{d_i}z\right)\right] \qquad 2\text{-}2$$

where n is the number of wavelength bands, F_i are the fractions of solar energy in each band, and k_{d_i} are the corresponding attenuation coefficients. We estimate $Q_{sw\downarrow}(z) = f(z)Q_{sw\downarrow}(0)$ as the amount of solar radiation absorbed down to depth z; for $Q_{sw\downarrow}(0)$, see Table 2-1. For ultraviolet and infrared bands, we used the attenuation coefficients provided by Olesen and Maberly (2001) and Jellison and Melack (1993), respectively, as summarized in Woolway *et al.* (2015). Visible light, accounting for less than half ($F_i = 0.42$) of incoming solar radiation (Gueymard *et al.*, 2002), can penetrate into deeper layers. As a result, its attenuation coefficient depends on

the transparency of near-surface water. This data was not available for our field campaign; instead, hyperspectral underwater irradiance measurements made with an autonomous profiler (Minaudo *et al.*, 2021) the following year during the same period at the LéXPLORE platform were used to estimate $k_{d_{visible}}$. In the second half of April 2020, the weighted average of spectral attenuation coefficients was calculated as $\overline{k_d} = 0.45 \pm 0.05$ m^{-1}, and was implemented in the calculations (Figure 2-5a). Most of the solar radiation was absorbed in the layer closest to the surface (Figure 2-5a), where the temperature increase was strongest.

Table 2-1. Bulk models for radiative, sensible, and latent heat fluxes. The calibrated values for Lake Geneva are indicated by coefficients $\mathcal{C}_i$. Details are given in Rahaghi *et al.* (2018).

Surface heat flux	Formula	Reference
Incoming shortwave radiation	$$Q_{sw\downarrow} = Q_{sc}F_{dir}(1 - A_{dir}) + Q_{sc}F_{diff}(1 - A_{diff})$$ $$F_{dir} = (1 - C)[(1 - C) + \frac{C}{2}]^{-1}$$ $$F_{diff} = 1 - F_{dir}$$	Cogley (1979); Fink *et al.* (2014)
Incoming longwave radiation	$$Q_{lw\downarrow} = \varepsilon_{atm}\sigma(T_{air} + 273.15)^4$$ $$\varepsilon_{atm} = 1.24\mathcal{C}_1(1 + \mathcal{C}_2 C^2)\left(\frac{e_a}{T_{air} + 273.15}\right)^{1/7}$$ $$\mathcal{C}_1 = 0.983, \mathcal{C}_2 = 0.11$$	Brutsaert (1975)
Outgoing longwave radiation	$$Q_{lw\uparrow} = \varepsilon_{water}\sigma(T_{water} + 273.15)^4$$	-
Latent and Sensible heat flux	$$Q_{lat} = \rho_{az}L_v u_* q_*, Q_{sen} = \rho_{az}C_{p,a}u_* T_*$$ $$f_m(\zeta) = \frac{\kappa z_u}{u_*}\frac{\partial u}{\partial z}, f_e(\zeta) = \frac{\kappa z_q}{q_*}\frac{\partial q}{\partial z}, f_h(\zeta) = \frac{\kappa z_t}{T_*}\frac{\partial T}{\partial z}$$ $$\zeta = \frac{z}{L_{MO}} = \frac{z\kappa g\left[\frac{Q_{sen}}{C_{p,a}} + 0.61\frac{(T_{a,z} + 273.15)Q_{lat}}{L_v}\right]}{\rho_{az}u_*^3 T_v}$$ $$z_0 = 0.013\,u_*^2/g + \mathcal{C}_3\,\nu_a/u_*$$ $$z_{0q} = z_{0t} = z_0\exp[-\mathcal{C}_4(u_* z_0/\nu_a)^{0.25} + 2.57]$$ $$\mathcal{C}_3 = 0.01, \mathcal{C}_4 = 1.52$$	Monin and Obukhov (1954)

Two episodes of different wind conditions were investigated in detail (yellow shaded bands in Figure 2-5b), hereinafter called Episode 1 and Episode 2.

2.3.3   Episode 1: Wind speed mostly above 1.5 m s^{-1}

During Episode 1, the ZiviCat moved continuously along the track shown in Figure 2-2c. The wind speed first progressively increased and then remained just above 1.5 m s^{-1} (Figure 2-6a). The wind direction remained nearly constant (onshore winds; Figure 2-2c). The air temperature was higher than the LSWT (Figure 2-6b). In the early stage, LSWT spatial gradients were relatively small, the near-surface water layer was strongly stratified, and there were only low amplitude swells on the surface (Figure 2-6b, c). As the wind continued to blow, slick/non-slick patterns appeared on the water surface. Surface and near-surface conditions hardly changed while the ZiviCat operated inside the slick (Figure 2-6d). Tracks of the ZiviCat and the boat movements, which disturbed the stratification and caused upwelling of colder water to the surface, are clearly visible. When a sharp front between the slick and a larger cold area appeared in the BLIMP thermal images, we navigated the ZiviCat towards that front (thermal contrast of up to 2°C). This thermal front coincided with a surface roughness gradient, i.e., a slick/non-slick boundary. Figure 2-6e shows where the ZiviCat just passed the front and entered the cold area. The very rapid drop in LSWT and near-surface water temperatures is evident in the thermal image (Figure 2-6e) and the temperature time series (Figure 2-6b), respectively. Simultaneously, small well-developed sharp-crested GCW appeared in the RGB image as the Zivicat entered the non-slick area (Figure 2-6e). In the last panel (Figure 2-6f), the ZiviCat was entirely inside the cold/rippled area. The GCW were well-developed, and the stratification in the upper 25 cm of the water column had disappeared, with temperatures in that layer below those in the warm slick (Figure 2-6b, c).
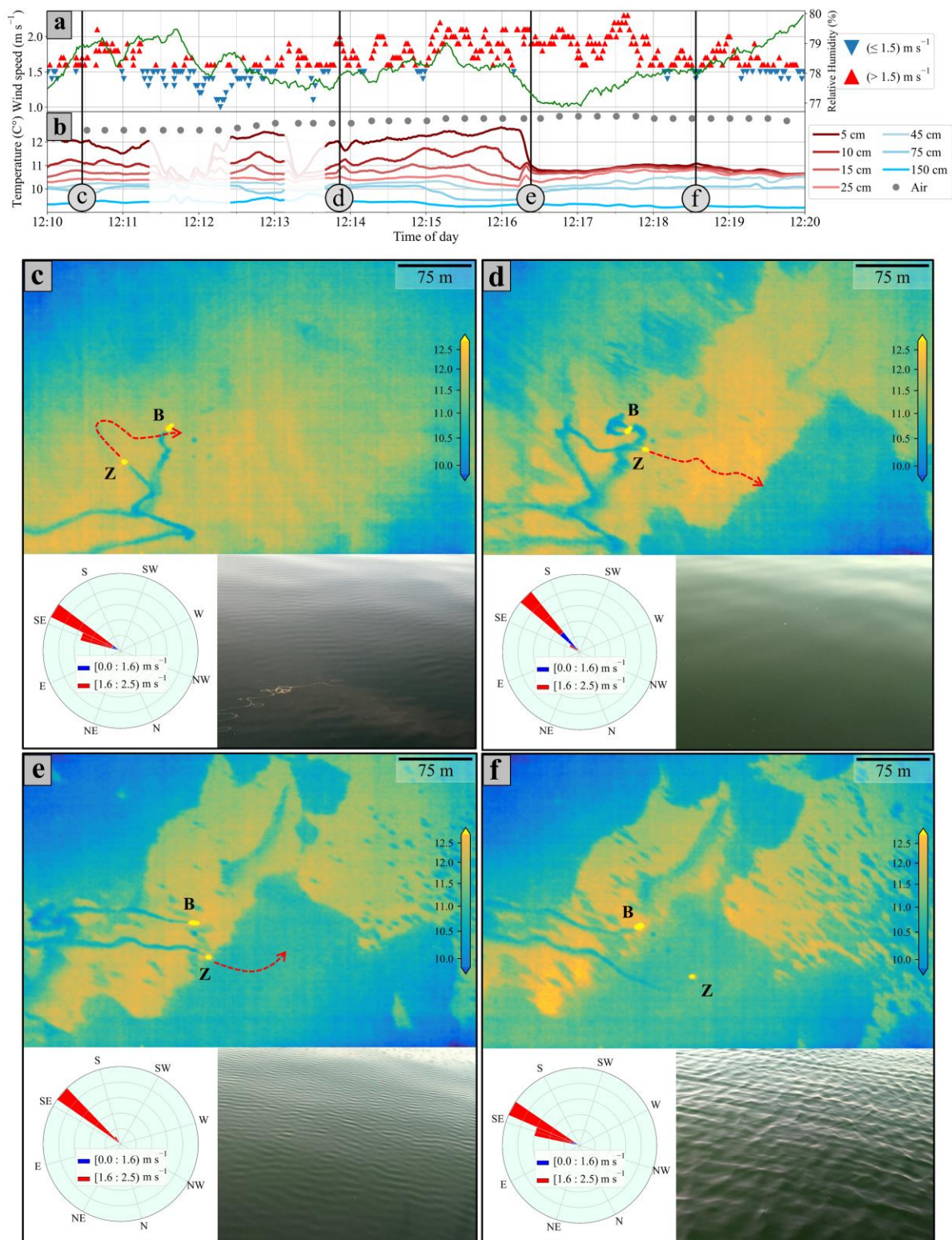
Figure 2-6. Surface temperature and roughness evolution during Episode 1 with wind speed > 1.5 m s^{-1}. a). Wind history and Relative Humidity (RH; green line) during this time window. b) Time series of the near-surface water temperatures at different depths and air temperature at 3-m height between 12:10 and 12:20 (local time). Two sharp temperature drops at ~12:12 and 12:13, indicated by the lighter colored segments, occurred when the ZiviCat traversed boat

40

tracks, which had caused upwelling of cold water. c)-f) Four snapshots at different times are marked by vertical bars in a) and b). Each panel consists of (clockwise): (i) a thermal image taken by the BLIMP (top; the ZiviCat and the accompanying boat are marked with letters Z and B, respectively; the colorbar indicates water temperature in °C), (ii) a ZiviCat RGB camera image of the lake surface (bottom right), with near- and far-field distance scales of 1.2 and 4.5 m (Gerum *et al.*, 2019), respectively, and (iii) a wind rose diagram showing the wind magnitude and direction (bottom left). Wind data present one-min averages. The North on the rose diagram is aligned with the North in the IR images, and thus, the wind direction can be superimposed onto the thermal images. The tracks of the ZiviCat (Z) and the boat (B) in the thermal images are caused by upwelling of colder water (propellers at ~30-cm and ~50-cm depth, respectively). In each thermal image, the ZiviCat trajectory from one image to the next is approximated by a red dash-lined arrow. Colder upper left and lower right corners of the thermal images are artifacts (Rahaghi *et al.*, 2019b).

The thermal images in this sequence also show the rapid time evolution of surface water temperature in response to forcing by steady winds exceeding the 1.5 m s^{-1} threshold. In the upper right and lower left sectors of the thermal images, large areas of colder water progressively expanded (Figure 2-6d-f). At the same time, in the upper right sector, within the large warm slick, many small "islands" of colder water appeared almost simultaneously. They stretched in the wind direction and continuously increased in size and number within minutes (Figure 2-6e, f).

2.3.4   Episode 2: Wind speed mostly below 1.5 m s^{-1}

After ~12:25, the wind speed remained low for 1.5 h, rarely exceeding the threshold of 1.5 m s^{-1}, and surface heating by solar radiation continued (Figure 2-5). The second episode of interest occurred at ~13:50 when wind speed exceeded 1.5 m s^{-1} during two short intervals (each about 2 min) (Figure 2-7a). The wind direction remained nearly constant (off shore winds; Figure 2-2d). The ZiviCat continuously moved along the track indicated in Figure 2-2d.

The time evolution of surface roughness, LSWT, and wind data during Episode 2 is shown in Figure 2-7c-f. LSWT was almost uniform in the center of Figure 2-7c, even though GCW started to form. Two brief periods of wind speeds > 1.5 m s^{-1} generated wind-induced small ripples on the water surface, as seen in the RGB images (Figure 2-7c, d). However, the GCW appear not to be as sharp-crested as in Figure 2-6f. There was a stronger near-surface stratification compared to Episode 1 (Figure 2-7b) due to continued strong solar radiation and low wind speed.
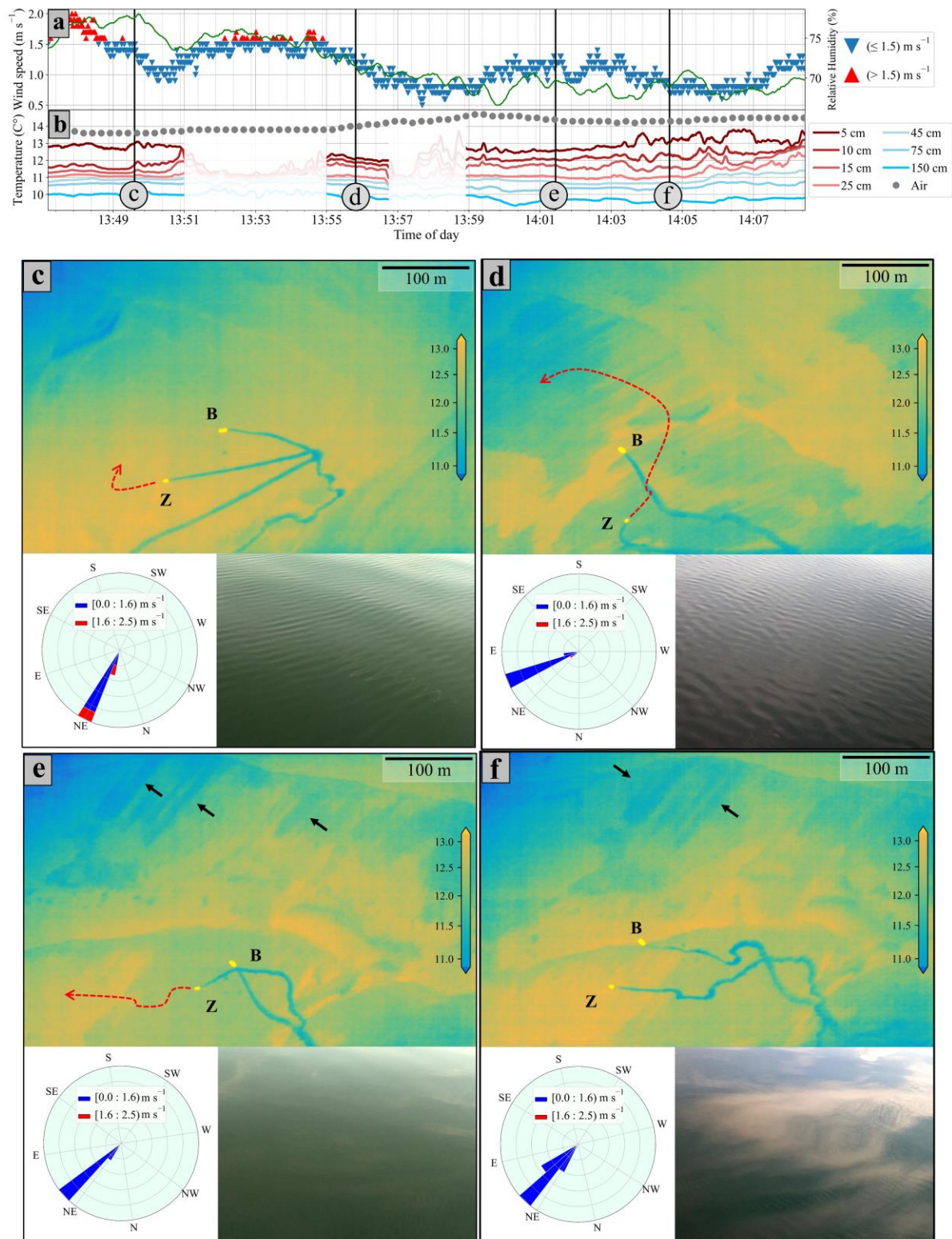
Figure 2-7. Surface temperature and roughness evolution during Episode 2 at low wind speed. See the caption of Figure 2-6 for details. The whitish-grayish shades on the water surface in the RGB images in e) and f) are cloud reflections on the mirror-like water surface. Black arrows in the thermal images point at long streak-like features.

The ZiviCat then entered a cooler patch (Figure 2-7d), where GCW had further developed and surface temperatures had dropped slightly ($< 1°C$, Figure 2-7b, d). However, unlike in Episode 1, in terms of both duration and wind speed, wind forcing was not enough to break up the near-surface stratification. LSWT patterns can be seen on the surface but with weaker temperature gradients than in Episode 1. Thereafter, the ZiviCat advanced into progressively warmer surface patches (Figure 2-7e, f) and stratification returned to similar values as in Figure 2-7c, with higher fluctuations due to the passing of a packet of what appears to be long waves generated by a passing boat (Figure 2-7f).

Even after wind speeds decreased below 1.5 m s^{-1}, cooler patches are visible in the thermal images in Figure 2-7d-f. Real-time monitoring of surface roughness and surface water temperature indicated that even though wind-induced GCW had disappeared rapidly (RGB images in Figure 2-7e, f), the associated heterogeneity in the LSWT continued to develop and change in shape; however, at a much slower rate and with much smaller horizontal gradients than in Episode 1 (Figure 2-6). A noteworthy feature at the top of the thermal images of Figure 2-7e, f is the formation of long, streak-like warm structures aligned with the wind.

2.4   Discussion

Our measurements were carried out under stable ABL conditions when a strong Diurnal Warm Layer (DWL) had formed near the surface, winds were light and heat flux was into the lake. Above a wind threshold of $\sim 1.5 \text{ m s}^{-1}$, smooth surface slick/rough surface non-slick patterns appeared on the surface, causing well-developed Gravitational Capillary Waves (GCW) in the rough surface areas. The LSWT in these rough patches was up to $1.5°C$ cooler than in the surrounding smooth surface slicks with sharp temperature gradients between the two. DWL stratification disappeared in the near-surface layer of the rough patches. This led to a rapid spatial redistribution of LSWT patterns with strong horizontal thermal contrasts. Our data indicate that there was a higher surfactant concentration in smooth slicks than in rough surface areas. In the following, we will further describe the nature of the surfactant material and discuss how the interplay of surfactants, low wind, DWL formation, and GCW development affects the dynamics of the near-surface layer.

2.4.1 Natural surfactants

In oceanic studies, it has been shown that slicks have higher surfactant concentrations (Wurl *et al.*, 2016). However, such a study has not been carried out in a lake before. To investigate the surfactant distribution in smooth and rough areas, water samples were collected at the surface and the near-surface water layer of Lake Geneva when winds were above the threshold speed of 1.5 m s^{-1}. The samples were analyzed for the presence of surfactants. The analysis revealed that three peaks (P) frequently appeared in the Excitation Emission Matrix (EEM) (Figure 2-4a). The study by Salter (2010) showed that the enrichment factors derived from these peaks strongly correlate with the EF of surfactant activity in an estuarine region during different seasons. Peak P1 corresponds to terrestrial humic substances, whereas components P2 and P3 are linked to marine and terrestrial humic materials (Murphy *et al.*, 2008) and tryptophan-like components (Wolfbeis, 1985), respectively. However, neither of these two substances shows as distinct a difference in EEM concentration between slick and non-slick areas as peak P1 does. Although the chemical composition of slicks can vary significantly spatiotemporally (Frew *et al.*, 2006), our results suggest that the Surface Micro Layer (SML) in general, and slicks, in particular, are more likely to be enriched by allochthonous production rather than by autochthonous activities (Salter, 2010), as would be expected in inland waters (Hunter and Liss, 1981). Further extensive sampling campaigns are required to map the SML composition in Lake Geneva in more detail.

The surfactant analysis of 28 water sample sets collected on four different days established that there is a significant difference in surfactant concentration between smooth slicks and rough non-slick areas, with concentrations in slicks being much higher, in agreement with observations in the ocean (Wurl *et al.*, 2016). The larger interquartile range in the slick areas (Figure 2-4c) indicates higher variability in enrichment, suggesting that the thickness and characteristics of the surface surfactant film varies more within slicks than in rough surface areas. This can affect solar radiation penetration and lead to LSWT variability within warm slicks, as observed in Figure 2-6 and Figure 2-7. It can also affect the slick response to wind forcing by modifying dilatational viscoelasticity in the uppermost layer of the water (Frew, 1997). Thinner surfactant layers may break up more easily under wind forcing and open up rough non-slick areas within slicks (Figure 2-6f). Previous studies in the ocean also observed a wider interquartile range inside slicks (Wurl *et al.*, 2016). During our water sampling campaigns, direct visual

observations of the lake surface confirmed that smooth surfaces can be associated with surfactant-enriched slicks. Thus, the results of the surfactant study allow us to interpret the observed surface roughness in the RGB lake surface images taken by the ZiviCat on 18 April 2019 (Figure 2-6 and Figure 2-7) in terms of surfactant concentration.

2.4.2 Diurnal Warm Layer (DWL)

The meteorological conditions on 18 April 2019 were characterized by weak winds and a significant input of solar radiation into the upper layer of the lake (Figure 2-5a). For the surface heat flux, incoming solar radiation substantially exceeds cooling (Equation 2-1, Figure 2-5a). This situation leads to the formation of a Diurnal Warm Layer (DWL) (Price *et al.*, 1986). Under calm conditions (wind speed below 1.5 m s^{-1}) and intense incoming shortwave radiation (clear skies), DWL amplitudes in tropical oceans and lakes may reach up to several degrees (Augusto-Silva *et al.*, 2019; Bartosiewicz *et al.*, 2019; MacIntyre *et al.*, 2021a; Ward, 2006) confined to a shallow surface layer ($\mathcal{O}(1\ \mathrm{m})$) at around midday (Gentemann *et al.*, 2009). If wind speed increases slightly, the development of GCW and the resulting surface mixing contribute to a rapid and strong reduction in diurnal warming amplitude (Gentemann and Minnett, 2008).

During Field Campaign 2, the development of a DWL was confirmed from the analysis of the heat flux terms (Figure 2-5a). As a typical example, the absorption fractions of incoming shortwave radiation in different layers of the water column were calculated for light-wind conditions at ~14:30 using attenuation coefficients from Woolway *et al.* (2015) (Figure 2-5a) for infrared and ultraviolet bands and the estimated k_d for Lake Geneva for the visible range. Nearly 75% of short-wave radiation is absorbed in the uppermost 1.5 m of the water column, and a large part of that in the uppermost 5 cm. Since heat absorption in this 5-cm layer is significantly greater than surface cooling, an intense, stable near-surface stratification develops. Although the rise in LSWT can potentially enhance surface cooling by increasing outgoing longwave radiation and latent heat flux (Rahaghi *et al.*, 2019d), the persistent, intense solar radiation maintains the near-surface water stratification. These high-resolution stratification profile measurements in the near-surface layer, which allowed quantification of the DWL development, are the first-ever taken in a slick study. In previous oceanic studies, water surface temperatures were compared only to one temperature measured deeper in the water column (Marmorino and Smith, 2006b). The surface heat budget analysis in Figure 2-5 suggests that DWL

formation began earlier in the morning. However, the meteorological parameters needed to assess surface cooling were not available before 11:20.

2.4.3   Threshold wind speed

One of the objectives of this study was to investigate the effect of increasing wind speed on slick formation and on the dynamics of the diurnal warm layer. An analysis of all the data collected on 18 April 2019 reveals that whenever the wind speed exceeded a threshold, the near-surface stratification was altered, and patches of GCW were produced, causing mixing. Based on the ZiviCat weather station data measured 3 m above the water surface, we compared the results of Episodes 1 and 2 (respectively, Figure 2-6 and Figure 2-7) and determined a threshold value of $U \approx 1.5$ m s^{-1}, above which GCW start to grow. This value is close to the range (1.6 to 1.8 m s^{-1}) observed in a laboratory study (Donelan and Plant, 2009). Gentemann and Minnett (2008) reported that the DWL development in the ocean significantly changes when wind speed exceeds 1.5 m s^{-1}. The threshold also depends on wind gustiness and fetch, ABL stability, water temperature, and surface film concentration. Note that when this threshold wind speed was exceeded, the lake surface became patchy. However, warm patches (slicks) with no GCW still covered a significant part of the lake surface (Figure 2-6). When winds blow above the threshold wind speed for extended periods, the area covered by smooth slicks becomes progressively smaller (Figure 2-1).

2.4.4   Wave height estimate

The non-slick area (Figure 2-6f) is characterized by sharp-crested and well-developed GCW. GCW wave height can be estimated during Episode 1 based on significant wave height parameterization (Taylor and Yelland, 2001; Wang *et al.*, 2017):

$$H_s = 0.018U_{10n}^2(1 + 0.015U_{10n}) \qquad\qquad 2\text{-}3$$

Where H_s is significant wave height, and U_{10n} is 10-m height neutral wind speed. Using the same parameterization scheme as for calculating the heat budget (averaged meteorological measurements over the first episode), we estimated a wave height $H_s \approx 4.4$ cm. Although the above equation was derived mainly for higher wind speeds, the resulting wave height is in the range of wave height estimates obtained from ZiviCat RGB images in Figure 2-6f and visual inspection of the lake surface in the non-slick areas.

2.4.5   Episode 1: Wind speed above the 1.5 m s^{-1} threshold

In Episode 1, the most striking feature of the LSWT field was the sharp drop in stratification when moving from a slick to a non-slick area (Figure 2-6e). Using one-min averaged temperature data from the uppermost 25 cm of the water column, the buoyancy frequency (N) can be estimated. Just before entering the rough rippled area (at ~12:16), a value of N = 9.21×10^{-3} s^{-1} (~33 cycles per hour) was found. Stratification of this intensity is comparable to previous measurements in lakes under surface heating and low wind conditions (Augusto-Silva *et al.*, 2019; Bartosiewicz *et al.*, 2019). In the non-slick area (at ~12:18), the buoyancy frequency dropped to less than one cycle per hour. The strong horizontal LSWT gradient (1.5°C in 10 m; estimated by combining temperature data in Figure 2-6b and ZiviCat speed) between ~12:16 and ~12:17 can be explained by a sequence of two processes: (i) preferential absorption of shortwave solar radiation in the water column causes significant temperature gradients in a very thin layer below the surface, as discussed above (Figure 2-5a), and (ii) air-water momentum exchange increases substantially as GCW form due to the potentially significant contribution of the wave-form drag in momentum transfer compared to the background tangential skin friction (Banner and Peirson, 1998).

Frew (1997) reported that surface film-induced non-zero viscoelasticity can modify this surface exchange by dampening small waves or by changing the near-surface turbulence. Here, the observed effect of surfactant concentration is mostly associated with the former. Within slicks, wind-wave formation and growth are suppressed (most likely due to higher surfactant concentrations; Figure 2-4b), resulting in the absence of wave-induced mixing, which causes less efficient near-surface mixing than in non-slick areas. In particular, under low wind conditions, turbulence production by wave-induced motions exceeds that resulting from wind-driven shear (Savelyev *et al.*, 2020). The enhanced wave-induced mixing in non-slick regions can partly be attributed to the generation of small-scale (centimeter-scale) Langmuir circulation at the onset of wind-wave development (Tejada-Martínez *et al.*, 2020; Veron and Melville, 2001). In their laboratory experiments, Veron and Melville (2001) demonstrated that adding surfactants prevents wave formation and thus the generation of this small-scale circulation. The total wind stress increases as the wave field develops outside the slicks (Banner and Peirson, 1998). This effect can be seen as reduced wind drag (Shen *et al.*, 2019; Vanderplow *et al.*, 2020), and smaller stress exerted by the airflow (Benetazzo *et al.*, 2019) inside slicks. Therefore, slicks can be expected to remain warmer than non-slick areas under strong solar radiation and low wind

conditions. As a result, slicks can alter the dynamics of the air-water interface, causing spatial variability of LSWT between slicks and non-slick areas.

During Episode 1, a rapid transition from the warm stratified slick to a cold non-stratified non-slick area takes place over a distance of less than 10 m, as is evident from the destratification of the upper 25 cm of the water column and a more than 1.5°C drop in the subskin temperature (Figure 2-6b). The Monin-Obukhov length scale (L_{MO}) illustrates the balance between stabilizing buoyancy forces and Turbulent Kinetic Energy (TKE) produced by wind-induced mixing ($u_{*,water}$) under horizontally homogeneous and stationary conditions and ignoring shear- or wave-driven turbulence (Thompson *et al.*, 2019). This scaling is given by:

$$L_{MO} = \frac{u_{*,water}^3}{\kappa B}$$

2-4

Where $\kappa = 0.41$ is the von Karman constant and *B* is the effective buoyancy flux. Table 2-2 lists the parameters used to calculate L_{MO} together with their associated definitions. Following the methods outlined in the heat budget analysis (Figure 2-5a), correcting for stability of the atmospheric boundary layer and measurement height, and using 5-min averaged data, L_{MO} was estimated as ~5 cm for the non-slick area in Episode 1. This small L_{MO} value is the result of a large *B* (Figure 2-5) and a weak $u_{*,water}$ value. However, this estimate should be interpreted with caution, because the assumptions of horizontal homogeneity and stationary conditions may not be satisfied in the present case due to the observed patchiness (Figure 2-6 and Figure 2-7) which can affect B and $u_{*,water}$. Small ratios between L_{MO} and the actively mixing layer depth (~25 cm in the non-slick area in Episode 1; Figure 2-6b), previously observed (Augusto-Silva *et al.*, 2019; MacIntyre *et al.*, 2021a), imply that wind-induced shear dominates turbulence production only in shallow surface layers. On the other hand, wave-induced mixing can contribute significantly to TKE production even under non-breaking surface waves (Qiao *et al.*, 2016; Savelyev *et al.*, 2020).

Therefore, we investigated the mixing time that can be estimated from wave-induced turbulence production in the near-surface layer. Dai *et al.* (2010) determined the water-side eddy diffusivity induced by low amplitude mechanically-generated non-breaking surface waves. In their laboratory experiment, a wave amplitude of 1.5 cm generated a turbulent diffusivity K_z of $\mathcal{O}(10^{-4}\ m^2\ s^{-1})$ in the near-surface layer. Applying this diffusivity to the present case, a time scale

(h_{mix}^2/K_z) of ~10 min is obtained. Dai *et al.* (2010) also reported that with increasing wave amplitude, this time scale rapidly decreases while the mixing rate and the mixing depth increase.

Consequently, the actual time in Episode 1 would be shorter since wave amplitudes are greater, which is also evident from the LSWT time evolution in Figure 2-6c-f. Babanin and Haus (2009) measured turbulent dissipation below similar non-breaking laboratory waves. They observed that although turbulence was highly intermittent in space and time, turbulent dissipation rates reached values comparable to those reported under breaking waves. They indicated that the turbulent dissipation rate is very sensitive to wave amplitude, since it increases with the third power of wave amplitude. The above estimates suggest that the strong and rapid mixing in the rough non-slick areas observed in our study, is predominately produced by the presence of GCW and that wind stress-induced TKE in the near surface layer, estimated by L_{MO}, only makes a minor contribution. Furthermore, under stable ABL and low wind conditions, the drag coefficient is considerably smaller than in neutral and unstable cases (Kara *et al.*, 2005; Smith, 1988). This results in low $u_{*,water}$ and wind-induced TKE levels, thus underscoring the importance of wave-induced mixing under these conditions.

Table 2-2. Parameters used for the water-side Monin-Obukhov length scale and mixing time scale calculations.

Parameter	**Definition**	**Computed value**
$u_{*,water}$	$\left(\dfrac{\rho_a}{\rho_w}\right)^{\frac{1}{2}} u_{*,air}$ [a]	$0.0014 \ [m \ s^{-1}]$
B	$\dfrac{g\alpha}{\rho_w c_p} Q_{Net}^*$ [b]	$1.45 \times 10^{-7} \ [m^2 \ s^{-3}]$

(a) The air-side friction velocity is calculated following Zeng et al. (1998), accounting for atmospheric boundary layer stability and measurement height.

(b) The effective heat flux considers only that amount of shortwave radiation (mainly in the visible part) that heats the actively mixing layer (estimated to be 25 cm based on thermistor measurements, Figure 2-6b; (Imberger, 1985; Thompson et al., 2019). The remaining terms in the surface heat budget are not affected.

Given the above timescale, it can be expected that the water surface layer in the non-slick area reaches quasi-equilibrium within minutes after the wind speed threshold is exceeded, and surface waves are formed. The relatively constant LSWT observed in the non-slick region (12:17 to ~12:25) during the period when the wind speed was above the threshold further supports this.

The results confirm that the diurnal warming amplitude rapidly changes in response to slight variations in wind speed when GCW develop in the absence of surfactants and cause near-surface mixing (Gentemann and Minnett, 2008). The time evolution of the thermal contrast between slick and non-slick areas (Figure 2-6d-f) that appeared shortly after the wind speed exceeded the threshold illustrates that, at low wind speeds, the near-surface layer is particularly sensitive to wind speed changes.

The scenario described above for Episode 1 in Lake Geneva is different from previous observations in the ocean that reported slightly colder ($< 0.5°C$) surface temperatures in slicks (e.g., Frew *et al.,* 2004, Marmorino and Smith, 2006 and references given therein). Those ocean measurements were carried out under upward heat fluxes and thus unstable ABL conditions, whereas our measurements were taken under stable conditions ($\zeta = 0.93$) and net surface warming (Figure 2-5a), which is typical for the spring period over Lake Geneva (Rahaghi *et al.,* 2019b). The difference between our measurements and those carried out in the ocean illustrate two mechanisms through which slicks can affect the surface water temperature: In the ocean studies, the reduction of temperature in slicks was associated with the surfactants' ability to suppress convective motions close to the surface by thickening the water-side viscous sublayer (Bower and Saylor, 2011a). Therefore, cooled surface water could not be exchanged efficiently with warmer sub-surface water. In the present study, however, under net surface warming, the slick vs. non-slick temperature difference changed both in sign and intensity. Furthermore, surfactants inhibited mixing in slicks by suppressing the wind-wave formation and dampening short GCW amplitudes. Thus, the elevated surface water temperature due to the DWL effect was maintained, at least temporarily, inside slicks. This finding indicates that the impact of slicks on surface water temperature depends on: (i) the direction of air-water heat transfer, (ii) the intensity and duration of solar radiation and wind forcing, (iii) characteristics of the GCW field, and (iv) the type of the material inside slicks, as well as the presence of biological activity (Wurl *et al.*, 2018b).

The thermal images in Figure 2-6, particularly those captured at the later stages of LSWT development with winds above the 1.5 m s^{-1} threshold, showed sequentially arranged warm and cold patches, elongated in the wind direction. The elongation of all surface patches in the wind direction suggests that wind shear is the driving force in these dynamics. In particular, one can identify multiple islands of cold water that develop simultaneously over a large area inside a large warm slick (right-hand side of Figure 2-6f). All these features rapidly evolve in time, with

cold surface areas overall increasing in size. The LSWTs in these cold areas are comparable to those measured with the ZiviCat (Figure 2-6f), suggesting that they can be characterized by well-developed GCW and a near-surface destratification. Thus, air-water exchange processes can be expected to change strongly and rapidly with time and space, even under light winds. Considering the larger interquartile range observed in the slick areas (Figure 2-4c), it is likely that the observed simultaneous development of these islands of cold water was mainly due to the spatial heterogeneity in the thickness or composition of surfactant enrichment rather than to small-scale spatial variations in the wind field. Marmorino and Smith (2006b) reported that the ocean slick they studied did not change much over time.

2.4.6 Episode 2: Wind speed below the 1.5 m s^{-1} threshold

In Episode 2 (Figure 2-7), the period during which the wind speed exceeded the threshold was much shorter than in Episode 1 and lasted only about 2-min. Nevertheless, a drop in surface temperature was observed inside the rippled water surface area shortly after the second slight increase in wind (Figure 2-7b-d), although with much smaller amplitudes, barely affecting the near-surface stratification. In Figure 2-7b, the topmost temperature sensor (depth of about 5 cm) shows a noticeable decrease ($< 1°C$) after the two very short wind events impacted on the surface (Figure 2-7a). However, the second and third top thermistor measurements (Figure 2-7, depths of ~10 and 15 cm) revealed no signs of mixing due to the absence of sufficient wind stress, indicating that wind-induced mixing probably only affected the uppermost centimeters of the near-surface water layer (which could not be captured by our measurement system). This agrees with the findings of Dai *et al.* (2010) concerning the dependence of penetration depth on wave height. Despite the brief appearance of smooth and rough surfaces caused by that short wind pulse, the corresponding spatial variability in the surface temperature persisted over an extended period (Figure 2-7e, f). Length and time scales were not calculated for Episode 2 because the event was shorter than the timescale related to such a development, and GCW did not fully develop.

Elongated streak-like warm features appeared in the thermal imagery, aligned with the wind (e.g., black arrows in Figure 2-7e, f). Marmorino *et al.* (2008b) observed that striped patterns had formed on the upwind side of slicks aligned with wind direction. They suggested that Langmuir circulation (with a spacing of ~25 m) that developed under steadily increasing wind (up to 5 m s^{-1}) plays a major role in fragmenting slicks, with surface film cumulating in the convergent zones. A similar process for redistributing biogenic films was proposed by Ermakov

(2018a) who observed the formation of streaks on the upwind side of artificial slicks under higher wind conditions (8 m s⁻¹) with cross-wind scales of 7-10 m. Although the spatial scales (~10 to 20 m) in our observations are similar to the above studies, the formation of Langmuir cells is unlikely for such short-duration, low wind speed events (< 2.5 m s⁻¹). Even if a uniform wind field over the area of the thermal images (Figure 2-7c-f) were present, the conditions required for their formation would not be fulfilled (Leibovich, 1977). Warm streaks were previously observed under light wind conditions in Lake Geneva (Rahaghi *et al.*, 2019d), where ZiviCat measurements showed that warm near-surface water underwent downwelling to more than 1.5 m depth in those streaks. Large-scale upwelling and downwelling processes below the surface may also manifest themselves by streak-like features on the surface. Farrar *et al.* (2007) showed that internal waves under low wind speeds and intense solar radiation can cause similar surface temperature patterns at these scales, which favor the development of a DWL. Additional investigations with targeted measurement campaigns are needed to determine the origin and dynamics of these streaks and their role in near-surface layer dynamics.

Lemmin and D'Adamo (1996) reported that wind speed in Lake Geneva is less than 4 m s⁻¹ 80-90% of the time during the stratification period (May to October), and winds below 3 m s⁻¹ by far dominate the annual wind rose pattern (CIPEL, 2019). Rahaghi *et al.* (2019e) and Lemmin (2020) showed that the ABL is stable for the period from March to the beginning of August, at least during the daytime. The findings of the present study are therefore an important contribution to the understanding of the annual air-water exchange cycle. Furthermore, images regularly recorded with the remote sensing camera installation (Figure 2-1) confirmed that slicks are frequent during periods of stable ABL conditions. The results of the two episodes in the present study, therefore, can be considered representative for patch dynamics and air-water exchange under strong solar radiation and low wind speeds in Lake Geneva, and probably in other lakes under similar conditions.

2.5   Summary and conclusions

This field study carried out in Lake Geneva investigated, in a novel approach, processes that can cause nonuniformity in Lake Surface Water Temperature (LSWT) under commonly occurring light wind conditions and determined how this nonuniformity can be related to biogenic surfactant distribution. High-resolution measurements of surface temperature, near-surface water temperature profiles and real-time observations of surface roughness were combined. Surfactant concentrations are significantly lower in rough non-slick patches than in smooth slicks,

as determined from field observations and Enrichment Factor (EF) analyses. Such measurements taken under stable Atmospheric Boundary Layer (ABL) conditions have not been previously reported for inland waters, in this case a lake, even though they are key for better understanding and quantifying air-water exchange dynamics.

The data show that a Diurnal Warm Layer (DWL) developed in the near-surface water column when intense solar radiation input greatly exceeded heat loss from the lake under stable ABL conditions. Under calm conditions with wind speeds below a threshold of ~1.5 m s^{-1}, it is evident from surface images that the surface is essentially smooth, and LSWTs vary only slightly. Stratification with a strong temperature gradient (up to a few degrees) develops in the near-surface water column with the greatest thermal gradient being in the very shallow (a few centimeters) near-surface layer.

It was demonstrated that when light (< 2.5 m s^{-1}) winds rose above the threshold of ~1.5 m s^{-1}, smooth surface slick/rough surface non-slick patterns appeared on the surface, causing well-developed Gravitational Capillary Waves (GCW) to develop in the rough surface areas, thereby promoting near-surface water mixing. The LSWT in these rough patches was up to 1.5°C cooler than in the surrounding smooth surface slicks with sharp temperature gradients between the two. However, as wind continued to blow above the threshold, slicks broke up on certain parts of the surface and remained intact elsewhere; this may be due to the observed surfactant concentration variability. This led to a rapid spatial redistribution of LSWT patterns with strong horizontal thermal contrasts. The elongation of all rough surface patches in the wind direction suggests that wind shear is the driving force in the break-up of smooth slicks. It can be assumed that the time-integrated effects of the interaction between light winds and spatially varying natural films contribute to the spatial heterogeneity of LSWT and thus affect the spatial distribution of the exchange of heat, momentum and mass.

These lake observations contrast with results from previous oceanic studies where slicks were found to be cooler (< 0.5°C) than ambient surface areas under net surface cooling conditions. The present results suggest that the effect of natural films on surface water temperature development depends on the direction of the heat flux (downward in the present study vs. upward in ocean observations reported in the literature), as well as the time evolution of near-surface processes involved in the surface renewal and turbulent heat exchange. Most previous slick studies in oceans investigated the influence of surfactants on near-surface turbulence, where reduced convective motions decreased the renewal of relatively cold surface water. Our study, carried

out in a lake, highlighted the role of surfactants in retarding and dampening GCW, which is another mechanism through which slicks can affect surface water temperature.

In conclusion, the effect of high concentrations of natural surfactants on LSWT depends on atmosphere-water boundary layer dynamics. The results of the present study contribute to the understanding and the quantification of air-water exchange processes, which presently are lacking for stable Atmospheric Boundary Layer (ABL) conditions in lakes, and can be expected to be applicable to other lakes under similar boundary layer conditions.

Acknowledgments

Chapter 3 Spatiotemporal variability of turbulent energy fluxes under diurnal low wind conditions in Lake Geneva

Mehrshad Foroughan, Ulrich Lemmin, Seyed Mahmood Hamze-Ziabari, and David Andrew Barry

Ecological Engineering Laboratory (ECOL), Institue of Environmental Engineering (IIE), Faculty of Architecture, Civil and Environmental Engineering (ENAC), Ecole Polytechnique Fédérale de Lausanne (EPFL), Lausanne, Switzerland

Abstract

Low wind speeds ($< 3{\sim}4$ m s^{-1}) are frequent environmental conditions in many inland water bodies. Yet, the physical processes at the air-water interface and their impact on air-water exchanges remain understudied within this range compared to higher wind conditions. These processes exhibit significant spatiotemporal variability at small scales (1-100 m and minutes). Direct flux measurements were carried out using an autonomous catamaran in Lake Geneva under various environmental conditions to examine the impact of such heterogeneity on turbulent heat fluxes and momentum exchange. Specifically, this study highlights the role of surface and near-surface temperature variability, natural slicks, and transient low wind speeds around the threshold of wind gravity-capillary wave generation. To account for the short-term variability of these processes, wavelet-based flux analysis was utilized along with dynamic flux footprint tracking. The presence of slicks and surface water conditions were monitored using both an in situ onboard camera and a shore-based camera with a large-scale field of view. Surface microlayer samples were also collected from both slick and non-slick regions of the lake during multiple field campaigns. The findings reveal local flux variations associated with small-scale surface and near-surface temperature changes, including enhancements crossing a sharp surface temperature front. While a local decrease in energy fluxes inside slicks was noticed, the findings suggest that coexisting factors, such as surface temperature variability, could potentially obscure their effect on surface energy fluxes. Additionally, we noted flux variations in response to the lake surface state, such as the transition from calm to wind wave under low wind conditions. These results underscore the intricate interactions of various processes at the air-water interface, which must be considered for reliable long-term energy budget estimations, especially in environments dominated by low wind speeds.

Keywords: Low wind speed, Eddy covariance, Turbulent heat flux, Friction velocity, Natural slicks, Lake Geneva, Wavelet analysis, Gravity-capillary waves

3.1 Introduction

Surface heat fluxes, through their control of the energy budget and thermal structure of lakes, are crucial in regulating the physics and biogeochemistry of lakes in response to climate change (De Stasio Jr. *et al.*, 1996; Fink *et al.*, 2014). Energy exchange between the atmosphere and the lake is largely dependent on wind forcing (Fernández Castro *et al.*, 2021). Despite low wind speeds (< 4 m s^{-1}) being typical in lakes (Woolway *et al.*, 2018), air-water heat and momentum transfer dynamics are less explored than in high wind conditions, possibly due to the relatively lower fluxes involved. Weak wind forcing allows distinct spatial variabilities at the air-water boundary and near-surface water column to emerge, which are otherwise suppressed in highly turbulent and fully developed sea states.

Various processes contribute to the spatiotemporal heterogeneity of air-water interaction dynamics under low wind conditions. These include multiscale lateral surface temperature gradients, often accompanied by diurnal near-surface thermal stratification. Natural slicks are also observed in water bodies under low wind conditions, which are smooth areas surrounded by rippled water. In addition, low-wind conditions are typically characterized by gusts, particularly under an unstable Atmospheric Boundary Layer (ABL) (Edson *et al.*, 2007; Godfrey and Beljaars, 1991; Grachev *et al.*, 1998), and have a transient and intermittent nature in both speed and direction (Anfossi *et al.*, 2005). Such variable wind fields often translate into fetch-and-duration-limited surface wave growth and decay (Hwang and Wang, 2004). In natural environments, however, all these processes can coexist and interact with each other, producing short-term changes in surface and near-surface conditions (Foroughan *et al.*, 2022b). The present study is mainly focused on these water-side variations that can lead to spatiotemporal fluctuations in surface heat and momentum fluxes.

Surface temperature is the key coupling parameter at the air-water interface, which controls surface longwave radiation and turbulent heat fluxes (Xue *et al.*, 2015). Spatial heterogeneity of surface water temperature at various scales affects the bulk calculations of turbulent fluxes, as it is sensitive to space averaging of the input variables (Gulev, 1997; Hughes *et al.*, 2012). Under low wind conditions, distinct surface temperature variability can occur at small scales (Farrar *et al.*, 2007; Rahaghi *et al.*, 2019b; hereinafter, small-scale refers to lateral variations between 1 m and 100 m). Surface water temperature heterogeneity can increase area-averaged surface cooling, especially in weakly unstable conditions, exceeding homogeneous surface temperature estimates (Mahrt and Khelif, 2010; Rahaghi *et al.*, 2019c). Mahrt and Khelif (2010)

also demonstrated that the impact of surface temperature variations on air-water heat exchange is inversely related to the average air-water temperature difference and the square of the wind speed (the effect is more pronounced under near-neutral stability and low wind conditions.)

Lateral variability in surface temperature is usually accompanied by subsurface temperature gradients, especially during the day and under weak wind forcing. Due to the depth-dependent penetration of solar shortwave radiation and minimal surface mixing, strong near-surface stratification can develop, which isolates a relatively thin layer from the rest of the mixed layer (Ward, 2006). This diurnal thermocline (Imberger, 1985), also referred to as the Diurnal Warm Layer (DWL), particularly impacts bulk surface flux estimation (Alappattu *et al.*, 2017; Dong *et al.*, 2021; Fairall *et al.*, 1996a). Hughes *et al.* (2020b) showed that diurnal warm layer formation affects vertical heat transport within the near-surface layer. This effect might modulate air-water exchanges of energy and momentum (MacIntyre *et al.*, 2021a). However, water-side stability has rarely been investigated when estimating turbulent fluxes (Lükő *et al.*, 2022). This oversight may be attributed to the assumption that near-surface water is well-mixed, which is not the case for low wind conditions.

Beyond the smallscale, surface and near-surface temperature heterogeneity are strongly driven by submesoscale (100 m - 10 km) to mesoscale (> 10 km) currents, such as eddies, fronts, and filaments. These coherent motions create strong convergence zones (D'Asaro *et al.*, 2018; Foroughan *et al.*, 2022a) and act as major conduits for heat and material transport (McWilliams, 2016). Previous shipboard direct measurements addressing surface temperature heterogeneity were mostly carried out by transecting such relatively large-scale currents (Shao *et al.*, 2019). However, both shipboard and airborne Eddy Covariance (EC) setups often result in large flux footprint areas (Mahrt and Khelif, 2010), obscuring the effects of small-scale heterogeneity on surface fluxes. Additionally, obtaining concurrent small-scale water-side measurements is often not feasible.

Low wind speed conditions are also often marked by organized or random-like smooth patches at the air-water interface, particularly in inland waters and coastal regions. These regions are referred to as natural slicks when they contain high concentrations of biogenic surfactants originating from in situ biological activities (Kujawinski *et al.*, 2002b; Kurata *et al.*, 2016a; Žutić *et al.*, 1981a) or terrestrial sources (Hunter and Liss, 1981). The smooth appearance of natural slicks results from inhibition of wind wave generation and damping short gravity-capillary

waves (Alpers and Hühnerfuss, 1989). In addition to surface roughness modulation, by modifying small-scale near-surface turbulence (Bower and Saylor, 2011b; Frew, 1997), slicks can also induce surface temperature heterogeneity. They can become slightly colder than surrounding water by suppressing near-surface convective motion (Frew *et al.*, 2004a; Marmorino and Smith, 2006a) or warmer by decreasing wave-induced mixing during intense DWL formation (Foroughan *et al.*, 2022b) or enhancing biological activities (Wurl *et al.*, 2018a).

Studies have demonstrated that surfactants, regardless of whether they form natural slicks or not, have an impact on surface exchange processes that extends beyond their influence on surface temperature. Even under high wind conditions, Pereira *et al.* (2018a) report that biogenic surfactants reduce air-water CO_2 exchange. Direct eddy covariance measurements by Yang *et al.* (2021) demonstrated that surfactants could affect CO_2 transfer by up to 30% at the global average wind speed; however, the effect may not necessarily be unidirectional. Mustaffa (2020) demonstrated that surfactant concentrations above a certain threshold reduced CO_2 transfer velocity based on gas chamber measurements. Additionally, their research found that this effect was particularly pronounced within slicks. There are fewer studies investigating the impact of slicks and surfactants on air-water heat and momentum exchange, as compared to gas exchange. During a shipboard study, Frew *et al.* (2004a) observed a decrease in heat flux when crossing a slick using an eddy-covariance setup. To understand the impact of slicks and surfactants on CO2 exchange, the authors converted heat flux measurements into gas exchange transfer velocities.

Natural slicks are typically observed within a particular range of wind speeds (2-6 m s^{-1}; McKinney et al., 2012). However, under higher wind conditions, surfactants tend to disperse and mix downwards (Frew *et al.*, 2004a). Conversely, at lower wind speeds below the threshold for small-scale wave generation, natural slicks become indiscernible. Under low wind conditions, surface wave fields, predominantly composed of short Gravity-Capillary Waves (GCW), can be highly dynamic and adjust rapidly to transient wind fields (Mahrt *et al.*, 2020). Specifically, when wind speeds fluctuate around the wind-wave generation threshold, the surface state can transition between calm and dominated by short waves. Such transitions are often neglected in bulk parameterizations for turbulent heat and momentum fluxes, where low wind speeds are typically assumed to be entirely smooth or have roughness induced by capillary waves (Guseva *et al.*, 2023; Wu, 1994). In an earlier study at Lake Geneva, a wind speed of ~1.5 m s^{-1} was identified as the threshold for visible wind wave appearance under a stable ABL (Foroughan *et*

al., 2022b), which is consistent with laboratory observations by Donelan and Plant (2009). However, the impact of this transitional state has yet to be investigated in the context of air-water exchanges.

While high wind conditions typically draw more attention due to their association with strong surface fluxes, direct measurements targeting low wind speeds remain largely unexplored. This is particularly relevant for water bodies where low wind conditions dominate, and hence the integrated effects of small surface fluxes contribute significantly to the long-term energy budget (Figure 3-1). In Lake Geneva, light winds (< 4 m s^{-1}) prevail for 80-90% of the time during the stratification period (May to October; Lemmin and D'Adamo, 1996). This study introduces a novel method that combines direct flux measurements with short-term flux calculations while observing surface and near-surface temperature patterns and the presence of natural slicks on the water surface. The present study investigates the role of small-scale spatiotemporal variabilities emerging under low wind conditions in air-water exchange dynamics. Specifically, the present work aims to answer the following questions:

- What are the short-term spatiotemporal fluctuations in air-water heat and momentum exchange under low wind conditions?

- How do variations in surface temperature and near-surface stratification impact momentum and heat exchange under low wind conditions?

- To what extent do natural slicks and spatiotemporal heterogeneity in the GCW field during dynamic low wind conditions contribute to surface flux variability?

The study of these low-wind energy fluxes and their impact on the spatiotemporal variability of the heat content is crucial for a comprehensive understanding of the lake's energy balance and its response to changing environmental conditions.

Supporting Material provides details on certain aspects discussed in the manuscript with figures and tables prefixed with S.

3.2 Materials and methods

3.2.1 Study site

Lake Geneva (known locally as Lac Léman) is the largest lake in Western Europe and is often considered the birthplace of limnology (Forel, 1892). It is located between Switzerland

and France and has a crescent shape with two distinct basins. The Petit Lac is a narrow western basin with a maximum depth of 75 m, while the Grand Lac is a large eastern basin with a mean depth of 170 m and a maximum depth of 309 m (Figure 3-1A). The lake has a total volume of around 89 km^3 and a mean surface altitude of 372 m. During warmer seasons, Lake Geneva exhibits a thermally stratified profile, and the thermocline deepens during winter but typically does not disappear entirely. The lake experiences a variety of wind patterns, with over 20 types of winds identified by local fishermen. These patterns are generated by factors such as differential heating, pressure differences across the Alps, and large-scale atmospheric pressure gradients (Bohle-Carbonell, 1991). The surrounding topography, including the Jura and Alps (Figure 3-1A), channels two pressure gradient winds over much of the lake surface: The Vent, blowing from the southwest, and the *Bise*, blowing from the northeast. While these two winds are the primary external forcings for initiating large-scale circulations in the lake (Hamze-Ziabari *et al.*, 2022a, 2022c), most of the time, air-water exchange processes are driven by local low winds and light breezes (Figure 3-1A).

3.2.2   In situ observations

Multiple observations were used to investigate how small-scale heterogeneities impact short-term surface exchanges. The study employed a 7-m-long autonomous catamaran named ZiviCat, as our primary measurement platform (Figure 3-1C). The catamaran is equipped with RTK-GPS for positioning, communication, and data recording systems. This enables operators on the accompanying boat, the *Elodea*, to control and correct catamaran navigation and analyze data in real-time (Barry *et al.*, 2019). Navigation is achieved through preprogrammed and on-the-fly modifications of waypoints. The catamaran can also be controlled remotely when needed. Sensors are mounted on a set of spars located well forward of the catamaran to minimize hull disturbances. Figure 3-1B shows only a tiny fraction of the total observations carried out in the lake during those campaigns. Since the present study targets direct flux measurement, only straight transects where the catamaran is oriented towards the upwind direction ($< 60°$) are considered. Furthermore, due to the inherent intermittency of low wind speed directions and limitations of our shore-based remote camera system, long transects were not feasible in most cases. Figure 3-1 shows the details of the measurements.
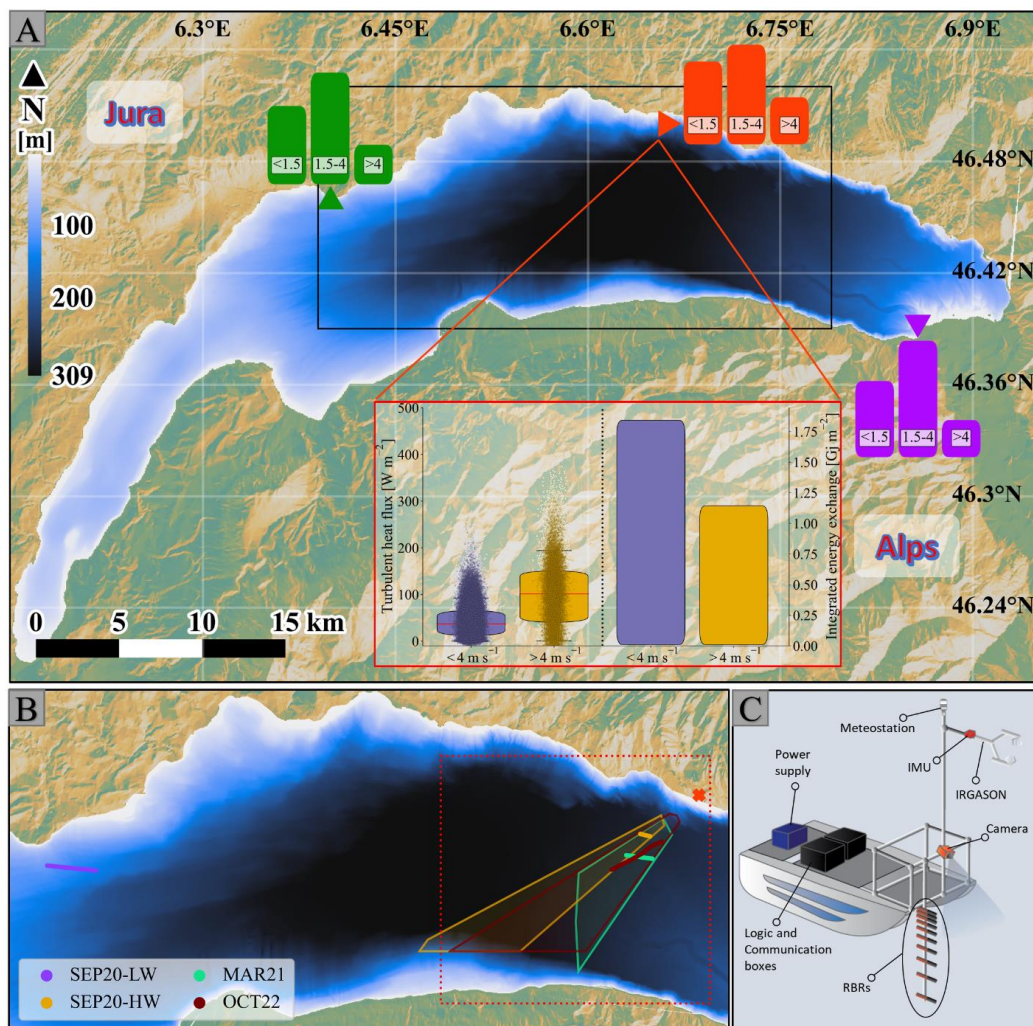
Figure 3-1. Overview of Lake Geneva with field campaign sites and measurement platform. A) Lake Geneva bathymetry and the surrounding topography. Three-year (2020-2022) wind speed histograms from three stations around the lake highlight the frequent occurrence of low wind conditions. The low wind bin was further categorized based on the threshold for short gravity-capillary wave generation (1.5 m s^{-1}) determined in Lake Geneva (Foroughan *et al.*, 2022b). The associated turbulent heat flux and the integrated energy transfer for the low and high wind speed range are displayed based on the data from the red (LéXPLORE; Wüest *et al.*, 2021) station using the bulk parametrization method discussed in Section 3.4.5. The black rectangle marks the zoom section in Panel B. B) Four flux measurement transects from four field campaigns were selected for this study. The legend provides the acronym for each campaign used throughout the manuscript. Figure 3-3 provides details of campaigns and environmental variables during each transect. The shaded areas indicate the stitched-together (multiple pan angles, see Section 3.2.3) field of view of the shore-based camera utilized for the SEP20-HW, MAR21, and OCT22 campaigns. The location of this camera is denoted by a red cross. The red dotted rectangle indicates the area depicted in Figure 3-5, Figure 3-6, and Figure 3-8. C) A simple schematic of the autonomous catamaran used for in situ measurements. Section 3.2.2 details onboard instruments and sensors.

On the water side, ZiviCat is equipped with a set of near-surface (down to 1.5 m) RBRsolo sensors (accuracy: 0.002°C, 1 Hz) to measure surface and near-surface water temperatures. While the notion of surface temperature can encompass a range of depths from the immediate skin layer of a few micrometers to a few meters below the surface (bulk), the present work considers the uppermost measurement at 5 cm below the surface as Lake Surface Water Temperature (LSWT). This measurement depth can be close to the subskin temperature, defined as the surface temperature, without considering the cool skin effect (Donlon *et al.*, 2002). On the airside, the catamaran is equipped with a meteostation (for mean wind speed and air temperature) and a relative humidity sensor at 3 m, a flux measurement unit at 2.8 m above the surface water, and an on-board camera, installed at 1 m), recording images every second of the surface water condition and wave states in front of the catamaran (Figure 3-1C). This provides a qualitative measure of surface roughness variation, for instance, due to slicks.

The flux measurement system was equipped with a Campbell Scientific IRGASON sonic anemometer, which was mounted on the central mast in front of the ZiviCat. The IRGASON is a hybrid design, combining a sonic anemometer and an infrared gas analyzer, that allows for the measurement of the three-dimensional wind velocity vector at a high frequency of 20 Hz with low errors of 0.08 m s^{-1} horizontally, 0.04 m s^{-1} vertically, and 0.025°C for sonic temperature. The manufacturer reports an error of 0.037 gm^{-3}°C^{-1} for water vapor measurement, which is used for calculating latent heat flux. To account for platform motion during flux measurements on a moving vessel, we also installed an inertial measurement unit (IMU) on the same bar, positioned behind the IRGASON at a distance of 75 cm from the measurement point of the sonic. We used the SBG IG-500N MEMS-IMU, which is equipped with a tri-axial accelerometer, gyroscope, and magnetometer and has errors of 4 mg, 1°/s, and 0.5 mG, respectively, with a sampling frequency of 50 Hz.

3.2.3   Shore-based time lapse camera

During three campaigns, SEP20-HW, MAR21 and OCT22, we utilized a shore-based remote camera to capture images of lake surface water. The imaging package, called TLB, is located on a steep hillside approximately 195 m above the lake surface and 440 m away from the shoreline. This package includes a Single-Lens Reflection (SLR) digital camera (Nikon D5600) with a resolution of 24.16 megapixels (6016 × 4016), which takes images every minute. The camera's field of view can be remotely adjusted in real time by panning and tilting in horizontal and vertical planes to monitor and track surface features in different parts of the lake.

The slanted (non-perpendicular) field of view of the camera provides valuable insight into the large-scale distribution of natural slicks on the lake and helps to identify their presence within the flux footprint. These slanted views are then rectified based on the GPS coordinates recorded by the ZiviCat using the Python package of Gerum *et al.* (2019).

3.2.4   Short-term underway flux measurements

Measuring air-water exchanges directly is often constrained by underlying assumptions such as homogeneity and steady-state conditions (Mauder *et al.*, 2021). These assumptions may not pose significant challenges in high wind conditions, but they can lead to increased uncertainty in low wind environments due to strong spatiotemporal variability of environmental state variables and high irregularity in wind forcing. Additionally, measuring air-water exchanges using an eddy covariance setup on a moving platform can add further uncertainty, as the motion effect must be removed from the signals before estimations can be made. Therefore, some alterations to the conventional direct flux calculation workflow are necessary when analyzing fluxes using a moving vessel under short-term spatiotemporal variability. Figure 3-2 illustrates the workflow and steps involved in the preprocessing stage.

3.2.4.1   Transects

Conducting field campaigns in low wind conditions presents a unique challenge, as the lack of relatively constant wind speed and direction makes preplanned transects difficult to execute. Instead, we relied on real-time wind field observations to set the transects. This required carefully orienting our catamaran in the upwind direction and adjusting the waypoints as necessary to maintain the desired trajectory. Moreover, we prioritize crossing over natural slicks as one of the objectives of the study. While this methodology may seem inefficient, it is currently the best viable option for investigating spatiotemporal flux variability under low wind conditions. Local weather predictions have yet to become reliable enough to allow for more advanced planning, so it is necessary to rely on real-time observations and careful selection of transects to gather meaningful data. Between September 2020 and October 2022, four transects were selected for this study (Figure 3-1B), carried out during the early afternoons (Figure 3-3) from early spring to mid-autumn in Lake Geneva. Environmental variables during each transect are summarized in Figure 3-3. Figure 3-1B shows that three of the transects were captured by our remote imaging system, allowing for a comprehensive view of the distribution and presence of natural slicks on a large scale.
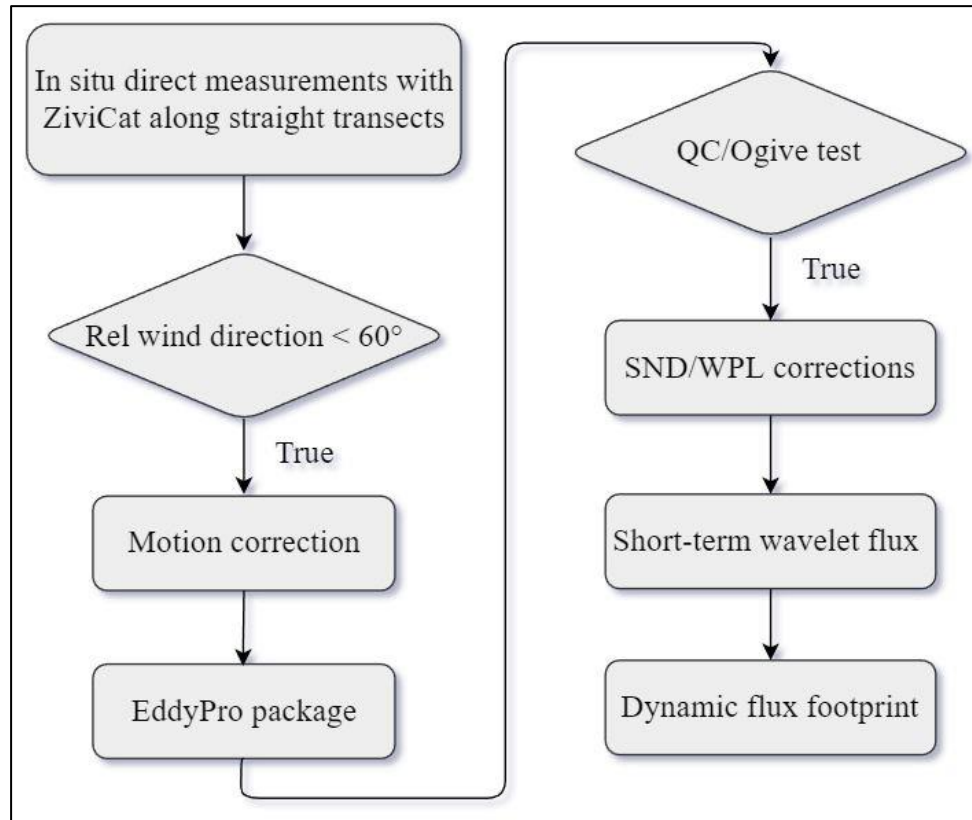
Figure 3-2. The workflow for short-term flux measurements includes: 1) Filtering transects with acceptable wind direction, 2) correcting velocity signals for platform motion, 3) using EddyPro software for preprocessing motion-corrected data and providing QC flags and ogive test, 4) applying wavelet transform correction for short-term flux estimation, and 5) estimating flux footprints. See Sections 3.2.4.1 to 3.2.4.5 for further details.

3.2.4.2 Motion correction

Fixed tower installations are the standard option for flux measurement studies, but their use can be restrictive in terms of the spatial range of flux footprints and the ability to capture spatiotemporal variability in natural environments. Mobile flux measurements are an option for tracking this broader variability, but it comes at the expense of introducing platform motion effects to velocity signals. While small platforms like catamarans are generally less susceptible to flow distortions than larger shipboard installations, they can be subject to higher frequency motions that may impact the accuracy of velocity signals measured by the sonic anemometer. We followed the methodology proposed by Edson and Fairall (1998), which involves using IMU and RTK-GPS measurements of the catamaran to correct motion effects. The motion correction procedure was highly effective in mitigating these motions (see Figure S3.0-1). These corrections are essential for ensuring the reliability of the flux measurements and subsequent flux calculations.
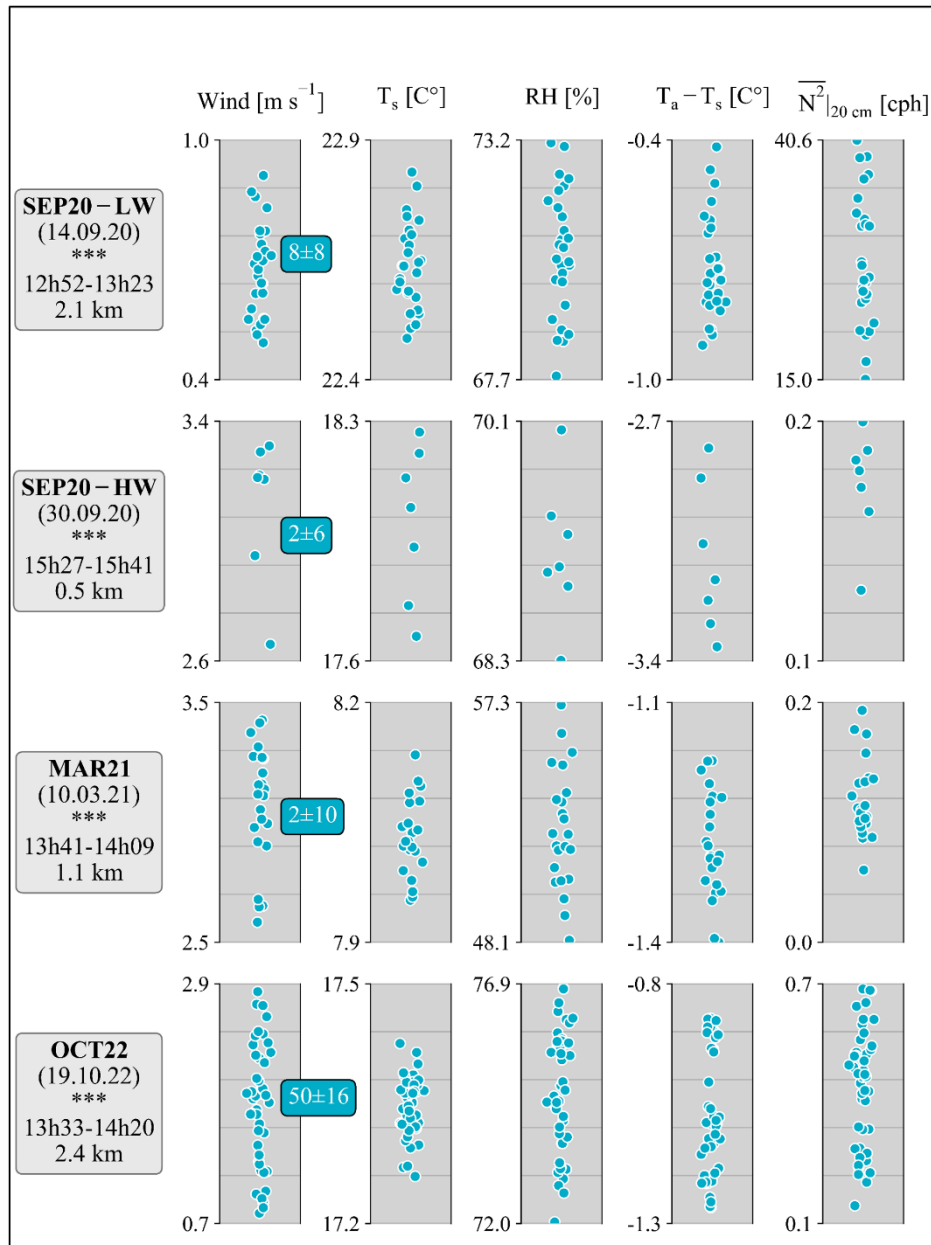
Figure 3-3. Local time, distance, and distributions of some environmental state variables based on one-minute averaged data for each transect. The wind distribution panels include text boxes displaying the mean and standard deviation of the relative wind direction in relation to IRGASON.

3.2.4.3 Corrections and quality control (QC)

To calculate the friction velocity (u_*), and sensible (SHF) and latent (LHF) heat fluxes, the following equations can be used (Mauder *et al.*, 2021):

$$u_* = \sqrt[4]{\left(\overline{w'u'}\right)^2 + \left(\overline{w'v'}\right)^2} \qquad 3\text{-}1$$

$$SHF = c_p \rho \overline{w'T'} \qquad\qquad 3\text{-}2$$

$$LHF = \lambda \rho \overline{w'q'} \qquad\qquad 3\text{-}3$$

Here, c_p represents the specific heat at constant pressure, ρ is the air density, and λ is the latent heat of vaporization. The buoyancy flux ($\overline{w'T'}$) and water vapor flux ($\overline{w'q'}$) were calculated using fluctuations of temperature, water vapor density, and motion-corrected vertical velocity measurements. However, the reliable estimation of fluxes through eddy covariance calculations required several corrections to be made (Mauder *et al.*, 2021). These corrections are critical for ensuring accurate and reliable flux measurements. In the present study, we utilized the EddyPro software package (Biosciences, 2017) for two purposes: 1) To preprocess motion-corrected signals and compute velocity and scalar fluctuation data that could be used in subsequent wavelet flux calculations, and 2) to facilitate the application of data quality tools and discard poor-quality transects.

The motion-corrected data underwent several preprocessing steps, including despiking, tilt correction, time-lag compensation and detrending, giving velocity and scalar fluctuations. Running mean detrending was used for computing turbulent fluctuations and minimizing low-frequency contributions to fluxes. To select the optimal time window, fluctuations were computed by choosing several linear increments for the running mean windows. These increments were in the range of 250 s to half of the data length. The resulting Ogive cospectra were then controlled, ensuring the measurements covered the entire range of turbulent frequencies. Finally, prior to conducting wavelet flux calculations, we applied the sensible heat flux (Schotanus *et al.*, 1983) and Webb-Pearman-Leuning (WPL; Webb *et al.*, 1980) corrections. The calculated averaged fluxes for each transect were consistent with EddyPro output, with a Mean Relative Error (MRE) of below 5% for all fluxes. This verifies the last post-processing steps performed on the output fluctuations.

The quality flags in the output files were determined based on two tests: the steady-state test and the developed turbulent conditions test. Since wavelet analysis relaxes the steady-state condition, the selected transects were controlled for developed turbulent conditions. Nonetheless, the majority of the fluxes performed well in the steady-state test. However, for OCT22, the momentum exchange was flagged as "1" due to its poor performance in the developed turbulence test, likely due to significant variations in wind direction during the transect. Although

this flag indicates suitability for general analysis (Foken *et al.*, 2005), we included it in our analysis with caution regarding its interpretation.

3.2.4.4   Wavelet flux calculations

Eddy covariance measurements, as conventionally used, assume steady-state conditions, and the covariances in Equations 3-1, 3-2, and 3-3 are often estimated using a relatively long averaging time (~30 min). However, this approach cannot identify the effects of short-term processes on surface fluxes. One of the alternatives introduced to resolve small-scale processes is wavelet analysis. Wavelet analysis, unlike Fourier, decomposes flux signals into localized wavelet functions through dilation and translation control. This enables time series decomposition into time and time-scales representing the signal with retained time localization, allowing the isolation of short-term processes (Schaller *et al.*, 2017; Torrence and Compo, 1998). The mathematical formulations of a continuous wavelet transform of an arbitrary discrete time series w(t) is:

$$W(a, b) = \int_{-\infty}^{\infty} w(t) \cdot \psi_{a,b}^{*}(t) dt \qquad \text{3-4}$$

$$\psi(t) = \frac{1}{\sqrt{a}} \psi \left(\frac{t - b}{a} \right) \qquad \text{3-5}$$

where $W(a, b)$ is the wavelet transform and $\psi(t)$ is the so-called wavelet function. Parameter a (dilation) controls the scale of the wavelet, determining the frequency of interest, and b (translation) represents the temporal position of the wavelet in the time series. While there are many forms of wavelet functions available, for our study, we opted to use the Mexican hat wavelet due to its precise time localization of single events and previous proven performance (Li *et al.*, 2023; Schaller *et al.*, 2017).

The time-frequency (time-scale) decomposition of the wavelet transform can be visualized in a normalized power scalogram of the wavelet transform (Figure S3.0-2). This transformation enables the detection of temporal variability across different time scales, as well as contributions to the energy of the time series at those scales. The global variance and covariance of signals can then be calculated as follows:

$$\sigma_x^2 = \frac{\delta t}{C_\delta} \frac{\delta j}{N} \sum_{n=0}^{N-1} \sum_{j=0}^{J} \frac{|W^2(a, b)|}{a(j)} \qquad \text{3-6}$$

$$\overline{w'q'} = \frac{\delta t}{C_\delta} \frac{\delta j}{N} \sum_{n=0}^{N-1} \sum_{j=0}^{J} \frac{\left[W_w(a,b) \cdot W_q^*(a,b)\right]}{a(j)} \qquad \text{3-7}$$

This equation includes the number of samples in the time series (N), the time step (δt), the wavelet-specific reconstruction factor (C_δ, which for Mexican hat equals 3.541), the spacing between discrete scales (δj), and the maximum number of scales (J). Equation 3-7 demonstrates the link between eddy covariance flux measurement and the wavelet cross-scalogram. Calculating fluxes over very short averaging times (one minute) may be possible by selecting an appropriate summation interval in Equation 3-7. By transforming the signal into the time and scale domain, low-frequency flux contributions are not neglected in short-term flux calculations. Additionally, the integrated wavelet flux over all scales and time steps can be compared to the averaged flux computed in the previous step, offering a way to verify these calculations. The MRE between these two fluxes was relatively small, falling just below the range of typical error in eddy covariance measurements (~5 to 10 %; Mauder *et al.*, 2006).

3.2.4.5 Dynamic flux footprint

This study is based on spatiotemporal measurements obtained from a moving platform. When using wavelet transforms to analyze short-term flux variations, such variations can arise from spatial inhomogeneity. As the ZiviCat travels along a transect, the flux footprint, which represents the source region of the flux, also changes. Therefore, monitoring upwind conditions can help track changes in the flux footprint and determine the consequent variations in turbulent fluxes. A similar approach was previously used to determine the influence of different spatial heterogeneities (such as sea-ice conditions) on air-water-ice exchanges (Prytherch and Yelland, 2021). In the present study, we employ the flux footprint estimation method of Kljun *et al.* (2015) that provides both 1D and 2D spatial distributions of flux origins in the upwind direction (examples of flux footprint distributions can be seen in Figure 3-4D and Figure 3-5G). Under the environmental conditions of this study, the peak locations of this distribution are generally situated upwind at a distance of 20 to 30 m, and it can extend up to 200 m.

Under low wind conditions, spatial heterogeneities can arise from variations in surface temperatures and natural slick distributions. As the ZiviCat's sensors record the entire transect, we can retrieve upwind measurements for each instance afterward. For example, the onboard camera records the surface water state at 1 Hz. This allows us to determine qualitatively the temporal

variation of slick occurrences along a transect. Therefore, the distance of a particular phenomenon, such as entering/leaving a slick, can be quantified with respect to a reference location by knowing the catamaran velocity (the ZiviCat maintained a constant speed during transects). Similarly, the 1D flux footprint distribution in space can be transformed into a grid of time spent starting from a reference time. Each instance can be labeled as slick or non-slick (1 or 0) based on observations. We can then calculate the weighted average of these labels within the footprint according to the source distribution and assign this average to our reference point as a slick or non-slick indicator using a specific threshold. In this study, an instance was designated as slick if over 50% of the slick was situated within the footprint. To create an overall flag of slick or non-slick for each individual wavelet flux, the flags can be further averaged within the corresponding averaging window of the short-term wavelet flux (one minute). This approach can also be used to estimate the corresponding variability of other water-side parameters, such as surface temperature and near-surface stratification.

The method described above is effective when the advective velocity of surface processes is much smaller than the platform speed (as was the case in the present study). Moreover, this method assumes cross-wind homogeneity of surface processes and requires the platform to travel directly upwind. However, if there is two-dimensional information available about the process of interest, it can be used to adjust the flagging system for the resulting 1D method. The results section discusses one such case for transect OCT22 (Section 3.3.4). Although one should be cautious when using such detailed footprint estimations, particularly under low wind conditions, due to the spatial scale of the observed processes the uncertainties associated with them may not affect the discussion presented in the following sections.

3.2.5 Surface water sampling

In addition to the main flux measurement campaigns, surface water sampling was conducted during some of the campaigns to associate the observed smooth patches with surfactant-enriched (natural) slicks. Sampling was carried out during the SEP20-HW and MAR21, as well as two other campaigns (results not presented). SEP20-HW sampling results were presented elsewhere (Foroughan *et al.*, 2022a). We sampled the uppermost 20-150 µm of the surface using the glass-plate method (Cunliffe *et al.*, 2013a) together with hand-dipping to collect bulk water following standard procedures (Cunliffe and Wurl, 2014). The samples were analyzed for enrichment (surface-to-bulk ratios) of Fluorescent Dissolved Organic Matter (FDOM), which is a reliable indicator of surfactant activity (Frew *et al.*, 2002; Salter, 2010). A total of

24 water samples (surface and bulk) were collected and grouped into slick and non-slick. The methodology is described in more detail in Foroughan et al (2022a, 2022b). Figure S3.0-3 shows the results of laboratory analysis for slick/non-slick comparisons along with a TLB image of an example of a surface water condition sampled during a campaign that was not included in this study. A further comparison of slick/non-slick samples for FDOM enrichment in Lake Geneva has been conducted recently (Foroughan *et al.*, 2022b).

3.3 Results

During the field campaigns in Lake Geneva, we measured diurnal surface fluxes with a focus on analyzing the short-term spatiotemporal variability of the air-water exchange of heat and momentum using wavelet analysis. This section highlights four transects (SEP20-LW, SEP20-HW, MAR21, and OCT22) conducted under different conditions. Each case represents a specific set of environmental state variables commonly observed under low wind conditions. SEP20-LW is linked to very low wind speed, calm surface conditions, and strong near-surface stratification during DWL formation. SEP20-HW describes traversing a sharp frontal slick under relatively high wind conditions. MAR21 features a well-developed GCW field and a gradual surface temperature change, with slicks making a brief appearance that was significantly shorter than the transect duration. The final observation (OCT22) relates to transient low wind speed around the wind-wave generation threshold and a large extent of slicks on the water surface, showcasing the surface wavefield's heterogeneity. After examining each transect, we combine all the data to analyze the intertransect variability of fluxes and compare the average fluxes to bulk parameterization estimations.

3.3.1 Calm condition with intense near-surface stratification (SEP20-LW)

This transect was conducted during a campaign in September 2020. The wind speed was below 1 m s^{-1}, resulting in calm water conditions without visible gravity-capillary waves forming on the surface (Figure 3-4G-I). However, as this campaign was carried out outside the field of view of the remote imaging system, it is uncertain whether this calm condition was limited to the area where the campaign took place. Intense near-surface stratification with a relatively high surface temperature was observed (Figure 3-3 andFigure 3-4D). Due to very low wind speeds and a lack of wave-induced mixing, there was minimal near-surface exchange, resulting in heat accumulation in a thin surface layer and the near-surface thermocline almost extending to the surface (Foroughan *et al.*, 2022b). Similar development of a diurnal warm layer was

previously observed in both oceanic and inland waters (e.g., Augusto-Silva *et al.*, 2019; Mac-Intyre, Amaral, *et al.*, 2021; Ward, 2006).
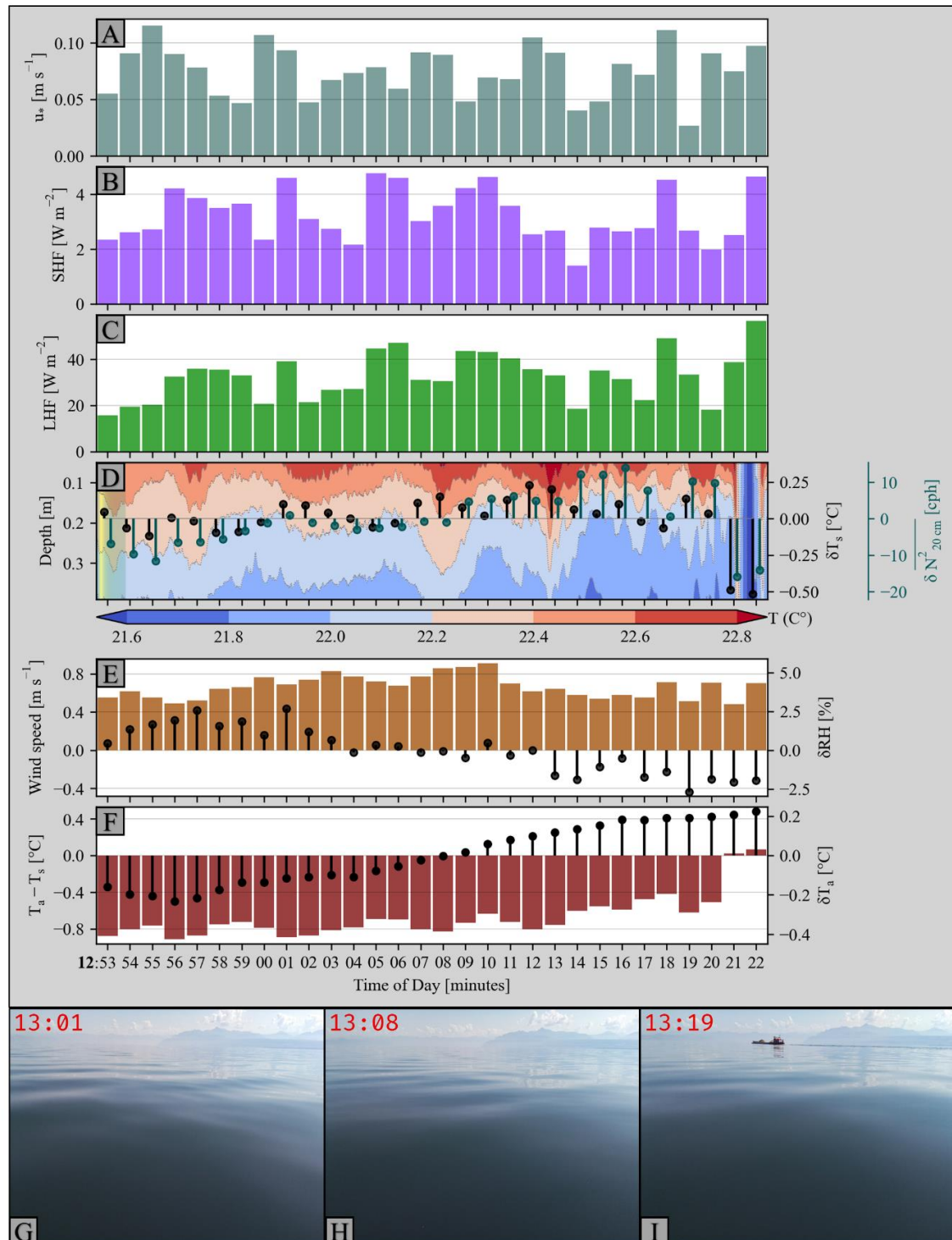

Figure 3-4. Air-water exchange variability during the SEP20-LW transect. A-C) Short-term fluctuations in friction velocity, sensible, and latent heat fluxes based on wavelet cross-scalograms with 60-s averaging windows. Water- and air-side variables (except temperature profiles) shown in the following panels were averaged within the same window as the fluxes. Surface

temperature and near-surface stratification (averaged in the top 20 cm) were estimated using the footprint analysis described in Section 3.2.4.5. D-F) Near-surface temperature profile based on the top six sensors (down to ~40 cm), wind speed, and air-water temperature difference. Overlaid on the temperature profile is a 1D representation of the flux footprint associated with the start time of the first bar. This provides an example of the spatial extent of the flux footprint converted into a temporal scale. The colormap used for the footprint corresponds to the source distributions (see Figure 3-5G for a 2D example). The colorbar for temperature profiles is shown horizontally below the plot. Panels D-F show anomalies in surface temperature, near-surface stratification, relative humidity, and air temperature, respectively, along the right vertical axis. G-I) Three snapshots from the ZiviCat onboard camera show the calm water surface under observed wind conditions. Panel I shows a dredging ship that frequently operates on Lake Geneva. White space between bar plots serves only as a visual aid.

A spatiotemporal variability was observed in surface and near-surface water temperature (Figure 3-4D), with alternating thermal distributions near the surface. While the wind speed increased and then decreased during the transect, the air temperature increased almost consistently. Consequently, the air-water temperature difference declined with the rise in air temperature. The relative humidity also decreases along this transect. (Figure 3-4E, F).

Variabilities in fluxes appear to follow two regimes (Figure 3-4A-C). First, from the start until 13:10, there was a gradual increase in wind speed, with the surface water remaining calm without visible wind waves throughout the transect (Figure 3-4G-I). The increase in wind speed appears to be accompanied by an increase in both SHF and LHF. The friction velocity, however, did not follow the same variations as the turbulent heat fluxes. The second phase began after the wind dropped to around 0.5 m s^{-1}, and the air temperature approached the surface temperature. The turbulent heat fluxes generally decreased during this period, with a slightly increased correlation between SHF, LHF, and friction velocity. Notably, from 13:14 to 13:20, all fluxes exhibited an inverse correlation with the variation in near-surface stratification. In addition, during this transect, the passage of a large boat mixed the near-surface water column thoroughly (Figure 3-4D, I). Such mixing seemed to link to an abrupt increase in fluxes, as the LHF reached its maximum value during this transect.

Wind conditions similar to those observed during the present study, and the associated absence of wind-generated gravity-capillary waves, are common on the lake (Figure 3-1). However, the absence of waves obscures the study of natural slicks, as the presence and patterns of slicks are not distinguishable when no waves are generated. This effect is discussed further when describing the OCT22 transect in Section 3.3.4.

3.3.2   Strong surface temperature gradient (SEP20-HW)

A 10-km-long frontal slick was documented in Lake Geneva a few weeks later after the previous campaign, revealing the formation and evolution of an elongated natural slick that coincided with the LSWT front (Foroughan *et al.*, 2022a). In this study, we present the results of a transect with an appropriate relative wind direction and a sufficient length for short-term flux estimations. Along with the slick, the prominent feature observed was the sharp temperature gradient measured by the ZiviCat (Figure 3-5D). Moreover, during this campaign, there was a noticeable increase in FDOM enrichment in surface water inside slicks compared to non-slick regions (Foroughan *et al.*, 2022a).

In contrast to the previous case, this transect features a well-mixed near-surface water column and a relatively large air-water temperature difference, resulting in higher magnitudes of heat exchanges and friction velocity (Figure 3-5). The physical processes that led to the observed LSWT front and slick formation were detailed in previous work (Foroughan *et al.*, 2022a). The present study highlights the variability in surface fluxes due to the sharp LSWT front. The air-water exchanges, in general, showed a reduction in the cross-front direction, with larger fluxes on the warm side of the front than on the cold side. Despite the slightly higher wind speed and the presence of a developed wave field, the fluxes showed a greater dependence on the air-water temperature difference than wind speed. In particular, heat fluxes increased abruptly when the flux footprint crossed the sharp temperature gradient (Figure 3-5B, C).

Although the wide and persistent slicks were developed along with the temperature front, no strong variability due to these slicks was observed in the fluxes. The frontal slick broke apart and a small "island" of the rippled region was formed in the northernmost part of the front where the ZiviCat transects were conducted (Figure 3-5G). There were also smaller natural slicks on the cold side of the front. However, due to the small spatial scales of these slicks, they did not contribute to the flux footprint based on the threshold defined in Section 3.2.4.5.
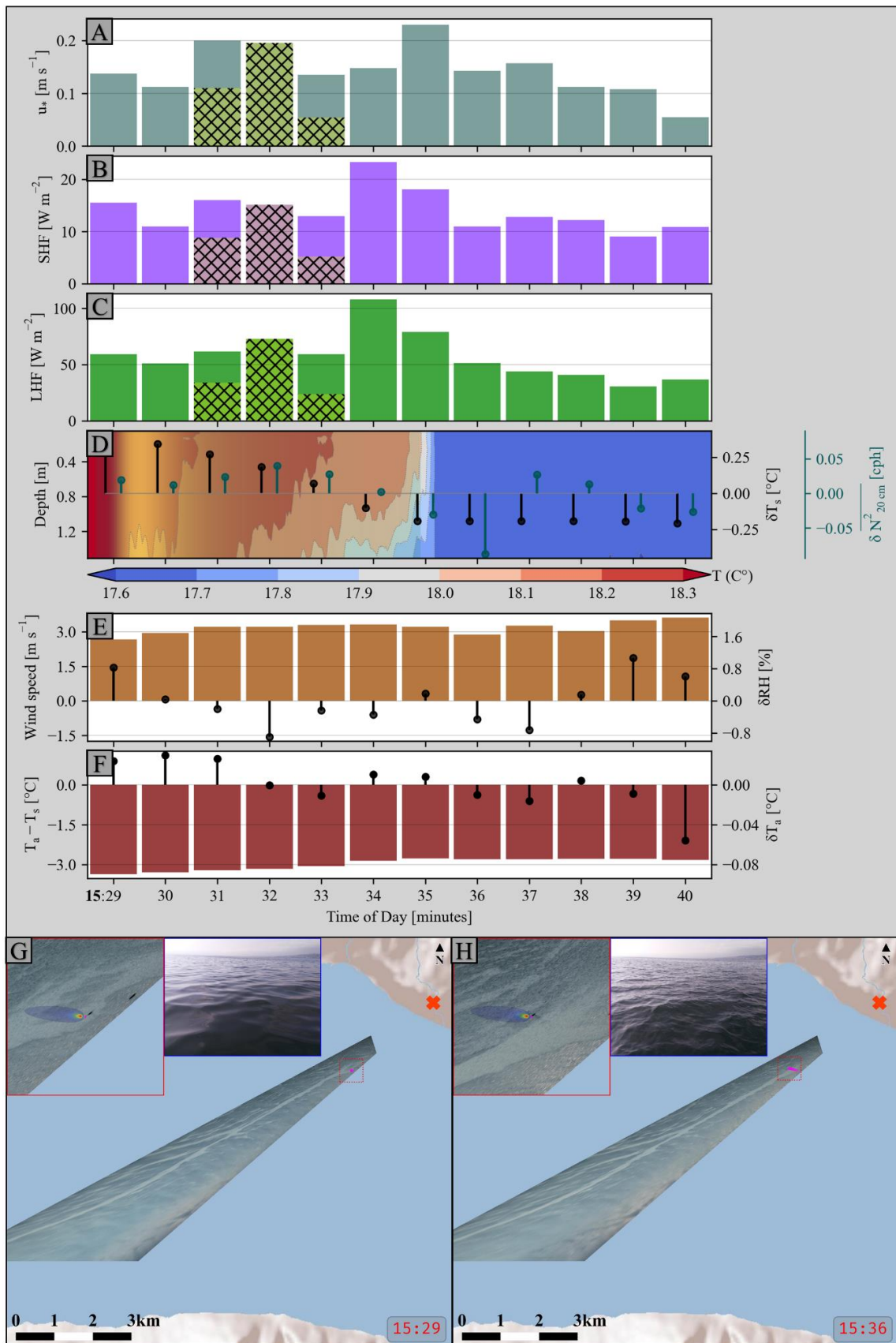
Figure 3-5. Air-water exchange variability during the SEP20-HW transect is shown in panels A-F, as described in the caption of Figure 3-4. However, the near-surface temperature contour plot spanned down to 1.5 m. Highlighted cross-hatched segments on fluxes indicate slick contributions based on their presence in the flux footprint (Section 3.2.4.5). G, H) Two snapshots of the ZiviCat carrying out this transect, with underlying maps depicting the region in Figure 3-1B and the red cross indicating the location of the camera package. Rectified images taken by the TLB are overlaid on the map. Two smaller images on the top left show a zoom section of the map marked by the red dotted triangle (red outline) and an image taken by the onboard camera system at the same time (blue outline) displaying the in situ state of the surface water. Two-dimensional flux footprints are superimposed on the zoom section. The magenta points indicate ZiviCat's location and past tracks based on GPS data. The rectified shape of the ZiviCat and the boat can be seen around this magenta point as small dark lines in the zoom section. There is a small offset between the rectified outlines and ZiviCat GPS locations due to a calibration error during rectification. The local time at which each snapshot was taken is indicated in the bottom right corners.

3.3.3   Well-developed GCW field (MAR21)

The MAR21 transect was characterized by relatively high wind conditions and sharp-crested wind waves. The vertical temperature gradients were much smaller, and the early spring surface temperatures recorded during this transect were the lowest among all the observations in the present study. An elongated slick was observed using the remote imaging package and crossed by the ZiviCat during the transect. Similar to SEP20-HW, surface water was sampled inside and outside the slick for this campaign, and the results were incorporated into the overall statistical analysis (Figure S3.0-3). The observed slick in Figure 3-6 was associated with higher FDOM enrichment.

Figure 3-6 shows that the wind speed was relatively high and gradually decreased towards the end of the transect. There were small variations in air temperature, and the surface temperature varied smoothly, unlike the previous frontal transect. Nevertheless, both surface temperature and near-surface stratification increased over the course of this section. Yet, the air-water temperature difference remained relatively stable. Relative humidity varied by up to 10% during the measurements. On the water side, even though vertical variations in temperature and stratification were small, some short oscillatory patterns were observed in the near-surface temperature profile.
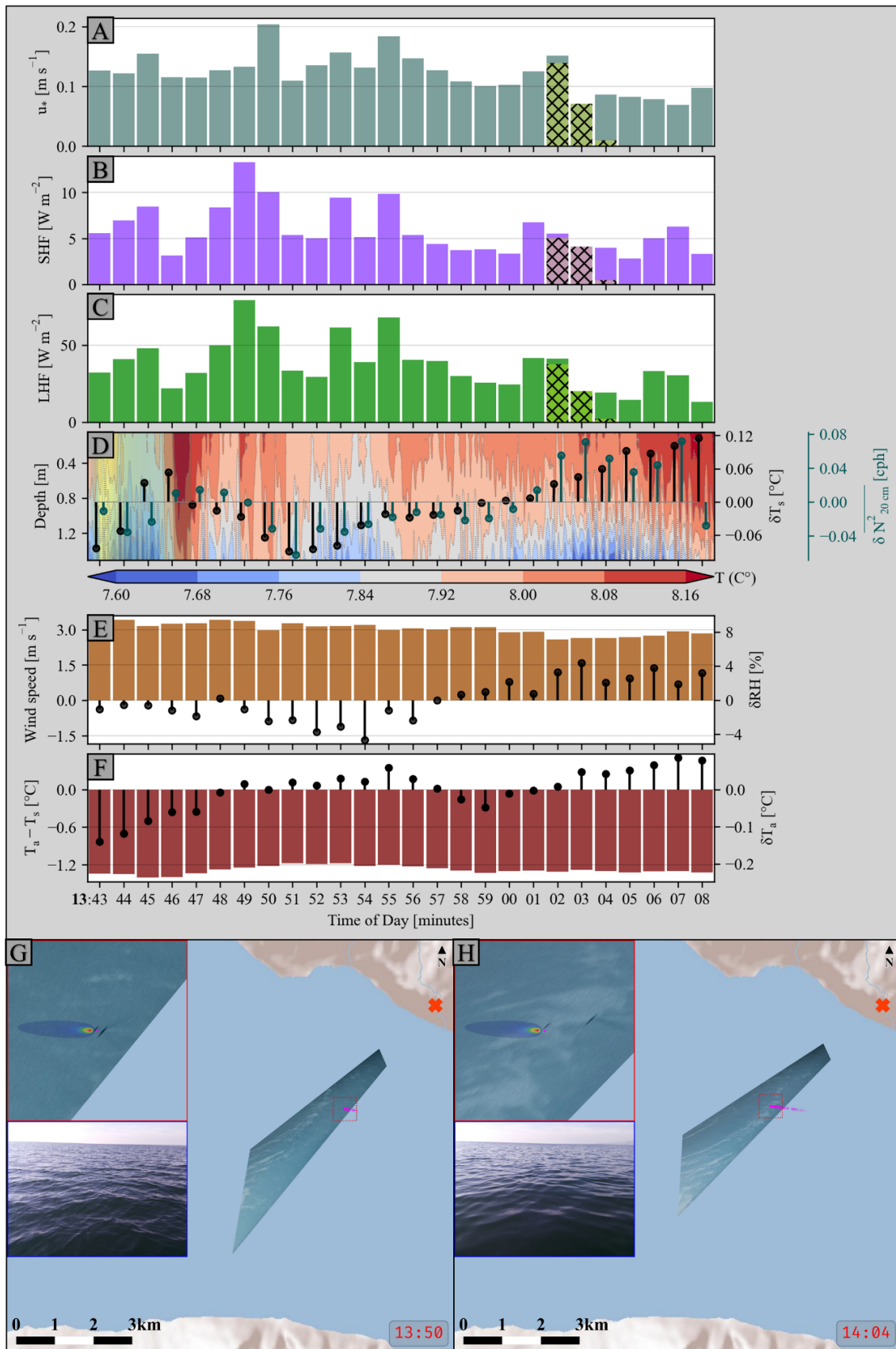
Figure 3-6. Air-water exchanges and associated variables during the MAR21 transect are shown in panels A-H, as described in Figure 3-4 and Figure 3-5 captions. In panel H, the TLB snapshot pans 5° more westward than in panel G. The dropped dots in the ZiviCat track correspond to missing images in the TLB recordings.

Figure 3-6A-C illustrates the impact of the observed slick towards the end of the transect in two intervals (14:02 and 14:03). The minimum momentum flux is observed in one of these intervals for friction velocity. However, SHF and LHF show no significant impact due to slicks compared to the surrounding fluxes. Nevertheless, near-surface stratification is highest within the slick, indicating lower near-surface mixing, which may be linked to the absence of small wind waves (Foroughan *et al.*, 2022b). The onboard camera images reveal that only small gravity-capillary waves are dampened inside the slick, while large waves still persist. Despite this, the damping of these short waves still has a significant impact on the water's reflective properties, making the slick observable from the remote camera package.

3.3.4 Intermittent low wind speed (OCT22)

This transect was part of a campaign conducted in mid-October 2022 within the TLB field of view, similar to the last two cases. The ZiviCat traveled offshore and transected various scales of natural slicks. This transect was characterized by a transient low wind condition. While spatiotemporal variations in wind speed were observed in previous cases, what sets this transect apart is that wind speed dropped below the threshold for wind-wave generation in the middle of the transect. This was reflected in the sequence of the generation, dissipation, and regeneration of gravity-capillary waves on the water surface during the transect, as inferred from in situ observations and the remote imaging package (Figure 3-8). Surface water sampling was not conducted during this campaign for technical reasons. However, based on circumstantial evidence from other campaigns and recent studies on Lake Geneva (Section 3.2.5), it is reasonable to classify the smooth patches as natural slicks.

As the platform moved along the transect, the air temperature gradually increased. Due to small variations in surface temperature, the difference between air and water temperature decreased. Towards the end of the transect, the relative humidity also went down (Figure 3-7D-F). However, one of the most significant factors affecting the dynamics of air-water exchange processes during this transect was the drop in wind speed below ~1.5 m s^{-1} from 13:48 to 14:02 for about 15 minutes. This wind speed appears to be the threshold for wind-driven wave generation in accordance with previous work in Lake Geneva (Foroughan *et al.*, 2022b). The reduction in
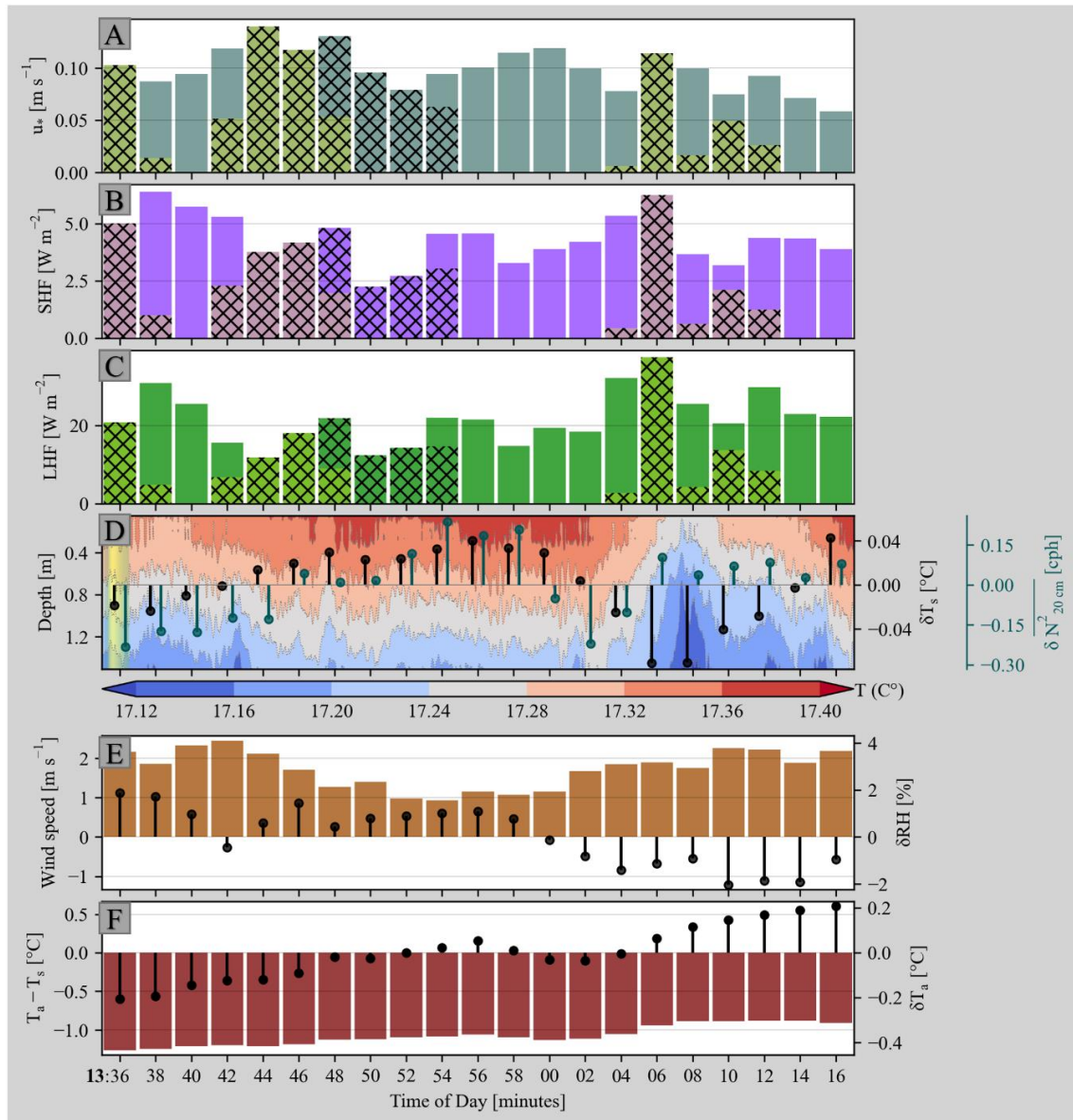
Figure 3-7. Air-water exchange variability during the OCT22 transect as well as the time series of some environmental state variables, are shown in panels A-F, as described in Figure 3-4 and Figure 3-5 captions. Given the relatively long duration of the OCT22 transect, two-minute averages are presented for better visualization rather than 60-second intervals. Figure 3-8 also shows the corresponding TLB images for this transect. The non-highlighted hatched regions in the flux time series represent the time when the ZiviCat operated inside slicks while the wind speed simultaneously dropped, leading to calm surface water in both slick and non-slick regions (approximated from Figure 3-8C, D). The slick/non-slick flags were estimated using both the on-board camera and TLB images.

wind speed coincided with the development of a thin warm layer close to the surface and an increase in near-surface stratification. The most prominent feature in the near-surface tempera-

ture was a cold upwelling region that appeared approximately between 14:04 and 14:08, corresponding to 250 m of distance. The catamaran then moved into warmer water subsequently.

The turbulent heat fluxes appear to follow such intermittency in wind-wave dynamics. Although the fluxes are generally lower compared to other campaigns, they decrease to very low values during the slick passage, followed by wind drop and calm conditions. The highest flux is observed during the early stages of wind wave formation and subsequently in the cold upwelling region towards the end of the transect (Figure 3-7A-D andFigure 3-8E). After this peak, heat fluxes remain relatively stable, provided wind speed remains above the wave generation threshold. Similar to the SEP20-LW campaign, the momentum exchange in this study is also decoupled from latent and sensible heat in low wind conditions, and the friction velocity becomes very low near the end of the transect. However, it should be noted again that the momentum flux in this transect was flagged by the QC step and requires caution in interpretation.

The transient wind speed and the widespread presence of natural slicks during this transect created a complex spatiotemporal dynamic in GCW field, as illustrated in Figure 3-8. The ZiviCat started from a location close to the shore and navigated towards the center of the lake, with the wind coming from the southeast during this period. Due to the relatively low wind speed, the waves were not as sharp-crested as in MAR21 and SEP20-HW in non-slick regions (Figure 3-8B, E, F). Around 13:45, the catamaran entered a wide slick (~600 m, Figure 3-8C). When the ZiviCat was in the middle of this large slick, wind speed dropped below 1.5 m s^{-1}, and the northern region of the lake became calm (Figure 3-8D). As wind waves disappeared from the surface, slick and non-slick patterns also vanished. However, we still approximated the extent of the large 600-m slick presence in the flux footprint using these images and marked them in the flux time series (Figure 3-7A-C). During this period, surface water did not differ significantly between slick and non-slick regions in terms of small gravity-capillary waves, at least qualitatively (Figure 3-8C, D).

Eventually, slick/non-slick patterns reemerged in this northern region when the wind rose again (Figure 3-8E, F). With small wind waves returning to the surface (Figure 3-8E) and fluxes increasing, the catamaran entered another filamentary slick that coincided with the relatively cold water. Throughout this transect, slicks appeared to cause a local reduction in surface heat fluxes, except in this particular case, where it coincided with such a cold, seemingly upwelled region.
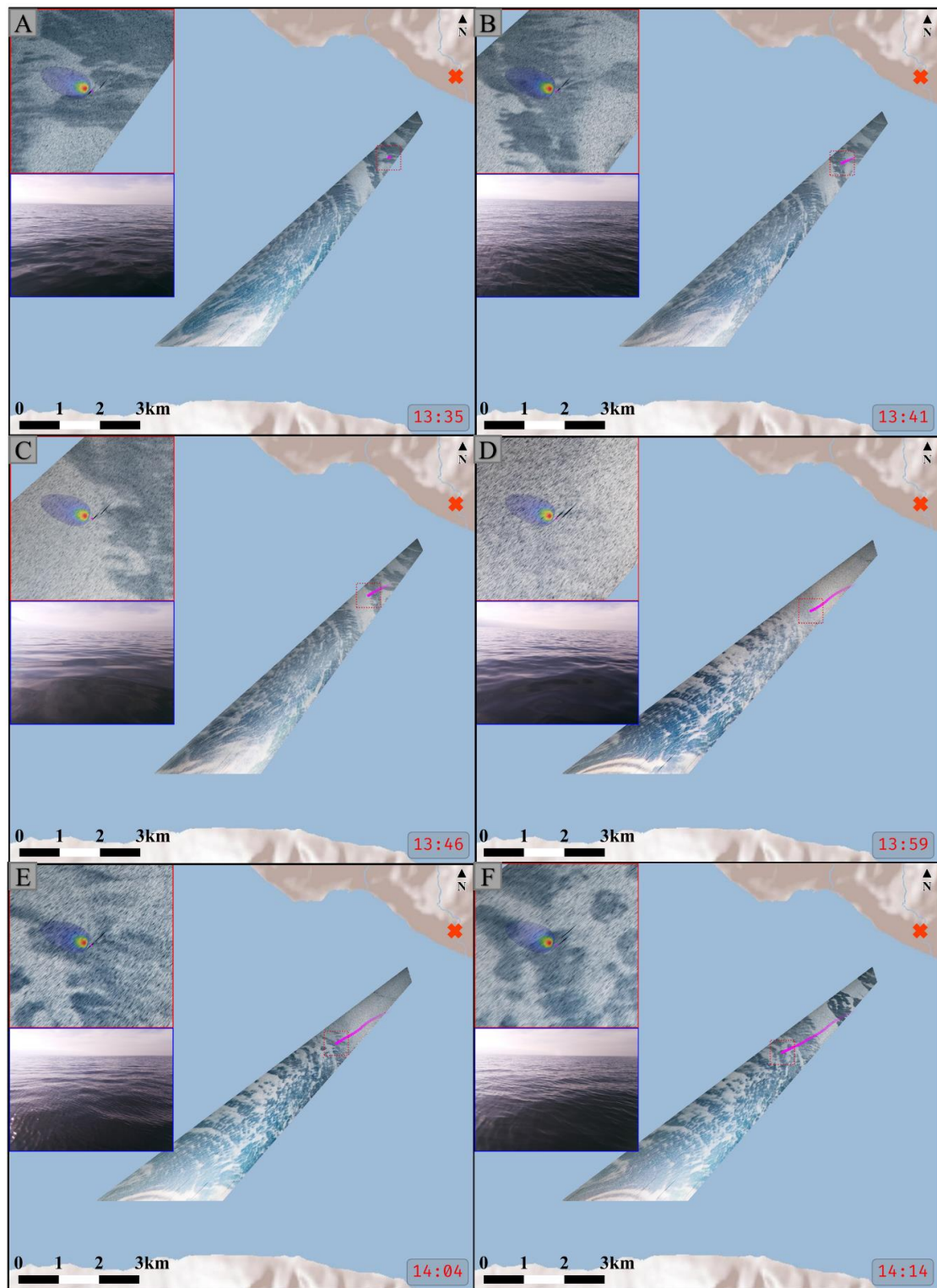
Figure 3-8. Six snapshots of the catamaran during the measurement process. The subfigures within the panels are described in Figure 3-5. The panels D-F have a pan angle of 5° more towards the west than the panels A-C. The two-dimensional flux footprint overlaid on the zoom section is directed towards the mean wind direction during the transect. The ZiviCat was unable to perform autonomous waypoint navigation due to software issues, so the trail was not perfectly straight, and the transect was controlled remotely.

3.3.5   Intertransect fluxes variabilities

Figure 3-9 provides an overview of 113 short-term (one minute) observations of friction velocity, SHF, and LHF derived from wavelet analysis during the transects discussed in this study. These transects cover a diverse range of environmental conditions, including low surface temperatures in early spring and high summer surface temperatures and variations in wind speed, relative humidity, water column stability, and air-water temperature differences between cases. This representation provides insight into the variabilities of fluxes observed across different cases.

Among the four transects analyzed in this study, the lowest latent heat flux was observed during OCT22. This observation featured moderate surface temperature and well-mixed near-surface conditions but also the highest relative humidity. SEP20-HW (front observation) had the greatest surface exchanges, with a large air-water temperature difference. Along with MAR21, these two observations had higher wind speeds, resulting in well-mixed near-surface temperature conditions. On the other hand, SEP20-LW was characterized by strong stratification and the development of a diurnal warm layer. This campaign had the smallest sensible heat flux and momentum exchange, but the latent heat flux was slightly greater than OCT22.

All measurements in this study were conducted under unstable atmospheric conditions, as indicated by the ABL stability parameter ($\zeta = \frac{z}{L}$), where z is the measurement height and L is the air-side Monin-Obukhov length. To further examine the intertransect variability, we compared the eddy covariance fluxes derived from Equations 3-1 to 3-3 to a collection of commonly used bulk parameterizations in marine environments (Figure 3-10), which were recently compiled into a Python package by Biri *et al.* (2023). Only eight of these bulk methods are applicable to this study given the low wind speed conditions. Table S3.0-1 summarizes the models, and further details can be found in Biri *et al.* (2023) and references therein. As we did not have access to radiation data, these models were run without the warm layer and cool skin options. Nonetheless, convective gustiness was incorporated into the models, as it has a considerable impact under unstable low-wind conditions (Guseva *et al.*, 2023).
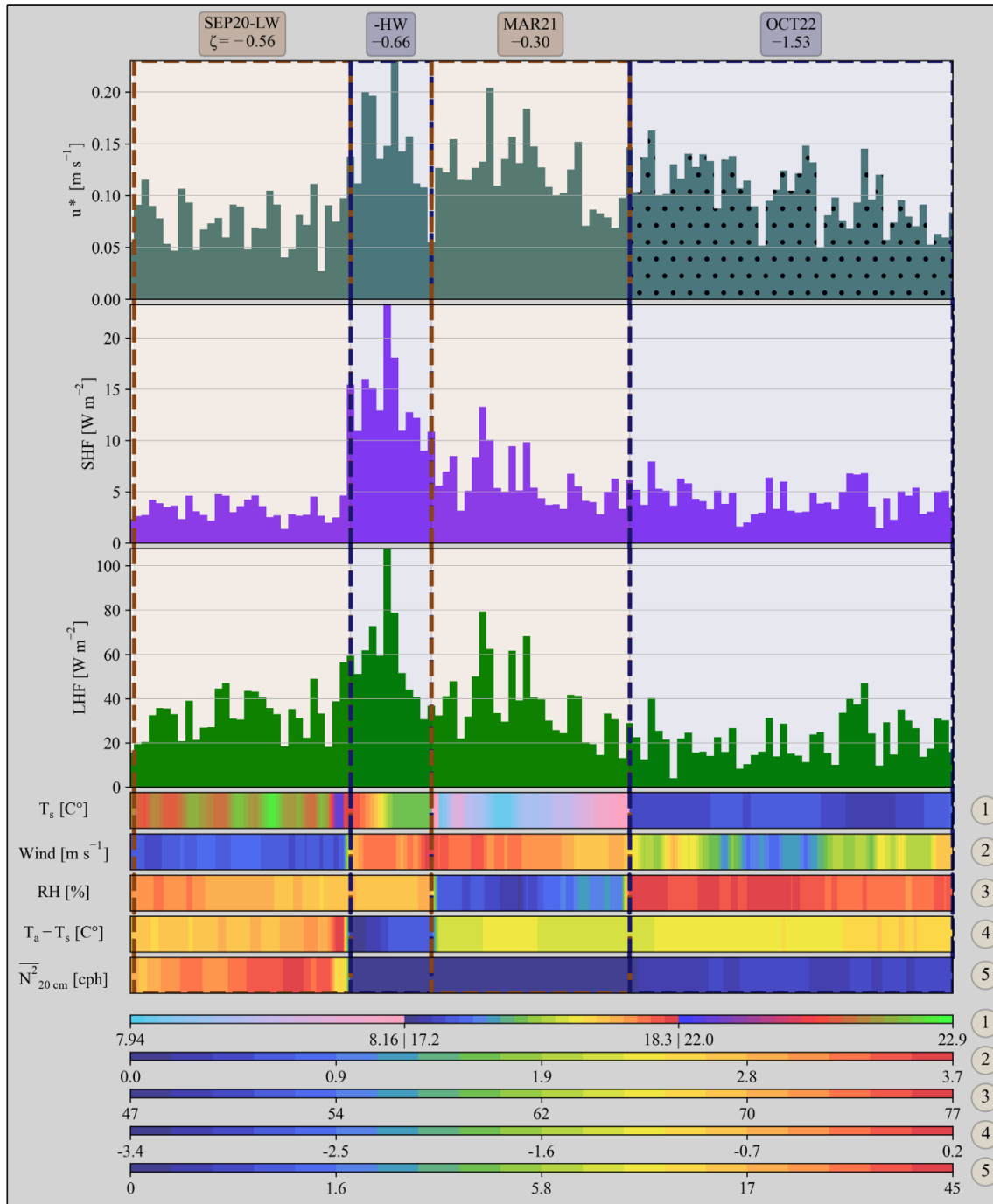
Figure 3-9. The intertransect variability of short-term friction velocity and turbulent heat fluxes. The top three panels show the fluxes for the four campaigns described in Sections 3.3.1 to 3.3.4. The middle panel illustrates the variability in some air-side and water-side parameters. To relate the variability maps to the colorbars at the bottom of the figure, use the numerical values on the right side of the plot. Due to the highly variable surface temperature between transects, three ranges are displayed with three different colormaps. The colorbar for near-surface stratification changes logarithmically for visualization purposes. The label for each figure and the atmospheric stability parameter exported from EddyPro are shown at the top of the plot. A dotted region superimposed on the fluxes indicates flag "1" in flux quality control during developed turbulence test.
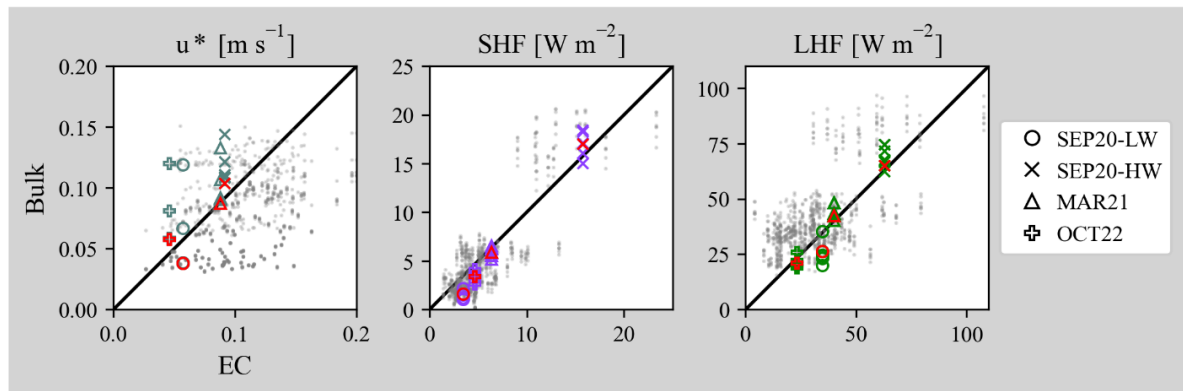
Figure 3-10. Comparison of eddy covariance-derived fluxes and empirical bulk parameterizations for momentum, sensible heat, and latent heat flux. Each transect is represented by a unique marker. Red markers indicate the closest models to the observations for each flux, based on Mean Average Error (MAE). Gray dots represent bulk estimates from one-minute averaged data, compared with short-term wavelet fluxes.

While the bulk models generally predicted comparable values for turbulent heat fluxes, momentum exchange predictions were more variable. The ECMWF parameterization (Table S3.0-1; Beljaars, 1995; ECMWF, 2019) had the closest agreement with the data for heat fluxes, with Mean Average Errors (MAE) of 3.8 W m^{-2} for LHF and 1.2 W m^{-2} for SHF. This parameterization has also been applied to Figure 3-1 estimations of three-year turbulent heat fluxes. The COARE3.5 (Table S3.0-1; Edson *et al.*, 2013) model had the most consistency with our data for the momentum flux, with a MAE of 0.011 m s^{-1}. As expected, short-term wavelet fluxes could not be accurately captured by bulk methods.

3.4 Discussion

This study uncovers the complex dynamics and interplay of various processes under low-wind conditions in Lake Geneva. Individual transects displayed diverse features of the air-water interface and associated exchanges within this wind regime, such as spatiotemporal variations in surface and near-surface temperatures, the occurrence of natural slicks, and a calm-to-wind-wave transition. A novel, underway direct flux measurement, combined with high-resolution concurrent air-side and water-side measurement techniques, was utilized to account for short-term fluctuations in surface fluxes and investigate the potential effects of these processes on air-water exchanges. We assessed the proposed methodology under low wind conditions and explored the processes that characterize air-water interaction.

3.4.1 Short-term flux measurements

Short-term air-water exchange estimation was achieved through direct flux calculations based on wavelet analysis, allowing flux determination on a one-minute timescale. The methodology was tested across multiple transects under varying environmental conditions, enabling surface flux variability monitoring with respect to environmental variables. Unlike eddy covariance measurements, this method does not require a steady-state assumption. On a mobile platform, however, it was not possible to distinguish completely between nonstationary and spatially heterogeneous conditions.

The one-minute averaging time window chosen for this study was short enough to account for some of the small-scale spatial variables, such as the observed natural slicks or local variation in surface temperature. This time window has been used in previous short-term flux studies (Laxague *et al.*, 2018; Schaller *et al.*, 2017). The short time window also results in high spatiotemporal flux variability. While some variations can be associated with the observed environmental state variables simultaneously measured by the ZiviCat, not all of them are linked to these parameters.

Short-term synchronous bursts of increase or decrease in friction velocity and turbulent heat fluxes were observed, particularly during relatively high wind transects (Figure 3-5 andFigure 3-6). As no evident connection was identified between these fluctuations and the measured environmental parameters present alongside the fluxes, this variability could potentially be attributed to coherent motions within the atmospheric surface layer. The bursts can be attributed to gustiness typically encountered in low-wind conditions within an unstable atmospheric boundary layer, which arises from random convective motions (Godfrey and Beljaars, 1991). This gustiness can be linked to the difference between scalar-averaged and vector-averaged wind speed (Grachev *et al.*, 1998; Wei *et al.*, 2016). In this study, the four cases exhibited a higher scalar-averaged velocity than vector-averaged velocity (See Table S3.0-2 for definitions), with a root mean square difference of 0.045 m s^{-1} between the two. This value is comparable to those observed for another lake under low-wind conditions (Wei *et al.*, 2016), suggesting the potential presence of convective gustiness. However, determining whether such variability is due to gustiness or other coherent motions in the unstable atmospheric boundary layer is not within the scope of the present study.

3.4.2 Surface temperature variability

During the SEP20-HW campaign, a sharp temperature gradient of 0.7°C in approximately 10 meters was observed in the middle of the transect. While the formation of this front and the associated slick were discussed elsewhere (Foroughan *et al.*, 2022a), this study focuses on the effect of these processes on surface energy flux. Short-term flux measurements showed that turbulent heat fluxes and friction velocity were higher on the warm side of the front than on the cold side. This cross-front variability in surface fluxes was also observed on a larger scale using shipboard eddy covariance measurements and bulk flux calculations across surface temperature fronts in the ocean (Iyer *et al.*, 2022; Shao *et al.*, 2019). The cross-front variability in the fluxes can be linked to the abrupt shift in air-water temperature difference, which was nearly equivalent to the surface temperature gradient (low air temperature variation). Enhanced surface heat fluxes near submesoscale fronts have been observed through both in situ measurements and numerical simulations (Shao *et al.*, 2019; Su *et al.*, 2018). However, such high-resolution short-term measurements crossing submesoscale fronts were not previously conducted. The observed enhancement at the front is likely caused by the increased water-side turbulence activity resulting from intense downwelling at the front (D'Asaro, 2014; Esters *et al.*, 2018).

The results suggest that in addition to strong surface temperature gradients, even small and localized temperature variations can contribute to short-term flux variability. During the MAR21 and OCT22 transects, we observed minor but distinct patterns of surface and near-surface temperature gradients. In MAR21, a local increase in surface temperature (0.05-0.1°C) appeared to reduce turbulent heat fluxes in the affected area. However, such surface temperature variations did not significantly alter the air-water temperature difference and were offset by air temperature variations.

During the OCT22 transect, a local region of cold water was observed, which coincided with an enhancement in turbulent heat fluxes. A recent study in Lake Geneva has documented summertime submesoscale cold filaments within large-scale cyclonic circulations (Hamze-Ziabari *et al.*, 2022b). Although their work measured larger temperature gradients than the present observation, the surface manifestation of a filamentary slick (Hamze-Ziabari *et al.*, 2022c) inside an apparent cyclonic rotating flow (Figure 3-8) and the spatial scale of the observed feature (~300 m) provide evidence linking the observed reduction in surface temperature to similar processes. As a result, the rise in surface heat fluxes may also be related to enhanced vertical motions within submesoscale filaments (McWilliams, 2017); however, comprehensive water-

side measurements are needed to substantiate this hypothesis. Such an increase in surface heat flux due to enhanced turbulent motions can also be observed when the ZiviCat transects the wake of a large boat during the SEP20-LW transect (Figure 3-4D, I).

During the SEP20-LW transect, an intense DWL formed, accompanied by significant spatio-temporal variability in near-surface (20 cm) stratification (~20 cph in 20/1.4 minutes/km). A correlation was observed between energy fluxes and water-side stability, particularly from 13:10 towards the end of the transect, where higher fluxes were associated with weaker strati-fication. Lükő *et al.* (2022) also demonstrates a decrease in SHF in more stable near-surface water based on long-term air-water exchange measurements in a lake. However, the intricate interplay of turbulence and near-surface stratification (Hughes *et al.*, 2020b; MacIntyre *et al.*, 2021a) must be considered when establishing these connections between air-side and water-side processes. Furthermore, it is important to note that these results rely on surface temperature measurements from a sensor at 5 cm depth; using radiometric measurements of skin temperature with the same methodology could yield a more accurate relationship between surface temperature heterogeneity and short-term flux variability.

3.4.3 Natural slicks

During low wind conditions, the most visually prominent features at the air-water interface are natural slicks. Our findings suggest that the extent and coverage fraction of slicks on the surface differ significantly among the observed cases. This may be due to both intermittent physical forcing and variations in surfactant concentration. As for the latter effect, surface water sampling campaigns in Lake Geneva have demonstrated that the FDOM pool can be enriched by both allochthonous and autochthonous contributions (Figure S3.0-3; Foroughan, Lemmin, *et al.*, 2022). Although seasonal shifts can influence both sources through changes in terrestrial inputs and biological activities, the present study is not intended to evaluate the impact of these processes on slick distributions within Lake Geneva.

The interplay between wind fields and near-surface currents also affects slick morphology and coverage (Ermakov *et al.*, 1992). Prior studies connected slick formation in lakes and oceans to large-scale surface currents (Ermakov, 2012; McKinney *et al.*, 2012). The frontal slick observed during the SEP20-HW transect aligned with the edge of mesoscale circulation (Foroughan *et al.*, 2022a). Similarly, shore-based images captured during the MAR21 and OCT22 transects displayed large-scale slick structures that resembled circulation patterns

within the lake (Figure 3-6G, H; Figure 3-8; (Hamze-Ziabari *et al.*, 2022a, 2022c). The northern region of the lake also showed large slicks that were not necessarily associated with circulations during the OCT22 observations. Compared to SEP20-HW and MAR21, the relatively low wind speed during this transect was not likely sufficient to break up or constrain the size of the observed slicks.

By conducting short-term underway measurements, this study provides a direct estimate of the potential impact of slicks on air-water exchanges. Slicks are assumed to reduce near-surface turbulence and alter wind wave properties, thereby impacting air-water fluxes. A qualitative analysis of the SEP20-HW and MAR21 observations shows that only small wind waves are dampened inside slicks, while larger gravity waves persist unaffected (Figure 3-5G, H Figure 3-6G, H). This follows from the theoretical formulation of wave damping that surfactants affect the slope spectrum most strongly in the high wave number regions (Bock and Mann, 1989; Lucassen-Reynders and Lucassen, 1970). Direct in situ measurements of the effect of slicks on turbulent energy flux are limited to a single case in oceanic studies, where a reduction in heat flux inside the slick was reported (Frew *et al.*, 2004a).

The present observation, however, shows that while there is some local decrease in surface fluxes inside slicks, it is not consistently evident across different cases. For instance, in both the SEP20-HW frontal slick and the cold region OCT22 transects, surface temperature variability influences flux variability more than the presence of slicks, with slicks having no discernible effect on exchanges. While slicks modify physical properties at the air-water interface and potentially modulate surface fluxes, their effect may be masked by other environmental variables, such as surface temperature heterogeneity. This is particularly true in natural settings where high concentrations of surfactants tend to accumulate in convergent areas, where submesoscale fronts and filaments coexist and potentially have a more substantial impact on air-water exchange processes.

3.4.4 Calm/wind-wave transitions

The OCT22 measurements demonstrate that low wind conditions can be characterized by the temporal variability of wind speed around the threshold for wind wave generation. The findings suggest a similar wind speed to previous research (Foroughan *et al.*, 2022b). Since the prior study was conducted under stable ABL conditions, it can be inferred that air-side stability has a minimal impact on this threshold. When the wind speed falls below 1.5 m s^{-1}, the surface

becomes calm, potentially with swells present, leading to a smooth surface water appearance akin to slicks (Figure 3-8D). As wind speed exceeds 1.5 m s^{-1}, wind waves begin to form in non-slick areas. The surface state's response time to wind forcing seems to be on the order of a minute for both transitions from calm to wind-wave generation and vice versa. This threshold can help refine the parameterization of surface roughness for estimating fluxes under low wind conditions, which have previously relied on assumptions of smooth or capillary waves throughout the entire low wind range (Guseva *et al.*, 2023).

During the calm condition transects (SEP20-LW), the lowest SHF and friction velocity were observed, yet it was undetermined whether an increase in wind speed above the threshold and transition to short gravity-capillary waves would affect the fluxes. In the OCT22 campaign, the re-emergence of small GCWs on the surface resulted in elevated heat fluxes (Figure 3-8E). However, given the proximity of this process to the observed cold region, it may be difficult to distinguish the impact of rising wind and associated newly generated waves from surface temperature variability. Nevertheless, the absence of waves, either inside slicks or during calm conditions, appears to enhance near-surface stratification through the removal of wave-induced mixing.

The October transect also showed that when the wind speed dropped in the northern region of the lake (the camera's near field), the southern area (the camera's far field) still featured slick/non-slick patterns (Figure 3-8D), suggesting that wind speeds remained above the 1.5 m s^{-1} threshold. These observations demonstrate that low wind conditions can exhibit local variability, which can result in spatial flux variations.

3.4.5   Intertransect variabilities and implications for bulk parametrization

The intertransect comparisons between fluxes under various environmental conditions provide insights into the dependency of turbulent heat and momentum fluxes on environmental state variables within the range discussed in this study. It appears that the air-water temperature difference and wind speed have the most impact on turbulent fluxes. Figure 3-1 highlights the differences in integrated turbulent heat fluxes under low versus high wind conditions, as recorded through single-tower meteorological data. A comparison between direct measurements and bulk parameterization (Figure 3-10) indicates a relatively small deviation between the two estimation methods for turbulent heat fluxes.

Nevertheless, LHF seems to be underestimated by most models for the calm condition transect (SEP20-LW) and overestimated for the cross-front transect (SEP20-HW). The bulk model for SHF seems consistently lower than measurements for low values and slightly higher for the high values presented in the present study. In addition, the difference between models for the SEP20-HW transect was also relatively high. Notably, the predicted momentum exchange variability is also considerably high within each transect, particularly in cases with very low wind speeds (SEP20-LW and OCT22). The results demonstrate that continued work is essential in developing bulk parameterizations under low wind conditions, particularly in relation to momentum exchange. Furthermore, the bulk estimates for short-term fluxes display significant scattering across all models, with a clear tendency to overestimate LHF and underestimate momentum exchange. This behavior is not unexpected given that empirical relationships within these formulas are based on steady-state and equilibrium conditions, which are not representative of short-term estimations (Zahn *et al.*, 2023).

The aim of this study is not to provide an evaluation of empirical bulk parameterizations but rather to highlight the short-term physical interactions that govern air-water exchanges under low wind conditions that can aid in improving such parameterizations. Future studies with larger datasets covering a range of environmental conditions, including stable conditions, are needed to fully evaluate the performance of these parameterizations under low wind conditions.

3.5   Conclusion

Low wind conditions are prevalent in lakes, yet surface flux dynamics are understudied compared to their high wind counterparts. The present study examines the spatiotemporal variation of air-water exchange of heat and momentum under low wind conditions. We presented a novel combination of mobile flux estimation and short-term wavelet flux calculations with dynamic footprint monitoring tested for the first time in a marine and aquatic environment. By applying this methodology across a range of environmental conditions and unstable atmospheric stability, we aimed to elucidate the role of physical processes particularly relevant in low wind conditions on surface flux dynamics. These processes comprise variations in surface and near-surface temperature on short spatiotemporal scales, the occurrence of natural slicks, and the shift from calm surface conditions to gravity-capillary wave generation. Through these measurements, we were able to partially isolate the influence of these processes on in situ air-water exchanges with unprecedented spatiotemporal resolution.

We observed a decrease in energy flux during the warm-to-cold transition of submesoscale fronts, as well as a local enhancement at the front location. Additionally, we found evidence of local flux variation in response to small-scale surface and near-surface temperature variability. The findings indicate a general local decrease in heat fluxes at slicks, but isolating the effect of slicks may be challenging in a natural environment, as they can coincide with other more influential processes affecting air-water energy exchange. Last, we propose two distinct water surface states under fetch-and-duration-limited variable low wind conditions: one below approximately 1.5 m s^{-1} (based on 3 m measurements), characterized by calm and smooth surface water, and another above this value where gravity-capillary waves are present. The transition from calm to wind-wave appears to enhance turbulent heat fluxes.

Although numerous uncertainties persist under low wind conditions, particularly regarding momentum exchange, our methodology can be utilized to investigate more air-side variability, including gusts during low wind unstable conditions and stable atmospheric boundary layer periods. Moreover, simultaneous measurements of quantitative wave fields and surface microlayer composition beyond visible slicks could complement current water-side measurements. These short-term measurements must also be supplemented by long-term flux measurements under low winds to better understand the temporal variability of these processes on longer time scales and evaluate the performance of empirical bulk parameterizations for air-water exchanges. The results provide insight into air-water exchange processes under low wind conditions, which have a significant contribution to the long-term energy budget in inland water bodies. Reliable estimations of these fluxes are crucial for local climate predictions, particularly under changing environmental conditions.

Acknowledgments and data availability

Supporting Information for Chapter 3

Mehrshad Foroughan, Ulrich Lemmin, Seyed Mahmood Hamze-Ziabari, and David Andrew Barry

Ecological Engineering Laboratory (ECOL), Institue of Environmental Engineering (IIE), Faculty of Architecture, Civil and Environmental Engineering (ENAC), Ecole Polytechnique Fédérale de Lausanne (EPFL), Lausanne, Switzerland

In this supplementary material, we offer a comprehensive set of figures and tables that provide further information on the methodologies employed and specific results referenced in the main manuscript. These additional resources aim to enhance the reader's understanding and provide a more in-depth perspective on the study's findings.
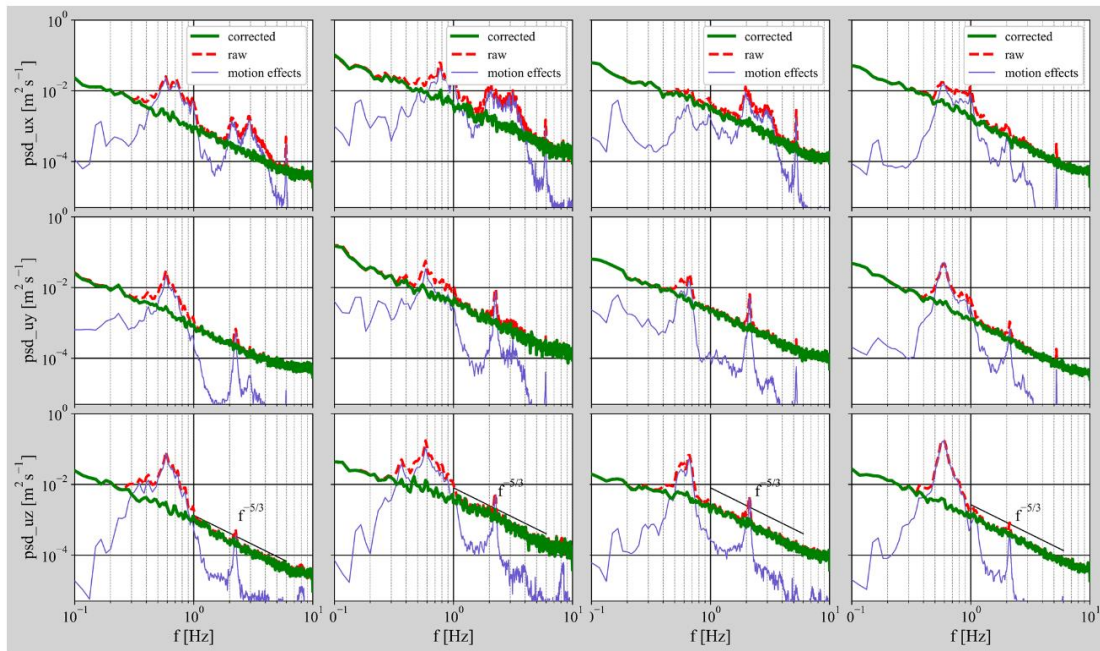
Figure S3.0-1. The power spectral density for the four transects discussed in the main text is displayed for the three components of measured velocities obtained from the IRGASON instrument. The panels, arranged from left to right, follow the same order as the campaigns discussed in the main text: SEP20-LW, SEP20-HW, MAR21, and OCT22. We followed the methodology proposed by Edson and Fairall (1998) to remove motion effects, including three-dimensional angular velocities, integrated linear accelerations, and platform velocity, from the raw signal. This procedure yields modified values where motion-induced peaks are effectively removed. The corrected data is then used in subsequent steps detailed in the main text. The straight line depicted in the figure represents the expected slope of -5/3 within the inertial subrange.
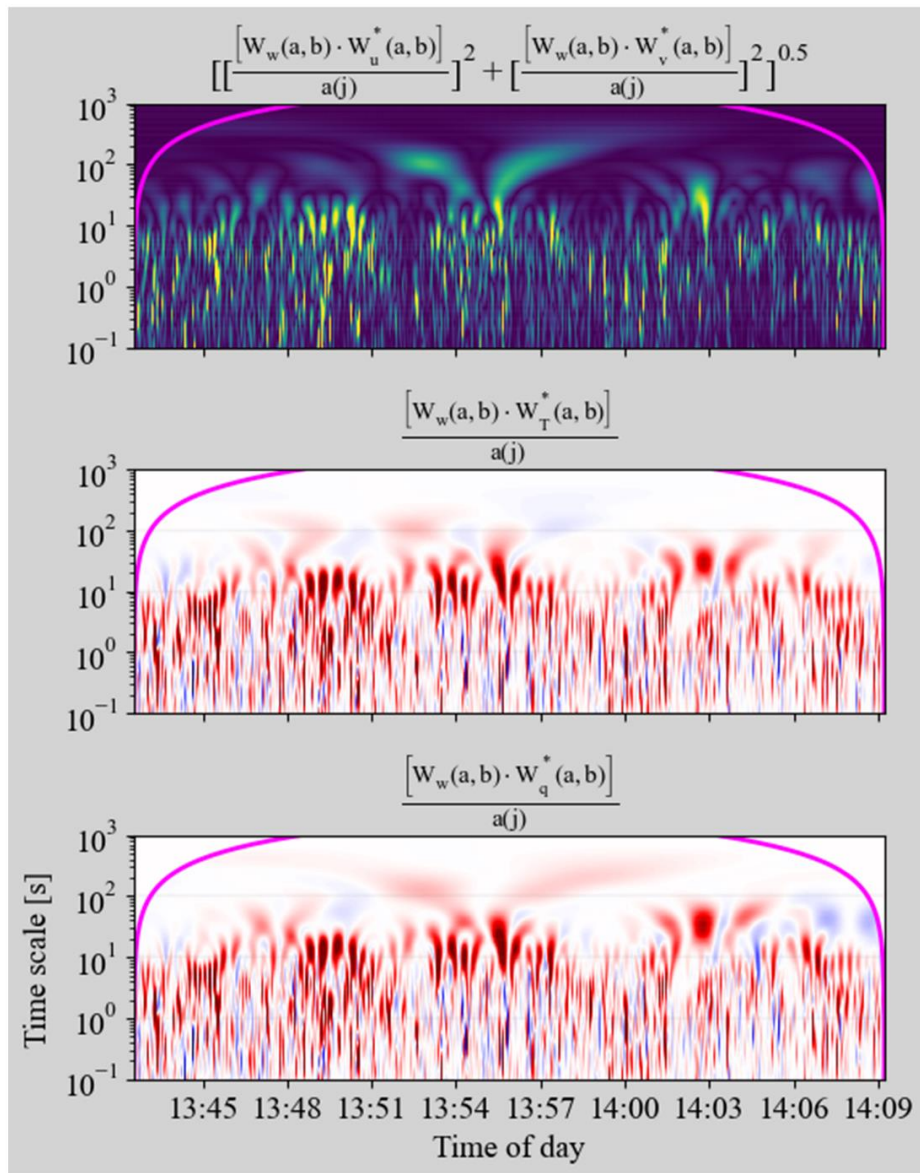
Figure S3.0-2. The wavelet cross-scalogram for the MAR21 transect, presented here as an example, demonstrates the time/time-scale decomposition of momentum flux, as well as sensible and latent heat fluxes. Refer to Equation 3-7 in the main text for panel titles. These cross-scalograms can be fully integrated for comparison with eddy covariance measurements, or partially integrated to provide short-term flux variations in accordance with Equation 3-7. The magenta line represents the cone of influence (COI). Data outside this region should be discarded due to edge effects.

Surface condition	Enrichment factor (peak T)
Slick ★	2.77
Non-Slick ★	0.76
Slick ★	1.36
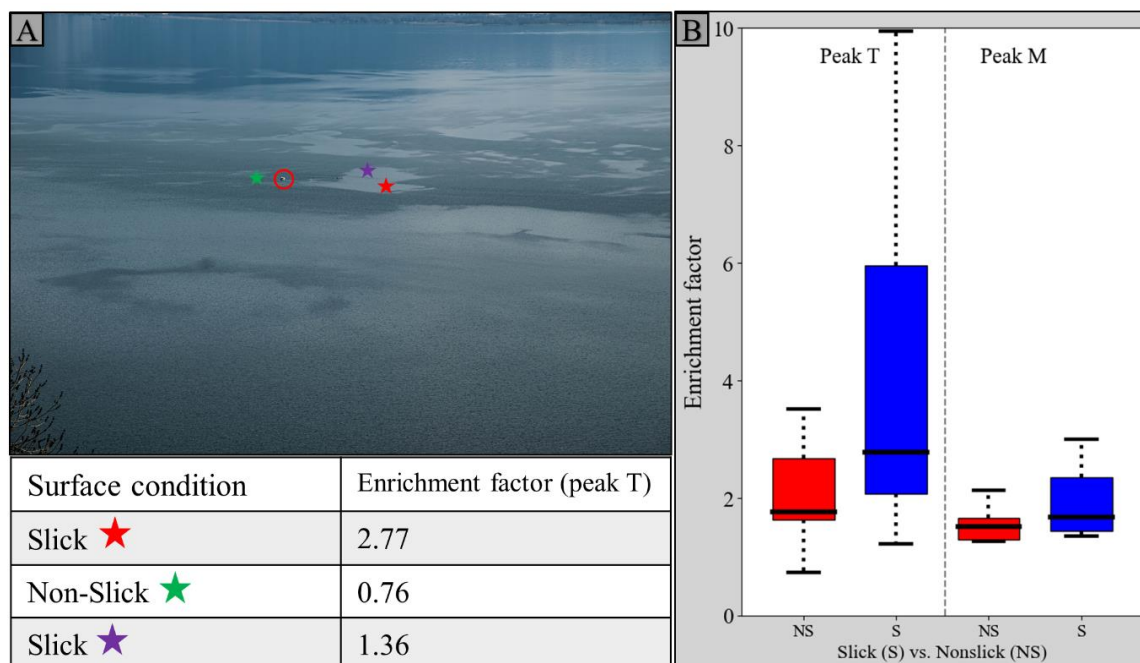
Figure S3.0-3. A) An example of slick/non-slick patterns observed during a field campaign in Lake Geneva. Although the transects from this campaign were excluded from short-term flux estimations, the sampling results were still utilized in the analysis. The campaign took place on March 26th, 2021. The locations of three samples collected from surface and subsurface water are indicated by colored stars, and the corresponding enrichment factors for protein-like (peak T) Fluorescent Dissolved Organic Matter (FDOM) are presented in the table below. The red circle indicates the boat from which sampling was conducted. B) The results for two distinct FDOM components from slick and non-slick water samples. These components correlate with surfactant activity, primarily of autochthonous origins (Salter, 2010). A permutation test was conducted to determine whether differences between slick and non-slick samples were statistically significant. The p-value for peak T was less than 0.03 and less than 0.06 for peak M. Detailed information on laboratory analysis and peak extraction from the Excitation Emission Matrix (EEM) can be found in Foroughan *et al.* (2022b).

Table S3.0-1. A summary of empirical bulk parameterizations employed in this study sourced from the AirSeaFluxCode Python package. For more detailed information about these models, please refer to the descriptions provided along with the software package (Biri *et al.*, 2023). The last column indicates how the transfer coefficients were defined (NC = neutral coefficients, RL= roughness length).

Parameterization	**References**	**Transfer Coefficients**
S88	(Smith, 1988)	RL
YT96	(Yelland *et al.*, 1998; Yelland and Taylor, 1996)	NC
UA	(Zeng *et al.*, 1998)	RL
NCAR	(Large and Yeager, 2004, 2009)	NC
C30 (COARE 3.0)	(Fairall *et al.*, 2003)	RL
C35 (COAR 3.5)	(Edson *et al.*, 2013)	RL
ECMWF	(Beljaars, 1995; ECMWF, 2019)	RL
Beljaars	(Beljaars, 1995; Zeng and Beljaars, 2005)	RL

Table S3.0-2. Definitions for scalar-averaged and vector-averaged velocities. The discrepancy between these two values becomes particularly significant during low wind conditions under an unstable atmospheric boundary layer, which suggests the presence of convective random gusts.

Scalar-averaged velocity	$\overline{U_s} = \overline{(u^2 + v^2)^{1/2}}$
Vector-averaged velocity	$\overline{U_v} = (\bar{u}^2 + \bar{v}^2)^{1/2}$

Chapter 4   A persistent submesoscale frontal slick: A novel marker of the mesoscale flow field in a large lake (Lake Geneva)

Mehrshad Foroughan, Seyed Mahmood Hamze-Ziabari, Ulrich Lemmin, and David Andrew Barry

Ecological Engineering Laboratory (ECOL), Institue of Environmental Engineering (IIE), Faculty of Architecture, Civil and Environmental Engineering (ENAC), Ecole Polytechnique Fédérale de Lausanne (EPFL), Lausanne, Switzerland

Abstract

Submesoscale fronts often become visible when the accumulation of biosurfactants in the water surface microlayer causes smooth surfaces, called frontal slicks, to develop. Based on in situ and remotely-sensed data, a frontal slick was documented for the first time in a lake (Lake Geneva). A quasi-stationary ~10-km long slick formed on the warm side of a surface temperature front with strong horizontal velocity strain. The slick width increased from ~50 to ~200 m in ~1.5 h due to "feeding" by wind-driven, rapidly-moving smaller slicks. Numerical modeling results, confirmed by satellite data, indicated that the boundary between mesoscale gyres isolated warm surface water from cold water associated with wind-induced coastal upwelling. Measurements and modeling suggest that frontogenetic sharpening of the submesoscale temperature gradient created an active front with strong convergent flow. Such dynamics must be considered in buoyant material transport and the vertical exchange of surface water with deeper layers in lakes.

4.1   Introduction

In oceans, submesoscale motions (horizontal scales 0.1-10 km; McWilliams, 2016) can cause convergence and have significant vertical velocities within structures such as fronts when surface divergence, δ, and vertical vorticity, ζ, have larger magnitudes than the Coriolis frequency, f, i.e., $|\delta/f| \geq 1$ and $|\zeta/f| \geq 1$ (Mahadevan and Tandon, 2006). Fronts are elongated in one direction and have a narrow width (McWilliams, 2021). In coastal waters, oceanic fronts were observed in regions with prominent upwelling or along the edges of high-discharge river plumes (Akan *et al.*, 2018; Garvine, 1974; O'Donnell *et al.*, 1998; Wang *et al.*, 2021). They can also develop within strongly sheared currents in the open ocean, where mesoscale straining sharpens preexisting density gradients, also referred to as frontogenesis (Gula *et al.*, 2014; McWilliams, 2021). Although their significance in the lateral and vertical transport of energy and material in oceans is recognized (Choi *et al.*, 2020; McWilliams, 2016), front studies in lakes are rare, and are mainly limited to thermal bars observed in the nearshore zone during spring and fall (Fichot *et al.*, 2019; Naumenko *et al.*, 2012).

Density fronts are typically associated with strong convergence that leads to the accumulation of surface material (e.g., D'Asaro *et al.*, 2018). As a result, fronts can be observed as bands of materials floating on the surface, sometimes exhibiting distinct wave-field characteristics (Rascle *et al.*, 2017, 2020) in response to wave-current interactions (Kudryavtsev *et al.*, 2005; Phillips, 1984). Surface roughness can also vary near frontal convergence zones due to the accumulation of biogenic surfactants, usually under low wind conditions (< 6 m s^{-1}). Accumulation of natural surfactants, typically derived from biological processes (Kujawinski *et al.*, 2002b; Kurata *et al.*, 2016a; Žutić *et al.*, 1981a), create relatively smooth surfaces known as slicks by damping short Gravity-Capillary Waves (GCW) (Watson *et al.*, 1997).

Slicks can therefore reveal underlying flow structures, such as density fronts in satellite or airborne optical and radar images (Font *et al.*, 2002; Karimova, 2012). Marmorino *et al.* (2002) explored frontal dynamics on a continental shelf by observing slick evolution. Ryan *et al.* (2010) studied recurring slicks linked to a surface temperature front induced by coastal upwelling. Despite their relevance to near-surface hydrodynamics, frontal slicks in lakes are yet to be investigated.

In order to gain insight into frontal slick dynamics in a lake, we investigated a frontal slick that extended across a considerable portion of the width of Lake Geneva. Measurements indicate

that the slick was associated with a Lake Surface Water Temperature (LSWT) submesoscale front. The measurements were complemented by three-dimensional (3D) numerical modeling of the lake hydrodynamics that showed how the front developed. Satellite imagery of LSWT confirmed the presence of the simulated front. The following questions are addressed:

- How does the frontal slick evolve in relation to the frontal dynamics?

- What causes the LSWT gradients and submesoscale currents responsible for the observed front formation and sharpening?

- What are the spatiotemporal variations in temperature and currents in the near-surface layer (down to ~1.5 m depth) across the front?

The Supplementary Information (SI) provides details on certain aspects discussed in the manuscript with figures and texts prefixed S.

4.2 Materials and methods

4.2.1 Study site

Lake Geneva (*Lac Léman*) is a warm oligomictic lake located between Switzerland and France at a mean altitude of 372 m. It is Western Europe's largest lake with a length of 70 km, a maximum width of 14 km, a surface area of 582 km^2, a volume of 89 km^3, and a maximum depth of 309 m. The surrounding mountainous topography guides the wind field, resulting in two dominant strong winds coming from the northeast and southwest called the *Bise* and *Vent*, respectively (Lemmin and D'Adamo, 1996a).

4.2.2 Measurement Methods

In situ field and remote data were collected using the following equipment and methods:

- An mobile two-platform measurement system (Figure S4.0-1, Text S1: Measurement Methods; Barry *et al.*, 2019; Rahaghi *et al.*, 2019) composed of:

  - A 7-m long autonomous catamaran called ZiviCat that measured near-surface water temperatures (down to 1.5 m), near-surface currents (0.5 to 1 m depth), and wind speed and direction. A forward-facing RGB camera recorded images of surface water roughness. All ZiviCat data could be visualized in real time on the accompanying boat (*Elodea*).

- o A 9-m^3 balloon called BLIMP at ~400 m height, tethered to the boat, carried an imaging package that recorded RGB and infrared (IR) images (Figure 4-3a) to examine the spatial variability of the Lake Surface Water Temperature (LSWT). Images could be visualized in real time on the boat (Liardon and Barry, 2017b).

- Smooth patches and the rippled water around the frontal slick were sampled to determine surfactant concentrations. Water samples were collected using the glass-plate method for the uppermost 20-150 µm of the surface (Cunliffe *et al.*, 2013a) and hand-dipping to collect bulk water (20 cm below the surface) following standard procedures (Cunliffe and Wurl, 2014). The water sample analysis is described in Text S2: Surface Microlayer Sampling.

- A shore-based imaging system, called TLB, installed 192 m above the lake surface on the lake's steeply rising northern shore, took (angled-view) RGB images that allowed surface slick detection across most of the lake's width (for location, see Figure 4-1a). Images can be visualized in real time on the boat and the tilt and pan angles of the camera can be remotely controlled from the boat.

- Advanced Very High Resolution Radiometer (AVHRR) satellite data with a 1-km grid resolution was used to obtain whole-lake LSWT images (Riffler *et al.*, 2015).

All the above was combined with 3D numerical modeling of Lake Geneva, based on the validated model setup of Cimatoribus *et al.* (2018), which provided details of the lake hydrodynamics during the field measurement campaign (Text S3: Numerical Simulations).

4.3   Results

The field campaign was carried out on Lake Geneva on 30 September 2020, during the summer stratification season with a thermocline at ~20 to 30 m depth. Observations were made between 14:00 and 16:30 (local time) when a ~10 km long, slow-moving frontal slick evolved (Figure 4-1c). The wind was from the west and wind speed varied between 3 and 5 m s^{-1} (Figure 4-3a).

4.3.1   Frontal slick evolution

Images taken with the remote TLB camera are dominated by a long narrow slick with a sharp edge on the western (upwind) side extending across most of the width of the lake basin

(Figure 4-1c). Over a period of 1.5 h, the slick changed little in shape, was only slightly displaced and did not change its orientation suggesting a frontal slick. This was further confirmed by comparing its position in the first and last images (Figure 4-1b). The frontal slick forms to the east of a sharp temperature gradient (Figure 4-3).

Geo-rectified snapshots of the frontal slick (Figure 4-1d) showed that it had a large aspect ratio that decreased over time (Figure 4-1e), i.e., it widened almost four-fold (from ~50 to ~200 m) during 1.5 h while moving very slowly eastward. (Figure 4-1e, 3c and Movie S1). The rapid movement of these smaller slicks with the wind (~3 m s^{-1}, Figure 4-1d) suggests that wind-driven drift currents drive their kinematics, whereas the frontal slick maintained a large angle with the wind. The slow eastward movement of the frontal slick indicated that its motion was predominantly controlled by underlying lake hydrodynamics.

Slicks in the images have smooth surfaces that are caused by the accumulation of surfactants. To verify that surfactant concentrations are different in the observed smooth frontal slick and the rough-surface surrounding areas, ten water samples were collected around the northern tip of the frontal slick (Figure 4-1c) between 14:45 and 15:20. Higher enrichment of Fluorescent Dissolved Organic Matter (FDOM), a proxy for natural surfactants (Frew et al., 2002; Salter, 2010), was found inside the frontal slick (Text S2: Surface Microlayer Sampling, Figure S4.0-2) whose smooth surface suppressed GCW formation as confirmed by images simultaneously taken by the ZiviCat RGB camera (Movie S2).

4.3.2   Mesoscale and submesoscale flow structures leading to front formation

During the six days preceding the campaign, strong *Vent* wind events from the southwest with wind speeds up to 10 m s^{-1} prevailed over the lake (Figure S4.0-2a-c). They produced a set of rotational flow patterns seen in the results of the high-resolution 3D modeling (Figure 4-2b) and caused coastal upwelling along the northern shore. On 30 September, two Anticyclonic Gyres (AG1 and AG2; clockwise rotating) and the two Cyclonic Eddies (CE1 and CE2; counterclockwise) formed in the eastern and central parts of the lake (Figure 4-2b), and a thermal front had developed between AG1 and AG2. Good agreement is found between the large-scale modeled LSWT and that in the satellite image for the same time; both indicate a horizontal LSWT difference between the western and the eastern parts of the lake, separated by a sharp front at about the same location (Figure 4-3a, b), thus confirming the validity of the modeling results.
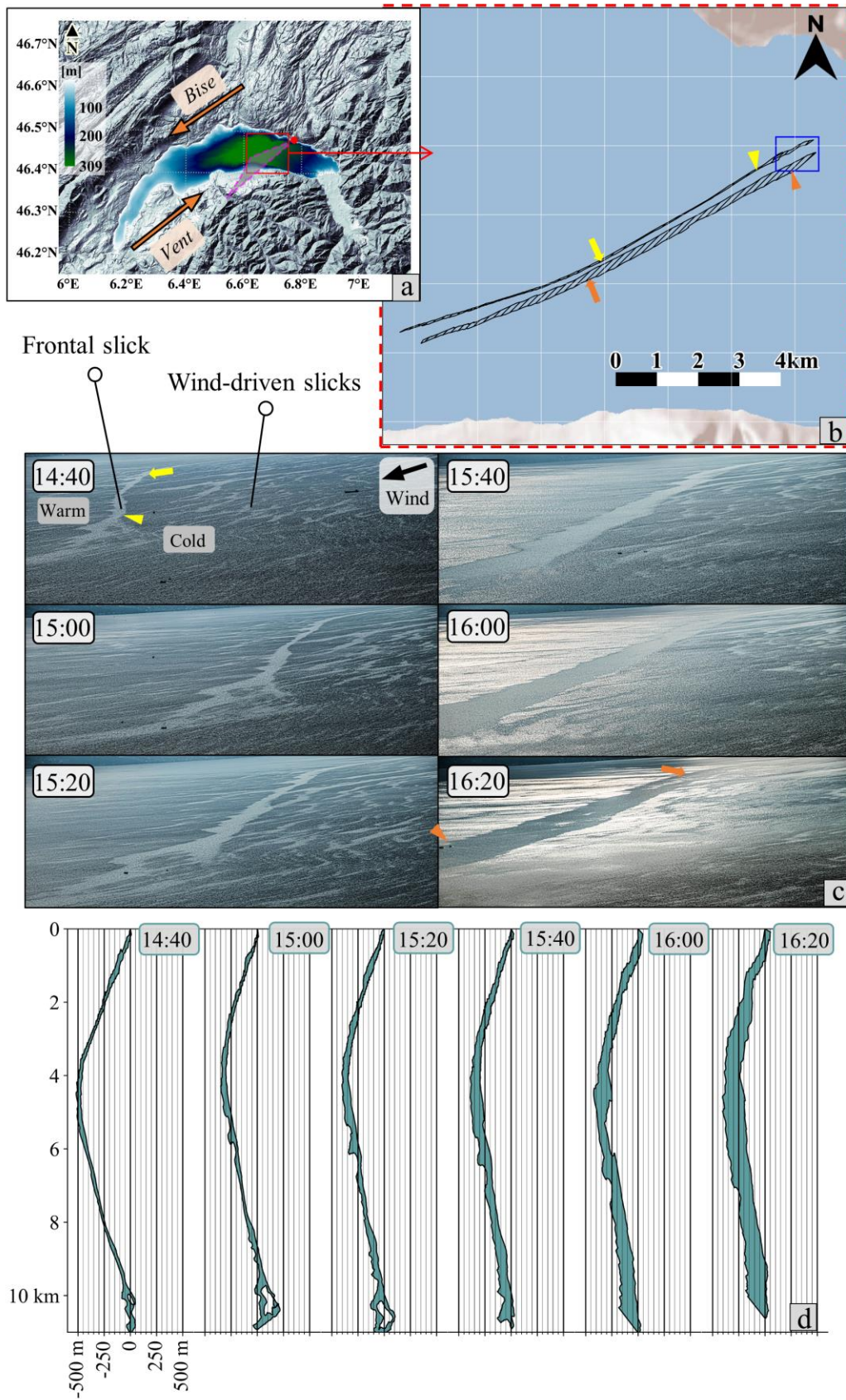
Figure 4-1. a) Lake Geneva's bathymetry and the surrounding mountainous topography, Red dot: location of on-shore camera TLB. Red square: study site for images in (c). *Bise* and *Vent* are the two dominant, strong large-scale winds blowing over most of Lake Geneva. b) Map showing the georeferenced outlines of the first and last frontal slick images in (c). Blue rectangle: northern end of the slick where the in situ measurements (Figure 4-3) were taken. c) Six TLB camera snapshots show the time evolution of the frontal slick. The approximate wind direction, two types of slicks, and the cold/warm side of the front are indicated in the first image. At 14:50, the camera was turned 5° to the east to follow the slick. The northern tip of the slowly moving slick left the field of view in later images. Locations of yellow and orange symbols correspond to those in (b) for reference. d) Geo-rectified (Gerum *et al.*, 2019) outlines of the frontal slick for the images in panel (c), illustrating its expansion over time. The water depth below the slick is always > 100 m.

The lateral displacement between the front location seen in the measurements (Figure 4-1) and in the satellite image and the simulated LSWT front may be due to limitations in the atmospheric forcing model (Text S3: Numerical Simulations) and the selected drag coefficient (Rascle *et al.*, 2020).

The high-resolution simulation permitted identification of submesoscale processes. Filamentary structures are evident in the instantaneous field of horizontal divergence, δ, and vertical vorticity, ζ (Figure 4-2a-d). Their high normalized values $|\delta/f| \geq 1$ and $|\zeta/f| \geq 1$ in the frontal region suggest that submesoscale processes were well developed (McWilliams, 2017). Previous submesoscale-resolving models (Shcherbina *et al.*, 2013) showed fronts and vortices emerging in regions with strong cyclonic vorticity similar to the vorticity field in Figure 4-2e. The strong convergence in Figure 4-2d indicates compensating downward motion of the denser water (Figure 4-2c), which can lead to frontogenic sharpening of the background LSWT gradient. Strong current gradients along the lake's northern shore may suggest slick formation; however, no remote observations are available for further analysis. Even though the model was run in hydrostatic mode, the results of temperature and velocity fields in the vertical direction (Figure 4-2c) offer, at least qualitatively, insight into the 3D flow structure of the front. Mahadevan and Tandon (2006) had pointed out that vertical velocities in a submesoscale front can be $\mathcal{O}(1$ mm s$^{-1})$, which is also seen in the present results.
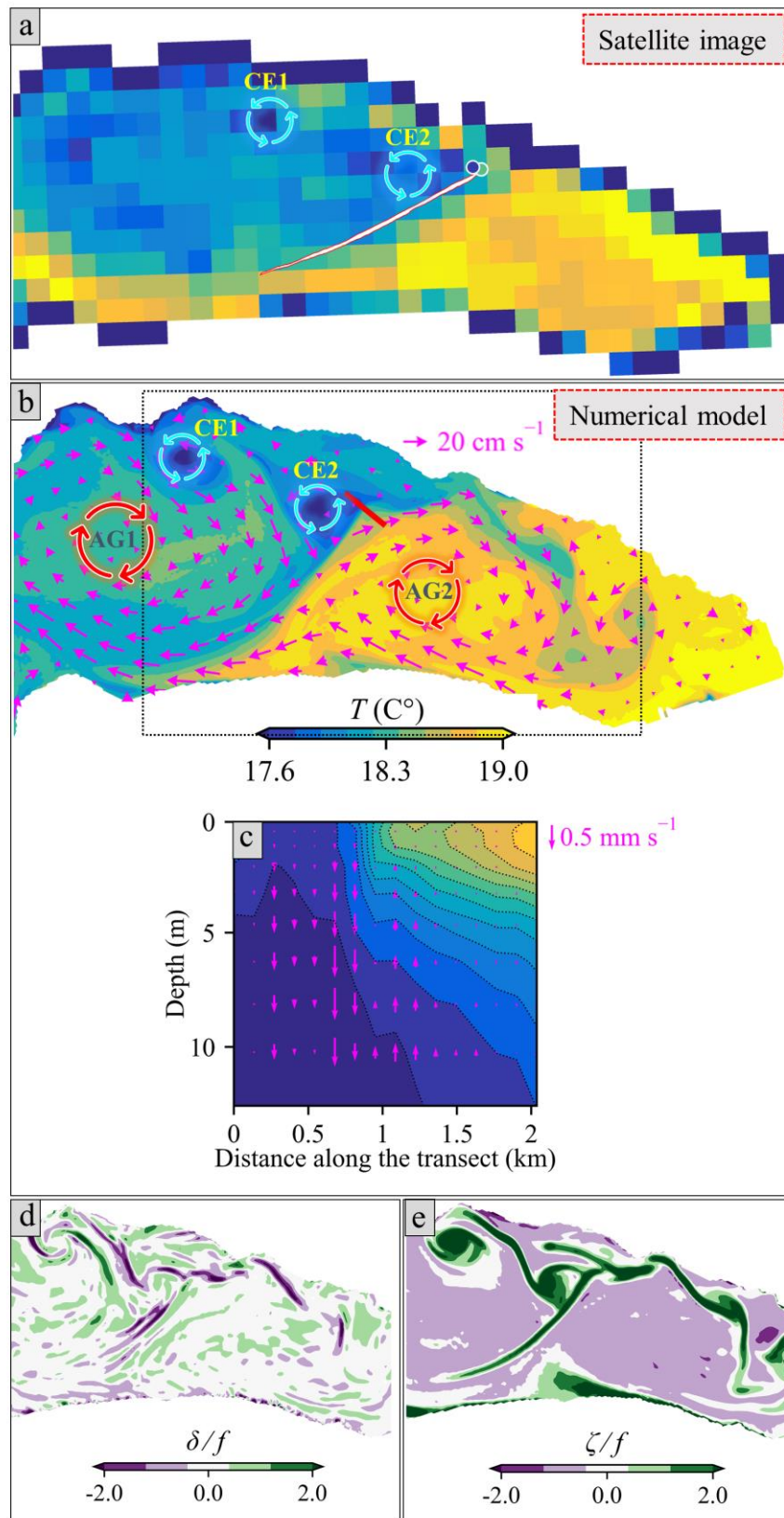
Figure 4-2. a) LSWT derived from the AVHRR satellite data (1 km grid cells) at 17:00 on 30 September 2020. Nearshore grid cells have lower temperatures since they also cover some surrounding land. Superimposed on the map is the frontal slick outline (Figure 4-1b) at 16:00 (white), along with two samples of in situ temperature measurements (at 5 cm depth) taken on both sides of the front (Figure 4-3b). b) Snapshot of numerical simulation results at 16:00, 30 September 2020 of lake surface temperature with magenta arrows indicating currents. Gyres (AG1, AG2) and eddies (CE1, CE2) are highlighted with rotating arrows. The black dotted-lined rectangle marks the section of the lake displayed in (d) and (e). Colorbar: temperature range corresponding to panels (a) to (c). c) Temperature and vertical velocity in a vertical plane along the red transect in (b). d) horizontal divergence ($\delta = \partial u/\partial x + \partial v/\partial y$), and e) vertical vorticity ($\zeta = \partial v/\partial x - \partial u/\partial y$) normalized by the Coriolis frequency (f), derived from the simulated surface currents.

4.3.3 Surface and near-surface cross-front variability

The frontal slick (Figure 4-1) and the thermal front (Figure 4-2) occur in the same area of the lake. To determine whether a relationship exists between the two, in situ measurements were carried out with the catamaran ZiviCat and the BLIMP balloon. The ZiviCat traversed the northern end of the LSWT front between ~15:29 and ~16:29 at five locations (Figure 4-3c, d, Movie S2.), following a zigzag trajectory. The orientation of the tracks was selected based on monitoring of the frontal slick as seen in the TLB images, in the RGB images taken by the camera mounted on the front of the ZiviCat, and by the sharp temperature gradient in the remote BLIMP IR images (Figure 4-3a). All these data were available in real time on the boat accompanying the ZiviCat. During this period, the wind was blowing eastward towards the frontal slick (Figure 4-3a), as is evident from the motion of small slicks (Movie S1.). In situ near-surface temperature measurements (Figure 4-3c), IR images obtained with the BLIMP package (Figure 4-3a), and pictures taken by the ZiviCat's onboard camera (Movie S2.) confirm that the west (upwind) side of the slick coincides with the sharpest horizontal temperature gradient (0.7°C in ~10 m), i.e., the LSWT and surface roughness were simultaneously modified in the cross-front direction over a relatively short distance. The smooth surface on the warm side of the front was only $\mathcal{O}(100 \text{ m})$ long (Figure 4-3c).

Although a sharp LSWT gradient is evident from the BLIMP images (Figure 4-3a, Movie S2.) and from the topmost thermistors, the two bottom thermistors recorded a more gradual change, i.e., a longer transition distance of $\mathcal{O}(100 \text{ m})$ (Figure 4-3c). This cross-front difference between the surface and 1.5-m temperature variations suggest a downward penetration of cold surface water in the front, as also seen in the numerical simulation results (Figure 4-2c). However, with

distance from the transition zone in the front, temperature profiles on both sides indicate well-mixed conditions in the upper 1.5 m of surface water (Figure 4-3b, c).

The measured near-surface currents also revealed abrupt changes across the front (Figure 4-3a). The high-resolution Acoustic Doppler Current Profiler (ADCP) measurements (depth-averaged from ~0.5 m to ~1 m) were corrected for phase-wrapping effects and ZiviCat movement. On the cold western side of the LSWT front, currents were almost aligned with the wind direction (Figure 4-3a) and were nearly perpendicular to the front. Currents on the warm side, however, were directed to the northeast, forming an angle with the wind, consistent with anticyclonic circulation on the eastern side of the front in the model results (Figure 4-2b).

Current gradients in the cross-front direction were estimated as:

$$\frac{\partial \mathcal{U}}{\partial x} \approx \frac{\Delta \mathcal{U}}{\Delta x} = \frac{\bar{\mathcal{U}}_{10\,\text{m,warm}} - \bar{\mathcal{U}}_{10\,\text{m,cold}}}{10\,\text{m}} \qquad (1)$$

where x is in the cross-front direction and $\bar{\mathcal{U}}_{10\,\text{m}}$ are the depth-averaged cross-front or along-front velocity components, averaged within a 10-m wide horizontal slice in the cross-front direction. Assuming that along- and cross-front velocities only vary in the cross-front direction (Garvine, 1974; Rascle *et al.*, 2020; Figure 4-3a), both the horizontal divergence, δ, and vertical vorticity, ζ, can be derived from the current gradients as $\partial \mathcal{U}|_{\text{cross-front}}/\partial x$ and $\partial \mathcal{U}|_{\text{along-front}}/\partial x$, respectively. The mean convergence and vorticity based on the first four transects and normalized by the Coriolis frequency, f, were calculated as 52 ± 25 for horizontal divergence, δ, and 56 ± 29 for vertical vorticity, ζ. These values are an order of magnitude higher than those simulated, which have much lower spatial resolution (Figure 4-2d, e). However, they are comparable to the values reported by Rascle *et al.* (2020) near the front.
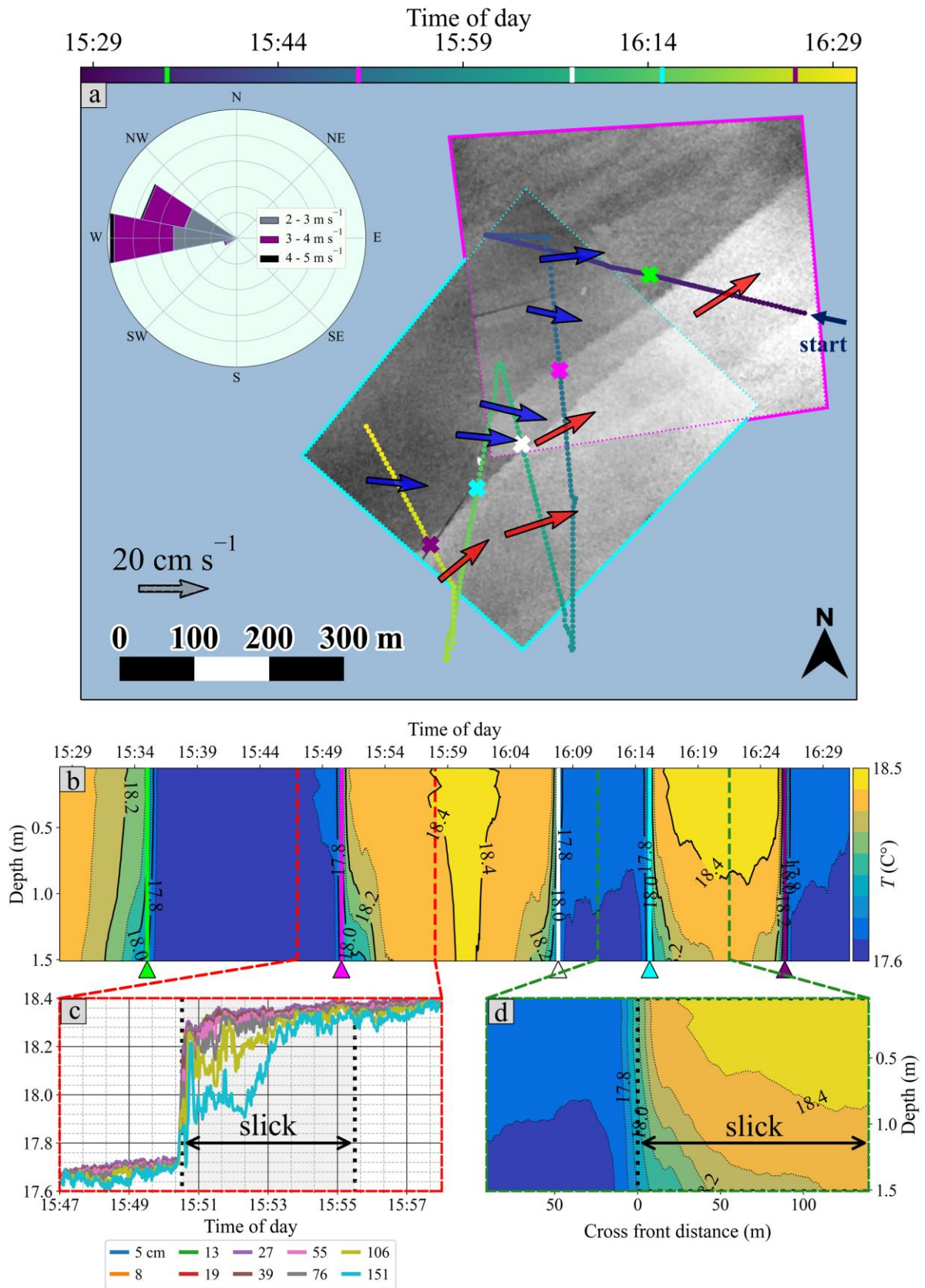
Figure 4-3. a) Enlargement of the blue square in Figure 4-1b showing: (i) ZiviCat tracks from ~15:29 to ~16:29 (crosses indicate locations where the ZiviCat traversed the LSWT front), (ii) two partially overlapping BLIMP infrared (IR) greyscale images (darker indicates colder) showing the front, with a slight eastward drift (~3 cm s^{-1}) between them. Top left (time: 15:50): cold western side of the front (dark grey); bottom right (time: 16:15): warm eastern side of the front (light grey), (iii) depth-averaged (0.5 to 1 m) horizontal ADCP velocities on the warm eastern side (red arrows) and the cold western side (blue arrows) of the front (velocity scale given by the dashed arrow), and (iv) 1 h mean-wind speed and direction measured by the ZiviCat meteostation. Colorbar on top of panel (a): time along the ZiviCat track. Colors of the BLIMP image frames (magenta and cyan) correspond to those of the crosses of frontal crossing. b) One-minute moving average temperature pattern in the top 1.5 m of the water along the ZiviCat zigzag trajectory shown in panel (a), repeatedly traversing the front as marked by tri-angles (colors correspond to crosses in (a)) at the bottom of the panel. c) Detailed time series of the ten near-surface thermistors during the second crossing of the front, marked by red ver-tical dashed lines in (b) corresponding to a cross-front distance of ~100 m. The extent of the frontal slick on the lake surface during this transect is indicated by two vertical black dashed lines. Thermistor depths are given in the legend. d) Detailed cross-front temperature variation (fourth crossing), marked by green vertical dashed lines in (b) with the same temperature range.

4.4   Discussion

4.4.1   Development of the frontal slick

A combination of in situ and remotely sensed observations provided a comprehensive picture of a frontal slick development in Lake Geneva (sketch in Figure S4.0-1). The surface micro-layer water samples showed that the smooth band on the warm side of the LSWT front had higher concentrations of surfactants (Figure S4.0-2), emphasizing the role of natural sur-factants in manifesting frontal dynamics by inhibiting GCW development, as confirmed in the RGB images taken by the ZiviCat when crossing the frontal slick (Movie S2.). A previous study in Lake Geneva showed that smooth slicks are associated with biogenic surfactants (Foroughan *et al.*, 2022b) and that they suppress GCW development.

The multiscale appearance of slicks on the lake surface water (Figure 4-1c, Movie S1.) indicates that different processes affect the surfactant distribution and revealed two distinct types of slicks: (i) a large persistent frontal slick (manifesting a density front) that hardly changed loca-tion (Figure 4-3a), and (ii) numerous smaller slicks that continually changed shape, and rapidly moved in the direction of the wind. The small slicks appear to originate from relatively distant locations; thus, the frontal slick can collect materials coming from a wide surface area.

Also noteworthy is the asymmetric edge morphology and distribution of smooth areas between the upwind (cold) and downwind (warm) sides of the frontal slick. The edge on the upwind (western) side of the front is relatively uniform and smooth, whereas on the downwind eastern side, there are protrusions and occasionally some small elongated slicks "escape." Such wave-form edge patterns resemble an instability mechanism previously observed during the disintegration of large slicks (Marmorino *et al.*, 2008a). However, the present frontal slick is in the integration phase, i.e., the input of small slicks to the front is significantly greater than the output (Figure 4-1d). Frontal slick width evolution appears to be controlled primarily by these dynamics.

Numerical modeling shows that the thermal front (and, consequently, the frontal slick) is characterized by a strong vertical velocity (Figure 4-2c), as was also reported by Mahadevan and Tandon (2006). This downwelling explains the sharp western edge of the frontal slick. ZiviCat observations indicate that the mean horizontal velocity orientation changes significantly across the front (Figure 4-3a). The near-surface current field on the cold western side is nearly aligned with the wind, whereas the warm eastern side of the front is more oriented along the direction of the front (Figure 4-3a); this may slow down the transport of surfactants leaving the front on the eastern side.

4.4.2   LSWT front formation and sharpening

Although the observed frontal slick appears to have a time scale of hours (this slick was not present in the TLB images of the previous/following day), model results suggest that *Vent* episodes over the preceding six days primarily triggered the basin-scale events that contributed to the front formation. Previous studies demonstrated that *Vent* events generate gyres in the central part of Lake Geneva (Cimatoribus *et al.*, 2019; Razmi *et al.*, 2018), and that Ekman-type coastal upwelling occurred along the lake's northern shoreline during winter (Reiss *et al.*, 2020). Although our observations were made in a different season/stratification, a similar process was observed in the simulation results (Figure S4.0-3d, e). Cold waters upwelled along the northern shore and were advected by strong near-surface currents of the central anticyclonic gyre (AG1, Figure S4.0-2g), eventually forming a cold pool of water in the west and middle of the lake (Figure S4.0-2f). The time-integrated effect of the *Vent*-induced upwelling and vertical mixing with deeper, colder water, combined with strong currents circulating local cold surface water, led to an intense LSWT drop for the whole lake (Figure S4.0-3). However, the boundary between the two AGs isolated warmer surface waters in the east, from the colder waters in the

west, thereby forming the LSWT front (Figure 4-2b), also made evident by the high normalized values of $|\delta/f| \geq 1$ and $|\zeta/f| \geq 1$ in the frontal region (Figure 4-2d, e). This is confirmed by the satellite image (Figure 4-2a). Cold water captured by CE2 further intensified the temperature gradient along the upper section of the front (Figure 4-2a, b, Figure S4.0-2f). Oceanic fronts have also been observed along the edges of mesoscale eddies (McWilliams, 2021).

Such a horizontal basin-scale density gradient and an intense deformation flow associated with mesoscale circulations resulted in a strong submesoscale front. Frontogenesis, i.e., sharpening of horizontal density gradients, occurs through surface convergence and downwelling on the cold side of the front. The numerical simulation results, consistent with the in situ measurements, illustrate large lateral temperature and velocity gradients, cyclonic vorticity and convergence, all suggesting that the observed front is at the stage of accelerated frontal sharpening. The simulated vertical velocity in the cross-front plane is indirect evidence of cold-water downward penetration at the front as indicated by the isotherm pattern (Figure 4-2c). The in situ measurements confirmed that the cold water sinks below the warm water at the front (Figure 4-3d).

Submesoscale fronts usually last for a few hours or days, can be sharpened exponentially fast, remain active for a relatively short period (McWilliams, 2021), and eventually become inactive and turn into "fossil" structures (Rascle *et al.*, 2020). The present observations show that the upwind edge location of the frontal slick is determined by the active, sharp LSWT front (Figure 4-3, Movie S2.), in contrast to previous frontal slick studies (Marmorino *et al.*, 2002; Ryan *et al.*, 2010).

The processes leading to the observed frontal dynamics and the frontal slick formation can be summarized as follows (Figure S4.0-1): A thermal front was produced by the interaction of rotational flow patterns that resulted from strong wind forcing during the days preceding the measurement campaign. It separates warm-water regions from cold-water regions (Figure 4-2). The cold water approaches the front from the northwest, slightly clockwise from the wind as expected for an Ekman layer (Figure 4-3a). When it reaches the front, it sinks beneath the warm water (Figure 4-2c and Figure 4-3d). At the same time, small slicks transporting surfactants are driven by the wind towards the front (Figure 4-1). When these slicks reach the front, the buoyant surfactants cannot sink with the cold water. Instead, they cross over the front and are deposited at its southern edge forming a frontal slick along the length of the front (Figure 4-1 andFigure

4-3c). With time, more and more of the small slicks feed into the frontal slick, thereby increasing the amount of accumulated surfactant and as a result, the frontal slick south of the thermal front widens in the nearly calm warm waters (Figure 4-1).

From long-term records of our shore-based imagery system TLB, filamentary slicks with spatial scales comparable to the one in the current study occur frequently and have a life span of hours. Such similarity in time scales may further emphasize the role of submesoscale dynamics in frontal slick formation which in turn can affect the dispersion of surface materials in the lake. In addition, TLB long-term records indicate that the location and the orientation of submesoscale slicks in the widest part of the lake change; this reflects the dynamics of the underlying gyre pattern (Cimatoribus *et al.*, 2019). A frontal slick such as the one observed here can be classified as part of a broader category of submesoscale currents commonly observed in oceanic surface waters and recently in Lake Geneva (Hamze-Ziabari *et al.*, 2022b).

4.5 Summary and conclusions

Field observations carried out in Lake Geneva documented for the first time the existence of a persistent submesoscale frontal slick in a lake. It was ~10-km-long and evolved along the warm side of a surface temperature front. Numerical simulation results show that the background temperature gradient generated by time-integrated wind-induced upwelling and barrier-forming confluent currents due to mesoscale circulation result in a LSWT front in the lake. This was confirmed by satellite data. Cross-front in situ measurements: (i) support simulation results, (ii) point to the submesoscale character of the observed front, possibly sharpened frontogenically by strong convergent motions, and (iii) confirm that the frontal slick is the surface marker of the LSWT front. The results demonstrate the effectiveness of a submesoscale current pattern in accumulating surface materials and promoting slick formation. Long-term records of the remote imagery package indicate that submesoscale slicks are a ubiquitous feature on Lake Geneva, and are likely to occur on similar-sized lakes under comparable conditions. Such frontal slicks and their underlying processes represent a novel transport mode for surface material, including pollutants, and their downward transfer in lakes, and therefore should be considered in the development of effective lake management concepts.

Acknowledgments and data availability

Supporting Information for Chapter 4

Mehrshad Foroughan, Seyed Mahmood Hamze-Ziabari, Ulrich Lemmin, and David Andrew Barry

Ecological Engineering Laboratory (ECOL), Institue of Environmental Engineering (IIE), Faculty of Architecture, Civil and Environmental Engineering (ENAC), Ecole Polytechnique Fédérale de Lausanne (EPFL), Lausanne, Switzerland

Text S1: Measurement Methods

- In situ measurements were taken by a mobile two-platform system (Figure S4.0-1) composed of:

1. A 7-m long autonomous catamaran called ZiviCat whose trajectory can be preprogramed by giving a series of waypoints. It is equipped with a set of near-surface (down to 1.5 m) water temperature sensors (RBRsolo, accuracy: 0.002°C, 1 Hz), a downward-looking 2 MHz Nortek Aquadopp high-resolution (HR) Acoustic Doppler Current Profiler (ADCP) covering the range of 0.5 to 1 m depth, a weather station (Airmar 200WX IPX7) at 3 m height with motion-corrected outputs, a relative humidity sensor, and two RGB Raspberry Pi cameras (installed at 1.2 m above the water surface) to record images of the lake surface for a qualitative measure of surface roughness (one recording near-field in front of the ZiviCat and the other recording farther away). The sensor spar is located well forward of the catamaran to minimize hull disturbances. The ZiviCat was equipped with positioning (RTK-GPS), stability (IMU), data recording, and communication systems to allow operators on the accompanying boat, the *Elodea*, to control and correct catamaran navigation and analyze data in real-time (Barry *et al.*, 2019). Due to Swiss regulations, the ZiviCat must always be accompanied by a boat.

2. A 9-m^3, helium-filled balloon called BLIMP was attached to a winch on the accompanying boat. The balloon, which was positioned ~400 m above the lake during the measurement campaign, produced 0.8 m resolution images. A FLIR Tau 2 Long-wave Infrared (IR) camera (7.5-13.5 µm spectral range, 640×512-pixel resolution, 14-bit digital output) and a Raspberry Pi RGB camera for visual inspection are integrated into the imaging package, along with equipment for positioning (GPS), orientation, tilt angles, and communication with the boat (Liardon and Barry, 2017b). BLIMP infrared images are treated for nonuniformity correction, following Rahaghi *et al.* (2019a).

1. BLIMP camera package
2. Temperature sensors
3. Near-surface ADCP
4. Onboard cameras
5. Meteostation
6. Logic and communication boxes
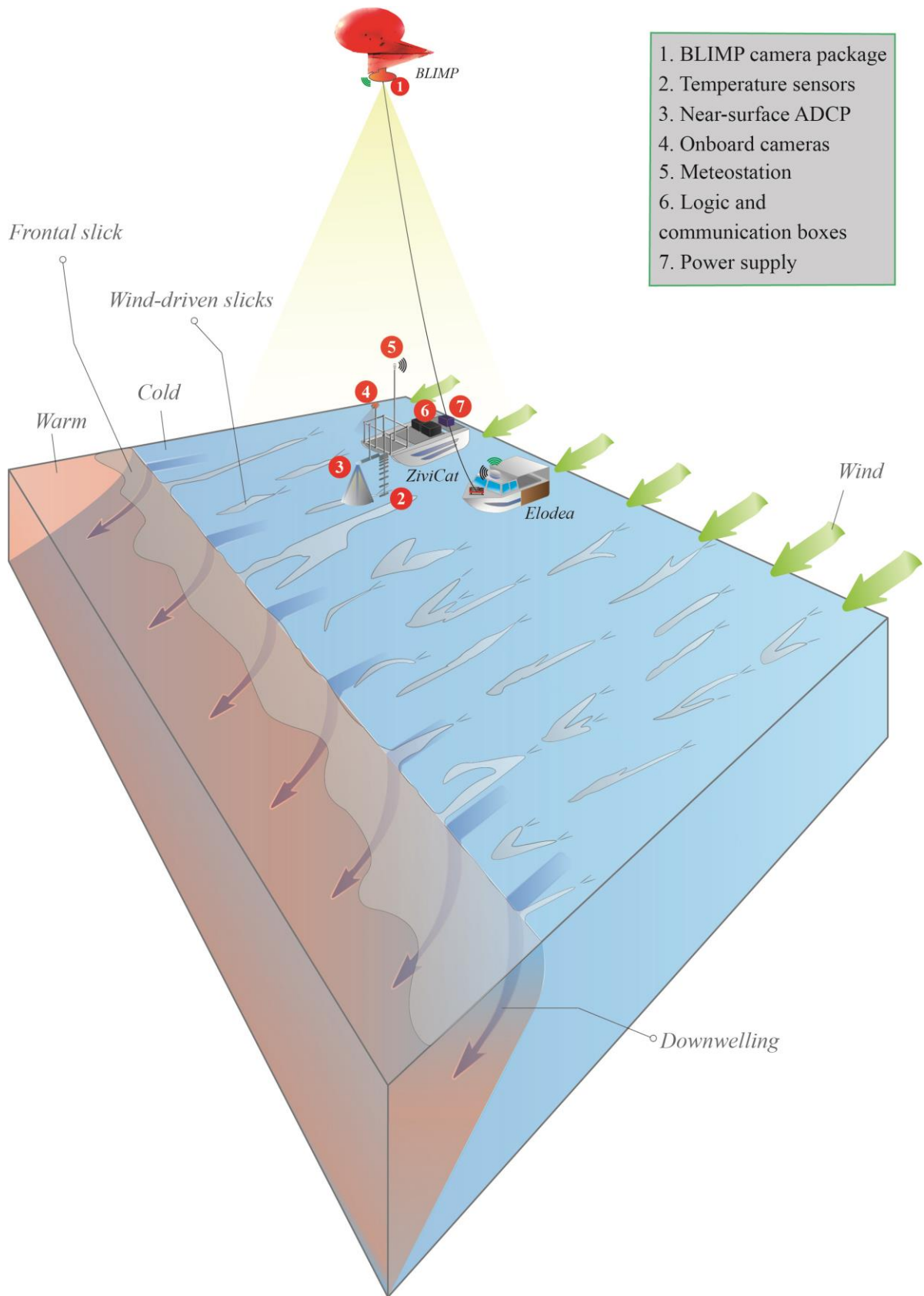7. Power supply

Figure S4.0-1. Sketch depicting the frontal dynamics and frontal slick formation observed in the present study. A thermal front was produced by the interaction of rotational flow patterns

that resulted from strong wind forcing during the days preceding the measurement campaign. It separates warm-water regions from cold-water regions (Figure 4-2). The cold water approaches the front from the northwest, oriented slightly clockwise from the wind, as would be expected for an Ekman layer. When the cold water reaches the front, it sinks beneath the warm water (Figure 4-2c and Figure 4-3d). At the same time, small slicks transporting surfactants are driven by the wind towards the front (Figure 4-1). When the slicks reach the front, the buoyant surfactants in the slicks cannot sink with the cold water. Instead, they cross over the front and are deposited at its southern edge, forming a frontal slick along the length of the front (Figure 4-1). Thus, each small slick transports its surfactant to the front. With time, more of the small slicks feed into the big frontal slick, thereby increasing the amount of surfactants. As a result, the frontal slick southward of the thermal front widens in the nearly calm warm waters (Figure 4-1). This sketch also shows the mobile two-platform measurement system used to study the front and the frontal slick. It consists of the 9-m3 balloon called BLIMP and the remotely operated catamaran called ZiviCat. Data collected by the BLIMP and ZiviCat were transmitted to the accompanying boat, the *Elodea*, where they could be visualized in real time. The legend identifies the different sensors on the BLIMP and ZiviCat.

- Shore-based time lapse camera

The shore-based imaging package TLB is a time-series imagery system mounted on a steep hillside approximately 195 m above the lake surface water and 440 m away from the shoreline. The TLB gives a slanted (non-perpendicular) field of view of the lake surface. The package includes a Single-Lens Reflection (SLR) digital camera (Nikon D5600) with an image resolution of 24.16 megapixels (6016 × 4016), taking images every minute. The camera view field can be remotely adjusted in real-time to monitor and track surface features in different parts of the lake by panning and tilting the package in the horizontal and vertical planes.

Text S2: Surface Microlayer Sampling

The glass-plate method was used in the field to sample the uppermost 20-150 µm of the surface (Cunliffe *et al.*, 2013a). Bulk water (20 cm below the surface) was also collected following standard procedures (Cunliffe and Wurl, 2014). The samples were brought back to the laboratory for further analysis on the same day. They were tested for the enrichment of Fluorescent Dissolved Organic Matter (FDOM), which correlates with surfactant activity (Salter, 2010). An Excitation Emission Matrix (EEM) was generated for each sample (Figure S4.0-2a) using a Fluorescence Spectrometer (Perkin Elmer). The EEM was generated by assembling emission spectra (250-600 nm) within an excitation range (250-550 nm). Since different FDOM fluoresce differently, one or more peaks may appear in the EEM. Parallel factor analysis was applied (PARAFAC; Stedmon and Bro, 2008) to the EEMs of all samples (Figure S4.0-2b) to

determine the location of peaks (emission/excitation wavelength) and the contribution of each sample to that peak. The Enrichment Factor (EF) was calculated as the ratio of surface fluorescence intensity to the bulk values for each peak, which is proportional to their concentrations.

Ten water sample sets (surface and bulk) were collected and separated into two groups: slick, and non-slick. The enrichment factor was usually > 1 for the smooth slicks and for the rippled non-slick areas (Figure S4.0-2c). Two peaks were observed at around 360 and 410 nm. Figure S4.0-2c shows that the boxes for the slick and non-slick areas are clearly separate. A systematic spatial variability of FDOM between the frontal slick and rough non-slick areas is evident, with wider scatter inside the slick (Figure S4.0-2c). For these two peaks, the interquartile range of the slick area is significantly larger than that of the non-slick areas. The two maxima observed at 360 nm (Peak T) and 410 nm (Peak M) are linked to tryptophan-like components (Wolfbeis, 1985) and marine and terrestrial humic materials (Murphy *et al.*, 2008), respectively. Note that there is a significant difference in surfactant concentration between smooth slicks and rough non-slick areas, with concentrations in slicks being much higher, in agreement with observations in the ocean (Wurl *et al.*, 2016). The larger interquartile range in the slick areas (Figure S4.0-2c) indicates higher variability in enrichment, suggesting that the thickness and characteristics of the surface surfactant film varies more within slicks than in rough surface areas.
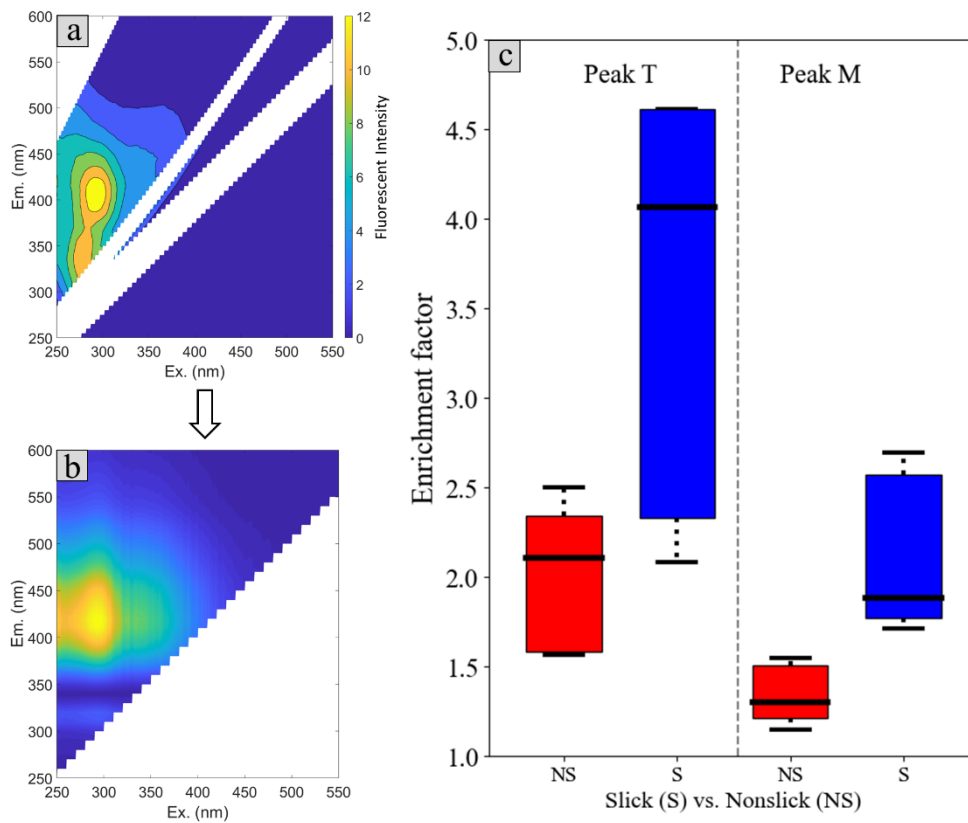
Figure S4.0-2. a) An example of an Excitation Emission Matrix (EEM) matrix after Rayleigh and Raman scattering are removed. b) Peak classification using PARAFAC analysis. c) Box plot of the FDOM enrichment factor for the peaks T and M (Tryptophan-like and marine/terrestrial humic-like materials) observed in the EEM matrix. Red/blue boxes show the interquartile range (25-75%) for Non-slick (NS) and Slick (S) areas, respectively. Tails (dashed lines) indicate the 1-99 percentile range. In each box, the black lines represent the medians. The colorbar in (a) indicates fluorescence intensity in (a) and (b).

Text S3: Numerical Simulations

We employed a hydrostatic version of the MITgcm code solving the 3D Boussinesq Navier-Stokes equations. The model integrates the three-dimensional Reynolds-averaged Navier-Stokes equations on a sphere under the Boussinesq and both hydrostatic and non-hydrostatic approximations (Marshall *et al.*, 1997). The model was run in the hydrostatic mode with an implicit free surface. Originating from the oceanographic community, this code has successfully been applied to lakes (Djoumna *et al.*, 2014; Dorostkar *et al.*, 2017; Dorostkar and Boegman, 2013). The model was previously calibrated to realistically reproduce the stratification, mean flow, and internal seiche variability in Lake Geneva (Cimatoribus *et al.*, 2019). It was used to study nearshore currents and internal seiche variability, coastal upwelling, and river

plume dispersion in Lake Geneva (Cimatoribus *et al.*, 2018, 2019; Reiss *et al.*, 2020; Soulignac *et al.*, 2021).

The bathymetry of Lake Geneva was interpolated from a high-resolution survey dataset. Two Cartesian grids were generated. A Low Resolution (LR) grid, with a horizontal resolution of 173-260 m and 35 depth layers, was initialized from rest on 3 June 2019 using the measured temperature profile from the Commission Internationale pour la Protection des Eaux du Léman (CIPEL) station SHL2 (located in the center of the lake, 46°27'10.8"N 6°35'16.8"E; depth 305 m) as the horizontally uniform initial condition. The integration time step of the LR model was 20 s and the spin-up was almost six months. The LR model was used to initialize the High Resolution (HR) version of the model with a grid resolution of 113 m horizontally and 50 layers in the vertical (layer thickness ranging from 0.30 m at the surface to approximately 12 m in the deepest layer). The initial time step was set to 6 s for stability, and then gradually increased to 30 s. The starting date of the HR model simulation was 10 January 2020 and simulations continued for ten months.

The model was forced by realistic atmospheric fields (wind, temperature, humidity, solar radiation) extracted from the COnsortium for Small-scale MOdeling (COSMO) atmospheric model of MeteoSwiss (Voudouri *et al.*, 2017). The COSMO time step for the forcing data was 1 h and the spatial resolution was 1 km × 1 km. The model uses the bulk formulation from Large and Pond (1981) to compute the atmospheric fluxes. Due to the limited resolution of the atmospheric forcing model, spatiotemporal variations smaller than those resolved by the atmospheric model may result in underestimated velocity variability for periods shorter than approximately 10 h (Cimatoribus *et al.*, 2019).
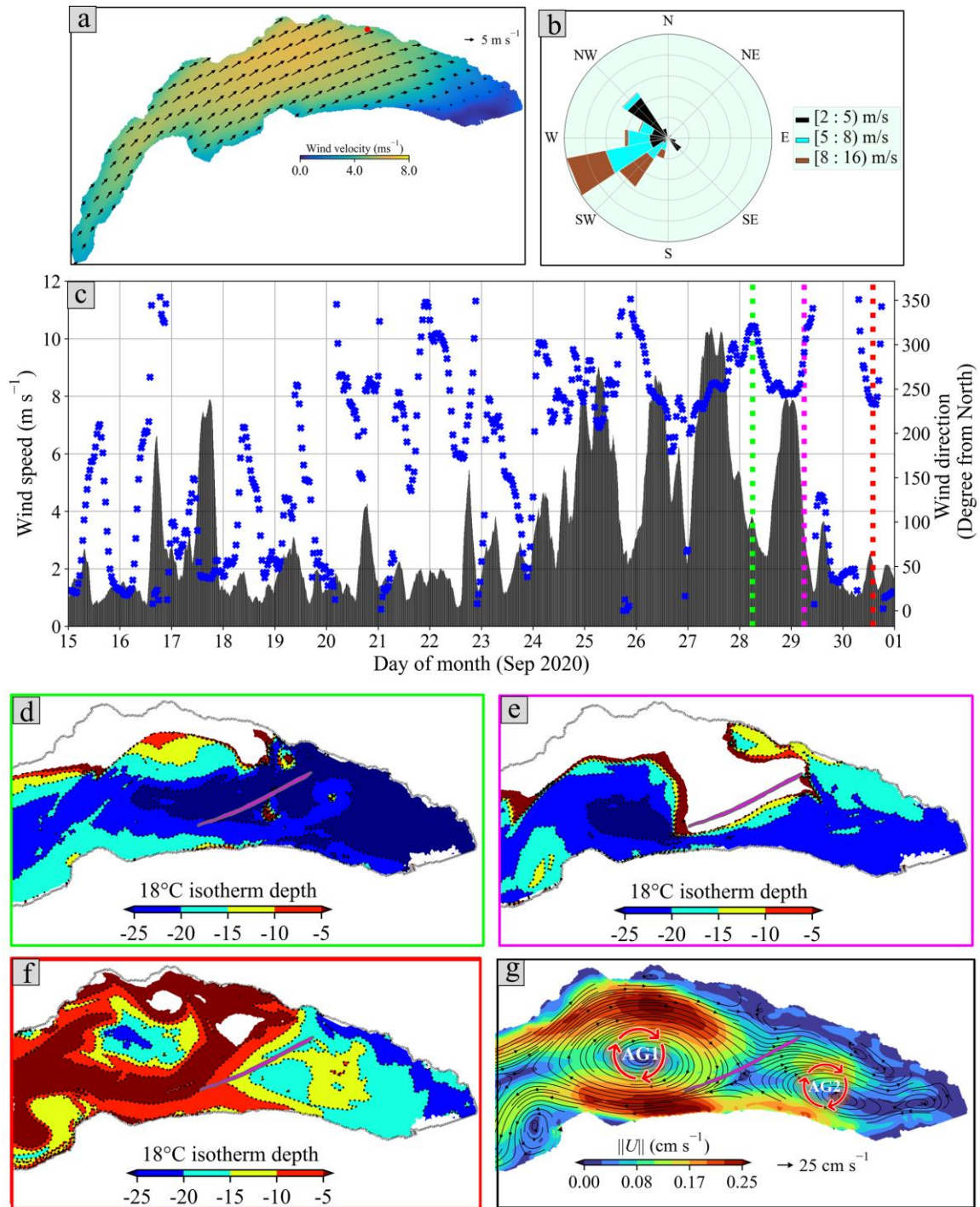
Figure S4.0-3. a) Wind velocity at 10 m above the lake derived from COSMO meteorological model outputs (Text S3), averaged for the six days preceding the field campaign on 30 September 2020. b) Windrose of the wind data collected for the same period by a weather station indicated by a red dot on the wind map. c) The wind time series (speed: shaded black, direction: blue dots) from the same meteostation in b) for the second half of September 2020. The red

vertical dotted line indicates the time of the measurement as presented in Figure 4-3 and corresponds to panel (f). The green and magenta vertical dotted lines correspond to panels (d) and (e). (d-f) Modeled 18°C (averaged between in situ warm and cold sides of the front) isothermal surfaces at two instants during high wind episodes (d and e) and one instant during the in situ measurements (f). The colorbar shows the depth range of the isothermal surfaces at each instant. White indicates that the 18°C isotherms have reached the surface, and Lake Water Surface Water Temperature (LSWT) drops below this value. The deeper the 18°C isotherm depth is, the warmer the layer above it will be. g) Depth-averaged near-surface (top 5 m) current magnitude (colorbar) and direction (arrows), which are averaged for 72 h preceding the in situ measurements. The locations of the large clockwise rotating gyres, marked AG1 and AG2, correspond to those shown in Figure 4-2 in the main text. Superimposed on the maps (d-g) is the frontal slick outline at 16:00 (magenta) in Figure 4-1 in the main text.
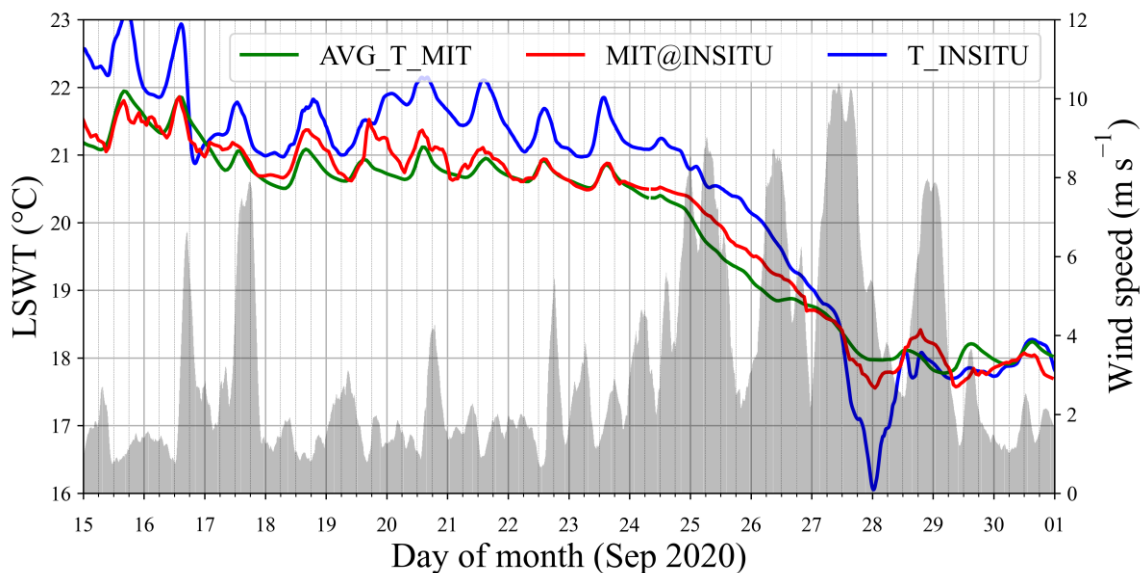
Figure S4.0-4. For the two weeks prior to the field campaign on 30 September 2020, comparison of in situ subsurface temperature, at 0.25 m depth (blue) from a measurement platform (Wüest *et al.*, 2021) indicated in Figure S4.0-2a (red dot) with simulated LSWT evolution, for the location of the platform (red), and spatially averaged for the whole lake (green). The wind speed, measured at the red dot station in Figure S4.0-3, is again shown in the background. For wind direction, see Figure S4.0-3c.

Movie S1.

A time-lapse movie was created using images taken with the shore-based imaging package (TLB; Text S1) at one-minute intervals. Cropped and enhanced images are used for clearer representation. From 14:28 to 16:29 (local time), the movie shows the slick evolution during the measurement campaign (30 September 2020). For technical reasons, a few images were missed by the imaging package. In response to the eastward movement of the frontal slick, the

camera was rotated horizontally twice (1 degree at 14:48; 5 degrees at 14:51). The in situ measurement platform composed of the autonomous catamaran ZiviCat, the balloon BLIMP, and the accompanying boat *Elodea* (Text S1) can all be seen in the movie. The BLIMP is only visible in the earlier frames since later it is out of the camera's field of view.

Movie S2.

The time-lapse movie created for 15:28 to 16:28 using:

1. Images taken by the first ZiviCat onboard camera (Text S1) displaying a far-field view of the surface water appearance in the front of the ZiviCat (top left panel).

2. Images taken by the second ZiviCat onboard camera (Text S1) displaying a near-field view of the surface water appearance just in front of the ZiviCat, where reflections of some sensors can be seen on the water (top right panel).

3. Grayscale infrared images taken by the BLIMP (Text S1), in which the boat and the ZiviCat appear as light spots, and the rope connecting the balloon to the boat is often visible. Darker shades indicate a colder surface temperature while lighter shades indicate a warmer surface temperature (middle left panel).

4. A map with a zoomed section showing the ZiviCat (green dot) movement along its track. The track is color-coded with red (warm) and blue (cold) to link the transect with the two sides of the thermal front. This section also includes a timer corresponding to the top and middle panels (middle right panel).

5. Images taken from the shore-based time-lapse camera TLB (same as Movie S1) with the corresponding time in red shown in the bottom panel. Since the time intervals between the bottom panel (every one minute) and the top and middle panels (every one second) differ, the time-lapse camera images fade as the difference between the two increases.

Chapter 5   Conclusions and Outlook

"Acquire thirst and stop searching here and there

For water—it will then gush everywhere."

Rumi

5.1 Summary and conclusions

This thesis investigates the specific physical characteristics of low wind conditions in relation to the processes at the air-water interface and atmosphere-lake energy exchanges in Lake Geneva, with a particular focus on natural slicks. Slicks, often observed as smooth patches or regions with varying colors under light wind conditions, are created by horizontal surface roughness gradients. Despite their frequent occurrence, natural slicks have not been investigated in Lake Geneva and, more broadly, rarely studied within the limnology community. In contrast, the phenomenon has been relatively well-researched in the oceanographic field, particularly in relation to air-water exchanges. Thus, one of the minor objectives of this research is to introduce the phenomenon of natural slicks to scientists studying the physical and biogeochemical aspects of lakes. This thesis provided new insights and novel methodologies for understanding the impact of slicks on surface temperature and air-water energy exchange variability. Additionally, it documented and explained an example of large-scale slick formation with unprecedented spatiotemporal resolution compared to oceanic studies. Furthermore, we sampled and analyzed the materials forming the slicks in Lake Geneva to verify their connection with the smooth patchiness and improve our understanding of their material composition. The findings presented primarily depended on in situ measurements with an autonomous catamaran, supplemented by airborne and shore-based remote observations, as well as results from 3D numerical simulations of the lake's hydrodynamics.

The study of natural slicks typically falls within the broader research area of Surface Microlayer (SML). Although SML and slick studies ideally involve interdisciplinary approaches, integrating physical and biogeochemical analyses, the primary focus of this thesis is on the effects of slicks on physical processes. Numerous surface and subsurface sampling campaigns conducted in the lake revealed higher enrichment of Fluorescence Dissolved Organic Matter (FDOM), which serves as a proxy for biogenic surfactants, within slicks compared to surrounding non-slick regions. Moreover, surface enrichment values exceeding one, even in non-slick water, indicate that non-visible surfactant enrichment, typically associated with soluble surfactants, is

prevalent in the lake's SML. This observation holds true, particularly under the low wind conditions under which the campaigns took place. The analysis of samples collected at various times of the year and from different parts of the lake indicates that the biogenic materials enriched at the surface have both autochthonous and allochthonous origins.

Studying biogenic slicks in their natural environment inevitably involves interactions with various coexisting processes. These processes include small-scale surface and near-surface temperature variability, the development of intense near-surface stratification under strong solar radiation, and fetch- and duration-limited low wind conditions that lead to intermittent generation and decay of short Gravity-Capillary Waves (GCW). Although these complex conditions pose challenges in pursuing research objectives, they represent the actual setting in which natural slicks occur, making it essential to study them in such contexts. In this study, Chapter 2 and Chapter 3 particularly focused on these interactions, emphasizing small-scale processes, whereas Chapter 4 broadened the scope to explore the large-scale evolution of natural slicks in Lake Geneva.

Unlike previous oceanic observations, which noted that surface temperature was often reduced inside slicks, Chapter 2 presents a different mechanism where slicks exhibit higher temperatures than the surrounding non-slick waters. This phenomenon occurred when there was strong shortwave radiation and intermittent light wind conditions. The accumulation of heat in near-surface waters due to solar radiation exceeds heat losses from surface cooling, creating a diurnal warm layer with strong thermal stratification in the uppermost surface layer. When wind speed exceeds the surface wave generation threshold (determined to be around 1.5 m s^{-1}), wind waves appear on the surface but only in non-slick areas. This leads to intense near-surface stratification being maintained within slicks, while enhanced wave-induced mixing in non-slick areas blends the warm surface layer with the relatively cold water below. These processes produce sharp surface temperature gradients of up to $1.5°C$ and distinct surface temperature patches that align with slick and non-slick patterns. The findings are particularly relevant to any water body during warm seasons, where a diurnal warm layer typically develops. Specifically, when very low wind conditions (~1.5 m s^{-1}) prevail, as in the case of Lake Geneva (Figure 1-2), slicks can significantly contribute to the heterogeneity of lake surface temperatures, which in turn, can affect surface energy fluxes (Chapter 3). Additionally, the observations offer insights into near-surface mixing mechanisms under very low wind conditions, highlighting the critical role of short wind waves.

Expanding on the impact of slicks on surface temperature, in Chapter 3, we employed direct flux measurements to determine the influence of slicks on air-water energy exchange. The relatively small spatial extent of slicks, combined with the inherent variability of low wind speed conditions, presents challenges to standard best practices for direct flux measurement. To overcome these challenges, a series of field campaigns were conducted, deploying an eddy covariance measurement setup on a mobile platform while concurrently capturing spatiotemporal variations in the air- and water-side variables. Wavelet analysis, rather than conventional direct flux calculations, was utilized to assess flux variability in shorter time windows (one minute). This research unveiled how spatiotemporal flux variability under low wind conditions could be affected by slicks, surface and near-surface temperature fluctuations, and wind wave generation when wind speed oscillates around the 1.5 m s^{-1} threshold. However, these results indicate the complex interplay between coexisting physical factors affecting fluxes. For instance, the role of slicks in modulating air-water exchange can be masked by other environmental variables, such as surface temperature heterogeneity, which previous oceanic measurements overlooked. These findings were possible through a detailed analysis of the proposed methodology for investigating short-term flux variations. This study marks the first instance to combine flux measurements in an aquatic and marine environment with short-term flux estimations, offering a useful tool to address flux variability related to spatiotemporal heterogeneities that cannot be accommodated by fixed towers or extensive time window averages.

During the studies presented in Chapter 2 and Chapter 3, the slicks we encountered were often part of larger surface features that remained undetected due to the small-scale focus of our measurements. However, thanks to the shore-based remote observations, we were able to uncover their large-scale patterns in Chapter 3. Chapter 4 documented a unique observation of a 10-km natural slick spanning almost the entire width of the lake. The findings suggest that the slick developed in conjunction with a sharp LSWT gradient, evolving on the warm side of the front. The significant expansion of this "frontal slick," which increased its width fourfold in less than two hours, primarily resulted from continuous "feeding" by wind-driven, rapidly moving smaller slicks. Such a detailed analysis of frontal slick formation was never conducted in oceanic studies. This observation underscores a critical stage in the life cycle of slick formation in the lake, driven by submesoscale frontogenetic sharpening of surface temperature gradients. Following strong wind events in the lake, the induced lateral density gradients mainly arise from upwelling processes (Reiss *et al.*, 2020) and strong flow deformation due to the excitation of large-scale rotational flow (Hamze-Ziabari *et al.*, 2022a), fostering frequent development of

submesoscale currents in the lake. Consequently, this observation highlights the essential role of submesoscale coherent motion in large-scale slick formation in the lake and suggests a proxy for estimating their distribution throughout the year. Additionally, the strong convergence, both computed and inferred from the accumulation of small-scale slicks and their merging into frontal slicks, illustrates how surface material transport is also dominated by these structures, at least during their active phase.

This study had certain limitations, including a primary focus on warmer seasons and diurnal conditions, even though slicks have been demonstrated to be present throughout the year, day and night. Additionally, mainly due to the intermittent nature of low wind conditions, the observations were generally sparse and less systematic, relying predominantly on on-the-fly decisions during the campaign based on instantaneous changes in environmental conditions. However, based on the knowledge gained throughout this PhD research, several recommendations can be made regarding instrumentation and measurement strategies. As slicks are manifested by wave damping, their investigation can greatly benefit from quantitative observations of the surface wave field. One possibility is to utilize the existing optical imaging system on the ZiviCat for this purpose. Specifically, the surface wave variations attributed to slicks can be estimated by employing stereo-imaging techniques and reconstructing the surface state in front of the ZiviCat. In addition to wave-related measurements, capturing skin temperature data complements the near-surface temperature measurements on the ZiviCat. This provides valuable insights into the effect of slicks on surface temperature. Skin temperature measurements serve as a reliable parameter for calibrating thermal images obtained from the BLIMP system, further enhancing the accuracy of temperature assessments in relation to slick presence.

In the context of direct flux measurement and investigating the role of slicks (Chapter 3), longer transects were preferred whenever possible to ensure an adequate number of high-frequency samples for reliable flux estimates. As a general guideline, for direct flux estimations, straight transects lasting longer than 15 minutes are optimal for achieving this objective. Additionally, an alternative strategy for in situ observation of slicks involves utilizing stationary measurement intervals, which enables Eulerian data collection. While stationary platforms have certain disadvantages compared to moving platforms, such as a passive measurement approach and challenges orienting into the wind field, they offer the advantage of collecting a larger number of samples. In the final analysis, this increased sample size simplifies the statistical analysis and inference of the observations. Finally, anecdotal evidence suggests that during low wind days,

with wind velocities fluctuating around the wave generation threshold (1.5 m/s), the wind tends to be lowest around noon, specifically between 11:30 and 14:30, falling below the wind generation threshold. Consequently, slicks are rarely observed under such very low wind conditions during a typical one-day measurement campaign. To address this, field campaigns could be planned to cover the morning hours or late afternoon, as these periods are more likely to exhibit favorable wind conditions for detecting slicks. However, the underlying physical explanation for this temporal pattern of low wind behavior remains elusive to the author and requires further investigation.

Nevertheless, the observations, results, and implications of this thesis extend beyond the specific characteristics of Lake Geneva and are applicable to other inland water bodies, as well as coastal and oceanic waters. Relatively small water bodies such as Lake Geneva can play a crucial role as bridges between oceans and laboratory studies. While distinctly different physical characteristics, such as frequent low wind conditions, fetch- and duration-limited wind and wave fields, and low salinity, exist in these water bodies, studies with a focus on SML can still replicate those on a larger scale with a more significant global impact.

5.2 Future work

Finally, the author of this thesis suggests possible directions for future research based on the observations and research gaps identified throughout this dissertation.

5.2.1 Investigating the spatiotemporal variations of natural surfactants in Lake Geneva, including their dependence on seasonal changes, wind speed, underlying hydrodynamics, and inflows to the lake

We noted varying slick coverage across regions and throughout the year. In addition to the influence of physical forcings, surfactant availability may reasonably be considered another contributing factor. Variations in visible slicks likely extend to non-visible surfactant-enriched surfaces as well. In fact, the pronounced spatial and temporal heterogeneity of SML characteristics is one of the primary sources of uncertainty regarding surfactants' impact on interfacial processes and air-water exchanges (Yang *et al.*, 2021). The proposed research aims to conduct systematic point sampling in Lake Geneva under various environmental conditions. By broadening the focus beyond slick/non-slick sampling, the study is no longer limited to the seemingly random occurrence of slicks under intermittent low wind conditions that interact with underlying hydrodynamics; hence sampling could be done systematically.

In particular, the following variations are relevant to consider: (1) Seasonal variations, primarily addressing changes in primary production and its fluctuating vertical extent throughout the year. Large-scale forcings, such as temporal variation in stratification and river inflows, can also be considered. (2) Wind speed, reasonably regarded as the main force in dispersing and redistributing the SML, can be incorporated as a state variable. The SML condition under different wind speeds (and potentially wind history) can be evaluated. (3) Recent studies on meso- to submeso-scale currents in Lake Geneva (Hamze-Ziabari *et al.*, 2022a) offer relatively accurate predictions of their occurrence and areas of influence. Thus, spatial variations in surface convergence due to these structures can be anticipated, and the SML sampling campaign can utilize this information when determining the spatial distribution of sampling points across the lake. (4) The final factor also influencing the sampling strategy's spatial design involves selecting locations near natural tributaries (rivers and streams) and anthropogenic inflows, such as wastewater treatment outputs.

SML sampling can be performed on a boat equipped with a meteorological station and ideally with surface and near-surface point temperature measurements. The simplest approach could involve using the methodology from this thesis, which combined glass plate sampling with hand-dip bulk water samples analyzed for FDOM using Fluorescence Spectrometry. While this method offers insight into surfactant origins, more direct techniques, such as measuring Surfactant Activity (SA) (Mustaffa *et al.*, 2020) or estimating surface tension reduction (Wei and Wu, 1992), could be included in the analysis. Additionally, sampling deeper layers beyond the hand-dip method's reach is possible. Creating a matrix of variables against surfactant enrichment can yield vital information, particularly for air-water exchanges. Besides addressing SML variability, other objectives, such as the relationship between bulk water and SML enrichment, can be explored in connection with the variables, which remains a controversial topic in this research area (Yang *et al.*, 2021). Satellite imagery and 3D numerical simulations can complement SML sampling by providing data on large-scale variations in surface roughness, convergence and divergence locations, and other proxies like Chl-a and surface temperature.

This methodology can indeed be applied to other lakes and coastal regions, preferably where information on the underlying hydrodynamics and prevalent wind conditions is available. Ultimately, such a study could offer a measurable proxy or model for the extent and influence

of SML based on environmental state variables that can be integrated into bulk parameterizations for air-water energy and material exchanges.

5.2.2   Quantifying short- and long-term air-water exchange variability under low wind conditions through concurrent SML sampling and wave state monitoring

Despite recent research on air-water exchanges under low wind conditions, many questions remain elusive. For example, momentum exchange and the associated drag coefficient under low wind conditions present a significant challenge due to characteristics like gustiness under unstable conditions and variable wave fields with possible short gravity-capillary waves. Moreover, air-water exchanges under stable atmospheric conditions, although less common, are understudied and often have large uncertainties. A few modifications to the methodology in Chapter 3, primarily involving more concurrent measurements, can be suggested: (1) Previously, SML enrichment was continuously measured using a rotating disk on a catamaran to study surfactant enrichment in water bodies. These in situ evaluations of SML conditions can be combined with flux measurement instrumentation. (2) Surface wave state can be quantitatively determined (beyond slick/non-slick labeling) using common wave measurement methods, such as laser slope gauges (Bock and Hara, 1995) or stereo imaging (Bergamasco *et al.*, 2016), to construct a three-dimensional wave state field. (3) Wind and temperature profile measurements on the air side can also be incorporated into the analysis, providing more information on atmospheric surface layer conditions. (4) If the focus is on more water-side controlled exchanges like CO_2, concurrent measurements with an Acoustic Doppler Velocimeter (ADV) can effectively explore near-surface turbulent conditions. These comprehensive measurements can offer insights into the isolated effects of short-term processes that contribute to long-term flux estimations.

Therefore, short-term spatiotemporal measurements should be complemented by long-term, single-point flux installations. Although fixed-point measurements pose limitations in addressing spatial heterogeneity, they offer opportunities to broaden the range of environmental state variables, such as nighttime measurements and cold seasons. While water-side measurements within the platform's flux footprint may not be feasible, large averaging windows can approximate single-point measurements. Concurrent surface wave state measurements would make a valuable addition to such installations. Moreover, SML sampling can be conducted systematically within achievable time intervals. Ultimately, these

measurements can be used to enhance bulk parameterizations under low wind conditions or suggest new parameterizations based on variables like surface wave state.

5.2.3   Role of submesoscale currents in surface energy flux

The critical role of submesoscale currents in vertical and horizontal energy and material transport is well-established in marine environments, with a growing body of literature supporting this (McWilliams, 2021). Evidence suggests that these structures may also play a significant role in air-water exchanges in the ocean (Su *et al.*, 2018). In Chapter 4, some results echo previous oceanic studies, revealing how these structures locally enhance surface fluxes with unprecedented resolution. As mentioned earlier, the knowledge developed in the laboratory regarding submesoscale current occurrence forecastability can be effectively combined with the underway flux measurements described in Chapter 3 to examine the effects of various submesoscale currents, such as fronts, filaments, and eddies, on air-water exchanges. Additionally, since these coherent motions are relatively short-lived, with life cycles dependent on the frontogenetic sharpening of lateral gradients (McWilliams, 2017), the impact of their temporal variability on surface fluxes can also be addressed.

Field campaigns can be designed to transect these structures based on a preliminary analysis of their spatial distribution in the lake and probable occurrence time window using numerical models. In situ verification of their presence can be achieved through concurrent measurements by vessel-mounted ADCPs, near-surface temperature (as in Chapter 4), or simultaneous CTD profiles taken on an accompanying boat. Given the ubiquity of submesoscale currents in various environments, including large lakes and oceans, this study can provide valuable insights into the role of these coherent motions in modulating air-water exchanges. This knowledge has the potential to be incorporated into bulk models, ultimately improving predictions of energy and material transfer between air and water on a global scale.

5.2.4   Ground-based remote sensing of lake's surface roughness: Long-term monitoring of slicks and wave fields with implications for air-water exchange measurements

One limitation of satellite-based SAR imagery for studying slicks is the sparse temporal resolution of the products, which is common in many spaceborne remote sensing products. For example, Sentinel 1 provides snapshots every few days. While this information is still valuable for examining the large-scale distribution of slicks and validating numerical simulations of the surface velocity field (Hamze-Ziabari *et al.*, 2022c), it is insufficient to infer details about

slicks' surface coverage and temporal evolution. Estimating slick coverage is crucial for up-scaling slick effects on air-water exchanges (Mustaffa *et al.*, 2020). The optical imagery system presented in this thesis can somewhat mitigate these limitations, but there are still constraints on using sunlight specular reflection to study slicks, as it is not feasible during foggy conditions or at nighttime. One possible solution is the installation of a ground-based microwave radar system to monitor slicks. If such solutions prove to be viable, their applications could extend beyond studying slicks to include wave field estimations (Cheng and Chien, 2017; Hwang and Ainsworth, 2020; Jackson *et al.*, 1992; Ziemer, 2008), particularly in response to surface wind and current variations. Additionally, capturing the characteristics of the surface wave field can be used for air-water exchange estimations.

Specifically, parameterizing gas transfer velocity using the mean square slope of small-scale waves could yield more consistent gas flux estimates compared to simple wind speed parameterizations (Frew *et al.*, 2004a). The small-scale wave field is influenced by multiple factors, such as wind stress and its time history, fetch-dependent wave age, wave-wave and wave-current interactions, atmospheric boundary layer stability, and SML concentration. Consequently, unlimited sea state variations are possible at any given wind speed. This implies that a more effective approach to parameterizing gas transfer would involve directly using surface roughness, focusing on the net effect of these combined factors in determining the ambient sea state. Such measurements can offer unique high temporal resolution along with relatively large spatial extent estimations of air-lake gas exchange.

5.2.5 Natural slick kinematics: Role of wind, wave, and near-surface current

One intriguing question regarding the physical interfacial processes that still remains elusive is the percentage of wind speed transferred to surface currents the consequent drift of surface materials (Wagner *et al.*, 2022). A rule of thumb states that surface currents are around 2-4% of wind speed. However, it is still debated how close to the surface qualifies as a "surface" current, possibly depending on the floating material, how velocity changes with depth (van der Mheen *et al.*, 2020), and whether such an estimation can be applied to thin floating materials like slicks. The problem becomes more critical when considering surface waves and the associated Stokes drift (Calvert *et al.*, 2021), as well as large-scale underlying currents. Enhancing slick kinematic estimations can be significant in at least two aspects: (1) Slicks are recognized as hotspots for accumulating various materials, including pollutants such as microplastics (Davaasuren *et al.*, 2018; Sun *et al.*, 2021). Consequently, tracking slicks can provide valuable

insights into lateral pollutant transport within the lake. (2) Oceanic oil spills pose a significant environmental challenge, and accurately predicting their movement and fate is crucial (Fifani *et al.*, 2021). Biogenic slicks can serve as safe and naturally occurring in situ analogs for oil spills, enabling the study of their kinematics under the combined effects of wind, waves, and near-surface currents.

Chapter 4 observations reveal that small-scale slicks accumulated at the surface temperature front have different velocities than the frontal slick itself, illustrating the complex physics involved in surface material transport. The shore-based imagery systems deployed in this work provide relatively high temporal resolution for estimating slick velocity vectors using an appropriate image processing methodology. These results can then be coupled with a set of field campaigns in the field of view of TLBs that measure wind speed and near-surface currents. This combination provides insights into the combined effect of wind, waves, and surface currents on the kinematics of thin surface layers such as oil and natural slicks. Ultimately, such a model can be incorporated into numerical simulations to investigate, for instance, the fate of surface pollutants and their potential beaching locations around the lake and coastal environments (Filella *et al.*, 2021).

Bibliography

Adrian, R. J. (2013). Structure of Turbulent Boundary Layers. In *Coherent Flow Structures at Earth's Surface*. https://doi.org/10.1002/9781118527221.ch2

Akan, Ç., McWilliams, J. C., Moghimi, S., and Özkan-Haller, H. T. (2018). Frontal dynamics at the edge of the Columbia River plume. *Ocean Modelling*, *122*, 1–12. https://doi.org/10.1016/j.ocemod.2017.12.001

Alappattu, D. P., Wang, Q., Yamaguchi, R., Lind, R. J., Reynolds, M., and Christman, A. J. (2017). Warm layer and cool skin corrections for bulk water temperature measurements for air-sea interaction studies. *Journal of Geophysical Research: Oceans*, *122*(8), 6470–6481. https://doi.org/10.1002/2017JC012688

Alpers, W. (1985). Theory of radar imaging of internal waves. *Nature*, *314*(6008), 245–247. https://doi.org/10.1038/314245a0

Alpers, W., and Hühnerfuss, H. (1989). The damping of ocean waves by surface films. A new look at an old problem. *Journal of Geophysical Research*, *94(C5)*, 6251–6265. https://doi.org/10.1029/JC094iC05p06251

Anfossi, D., Oettl, D., Degrazia, G., and Goulart, A. (2005). An analysis of sonic anemometer observations in low wind speed conditions. *Boundary-Layer Meteorology*, *114*(1), 179–203. https://doi.org/10.1007/s10546-004-1984-4

Augusto-Silva, P. B., MacIntyre, S., de Moraes Rudorff, C., Cortés, A., and Melack, J. M. (2019). Stratification and mixing in large floodplain lakes along the lower Amazon River. *Journal of Great Lakes Research*, *45*(1), 61–72. https://doi.org/10.1016/j.jglr.2018.11.001

Aurin, D., Mannino, A., and Lary, J. D. (2018). Remote Sensing of CDOM, CDOM Spectral Slope, and Dissolved Organic Carbon in the Global Ocean. *Remote Sensing of CDOM, CDOM Spectral Slope, and Dissolved Organic Carbon in the Global Ocean*. https://doi.org/10.3390/app8122687

Babanin, A. V., and Haus, B. K. (2009). On the existence of water turbulence induced by non-breaking surface waves. *Journal of Physical Oceanography*, *39*(10), 2675–2679. https://doi.org/10.1175/2009JPO4202.1

Bai, Y., Cui, Z., Su, R., and Qu, K. (2019). Seasonal and Spatial Changes in FDOM Compositions in the Continental Shelf Area of the East China Sea. *Atmosphere-Ocean*, 1–15. https://doi.org/10.1080/07055900.2019.1686696

Banner, M. L., and Peirson, W. L. (1998). Tangential stress beneath wind-driven air-water interfaces. *Journal of Fluid Mechanics*, *364*, 115–145. https://doi.org/10.1017/S0022112098001128

Barry, D. A., Liardon, J.-L., Paccaud, P., Klaus, P., Shaik, N., Rahaghi, A. I., et al. (2019). A low-cost, autonomous mobile platform for limnological investigations, supported by high-resolution mesoscale airborne imagery. *PLOS ONE*, *14*, e0210562. https://doi.org/10.1371/journal.pone.0210562

Bartosiewicz, M., Przytulska, A., Deshpande, B. N., Antoniades, D., Cortes, A., MacIntyre, S., et al. (2019). Effects of climate change and episodic heat events on cyanobacteria in a eutrophic polymictic lake. *Science of The Total Environment*, *693*, 133414. https://doi.org/10.1016/j.scitotenv.2019.07.220

Beljaars, A. C. M. (1995). The parametrization of surface fluxes in large-scale models under free convection. *Quarterly Journal of the Royal Meteorological Society*, *121*(522), 255–270. https://doi.org/10.1002/qj.49712152203

Benetazzo, A., Cavaleri, L., Ma, H., Jiang, S., Bergamasco, F., Jiang, W., et al. (2019). Analysis of the effect of fish oil on wind waves and implications for air–water interaction studies. *Ocean Science*, *15*(3), 725–743. https://doi.org/10.5194/os-15-725-2019

Bergamasco, F., Benetazzo, A., Barbariol, F., Carniel, S., and Sclavo, M. (2016). Multi-view horizon-driven sea plane estimation for stereo wave imaging on moving vessels. *Computers and Geosciences*, *95*, 105–117. https://doi.org/10.1016/j.cageo.2016.07.012

Biosciences, L. (2017). EddyPro software instruction manual. *LI-COR Inc., Lincoln, Nebraska, USA*.

Biri, S., Cornes, R. C., Berry, D. I., Kent, E. C., and Yelland, M. J. (2023). AirSeaFluxCode: Open-source software for calculating turbulent air-sea fluxes from meteorological parameters. *Frontiers in Marine Science*, *9*. Retrieved from https://www.frontiersin.org/articles/10.3389/fmars.2022.1049168

Bock, E. J., and Hara, T. (1995). Optical Measurements of Capillary-Gravity Wave Spectra Using a Scanning Laser Slope Gauge. *Journal of Atmospheric and Oceanic Technology*, *12*(2), 395–403. https://doi.org/10.1175/1520-0426(1995)012<0395:OMOCGW>2.0.CO;2

Bock, E. J., and Mann, J. A. (1989). On ripple dynamics: II. A corrected dispersion relation for surface waves in the presence of surface elasticity. *Journal of Colloid and Interface Science*, *129*(2), 501–505. https://doi.org/10.1016/0021-9797(89)90464-5

Bohle-Carbonell, M. (1991). Wind and currents- Response patterns of Lake Geneva. In *Annales Geophysicae* (Vol. 9, pp. 82–90).

Bower, S. M., and Saylor, J. R. (2011a). The effects of surfactant monolayers on free surface natural convection. *International Journal of Heat and Mass Transfer*, *54*(25), 5348–5358. https://doi.org/10.1016/j.ijheatmasstransfer.2011.08.008

Bower, S. M., and Saylor, J. R. (2011b). The effects of surfactant monolayers on free surface natural convection. *International Journal of Heat and Mass Transfer*, *54*(25), 5348–5358. https://doi.org/10.1016/j.ijheatmasstransfer.2011.08.008

Brutsaert, W. (1975). On a derivable formula for long-wave radiation from clear skies. *Water Resources Research*, *11*(5), 742–744. https://doi.org/10.1029/WR011i005p00742

Calamita, E., Piccolroaz, S., Majone, B., and Toffolon, M. (2021). On the role of local depth and latitude on surface warming heterogeneity in the Laurentian Great Lakes. *Inland Waters*, *11*(2), 208–222. https://doi.org/10.1080/20442041.2021.1873698

Calvert, R., McAllister, M. L., Whittaker, C., Raby, A., Borthwick, A. G. L., and Bremer, T. S. van den. (2021). A mechanism for the increased wave-induced drift of floating marine litter. *Journal of Fluid Mechanics*, *915*. https://doi.org/10.1017/jfm.2021.72

Carlson, D. J. (1987). Viscosity of sea-surface slicks. *Nature*, *329*(6142), 823–825. https://doi.org/10.1038/329823a0

Cheng, H.-Y., and Chien, H. (2017). Implementation of S-band marine radar for surface wave measurement under precipitation. *Remote Sensing of Environment*, *188*, 85–94. https://doi.org/10.1016/j.rse.2016.10.042

Cheng, J., Cheng, X., Meng, X., and Zhou, G. (2019). A Monte Carlo emissivity model for wind-roughened sea surface. *Sensors*, *19*(9), 2166. https://doi.org/10.3390/s19092166

Choi, J., Troy, C., Hawley, N., McCormick, M., and Wells, M. (2020). Lateral dispersion of dye and drifters in the center of a very large lake. *Limnology and Oceanography*, *65*(2), 336–348. https://doi.org/10.1002/lno.11302

Cimatoribus, A. A., Lemmin, U., Bouffard, D., and Barry, D. A. (2018). Nonlinear dynamics of the nearshore boundary layer of a large lake (Lake Geneva). *Journal of Geophysical Research: Oceans*, *123*(2), 1016–1031. https://doi.org/10.1002/2017JC013531

Cimatoribus, A. A., Lemmin, U., and Barry, D. A. (2019). Tracking Lagrangian transport in Lake Geneva: A 3D numerical modeling investigation. *Limnology and Oceanography*, *64*(3), 1252–1269. https://doi.org/10.1002/lno.11111

CIPEL. (2019). *Rapports sur les études et recherches entreprises dans le bassin lémanique, Campagne 2018*. Nyon, Switzerland: Commission internationale pour la protection des eaux du Léman (CIPEL). Retrieved from https://www.cipel.org/catalogue/rapport-sci-entifique-2020-campagne-2019/

Coble, P. G. (1996). Characterization of marine and terrestrial DOM in seawater using excitation-emission matrix spectroscopy. *Marine Chemistry*, *51*(4), 325–346. https://doi.org/10.1016/0304-4203(95)00062-3

Cogley, J. G. (1979). The albedo of water as a function of latitude. *Monthly Weather Review*, *107*(6), 775–781. https://doi.org/10.1175/1520-0493(1979)107<0775:TAOWAA>2.0.CO;2

Cox, C. S., Zhang, X., and Duda, T. F. (2017). Suppressing breakers with polar oil films: Using an epic sea rescue to model wave energy budgets. *Geophysical Research Letters*, *44*(3), 1414–1421. https://doi.org/10.1002/2016GL071505

Crawford, T. M., and Duchon, C. E. (1999). An improved parameterization for estimating effective atmospheric emissivity for use in calculating daytime downwelling longwave radiation. *Journal of Applied Meteorology and Climatology*, *38*(4), 474–480. https://doi.org/10.1175/1520-0450(1999)038<0474:AIPFEE>2.0.CO;2

Cunliffe, M., and Wurl, O. (2014). *Guide to Best Practices to Study the Ocean's Surface*. Plymouth: Marine Biological Association of the United Kingdom for SCOR. Retrieved from http://www.scor-int.org/Publications/SCOR_GuideSeaSurface_2014.pdf

Cunliffe, M., Engel, A., Frka, S., Gašparović, B. Ž., Guitart, C., Murrell, J. C., et al. (2013a). Sea surface microlayers: A unified physicochemical and biological perspective of the air-ocean interface. *Progress in Oceanography*, *109*, 104–116. https://doi.org/10.1016/j.pocean.2012.08.004

Cunliffe, M., Engel, A., Frka, S., Gašparović, B. Ž., Guitart, C., Murrell, J. C., et al. (2013b). Sea surface microlayers: A unified physicochemical and biological perspective of the air-ocean interface. *Progress in Oceanography*, *109*, 104–116. https://doi.org/10.1016/j.pocean.2012.08.004

Dabuleviciene, T., Kozlov, I. E., Vaiciute, D., and Dailidiene, I. (2018). Remote sensing of coastal upwelling in the south-eastern Baltic Sea: Statistical properties and implications for the coastal environment. *Remote Sensing*, *10*(11), 1752. https://doi.org/10.3390/rs10111752

Dai, D., Qiao, F., Sulisz, W., Han, L., and Babanin, A. (2010). An experiment on the nonbreaking surface-wave-induced vertical mixing. *Journal of Physical Oceanography*, *40*(9), 2180–2188. https://doi.org/10.1175/2010JPO4378.1

D'Asaro, E. A. (2014). Turbulence in the upper-ocean mixed layer. *Annual Review of Marine Science*, *6*(1), 101–115. https://doi.org/10.1146/annurev-marine-010213-135138

D'Asaro, E. A., Shcherbina, A. Y., Klymak, J. M., Molemaker, J., Novelli, G., Guigand, C. M., et al. (2018). Ocean convergence and the dispersion of flotsam. *Proceedings of the National Academy of Sciences USA*, *115*(6), 1162–1167. https://doi.org/10.1073/pnas.1718453115

Davaasuren, N., Marino, A., Boardman, C., Alparone, M., Nunziata, F., Ackermann, N., and Hajnsek, I. (2018). Detecting microplastics pollution in world oceans using SAR remote sensing. In *IGARSS 2018 - 2018 IEEE International Geoscience and Remote Sensing Symposium* (pp. 938–941). https://doi.org/10.1109/IGARSS.2018.8517281

Davies, J. T. (1966). The effects of surface films in damping eddies at a free surface of a turbulent liquid. *Proceedings of the Royal Society of London. Series A. Mathematical and Physical Sciences*, *290*(1423), 515–526. https://doi.org/10.1098/rspa.1966.0067

De Santi, F., Luciani, G., Bresciani, M., Giardino, C., Lovergine, F. P., Pasquariello, G., et al. (2019). Synergistic use of synthetic aperture radar and optical imagery to monitor surface accumulation of cyanobacteria in the Curonian Lagoon. *Journal of Marine Science and Engineering*, *7*(12), 461. https://doi.org/10.3390/jmse7120461

De Stasio Jr., B. T., Hill, D. K., Kleinhans, J. M., Nibbelink, N. P., and Magnuson, J. J. (1996). Potential effects of global climate change on small north-temperate lakes: Physics, fish, and plankton. *Limnology and Oceanography*, *41*(5), 1136–1149. https://doi.org/10.4319/lo.1996.41.5.1136

Dietz, R. S., and Lafond, E. C. (1950). *Natural slicks on the ocean*. San Diego, California, USA: Navy Electronics Lab.

Djoumna, G., Lamb, K. G., and Rao, Y. R. (2014). Sensitivity of the parameterizations of vertical mixing and radiative heat fluxes on the seasonal evolution of the thermal structure of Lake Erie. *Atmosphere-Ocean*, *52*(4), 294–313. https://doi.org/10.1080/07055900.2014.939824

Donelan, M. A., and Plant, W. J. (2009). A threshold for wind-wave growth. *Journal of Geophysical Research*, *114*, C07012. https://doi.org/10.1029/2008JC005238

Dong, Y., Yang, M., Bakker, D. C. E., Liss, P. S., Kitidis, V., Brown, I., et al. (2021). Near-surface stratification due to ice melt biases arctic air-sea co2 flux estimates. *Geophysical Research Letters*, *48*(22), e2021GL095266. https://doi.org/10.1029/2021GL095266

Donlon, C. J., Minnett, P. J., Gentemann, C., Nightingale, T. J., Barton, I. J., Ward, B., and Murray, M. J. (2002). Toward improved validation of satellite sea surface skin temperature measurements for climate research. *Journal of Climate*, *15*(4), 353–369. https://doi.org/10.1175/1520-0442(2002)015<0353:TIVOSS>2.0.CO;2

Dorostkar, A., and Boegman, L. (2013). Internal hydraulic jumps in a long narrow lake. *Limnology and Oceanography*, *58*(1), 153–172. https://doi.org/10.4319/lo.2013.58.1.0153

Dorostkar, A., Boegman, L., and Pollard, A. (2017). Three-dimensional simulation of high-frequency nonlinear internal wave dynamics in Cayuga Lake. *Journal of Geophysical Research: Oceans*, *122*(3), 2183–2204. https://doi.org/10.1002/2016JC011862

ECMWF. (2019). IFS Documentation CY46R1 - Part IV: Physical Processes. In *IFS Documentation CY46R1* (Vols. 1–4). ECMWF. https://doi.org/10.21957/xphfxep8c

Edson, J., Crawford, T., Crescenti, J., Farrar, T., Frew, N., Gerbi, G., et al. (2007). The coupled boundary layers and air–sea transfer experiment in low winds. *Bulletin of the American Meteorological Society*, *88*(3), 341–356. https://doi.org/10.1175/BAMS-88-3-341

Edson, J. B., and Fairall, C. W. (1998). Similarity Relationships in the Marine Atmospheric Surface Layer for Terms in the TKE and Scalar Variance Budgets*. *Journal of the Atmospheric Sciences*, *55*(13), 2311–2328. https://doi.org/10.1175/1520-0469(1998)055<2311:SRITMA>2.0.CO;2

Edson, J. B., Hinton, A. A., Prada, K. E., Hare, J. E., and Fairall, C. W. (1998). Direct Covariance Flux Estimates from Mobile Platforms at Sea*. *Journal of Atmospheric and Oceanic Technology*, *15*(2), 547–562. https://doi.org/10.1175/1520-0426(1998)015<0547:DCFEFM>2.0.CO;2

Edson, J. B., Jampana, V., Weller, R. A., Bigorre, S. P., Plueddemann, A. J., Fairall, C. W., et al. (2013). On the exchange of momentum over the open ocean. *Journal of Physical Oceanography*, *43*(8), 1589–1610. https://doi.org/10.1175/JPO-D-12-0173.1

Elliott, S., Burrows, S., Cameron-Smith, P., Hoffman, F., Hunke, E., Jeffery, N., et al. (2018). Does marine surface tension have global biogeography? Addition for the oceanfilms package. *Atmosphere*, *9*(6), 216. https://doi.org/10.3390/atmos9060216

Engel, A., Bange, H. W., Cunliffe, M., Burrows, S. M., Friedrichs, G., Galgani, L., et al. (2017). The ocean's vital skin: Toward an integrated understanding of the sea surface microlayer. *Frontiers in Marine Science*, *4*(165), 165.

Ermakov, S., Lavrova, O., Kapustin, I., Ermoshkin, A., Molkov, A., and Danilicheva, O. (2018a). On the "comb" structure of the edges of slicks on the sea surface. *Sovremennye Problemy Distantsionnogo Zondirovaniya Zemli Iz Kosmosa*, *15*, 208–217. https://doi.org/10.21046/2070-7401-2018-15-7-208-217

Ermakov, S. A. (2012). Slicks in SAR imagery of the sea surface. In *SAR Image Analysis, Modeling, and Techniques XII* (Vol. 8536, p. 85360S). International Society for Optics and Photonics. https://doi.org/10.1117/12.976854

Ermakov, S. A., Salashin, S. G., and Panchenko, A. R. (1992). Film slicks on the sea surface and some mechanisms of their formation. *Dynamics of Atmospheres and Oceans*, *16*(3), 279–304. https://doi.org/10.1016/0377-0265(92)90010-Q

Ermakov, S. A., Kapustin, I., and Sergievskaya, I. (2011). Remote sensing and in situ observations of marine slicks associated with inhomogeneous coastal currents. In *Remote Sensing of the Ocean, Sea Ice, Coastal Waters, and Large Water Regions 2011* (Vol. 8175, p. 81750R). SPIE. https://doi.org/10.1117/12.898224

Ermakov, S. A., Lavrova, O., Kapustin, I., Ermoshkin, A., Molkov, A., and Danilicheva, O. (2018b). On the "comb" structure of the edges of slicks on the sea surface. *Sovremennye Problemy Distantsionnogo Zondirovaniya Zemli Iz Kosmosa*, *15*, 208–217. https://doi.org/10.21046/2070-7401-2018-15-7-208-217

Espedal, H. A., Johannessen, O. M., and Knulst, J. (1996). Satellite detection of natural films on the ocean surface. *Geophysical Research Letters*, *23*(22), 3151–3154. https://doi.org/10.1029/96GL03009

Esters, L., Breivik, Ø., Landwehr, S., ten Doeschate, A., Sutherland, G., Christensen, K. H., et al. (2018). Turbulence Scaling Comparisons in the Ocean Surface Boundary Layer. *Journal of Geophysical Research: Oceans*, *123*(3), 2172–2191. https://doi.org/10.1002/2017JC013525

Fairall, C. W., Bradley, E. F., Godfrey, J. S., Wick, G. A., Edson, J. B., and Young, G. S. (1996a). Cool-skin and warm-layer effects on sea surface temperature. *Journal of Geophysical Research: Oceans*, *101*(C1), 1295–1308. https://doi.org/10.1029/95JC03190

Fairall, C. W., Bradley, E. F., Godfrey, J. S., Wick, G. A., Edson, J. B., and Young, G. S. (1996b). Cool-skin and warm-layer effects on sea surface temperature. *Journal of Geophysical Research: Oceans*, *101*(C1), 1295–1308. https://doi.org/10.1029/95JC03190

Fairall, C. W., Bradley, E. F., Hare, J. E., Grachev, A. A., and Edson, J. B. (2003). Bulk Parameterization of Air–Sea Fluxes: Updates and Verification for the COARE Algorithm. *Journal of Climate*, *16*(4), 571–591. https://doi.org/10.1175/1520-0442(2003)016<0571:BPOASF>2.0.CO;2

Falkowska, L. (1999). Sea surface microlayer: a field evaluation of teflon plate, glass plate and screen sampling techniques. Part 2. Dissolved and suspended matter. *Oceanologia*, *No. 41 (2)*, 223–240.

Farrar, J. T., Zappa, C. J., Weller, R. A., and Jessup, A. T. (2007). Sea surface temperature signatures of oceanic internal waves in low winds. *Journal of Geophysical Research: Oceans*, *112*(C6). https://doi.org/10.1029/2006JC003947

Fernández Castro, B., Bouffard, D., Troy, C., Ulloa, H. N., Piccolroaz, S., Sepúlveda Steiner, O., et al. (2021). Seasonality modulates wind-driven mixing pathways in a large lake. *Communications Earth & Environment*, *2*(1), 1–11. https://doi.org/10.1038/s43247-021-00288-3

Fichot, C. G., Matsumoto, K., Holt, B., Gierach, M. M., and Tokos, K. S. (2019). Assessing change in the overturning behavior of the Laurentian Great Lakes using remotely sensed lake surface water temperatures. *Remote Sensing of Environment*, *235*, 111427. https://doi.org/10.1016/j.rse.2019.111427

Fifani, G., Baudena, A., Fakhri, M., Baaklini, G., Faugère, Y., Morrow, R., et al. (2021). Drifting speed of Lagrangian fronts and oil spill dispersal at the ocean surface. *Remote Sensing*, *13*(22), 4499. https://doi.org/10.3390/rs13224499

Filella, M., Rodríguez-Murillo, J.-C., and Turner, A. (2021). What the presence of regulated chemical elements in beached lacustrine plastics can tell us: the case of Swiss lakes. *Environmental Monitoring and Assessment*, *193*(11), 693. https://doi.org/10.1007/s10661-021-09384-5

Fink, G., Schmid, M., Wahl, B., Wolf, T., and Wüest, A. (2014). Heat flux modifications related to climate-induced warming of large European lakes. *Water Resources Research*, *50*(3), 2072–2085. https://doi.org/10.1002/2013WR014448

Flack, K. A., Saylor, J. R., and Smith, G. B. (2001). Near-surface turbulence for evaporative convection at an air/water interface. *Physics of Fluids*, *13*(11), 3338–3345. https://doi.org/10.1063/1.1410126

Foken, T., Göockede, M., Mauder, M., Mahrt, L., Amiro, B., and Munger, W. (2005). Post-Field Data Quality Control. In X. Lee, W. Massman, and B. Law (Eds.), *Handbook of Micrometeorology: A Guide for Surface Flux Measurement and Analysis* (pp. 181–208). Dordrecht: Springer Netherlands. https://doi.org/10.1007/1-4020-2265-4_9

Font, J., Rousseau, S., Shirasago, B., García-Górriz, E., and Haney, R. L. (2002). Mesoscale variability in the Alboran Sea: Synthetic aperture radar imaging of frontal eddies. *Journal of Geophysical Research: Oceans*, *107*(C6), 12-1-12–17. https://doi.org/10.1029/2001JC000835

Forel, F. A. (1892). *Le Léman: Monographie limnologique*. F. Rouge.

Foroughan, M., Hamze-Ziabari, S. M., Lemmin, U., and Barry, D. A. (2022a). A Persistent Submesoscale Frontal Slick: A Novel Marker of the Mesoscale Flow Field in a Large Lake (Lake Geneva). *Geophysical Research Letters*, *49*(20), e2022GL100262. https://doi.org/10.1029/2022GL100262

Foroughan, M., Lemmin, U., and Barry, D. A. (2022b). Effects of natural surfactants on the spatial variability of surface water temperature under intermittent light winds on Lake Geneva. *Journal of Limnology*, *81*(1), 2048. https://doi.org/10.4081/jlimnol.2022.2048

Frew, N. M. (1997). The role of organic films in air–sea gas exchange. In P. S. Liss and R. A. Duce (Eds.), *The sea surface and global change* (pp. 121–172). Cambridge: Cambridge University Press. https://doi.org/10.1017/cbo9780511525025.006

Frew, N. M., and Nelson, R. K. (1999). Spatial mapping of sea surface microlayer surfactant concentration and composition. *IEEE 1999 International*, *3*(508), 1472–1474.

Frew, N. M., Goldman, J. C., Dennett, M. R., and Johnson, A. S. (1990). Impact of phytoplankton-generated surfactants on air-sea gas exchange. *Journal of Geophysical Research*. https://doi.org/10.1029/jc095ic03p03337

Frew, N. M., Nelson, R. K., McGillis, W. R., Edson, J. B., Bock, E. J., and Hara, T. (2002). Spatial variations in surface microlayer surfactants and their role in modulating air-sea exchange. In M. A. Donelan, W. M. Drennan, E. S. Saltzman, and R. Wanninkhof (Eds.), *Gas Transfer at Water Surfaces* (Vol. 127, pp. 153–159). Washington, D.C.: American Geophysical Union (AGU). https://doi.org/10.1029/GM127p0153

Frew, N. M., Bock, E. J., Schimpf, U., Hara, T., Haußecker, H., Edson, J. B., et al. (2004a). Air-sea gas transfer: Its dependence on wind stress, small-scale roughness, and surface films. *Journal of Geophysical Research*, *109*, C08S17. https://doi.org/10.1029/2003JC002131

Frew, N. M., Bock, E. J., Schimpf, U., Hara, T., Haußecker, H., Edson, J. B., et al. (2004b). Air-sea gas transfer: Its dependence on wind stress, small-scale roughness, and surface films. *Journal of Geophysical Research*, *109*, C08S17. https://doi.org/10.1029/2003JC002131

Frew, N. M., Nelson, R. K., and Johnson, C. G. (2006). Sea slicks: variability in chemical composition and surface elasticity. In M. Gade, H. Hühnerfuss, and G. M. Korenowski (Eds.), *Marine surface films: chemical characteristics, influence on air-sea interactions and remote sensing* (pp. 45–56). Berlin: Springer. https://doi.org/10.1007/3-540-33271-5_6

Frka, S., Kozarac, Z., and Ćosović, B. (2009). Characterization and seasonal variations of surface active substances in the natural sea surface micro-layers of the coastal Middle Adriatic stations. *Estuarine, Coastal and Shelf Science*, *85*(4), 555–564. https://doi.org/10.1016/j.ecss.2009.09.023

Gade, M., Alpers, W., Hühnerfuss, H., Masuko, H., and Kobayashi, T. (1998). Imaging of biogenic and anthropogenic ocean surface films by the multifrequency/multipolarization SIR-C/X-SAR. *Journal of Geophysical Research: Oceans*, *103*(C9), 18851–18866. https://doi.org/10.1029/97JC01915

Gade, M., Hühnerfuss, H., and Korenowski, G. (Eds.). (2006). *Marine surface films: chemical characteristics, influence on air-sea interactions and remote sensing*. Berlin: Springer.

Gallardo, C., Ory, N. C., Gallardo, M. de los Á., Ramos, M., Bravo, L., and Thiel, M. (2021). Sea-surface slicks and their effect on the concentration of plastics and zooplankton in the coastal waters of Rapa Nui (Easter Island). *Frontiers in Marine Science*, *8*, 1490. https://doi.org/10.3389/fmars.2021.688224

Garabetian, F., Romano, J.-C., Paul, R., and Sigoillot, J.-C. (1993). Organic matter composition and pollutant enrichment of sea surface microlayer inside and outside slicks. *Marine Environmental Research*, *35*(4), 323–339. https://doi.org/10.1016/0141-1136(93)90100-E

Garbe, C. S., Schimpf, U., and Jähne, B. (2004). A surface renewal model to analyze infrared image sequences of the ocean surface for the study of air-sea heat and gas exchange. *Journal of Geophysical Research*, *109*, C08S15. https://doi.org/10.1029/2003JC001802

García-Flor, N., Guitart, C., Ábalos, M., Dachs, J., Bayona, J. M., and Albaigés, J. (2005). Enrichment of organochlorine contaminants in the sea surface microlayer: An organic carbon-driven process. *Marine Chemistry*, *96*(3), 331–345. https://doi.org/10.1016/j.marchem.2005.01.005

Garrett, W. D. (1971). A novel approach to evaporation control with monomolecular films. *Journal of Geophysical Research (1896-1977)*, *76*(21), 5122–5123. https://doi.org/10.1029/JC076i021p05122

Garrett, W. D. (1986). Physicochemical effects of organic films at the sea surface and their role in the interpretation of remotely sensed imagery. In *ONRL Workshop Proceedings: Role of Surfactant Films on the Interfacial Properties of the Sea Surface* (pp. 1–17). Office of Naval Research London Branch.

Garvine, R. W. (1974). Dynamics of small-scale oceanic fronts. *Journal of Physical Oceanography*, *4*(4), 557–569. https://doi.org/10.1175/1520-0485(1974)004<0557:DOSSOF>2.0.CO;2

Genin, A., Jaffe, J. S., Reef, R., Richter, C., and Franks, P. J. S. (2005). Swimming against the flow: A mechanism of zooplankton aggregation. *Science*, *308*(5723), 860–862. https://doi.org/10.1126/science.1107834

Gentemann, C. L., and Minnett, P. J. (2008). Radiometric measurements of ocean surface thermal variability. *Journal of Geophysical Research: Oceans*, *113*(8), C08017. https://doi.org/10.1029/2007JC004540

Gentemann, C. L., Minnett, P. J., and Ward, B. (2009). Profiles of ocean surface heating (POSH): A new model of upper ocean diurnal warming. *Journal of Geophysical Research*, *114*(7), C07017. https://doi.org/10.1029/2008JC004825

Gerum, R. C., Richter, S., Winterl, A., Mark, C., Fabry, B., Le Bohec, C., and Zitterbart, D. P. (2019). CameraTransform: A Python package for perspective corrections and image mapping. *SoftwareX*, *10*, 100333. https://doi.org/10.1016/j.softx.2019.100333

Gillet, C., and QuéTin, P. (2006). Effect of temperature changes on the reproductive cycle of roach in Lake Geneva from 1983 to 2001. *Journal of Fish Biology*, *69*(2), 518–534. https://doi.org/10.1111/j.1095-8649.2006.01123.x

Godfrey, J. S., and Beljaars, A. C. M. (1991). On the turbulent fluxes of buoyancy, heat and moisture at the air-sea interface at low wind speeds. *Journal of Geophysical Research: Oceans*, *96*(C12), 22043–22048. https://doi.org/10.1029/91JC02015

Goldman, J. C., Dennett, M. R., and Frew, N. M. (1988). Surfactant effects on air-sea gas exchange under turbulent conditions. *Deep Sea Research Part A. Oceanographic Research Papers*, *35*(12), 1953–1970. https://doi.org/10.1016/0198-0149(88)90119-7

Gove, J. M., Whitney, J. L., McManus, M. A., Lecky, J., Carvalho, F. C., Lynch, J. M., et al. (2019a). Prey-size plastics are invading larval fish nurseries. *Proceedings of the National Academy of Sciences of the United States of America*, *116*(48), 24143–24149. https://doi.org/10.1073/pnas.1907496116

Gove, J. M., Whitney, J. L., McManus, M. A., Lecky, J., Carvalho, F. C., Lynch, J. M., et al. (2019b). Prey-size plastics are invading larval fish nurseries. *Proceedings of the National Academy of Sciences of the United States of America*, *116*(48), 24143–24149. https://doi.org/10.1073/pnas.1907496116

Grachev, A. A., Fairall, C. W., and Larsen, S. E. (1998). On the determination of the neutral drag coefficient in the convective boundary layer. *Boundary-Layer Meteorology*, *86*(2), 257–278. https://doi.org/10.1023/A:1000617300732

Gueymard, C. A., Myers, D., and Emery, K. (2002). Proposed reference irradiance spectra for solar energy systems testing. *Solar Energy*, *73*(6), 443–467. https://doi.org/10.1016/S0038-092X(03)00005-7

Gula, J., Molemaker, M. J., and McWilliams, J. C. (2014). Submesoscale cold filaments in the Gulf Stream. *Journal of Physical Oceanography*, *44*(10), 2617–2643. https://doi.org/10.1175/JPO-D-14-0029.1

Gulev, S. K. (1997). Climatologically significant effects of space–time averaging in the north Atlantic sea–air heat flux fields. *Journal of Climate*, *10*(11), 2743–2763. https://doi.org/10.1175/1520-0442(1997)010<2743:CSEOST>2.0.CO;2

Guseva, S., Armani, F., Desai, A. R., Dias, N. L., Friborg, T., Iwata, H., et al. (2023). Bulk transfer coefficients estimated from eddy-covariance measurements over lakes and reservoirs. *Journal of Geophysical Research: Atmospheres*, *128*(2), e2022JD037219. https://doi.org/10.1029/2022JD037219

Hamze-Ziabari, S. M., Lemmin, U., Soulignac, F., Foroughan, M., and Barry, D. A. (2022a). Basin-scale gyres and mesoscale eddies in large lakes: a novel procedure for their detection and characterization, assessed in Lake Geneva. *Geoscientific Model Development*, *15*(23), 8785–8807. https://doi.org/10.5194/gmd-15-8785-2022

Hamze-Ziabari, S. M., Razmi, A. M., Lemmin, U., and Barry, D. A. (2022b). Detecting submesoscale cold filaments in a basin-scale gyre in large, deep Lake Geneva (Switzerland/France). *Geophysical Research Letters*, *49*(4), e2021GL096185. https://doi.org/10.1029/2021GL096185

Hamze-Ziabari, S. M., Foroughan, M., Lemmin, U., and Barry, D. A. (2022c). Monitoring Mesoscale to Submesoscale Processes in Large Lakes with Sentinel-1 SAR Imagery: The Case of Lake Geneva. *Remote Sensing*, *14*(19), 4967. https://doi.org/10.3390/rs14194967

Handler, R. A., Leighton, R. I., Smith, G. B., and Nagaosa, R. (2003). Surfactant effects on passive scalar transport in a fully developed turbulent flow. *International Journal of Heat and Mass Transfer*, *46*(12), 2219–2238. https://doi.org/10.1016/S0017-9310(02)00526-4

Herr, F. L., and Williams, J. (1986). *Role of surfactant films on the interfacial properties of the sea surface* (ONRL Workshop Proceedings No. C-11–86) (p. 283). London, UK: Office of Naval Research.

Howe, K. (2017). *DNA Analysis of Surfactant-Associated Bacteria in a Natural Sea Slick in the Gulf of Mexico Observed by TerraSAR-X* (PhD Thesis).

Hughes, K. G., Moum, J. N., and Shroyer, E. L. (2020a). Evolution of the velocity structure in the diurnal warm layer. *Journal of Physical Oceanography*, *50*(3), 615–631. https://doi.org/10.1175/JPO-D-19-0207.1

Hughes, K. G., Moum, J. N., and Shroyer, E. L. (2020b). Heat transport through diurnal warm layers. *Journal of Physical Oceanography*, *50*(10), 2885–2905. https://doi.org/10.1175/JPO-D-20-0079.1

Hughes, P. J., Bourassa, M. A., Rolph, J. J., and Smith, S. R. (2012). Averaging-related biases in monthly latent heat fluxes. *Journal of Atmospheric and Oceanic Technology*, *29*(7), 974–986. https://doi.org/10.1175/JTECH-D-11-00184.1

Hühnerfuss, H. (2006a). Basic physicochemical principles of monomolecular sea slicks and crude oil spills. In *Marine Surface Films* (pp. 21–35). Springer.

Hühnerfuss, H. (2006b). Oil on troubled waters—a historical survey. In M. Gade, H. Hühnerfuss, and G. M. Korenowski (Eds.), *Marine surface films: chemical characteristics, influence on air-sea interactions and remote sensing* (pp. 3–12). Berlin: Springer. https://doi.org/10.1007/3-540-33271-5_6

Hunter, K. A., and Liss, P. S. (1981). Organic sea surface films. In E. K. Duursma and R. Dawson (Eds.), *Marine Organic Chemistry* (Vol. 31, pp. 259–298). Amsterdam: Elsevier. https://doi.org/10.1016/S0422-9894(08)70331-3

Hwang, P. A., and Ainsworth, T. L. (2020). L-band ocean surface roughness. *IEEE Transactions on Geoscience and Remote Sensing*, *58*(6), 3988–3999. https://doi.org/10.1109/TGRS.2019.2960130

Hwang, P. A., and Wang, D. W. (2004). Field measurements of duration-limited growth of wind-generated ocean surface waves at young stage of development. *Journal of Physical Oceanography*, *34*(10), 2316–2326. https://doi.org/10.1175/1520-0485(2004)034<2316:FMODGO>2.0.CO;2

Imberger, J. (1985). The diurnal mixed layer. *Limnology and Oceanography*, *30*(4), 737–770. https://doi.org/10.4319/lo.1985.30.4.0737

Irani Rahaghi, A. (2018). *Large-scale and meso-scale surface heat flux patterns of Lake Geneva* (PhD Thesis). EPFL.

Iyer, S., Drushka, K., Thompson, E. J., and Thomson, J. (2022). Small-scale spatial variations of air-sea heat, moisture, and buoyancy fluxes in the tropical trade winds. *Journal of Geophysical Research: Oceans*, *127*(10), e2022JC018972. https://doi.org/10.1029/2022JC018972

Jackson, F. C., Walton, W. T., Hines, D. E., Walter, B. A., and Peng, C. Y. (1992). Sea surface mean square slope from Ku-band backscatter data. *Journal of Geophysical Research: Oceans*, *97*(C7), 11411–11427. https://doi.org/10.1029/92JC00766

Jarvis, N. L. (1962a). The effect of monomolecular films on surface temperature and convective motion at the water/air interface. *Journal of Colloid Science*, *17*(6), 512–522. https://doi.org/10.1016/0095-8522(62)90019-3

Jarvis, N. L. (1962b). The effect of monomolecular films on surface temperature and convective motion at the water/air interface. *Journal of Colloid Science*, *17*(6), 512–522. https://doi.org/10.1016/0095-8522(62)90019-3

Jellison, R., and Melack, J. M. (1993). Meromixis in hypersaline Mono Lake, California. 1. Stratification and vertical mixing during the onset, persistence, and breakdown of meromixis. *Limnology and Oceanography*, *38*(5), 1008–1019. https://doi.org/10.4319/lo.1993.38.5.1008

Johannessen, J. A., Shuchman, R. A., Digranes, G., Lyzenga, D. R., Wackerman, C., Johannessen, O. M., and Vachon, P. W. (1996). Coastal ocean fronts and eddies imaged with ERS 1 synthetic aperture radar. *Journal of Geophysical Research: Oceans*, *101*(C3), 6651–6667. https://doi.org/10.1029/95JC02962

Kara, A. B., Hurlburt, H. E., and Wallcraft, A. J. (2005). Stability-dependent exchange coefficients for air–sea fluxes. *Journal of Atmospheric and Oceanic Technology*, *22*(7), 1080–1094. https://doi.org/10.1175/JTECH1747.1

Karimova, S. (2012). Spiral eddies in the Baltic, Black and Caspian seas as seen by satellite radar data. *Advances in Space Research*, *50*(8), 1107–1124. https://doi.org/10.1016/j.asr.2011.10.027

Karimova, S., and Gade, M. (2016). Improved statistics of sub-mesoscale eddies in the Baltic Sea retrieved from SAR imagery. *International Journal of Remote Sensing*, *37*(10), 2394–2414. https://doi.org/10.1080/01431161.2016.1145367

Kawai, Y., and Wada, A. (2007). Diurnal sea surface temperature variation and its impact on the atmosphere and ocean: A review. *Journal of Oceanography*, *63*(5), 721–744. https://doi.org/10.1007/s10872-007-0063-0

Khakpour, H. R. (2012). *Statistics and turbulent structures of passive scalar transport in free surface flows* (PhD Thesis). The Johns Hopkins University.

Khakpour, H. R., Shen, L., and Yue, D. K. P. (2011). Transport of passive scalar in turbulent shear flow under a clean or surfactant-contaminated free surface. *Journal of Fluid Mechanics*, *670*, 527–557. https://doi.org/DOI: 10.1017/S002211201000546X

Kingsford, M. J., and Choat, J. H. (1986). Influence of surface slicks on the distribution and onshore movements of small fish. *Marine Biology*, *91*(2), 161–171. https://doi.org/10.1007/BF00569432

Kljun, N., Calanca, P., Rotach, M. W., and Schmid, H. P. (2015). A simple two-dimensional parameterisation for Flux Footprint Prediction (FFP). *Geoscientific Model Development*, *8*(11), 3695–3713. https://doi.org/10.5194/gmd-8-3695-2015

Komori, S., Kurose, R., Takagaki, N., Ohtsubo, S., Iwano, K., Handa, K., and Shimada, S. (2011). Sensible and latent heat transfer across the air–water interface in wind-driven turbulence. In S. Komori, W. R. McGillis, and R. Kurose (Eds.), *Gas Transfer at Water Surfaces 2010*.

Kowalczuk, P., Tilstone, G. H., Zablocka, M., Röttgers, R., and Thomas, R. (2013). Composition of dissolved organic matter along an Atlantic Meridional Transect from fluorescence spectroscopy and Parallel Factor Analysis. *Marine Chemistry*. https://doi.org/10.1016/j.marchem.2013.10.004

Kudryavtsev, V., Akimov, D., Johannessen, J., and Chapron, B. (2005). On radar imaging of current features: 1. Model and comparison with observations. *Journal of Geophysical Research: Oceans*, *110*(C7). https://doi.org/10.1029/2004JC002505

Kujawinski, E. B., Farrington, J. W., and Moffett, J. W. (2002a). Evidence for grazing-mediated production of dissolved surface-active material by marine protists. *Marine Chemistry*, *77*(2), 133–142. https://doi.org/10.1016/S0304-4203(01)00082-2

Kujawinski, E. B., Farrington, J. W., and Moffett, J. W. (2002b). Evidence for grazing-mediated production of dissolved surface-active material by marine protists. *Marine Chemistry*, *77*(2), 133–142. https://doi.org/10.1016/S0304-4203(01)00082-2

Kurata, N., Vella, K., Hamilton, B., Shivji, M., Soloviev, A., Matt, S., et al. (2016a). Surfactant-associated bacteria in the near-surface layer of the ocean. *Scientific Reports*, *6*(1), 19123. https://doi.org/10.1038/srep19123

Kurata, N., Vella, K., Hamilton, B., Shivji, M., Soloviev, A., Matt, S., et al. (2016b). Surfactant-associated bacteria in the near-surface layer of the ocean. *Scientific Reports*, *6*(1), 19123. https://doi.org/10.1038/srep19123

Kurose, R., Takagaki, N., Kimura, A., and Komori, S. (2016). Direct numerical simulation of turbulent heat transfer across a sheared wind-driven gas-liquid interface. *Journal of Fluid Mechanics*, *804*, 646–687. https://doi.org/10.1017/jfm.2016.554

Kuznetsova, M., Lee, C., Aller, J., and Frew, N. (2004). Enrichment of amino acids in the sea surface microlayer at coastal and open ocean sites in the North Atlantic Ocean. *Limnology and Oceanography*, *49*(5), 1605–1619. https://doi.org/10.4319/lo.2004.49.5.1605

Lamb, H. (1895). The calming effect of oil on water waves. Hydrodynamics. *Cambridge University Press, Article*, *304*, 552–555.

Large, G., and Yeager, S. (2004). Diurnal to decadal global forcing for ocean and sea-ice models: The data sets and flux climatologies. https://doi.org/10.5065/D6KK98Q6

Large, W. G., and Pond, S. (1981). Open ocean momentum flux measurements in moderate to strong winds. *Journal of Physical Oceanography*, *11*(3), 324–336. https://doi.org/10.1175/1520-0485(1981)011<0324:OOMFMI>2.0.CO;2

Large, W. G., and Yeager, S. G. (2009). The global climatology of an interannually varying air–sea flux data set. *Climate Dynamics*, *33*(2), 341–364. https://doi.org/10.1007/s00382-008-0441-3

Laxague, N. J. M., Haus, B. K., Ortiz-Suslow, D. G., and Graber, H. C. (2018). Quantifying highly variable air-sea momentum flux using wavelet analysis. *Journal of Atmospheric and Oceanic Technology*, JTECH-D-18-0064.1. https://doi.org/10.1175/JTECH-D-18-0064.1

Leibovich, S. (1977). On the evolution of the system of wind drift currents and Langmuir circulation in the ocean. Part 1. Theory and averaged current. *Journal of Fluid Mechanics*, *79*(4), 715–743. https://doi.org/10.1017/S002211207700041X

Lemmin, U. (2020). Insights into the dynamics of the deep hypolimnion of Lake Geneva as revealed by long-term temperature, oxygen, and current measurements. *Limnology and Oceanography*, *65*(9), 2092–2107. https://doi.org/10.1002/lno.11441

Lemmin, U., and Amouroux, A. (2013). The influence of climate change on Lake Geneva. *Climatic Change and Global Warming of Inland Waters*, 201–217.

Lemmin, U., and D'Adamo, N. (1996a). Summertime winds and direct cyclonic circulation: Observations from Lake Geneva. *Annales Geophysicae*, *14*(11), 1207–1220. https://doi.org/10.1007/s00585-996-1207-z

Lemmin, U., and D'Adamo, N. (1996b). Summertime winds and direct cyclonic circulation: Observations from Lake Geneva. *Annales Geophysicae*, *14*(11), 1207–1220. https://doi.org/10.1007/s00585-996-1207-z

Levich, V. G. (1962). *Physicochemical hydrodynamics*. Prentice-Hall.

Li, Y., Wu, Y., Tang, J., Zhu, P., Gao, Z., and Yang, Y. (2023). Quantitative evaluation of wavelet analysis method for turbulent flux calculation of non-stationary series. *Geophysical Research Letters*, *50*(5), e2022GL101591. https://doi.org/10.1029/2022GL101591

Liardon, J.-L., and Barry, D. A. (2017a). Adaptable imaging package for remote vehicles. *HardwareX*, *2*, 1–12. https://doi.org/10.1016/j.ohx.2017.04.001

Liardon, J.-L., and Barry, D. A. (2017b). Adaptable imaging package for remote vehicles. *HardwareX*, *2*, 1–12. https://doi.org/10.1016/j.ohx.2017.04.001

Lieber, L., Füchtencordsjürgen, C., Hilder, R. L., Revering, P. J., Siekmann, I., Langrock, R., and Nimmo-Smith, W. A. M. (2023). Selective foraging behavior of seabirds in small-

scale slicks. *Limnology and Oceanography Letters*, *8*(2), 286–294. https://doi.org/10.1002/lol2.10289

Lim, L., Wurl, O., Karuppiah, S., and Obbard, J. P. (2007). Atmospheric wet deposition of PAHs to the sea-surface microlayer. *Marine Pollution Bulletin*, *54*(8), 1212–1219. https://doi.org/10.1016/j.marpolbul.2007.03.023

Liss, P. S. (1983a). Gas Transfer: Experiments and Geochemical Implications. In P. S. Liss and W. G. N. Slinn (Eds.), *Air-Sea Exchange of Gases and Particles* (pp. 241–298). Dordrecht: Springer Netherlands. https://doi.org/10.1007/978-94-009-7169-1_5

Liss, P. S. (1983b). Gas Transfer: Experiments and Geochemical Implications. In P. S. Liss and W. G. N. Slinn (Eds.), *Air-Sea Exchange of Gases and Particles* (pp. 241–298). Dordrecht: Springer Netherlands. https://doi.org/10.1007/978-94-009-7169-1_5

Liss, P. S., and Duce, R. A. (1997). *The sea surface and global change*. Cambridge, UK: Cambridge University Press.

Lucassen, J. (1968a). Longitudinal capillary waves. Part 1.—Theory. *Transactions of the Faraday Society*, *64*, 2221–2229.

Lucassen, J. (1968b). Longitudinal capillary waves. Part 2.—Experiments. *Transactions of the Faraday Society*, *64*, 2230–2235.

Lucassen-Reynders, E. H., and Lucassen, J. (1970). Properties of capillary waves. *Advances in Colloid and Interface Science*, *2*(4), 347–395. https://doi.org/10.1016/0001-8686(70)80001-X

Lükő, G., Torma, P., Weidinger, T., and Krámer, T. (2022). Air-lake momentum and heat exchange in very young waves using energy and water budget closure. *Journal of Geophysical Research: Atmospheres*, *127*(12), e2021JD036099. https://doi.org/10.1029/2021JD036099

MacIntyre, S., Amaral, J. H. F., and Melack, J. M. (2021a). Enhanced turbulence in the upper mixed layer under light winds and heating: implications for gas fluxes. *Journal of Geophysical Research: Oceans*, *126*(12), e2020JC017026. https://doi.org/10.1029/2020JC017026

MacIntyre, S., Bastviken, D., Arneborg, L., Crowe, A. T., Karlsson, J., Andersson, A., et al. (2021b). Turbulence in a small boreal lake: Consequences for air–water gas exchange. *Limnology and Oceanography*, *66*(3), 827–854. https://doi.org/10.1002/lno.11645

Mahadevan, A., and Tandon, A. (2006). An analysis of mechanisms for submesoscale vertical motion at ocean fronts. *Ocean Modelling*, *14*(3), 241–256. https://doi.org/10.1016/j.ocemod.2006.05.006

Mahrt, L., and Hristov, T. (2017). Is the influence of stability on the sea surface heat flux important? *Journal of Physical Oceanography*, *47*(3), 689–699. https://doi.org/10.1175/JPO-D-16-0228.1

Mahrt, L., and Khelif, D. (2010). Heat fluxes over weak SST heterogeneity. *Journal of Geophysical Research: Atmospheres*, *115*(D11103), D11103. https://doi.org/10.1029/2009JD013161

Mahrt, L., Nilsson, E., Rutgersson, A., and Pettersson, H. (2020). Sea-surface stress driven by small-scale non-stationary winds. *Boundary-Layer Meteorology*, *176*(1), 13–33. https://doi.org/10.1007/s10546-020-00518-9

Manikantan, H., and Squires, T. M. (2020). Surfactant dynamics: hidden variables controlling fluid flows. *Journal of Fluid Mechanics*, *892*, P1. https://doi.org/DOI: 10.1017/jfm.2020.170

Marmorino, G. O., and Smith, G. B. (2006a). Reduction of surface temperature in ocean slicks. *Geophysical Research Letters*, *33*(14), L14603. https://doi.org/10.1029/2006GL026502

Marmorino, G. O., and Smith, G. B. (2006b). Reduction of surface temperature in ocean slicks. *Geophysical Research Letters*, *33*(14), L14603. https://doi.org/10.1029/2006GL026502

Marmorino, G. O., Askari, F., and Mied, R. (2002). Observations of the creation and evolution of small-scale oceanic frontal cusps and slicks. *Journal of Marine Systems*, *37*(1), 17–29. https://doi.org/10.1016/S0924-7963(02)00193-8

Marmorino, G. O., Toporkov, J. V., Smith, G. B., Sletten, M. A., Perkovic, D., Frasier, S., and Judd, K. P. (2007). Ocean mixed-layer depth and current variation estimated from imagery of surfactant streaks. *IEEE Geoscience and Remote Sensing Letters*, *4*(3), 364–367. https://doi.org/10.1109/LGRS.2007.895702

Marmorino, G. O., Smith, G. B., Toporkov, J. V., Sletten, M. A., Perkovic, D., and Frasier, S. J. (2008a). Evolution of ocean slicks under a rising wind. *Journal of Geophysical Research*, *113*, C04030. https://doi.org/10.1029/2007JC004538

Marmorino, G. O., Smith, G. B., Toporkov, J. V, Sletten, M. A., Perkovic, D., and Frasier, S. J. (2008b). Evolution of ocean slicks under a rising wind. *Journal of Geophysical Research*, *113*, C04030. https://doi.org/10.1029/2007JC004538

Marmorino, G. O., Holt, B., Molemaker, M. J., DiGiacomo, P. M., and Sletten, M. A. (2010). Airborne synthetic aperture radar observations of "spiral eddy" slick patterns in the Southern California Bight. *Journal of Geophysical Research: Oceans*, *115*(C5). https://doi.org/10.1029/2009JC005863

Marshall, J., Adcroft, A., Hill, C., Perelman, L., and Heisey, C. (1997). A finite-volume, incompressible Navier Stokes model for studies of the ocean on parallel computers. *Journal of Geophysical Research: Oceans*, *102*(C3), 5753–5766. https://doi.org/10.1029/96JC02775

Masse, A. K., and Murthy, C. R. (1990). Observations of the Niagara River thermal plume (Lake Ontario, North America). *Journal of Geophysical Research: Oceans*, *95*(C9), 16097–16109. https://doi.org/10.1029/JC095iC09p16097

Matt, S., Fujimara, A., Soloviev, A., and Rhee, S. H. (2011). Modification of turbulence at the air-sea interface due to the presence of surfactants and implications for gas exchange. part ii: numerical simulations.

Mauder, M., Liebethal, C., Göckede, M., Leps, J.-P., Beyrich, F., and Foken, T. (2006). Processing and quality control of flux data during LITFASS-2003. *Boundary-Layer Meteorology*, *121*(1), 67–88. https://doi.org/10.1007/s10546-006-9094-0

Mauder, M., Foken, T., Aubinet, M., and Ibrom, A. (2021). Eddy-Covariance Measurements. In T. Foken (Ed.), *Springer Handbook of Atmospheric Measurements* (pp. 1485–1515). Cham: Springer International Publishing. https://doi.org/10.1007/978-3-030-52171-4_55

McKenna, S. P., and McGillis, W. R. (2004). The role of free-surface turbulence and surfactants in air–water gas transfer. *International Journal of Heat and Mass Transfer*, *47*(3), 539–553. https://doi.org/10.1016/j.ijheatmasstransfer.2003.06.001

McKinney, P., Holt, B., and Matsumoto, K. (2012). Small eddies observed in Lake Superior using SAR and sea surface temperature imagery. *Journal of Great Lakes Research*, *38*(4), 786–797. https://doi.org/10.1016/j.jglr.2012.09.023

McWilliams, J. C. (2016). Submesoscale currents in the ocean. *Proceedings of the Royal Society A: Mathematical, Physical and Engineering Science*, *472*(2189), 20160117. https://doi.org/10.1098/rspa.2016.0117

McWilliams, J. C. (2017). Submesoscale surface fronts and filaments: Secondary circulation, buoyancy flux, and frontogenesis. *Journal of Fluid Mechanics*, *823*, 391–432. https://doi.org/10.1017/jfm.2017.294

McWilliams, J. C. (2019). A survey of submesoscale currents. *Geoscience Letters*, *6*(1), 3. https://doi.org/10.1186/s40562-019-0133-3

McWilliams, J. C. (2021). Oceanic frontogenesis. *Annual Review of Marine Science*, *13*(1), 227–253. https://doi.org/10.1146/annurev-marine-032320-120725

McWilliams, J. C., Colas, F., and Molemaker, M. J. (2009). Cold filamentary intensification and oceanic surface convergence lines. *Geophysical Research Letters*, *36*(18). https://doi.org/10.1029/2009GL039402

Mer, V. (1962). Retardation of evaporation by monolayers: transport processes. *New York/London*.

Meyers, T. P., and Dale, R. F. (1983). Predicting daily insolation with hourly cloud height and coverage. *Journal of Applied Meteorology and Climatology*, *22*(4), 537–545. https://doi.org/10.1175/1520-0450(1983)022<0537:PDIWHC>2.0.CO;2

van der Mheen, M., Pattiaratchi, C., Cosoli, S., and Wandres, M. (2020). Depth-dependent correction for wind-driven drift current in particle tracking applications. *Frontiers in Marine Science*, *7*. Retrieved from https://www.frontiersin.org/articles/10.3389/fmars.2020.00305

Milinković, A., Penezić, A., Kušan, A. C., Gluščić, V., Žužul, S., Skejić, S., et al. (2022). Variabilities of biochemical properties of the sea surface microlayer: Insights to the atmospheric deposition impacts. *Science of The Total Environment*, *838*, 156440. https://doi.org/10.1016/j.scitotenv.2022.156440

Minaudo, C., Odermatt, D., Bouffard, D., Rahaghi, A. I., Lavanchy, S., and Wüest, A. (2021). The Imprint of Primary Production on High-Frequency Profiles of Lake Optical Properties. *Environmental Science & Technology*, *55*(20), 14234–14244. https://doi.org/10.1021/acs.est.1c02585

Monin, A. S., and Obukhov, A. M. (1954). Basic laws of turbulent mixing in the surface layer of the atmosphere. *Transactions of the USSR Academy of Sciences, Geophysical Series*. Retrieved from http://www.mcnaughty.com/keith/papers/Monin_and_Obukhov_1954.pdf

Murphy, K. R., Stedmon, C. A., Waite, T. D., and Ruiz, G. M. (2008). Distinguishing between terrestrial and autochthonous organic matter sources in marine environments using fluorescence spectroscopy. *Marine Chemistry*, *108*(1–2), 40–58. https://doi.org/10.1016/j.marchem.2007.10.003

Mustaffa, N. I. H., Ribas-Ribas, M., Banko-Kubis, H. M., and Wurl, O. (2020). Global reduction of in situ CO2 transfer velocity by natural surfactants in the sea-surface microlayer. *Proceedings of the Royal Society A: Mathematical, Physical and Engineering Sciences*, *476*(2234), 20190763. https://doi.org/10.1098/rspa.2019.0763

Nakajima, R., Tsuchiya, K., Nakatomi, N., Yoshida, T., Tada, Y., Konno, F., et al. (2013). Enrichment of microbial abundance in the sea-surface microlayer over a coral reef: implications for biogeochemical cycles in reef ecosystems. *Marine Ecology Progress Series*, *490*, 11–22. https://doi.org/10.3354/meps10481

Naumenko, M. A., Guzivaty, V. V., and Karetnikov, S. G. (2012). Variability of the horizontal gradients of the air and the water surface temperatures in the vernal frontal zone period of Lake Ladoga. *Oceanology*, *52*(6), 735–740. https://doi.org/10.1134/S0001437012060082

Obernosterer, I., Catala, P., Lami, R., Caparros, J., Ras, J., Bricaud, A., et al. (2008). Biochemical characteristics and bacterial community structure of the sea surface microlayer in the South Pacific Ocean. *Biogeosciences*, *5*(3), 693–705. https://doi.org/10.5194/bg-5-693-2008

O'Donnell, J., Marmorino, G. O., and Trump, C. L. (1998). Convergence and downwelling at a river plume front. *Journal of Physical Oceanography*, *28*(7), 1481–1495. https://doi.org/10.1175/1520-0485(1998)028<1481:CADAAR>2.0.CO;2

Oesch, D., Jaquet, J. -M., Klaus, R., and Schenker, P. (2008). Multi-scale thermal pattern monitoring of a large lake (Lake Geneva) using a multi-sensor approach. *International Journal of Remote Sensing*, *29*(20), 5785–5808. https://doi.org/10.1080/01431160802132786

Oesch, D. C., Jaquet, J.-M., Hauser, A., and Wunderle, S. (2005). Lake surface water temperature retrieval using advanced very high resolution radiometer and Moderate Resolution Imaging Spectroradiometer data: Validation and feasibility study. *Journal of Geophysical Research: Oceans*, *110*(C12). https://doi.org/10.1029/2004JC002857

Olesen, B., and Maberly, S. (2001). The effect of high levels of visible and ultra-violet radiation on the photosynthesis of phytoplankton from a freshwater lake. *Archiv Fur Hydrobiologie*, *151*, 301–315.

Ory, N. C., Gallardo, C., Lenz, M., and Thiel, M. (2018). Capture, swallowing, and egestion of microplastics by a planktivorous juvenile fish. *Environmental Pollution*, *240*, 566–573. https://doi.org/10.1016/j.envpol.2018.04.093

Parks, G., Dean, C. W., Kluge, J. A., Soloviev, A. V., Shivji, M., Tartar, A., et al. (2020). Analysis of surfactant-associated bacteria in the sea surface microlayer using deoxyribonucleic acid sequencing and synthetic aperture radar. *International Journal of Remote Sensing*, *41*(10), 3886–3901. https://doi.org/10.1080/01431161.2019.1708508

Penezić, A., Drozdowska, V., Novak, T., and Gašparović, B. (2022). Distribution and characterization of organic matter within the sea surface microlayer in the Gulf of Gdańsk. *Oceanologia*, *64*(4), 631–650. https://doi.org/10.1016/j.oceano.2022.05.003

Pereira, R., Ashton, I., Sabbaghzadeh, B., Shutler, J. D., and Upstill-Goddard, R. C. (2018a). Reduced air-sea CO_2 exchange in the Atlantic Ocean due to biological surfactants. *Nature Geoscience*, *11*(7), 492–496. https://doi.org/10.1038/s41561-018-0136-2

Pereira, R., Ashton, I., Sabbaghzadeh, B., Shutler, J. D., and Upstill-Goddard, R. C. (2018b). Reduced air–sea CO2 exchange in the Atlantic Ocean due to biological surfactants. *Nature Geoscience*, *11*(7), 492–496. https://doi.org/10.1038/s41561-018-0136-2

Phillips, O. M. (1984). On the response of short ocean wave components at a fixed wavenumber to ocean current variations. *Journal of Physical Oceanography*, *14*(9), 1425–1433. https://doi.org/10.1175/1520-0485(1984)014<1425:OTROSO>2.0.CO;2

Pogorzelski, S. J., Kogut, A. D., and Mazurek, A. Z. (2006). Surface rheology parameters of source-specific surfactant films as indicators of organic matter dynamics. In *Hydrobiologia* (Vol. 554, pp. 67–81). https://doi.org/10.1007/s10750-005-1007-6

Price, J. F., Weller, R. A., and Pinkel, R. (1986). Diurnal cycling: Observations and models of the upper ocean response to diurnal heating, cooling, and wind mixing. *Journal of Geophysical Research*, *91(C7)*, 8411–8427. https://doi.org/10.1029/JC091iC07p08411

Prytherch, J., and Yelland, M. J. (2021). Wind, convection and fetch dependence of gas transfer velocity in an Arctic sea-ice lead determined from eddy covariance CO 2 flux measurements. *Global Biogeochemical Cycles*. https://doi.org/10.1029/2020gb006633

Qiao, F., Yuan, Y., Deng, J., Dai, D., and Song, Z. (2016). Wave–turbulence interaction-induced vertical mixing and its effects in ocean and climate models. *Philosophical Transactions of the Royal Society A: Mathematical, Physical and Engineering Sciences*, *374*(2065), 20150201. https://doi.org/10.1098/rsta.2015.0201

Rahaghi, A. I., Lemmin, U., Cimatoribus, A. A., Bouffard, D., Riffler, M., Wunderle, S., and Barry, D. A. (2018). Improving surface heat flux estimation for a large lake through model optimization and two-point calibration: The case of Lake Geneva. *Limnology and Oceanography: Methods*, *16*(9), 576–593. https://doi.org/10.1002/lom3.10267

Rahaghi, A. I., Lemmin, U., Sage, D., and Barry, D. A. (2019a). Achieving high-resolution thermal imagery in low-contrast lake surface waters by aerial remote sensing and image registration. *Remote Sensing of Environment*, *221*, 773–783. https://doi.org/10.1016/j.rse.2018.12.018

Rahaghi, A. I., Lemmin, U., Sage, D., and Barry, D. A. (2019b). Achieving high-resolution thermal imagery in low-contrast lake surface waters by aerial remote sensing and image registration. *Remote Sensing of Environment*, *221*, 773–783. https://doi.org/10.1016/j.rse.2018.12.018

Rahaghi, A. I., Lemmin, U., and Barry, D. A. (2019c). Surface water temperature heterogeneity at subpixel satellite scales and its effect on the surface cooling estimates of a large lake: Airborne remote sensing results from Lake Geneva. *Journal of Geophysical Research: Oceans*, *124*(1), 635–651. https://doi.org/10.1029/2018JC014451

Rahaghi, A. I., Lemmin, U., and Barry, D. A. (2019d). Surface water temperature heterogeneity at subpixel satellite scales and its effect on the surface cooling estimates of a large lake:

Airborne remote sensing results from Lake Geneva. *Journal of Geophysical Research: Oceans*, *124*(1), 635–651. https://doi.org/10.1029/2018JC014451

Rahaghi, A. I., Lemmin, U., Cimatoribus, A. A., and Barry, D. A. (2019e). The importance of systematic spatial variability in the surface heat flux of a large lake: A multiannual analysis for Lake Geneva. *Water Resources Research*, *55*(12), 10248–10267. https://doi.org/10.1029/2019WR024954

Rascle, N., Molemaker, J., Marié, L., Nouguier, F., Chapron, B., Lund, B., and Mouche, A. (2017). Intense deformation field at oceanic front inferred from directional sea surface roughness observations. *Geophysical Research Letters*, *44*(11), 5599–5608. https://doi.org/10.1002/2017GL073473

Rascle, N., Chapron, B., Molemaker, J., Nouguier, F., Ocampo-Torres, F. J., Osuna Cañedo, J. P., et al. (2020). Monitoring intense oceanic fronts using sea surface roughness: Satellite, airplane, and in situ comparison. *Journal of Geophysical Research: Oceans*, *125*(8), e2019JC015704. https://doi.org/10.1029/2019JC015704

Razmi, A. M., Barry, D. A., Bouffard, D., Vennemann, T., Barry, C. E., and Lemmin, U. (2018). Currents of Lake Geneva. In N. Chèvre, D. A. Barry, F. Bonvin, N. Graham, J.-L. Loizeau, H.-R. Pfeifer, et al. (Eds.), *Micropollutants in Large Lakes: From Potential Pollution to Risk Assessments* (pp. 141–172). Lausanne, Switzerland: EPFL Press. Retrieved from https://doi.org/10.1201/9781351240291

Reiss, R. S., Lemmin, U., Cimatoribus, A. A., and Barry, D. A. (2020). Wintertime coastal upwelling in Lake Geneva: An efficient transport process for deepwater renewal in a large, deep lake. *Journal of Geophysical Research: Oceans*, *125*(8), e2020JC016095. https://doi.org/10.1029/2020JC016095

Ribas-Ribas, M., Hamizah Mustaffa, N. I., Rahlff, J., Stolle, C., and Wurl, O. (2017). Sea Surface Scanner (S3): A Catamaran for High-Resolution Measurements of Biogeochemical Properties of the Sea Surface Microlayer. *Journal of Atmospheric and Oceanic Technology*, *34*(7), 1433–1448. https://doi.org/10.1175/JTECH-D-17-0017.1

Rickard, P. C., Uher, G., Upstill-Goddard, R. C., Frka, S., Mustaffa, N. I. H., Banko-Kubis, H. M., et al. (2019). Reconsideration of seawater surfactant activity analysis based on an inter-laboratory comparison study. *Marine Chemistry*, *208*, 103–111. https://doi.org/10.1016/j.marchem.2018.11.012

Riffler, M., Lieberherr, G., and Wunderle, S. (2015). Lake surface water temperatures of European Alpine lakes (1989–2013) based on the Advanced Very High Resolution Radiometer (AVHRR) 1 km data set. *Earth System Science Data*, *7*(1), 1–17. https://doi.org/10.5194/essd-7-1-2015

Robinson, I. (1997). Remote sensing of the sea-surface microlayer. In P. S. Liss and R. A. Duce (Eds.), *The Sea Surface and Global Change* (pp. 471–508). Cambridge: Cambridge University Press. https://doi.org/10.1017/CBO9780511525025.017

Romano, J. C. (1996). Sea-surface slick occurrence in the open sea (Mediterranean, Red Sea, Indian Ocean) in relation to wind speed. *Deep Sea Research Part I: Oceanographic Research Papers*, *43*(4), 411–423. https://doi.org/10.1016/0967-0637(96)00024-6

Romano, J. C., and Garabetian, F. (1996). Photographic records of sea-surface microlayers as a survey of pollution daily rhythm in coastal waters. *Marine Environmental Research*, *41*(3), 265–279. https://doi.org/10.1016/0141-1136(95)00019-4

Ryan, J. P., Fischer, A. M., Kudela, R. M., McManus, M. A., Myers, J. S., Paduan, J. D., et al. (2010). Recurrent frontal slicks of a coastal ocean upwelling shadow. *Journal of Geophysical Research: Oceans*, *115*(C12). https://doi.org/10.1029/2010JC006398

Sabbaghzadeh, B. (2018). *Surfactants and chromophoric dissolved organic matter (CDOM) in the Atlantic Ocean surface microlayer and the corresponding underlying waters* (PhD Thesis). Newcastle University.

Sabbaghzadeh, B., Upstill-Goddard, R. C., Beale, R., Pereira, R., and Nightingale, P. D. (2017). The Atlantic Ocean surface microlayer from 50°N to 50°S is ubiquitously enriched in surfactants at wind speeds up to 13 m s−1. *Geophysical Research Letters*. https://doi.org/10.1002/2017GL072988

Salter, M. E. (2010). *A Role for Natural Surfactants in Air-Sea Gas Exchange?* (Doctoral dissertation). University of Newcastle upon Tyne., Newcastle upon Tyne UK.

Salter, M. E., Upstill-Goddard, R. C., Nightingale, P. D., Archer, S. D., Blomquist, B., Ho, D. T., et al. (2011). Impact of an artificial surfactant release on air-sea gas fluxes during Deep Ocean Gas Exchange Experiment II. *Journal of Geophysical Research: Oceans*, *116*(C11).

Sarpkaya, T. (1996). Vorticity, free surface, and surfactants. *Annual Review of Fluid Mechanics*, *28*(1), 83–128. https://doi.org/10.1146/annurev.fl.28.010196.000503

Savelyev, I. B., Buckley, M. P., and Haus, B. K. (2020). The impact of nonbreaking waves on wind-driven ocean surface turbulence. *Journal of Geophysical Research: Oceans*, *125*(1), e2019JC015573. https://doi.org/10.1029/2019JC015573

Saylor, J. R., Smith, G. B., and Flack, K. A. (2001). An experimental investigation of the surface temperature field during evaporative convection. *Physics of Fluids*, *13*(2), 428–439. https://doi.org/10.1063/1.1337064

Schaller, C., Göckede, M., and Foken, T. (2017). Flux calculation of short turbulent events – comparison of three methods. *Atmos. Meas. Tech.*, *10*(3), 869–880. https://doi.org/10.5194/amt-10-869-2017

Schmidt, R., and Schneider, B. (2011). The effect of surface films on the air–sea gas exchange in the Baltic Sea. *Marine Chemistry*, *126*(1), 56–62. https://doi.org/10.1016/j.marchem.2011.03.007

Schotanus, P., Nieuwstadt, F. T. M., and De Bruin, H. A. R. (1983). Temperature measurement with a sonic anemometer and its application to heat and moisture fluxes. *Boundary-Layer Meteorology*, *26*(1), 81–93. https://doi.org/10.1007/BF00164332

Schuler, D. L., and Lee, J. S. (2006). Mapping ocean surface features using biogenic slick-fields and SAR polarimetric decomposition techniques. *IEEE Proceedings - Radar, Sonar and Navigation*, *153*(3), 260–270. https://doi.org/10.1049/ip-rsn:20045118

Scott, J. C. (1978). The historical development of theories of wave-calming using oil. In H. Rupert and S. Norman (Eds.), *History of Technology* (Vol. 3, pp. 163–186). University of Essex, Fluid Mechanics Research Institute.

Scully-Power, P. (1986). *Navy oceanographer shuttle observations: STS 41-G mission report* (Vol. 7611). Naval Underwater Systems Center.

Shao, M., Ortiz-Suslow, D. G., Haus, B. K., Lund, B., Williams, N. J., Özgökmen, T. M., et al. (2019). The variability of winds and fluxes observed near submesoscale fronts. *Journal of Geophysical Research: Oceans*, *124*(11), 7756–7780. https://doi.org/10.1029/2019JC015236

Shcherbina, A. Y., D'Asaro, E. A., Lee, C. M., Klymak, J. M., Molemaker, M. J., and McWilliams, J. C. (2013). Statistics of vertical vorticity, divergence, and strain in a developed submesoscale turbulence field. *Geophysical Research Letters*, *40*(17), 4706–4711. https://doi.org/10.1002/grl.50919

Shen, H., Perrie, W., and Wu, Y. (2019). Wind drag in oil spilled ocean surface and its impact on wind-driven circulation. *Anthropocene Coasts*, *2*(1), 244–260. https://doi.org/10.1139/anc-2018-0019

Shen, L., Yue, D. K. P., and Triantafyllou, G. S. (2004). Effect of surfactants on free-surface turbulent flows. *Journal of Fluid Mechanics*, *506*(506), 79–115. https://doi.org/10.1017/S0022112004008481

Smith, S. D. (1988). Coefficients for sea surface wind stress, heat flux, and wind profiles as a function of wind speed and temperature. *Journal of Geophysical Research: Oceans*, *93*(C12), 15467–15472. https://doi.org/10.1029/JC093iC12p15467

Soulignac, F., Lemmin, U., Ziabari, S. M. H., Wynn, H. K., Graf, B., and Barry, D. A. (2021). Rapid changes in river plume dynamics caused by advected wind-driven coastal upwelling as observed in Lake Geneva. *Limnology and Oceanography*, *66*(8), 3116–3133. https://doi.org/10.1002/lno.11864

Stedmon, C. A., and Bro, R. (2008a). Characterizing dissolved organic matter fluorescence with parallel factor analysis: A tutorial. *Limnology and Oceanography: Methods*, *6*(11), 572–579. https://doi.org/10.4319/lom.2008.6.572

Stedmon, C. A., and Bro, R. (2008b). Characterizing dissolved organic matter fluorescence with parallel factor analysis: A tutorial. *Limnology and Oceanography: Methods*, *6*(11), 572–579. https://doi.org/10.4319/lom.2008.6.572

Stolle, C., Nagel, K., Labrenz, M., and Jürgens, K. (2010). Succession of the sea-surface microlayer in the coastal Baltic Sea under natural and experimentally induced low-wind conditions. *Biogeosciences*, *7*(9), 2975–2988. https://doi.org/10.5194/bg-7-2975-2010

Su, Z., Wang, J., Klein, P., Thompson, A. F., and Menemenlis, D. (2018). Ocean submesoscales as a key component of the global heat budget. *Nature Communications*, *9*(1), 775. https://doi.org/10.1038/s41467-018-02983-w

Sun, Y., Ruf, C., Bakker, T., and Pan, Y. (2021). Effects of microplastics and surfactants on surface roughness of water waves. *ArXiv:2111.07021 [Physics]*. Retrieved from http://arxiv.org/abs/2111.07021

Taylor, J. D., and Cunliffe, M. (2014). High-throughput sequencing reveals neustonic and planktonic microbial eukaryote diversity in coastal waters. *Journal of Phycology*, *50*(5), 960–965. https://doi.org/10.1111/jpy.12228

Taylor, J. D., and Cunliffe, M. (2016). Multi-year assessment of coastal planktonic fungi reveals environmental drivers of diversity and abundance. *The ISME Journal*, *10*(9), 2118–2128. https://doi.org/10.1038/ismej.2016.24

Taylor, P. K., and Yelland, M. J. (2001). The dependence of sea surface roughness on the height and steepness of the waves. *Journal of Physical Oceanography*, *31*(2), 572–590. https://doi.org/10.1175/1520-0485(2001)031<0572:TDOSSR>2.0.CO;2

Tejada-Martínez, A. E., Hafsi, A., Akan, C., Juha, M., and Veron, F. (2020). Large-eddy simulation of small-scale Langmuir circulation and scalar transport. *Journal of Fluid Mechanics*, *885*, A5. https://doi.org/DOI: 10.1017/jfm.2019.802

Thompson, E. J., Moum, J. N., Fairall, C. W., and Rutledge, S. A. (2019). Wind limits on rain layers and diurnal warm layers. *Journal of Geophysical Research: Oceans*, *124*(2), 897–924. https://doi.org/10.1029/2018JC014130

Tilstone, G. H., Airs, R. L., Vicente, V. M., Widdicombe, C., and Llewellyn, C. (2010). High concentrations of mycosporine-like amino acids and colored dissolved organic matter in the sea surface microlayer off the Iberian Peninsula. *Limnology and Oceanography*, *55*(5), 1835–1850. https://doi.org/10.4319/lo.2010.55.5.1835

Torrence, C., and Compo, G. P. (1998). A Practical Guide to Wavelet Analysis. *Bulletin of the American Meteorological Society*, *79*(1), 61–78. https://doi.org/10.1175/1520-0477(1998)079<0061:APGTWA>2.0.CO;2

Torres, R., Shutler, J., Artioli, Y., Kitidis, V., Ciavatta, S., Ruiz-Villarreal, M., et al. (2020). Sensitivity of modeled CO_2 air–sea flux in a coastal environment to surface temperature gradients, surfactants, and satellite data assimilation. *Remote Sensing*, *12*(12), 2038. https://doi.org/10.3390/rs12122038

Tsai, W., and Liu, K.-K. (2003). An assessment of the effect of sea surface surfactant on global atmosphere-ocean CO_2 flux. *Journal of Geophysical Research*, *108(C4)*(C4), 3127. https://doi.org/10.1029/2000JC000740

Tsai, W. T. (1996a). Impact of a surfactant on a turbulent shear layer under the air-sea interface. *Journal of Geophysical Research: Oceans*, *101*(C12), 28557–28568. https://doi.org/10.1029/96JC02802

Tsai, W. T. (1996b). Impact of a surfactant on a turbulent shear layer under the air-sea interface. *Journal of Geophysical Research: Oceans*, *101*(C12), 28557–28568. https://doi.org/10.1029/96JC02802

Tsai, W.-T., and Yue, D. K. P. (1995). Effects of soluble and insoluble surfactant on laminar interactions of vortical flows with a free surface. *Journal of Fluid Mechanics*, *289*, 315–349. https://doi.org/10.1017/S0022112095001352

Upstill-Goddard, R. C., Frost, T., Henry, G. R., Franklin, M., Murrell, J. C., and Owens, N. J. P. (2003). Bacterioneuston control of air-water methane exchange determined with a laboratory gas exchange tank. *Global Biogeochemical Cycles*, *17*(4). https://doi.org/10.1029/2003GB002043

Vanderplow, B., Soloviev, A. V., Dean, C. W., Haus, B. K., Lukas, R., Sami, M., and Ginis, I. (2020). Potential effect of bio-surfactants on sea spray generation in tropical cyclone conditions. *Scientific Reports*, *10*(1), 19057. https://doi.org/10.1038/s41598-020-76226-8

Vercauteren, N., Bou-Zeid, E., Parlange, M. B., Lemmin, U., Huwald, H., Selker, J., and Meneveau, C. (2008). Subgrid-scale dynamics of water vapour, heat, and momentum over a lake. *Boundary-Layer Meteorology*, *128*(2), 205–228. https://doi.org/10.1007/s10546-008-9287-9

Vercauteren, N., Bou-Zeid, E., Huwald, H., Parlange, M. B., and Brutsaert, W. (2009). Estimation of wet surface evaporation from sensible heat flux measurements. *Water Resources Research*, *45*(6). https://doi.org/10.1029/2008WR007544

Vercauteren, N., Huwald, H., Bou-Zeid, E., Selker, J. S., Lemmin, U., Parlange, M. B., and Lunati, I. (2011). Evolution of superficial lake water temperature profile under diurnal radiative forcing. *Water Resources Research*, *47*(9). https://doi.org/10.1029/2011WR010529

Veron, F., and Melville, W. K. (2001). Experiments on the stability and transition of wind-driven water surfaces. *Journal of Fluid Mechanics*, *446*, 25–65. https://doi.org/10.1017/S0022112001005638

Voskuhl, L., and Rahlff, J. (2022). Natural and oil surface slicks as microbial habitats in marine systems: A mini review. *Frontiers in Marine Science*, *9*. Retrieved from https://www.frontiersin.org/articles/10.3389/fmars.2022.1020843

Voudouri, A., Avgoustoglou, E., and Kaufmann, P. (2017). Impacts of observational data assimilation on operational forecasts. In T. Karacostas, A. Bais, and P. T. Nastos (Eds.), *Perspectives on Atmospheric Sciences* (pp. 143–149). Cham: Springer International Publishing. https://doi.org/10.1007/978-3-319-35095-0_21

Wagner, T. J. W., Eisenman, I., Ceroli, A. M., and Constantinou, N. C. (2022). How Winds and Ocean Currents Influence the Drift of Floating Objects. *Journal of Physical Oceanography*, *52*(5), 907–916. https://doi.org/10.1175/JPO-D-20-0275.1

Wang, C., Fei, J., Ding, J., Hu, R., Huang, X., and Cheng, X. (2017). Development of a new significant wave height and dominant wave period parameterization scheme. *Ocean Engineering*, *135*, 170–182. https://doi.org/10.1016/j.oceaneng.2017.02.017

Wang, T., Barkan, R., McWilliams, J. C., and Molemaker, M. J. (2021). Structure of submesoscale fronts of the Mississippi River plume. *Journal of Physical Oceanography*, *51*(4), 1113–1131. https://doi.org/10.1175/JPO-D-20-0191.1

Ward, B. (2006). Near-surface ocean temperature. *Journal of Geophysical Research: Oceans*, *111*(2), C02004. https://doi.org/10.1029/2004JC002689

Watson, A. J., Bock, E. J., Jähne, B., Asher, W. E., Frew, N. M., Hasse, L., et al. (1997). Report Group 1 – Physical processes in the microlayer and the air–sea exchange of trace gases. In P. S. Liss and R. A. Duce (Eds.), *The Sea Surface and Global Change* (pp. 1–34). Cambridge: Cambridge University Press. https://doi.org/10.1017/CBO9780511525025.002

Webb, E. K., Pearman, G. I., and Leuning, R. (1980). Correction of flux measurements for density effects due to heat and water vapour transfer. *Quarterly Journal of the Royal Meteorological Society*. https://doi.org/10.1002/qj.49710644707

Wei, Y., and Wu, J. (1992). In situ measurements of surface tension, wave damping, and wind properties modified by natural films. *Journal of Geophysical Research: Oceans*, *97*(C4), 5307–5313. https://doi.org/10.1029/91JC02820

Wei, Z., Miyano, A., and Sugita, M. (2016). Drag and bulk transfer coefficients over water surfaces in light winds. *Boundary-Layer Meteorology*, *160*(2), 319–346. https://doi.org/10.1007/s10546-016-0147-8

Weidberg, N., Lobón, C., López, E., Flórez, L. G., Rueda, M. del P. F., Largier, J. L., and Acuña, J. L. (2014). Effect of nearshore surface slicks on meroplankton distribution: role of larval behaviour. *Marine Ecology Progress Series*, *506*, 15–30. https://doi.org/10.3354/meps10777

Whitney, J. L., Gove, J. M., McManus, M. A., Smith, K. A., Lecky, J., Neubauer, P., et al. (2021). Surface slicks are pelagic nurseries for diverse ocean fauna. *Scientific Reports*, *11*(1), 3197. https://doi.org/10.1038/s41598-021-81407-0

Wolfbeis, O. S. (1985). The fluorescence of organic natural products. In S. G. Schulman (Ed.), *Molecular Luminescence Spectroscopy. Part I: Methods and Applications* (pp. 167–370). New York, NY: Wiley. Retrieved from https://ci.nii.ac.jp/naid/10010161945/

Woolway, R. I., Jones, D., Feuchtmayr, H., and Maberly, S. C. (2015). A comparison of the diel variability in epilimnetic temperature for five lakes in the English Lake District. *Inland Waters*, *5*(2), 139–154. https://doi.org/10.5268/IW-5.2.748

Woolway, R. I., Verburg, P., Lenters, J. D., Merchant, C. J., Hamilton, D. P., Brookes, J., et al. (2018). Geographic and temporal variations in turbulent heat loss from lakes: A global analysis across 45 lakes. *Limnology and Oceanography*, *63*(6), 2436–2449. https://doi.org/10.1002/lno.10950

Wu, J. (1994). The sea surface is aerodynamically rough even under light winds. *Boundary-Layer Meteorology*, *69*(1), 149–158. https://doi.org/10.1007/BF00713300

Wu, X., Noss, C., Liu, L., and Lorke, A. (2019). Effects of small-scale turbulence at the air-water interface on microcystis surface scum formation. *Water Research*, *167*, 115091. https://doi.org/10.1016/j.watres.2019.115091

Wüest, A., Bouffard, D., Guillard, J., Ibelings, B. W., Lavanchy, S., Perga, M.-E., and Pasche, N. (2021). LéXPLORE: A floating laboratory on Lake Geneva offering unique lake research opportunities. *WIREs Water*, *8*(5), e1544. https://doi.org/10.1002/wat2.1544

Wurl, O., and Holmes, M. (2008). The gelatinous nature of the sea-surface microlayer. *Marine Chemistry*, *110*(1), 89–97. https://doi.org/10.1016/j.marchem.2008.02.009

Wurl, O., and Obbard, J. P. (2004). A review of pollutants in the sea-surface microlayer (SML): a unique habitat for marine organisms. *Marine Pollution Bulletin*, *48*(11), 1016–1030. https://doi.org/10.1016/j.marpolbul.2004.03.016

Wurl, O., Wurl, E., Miller, L., Johnson, K., and Vagle, S. (2011). Formation and global distribution of sea-surface microlayers. *Biogeosciences*, *8*(1), 121–135. https://doi.org/10.5194/bg-8-121-2011

Wurl, O., Stolle, C., Van Thuoc, C., The Thu, P., and Mari, X. (2016). Biofilm-like properties of the sea surface and predicted effects on air-sea CO_2 exchange. *Progress in Oceanography*, *144*, 15–24. https://doi.org/10.1016/j.pocean.2016.03.002

Wurl, O., Bird, K., Cunliffe, M., Landing, W. M., Miller, U., Mustaffa, N. I. H., et al. (2018a). Warming and inhibition of salinization at the ocean's surface by cyanobacteria. *Geophysical Research Letters*, *45*(9), 4230–4237. https://doi.org/10.1029/2018GL077946

Wurl, O., Bird, K., Cunliffe, M., Landing, W. M., Miller, U., Mustaffa, N. I. H., et al. (2018b). Warming and inhibition of salinization at the ocean's surface by cyanobacteria. *Geophysical Research Letters*, *45*(9), 4230–4237. https://doi.org/10.1029/2018GL077946

Xue, P., Schwab, D. J., and Hu, S. (2015). An investigation of the thermal response to meteorological forcing in a hydrodynamic model of Lake Superior. *Journal of Geophysical Research: Oceans*, *120*(7), 5233–5253. https://doi.org/10.1002/2015JC010740

Yang, M., Smyth, T. J., Kitidis, V., Brown, I. J., Wohl, C., Yelland, M. J., and Bell, T. G. (2021). Natural variability in air–sea gas transfer efficiency of CO2. *Scientific Reports*, *11*(1), 13584. https://doi.org/10.1038/s41598-021-92947-w

Yelland, M., and Taylor, P. K. (1996). Wind Stress Measurements from the Open Ocean. *Journal of Physical Oceanography*, *26*(4), 541–558. https://doi.org/10.1175/1520-0485(1996)026<0541:WSMFTO>2.0.CO;2

Yelland, M. J., Moat, B. I., Taylor, P. K., Pascal, R. W., Hutchings, J., and Cornell, V. C. (1998). Wind Stress Measurements from the Open Ocean Corrected for Airflow Distortion by the Ship. *Journal of Physical Oceanography*, *28*(7), 1511–1526. https://doi.org/10.1175/1520-0485(1998)028<1511:WSMFTO>2.0.CO;2

Yusup, Y., and Liu, H. (2016). Effects of atmospheric surface layer stability on turbulent fluxes of heat and water vapor across the water–atmosphere interface. *Journal of Hydrometeorology*, *17*(11), 2835–2851. https://doi.org/10.1175/JHM-D-16-0042.1

Zaitsev, Y. (1997). Neuston of seas and oceans. In P. S. Liss and R. A. Duce (Eds.), *The Sea Surface and Global Change* (pp. 371–382). Cambridge: Cambridge University Press. https://doi.org/10.1017/CBO9780511525025.013

Zappa, C. J., Laxague, N. J. M., Brumer, S. E., and Anderson, S. P. (2019). The impact of wind gusts on the ocean thermal skin layer. *Geophysical Research Letters*, *46*(20), 11301–11309. https://doi.org/10.1029/2019gl083687

Zeng, X., and Beljaars, A. (2005). A prognostic scheme of sea surface skin temperature for modeling and data assimilation. *Geophysical Research Letters*, *32*(14). https://doi.org/10.1029/2005GL023030

Zeng, X., Zhao, M., and Dickinson, R. E. (1998). Intercomparison of bulk aerodynamic algorithms for the computation of sea surface fluxes using TOGA COARE and TAO data. *Journal of Climate*, *11*(10), 2628–2644. https://doi.org/10.1175/1520-0442(1998)011<2628:IOBAAF>2.0.CO;2

Zhang, Z., Liu, L., Wu, Z., Li, J., and Ding, H. (1998). Physicochemical Studies of the Sea Surface Microlayer: I. Thickness of the Sea Surface Microlayer and Its Experimental Determination. *Journal of Colloid and Interface Science*, *204*(2), 294–299. https://doi.org/10.1006/jcis.1998.5538

Zhang, Z., Liu, L., Liu, C., and Cai, W. (2003). Studies on the sea surface microlayer: II. The layer of sudden change of physical and chemical properties. *Journal of Colloid and Interface Science*, *264*(1), 148–159. https://doi.org/10.1016/S0021-9797(03)00390-4

Ziemer, F. (2008). Wave and current observations in european waters by ground-based X-band radar. In V. Barale and M. Gade (Eds.), *Remote Sensing of the European Seas* (pp. 423–434). Dordrecht: Springer Netherlands. https://doi.org/10.1007/978-1-4020-6772-3_32

Ẑutić, V., Ćosović, B., Marčenko, E., Bihari, N., and Kršinić, F. (1981a). Surfactant production by marine phytoplankton. *Marine Chemistry*, *10*(6), 505–520. https://doi.org/10.1016/0304-4203(81)90004-9

Ẑutić, V., Ćosović, B., Marčenko, E., Bihari, N., and Kršinić, F. (1981b). Surfactant production by marine phytoplankton. *Marine Chemistry*, *10*(6), 505–520. https://doi.org/10.1016/0304-4203(81)90004-9

Curriculum vitae

Mehrshad Foroughan

Chemin du Mont-Blanc 9, 1023 Crissier, Switzerland • mehrshad.foroughan@epfl.ch • +41 787180837 •

EDUCATION

Ph.D., Ecological engineering laboratory, EPFL   Jun 2018- Jun 2023

- Doctoral advisor: *David Andrew Barry*
- Tentative thesis title: *"Natural slicks in Lake Geneva: From small-scale effects on air-water interactions to large-scale kinematics and dynamics"*

M.Sc., Mechanical Engineering, University of Tehran   Sep 2014- Feb 2017

- M.Sc. Thesis: *"Optimization of inflow channel geometry and fish friendly characteristic of a water turbine applying Response Surface Methodology integrated with CFD analysis"*

B.Sc., Mechanical Engineering, University of Tehran   Sep 2009- Sep 2013

PUBLICATIONS

Foroughan, M., Hamze-Ziabari, S. M., Lemmin, U., & Barry, D. A. (2022). A Persistent Submesoscale Frontal Slick: A Novel Marker of the Mesoscale Flow Field in a Large Lake (Lake Geneva). Geophysical Research Letters. https://doi.org/10.1029/2022GL100262

Foroughan, M., Lemmin, U., & Barry, D. A. (2022). Effects of natural surfactants on the spatial variability of surface water temperature under intermittent light winds on Lake Geneva. Journal of Limnology. https://doi.org/10.4081/jlimnol.2022.2048

Hamze-Ziabari, S. M., **Foroughan, M.**, Lemmin, U., & Barry, D. A. (2022). Monitoring Mesoscale to Submesoscale Processes in Large Lakes with Sentinel-1 SAR Imagery: The Case of Lake Geneva. Remote Sensing. https://doi.org/10.3390/rs14194967

Hamze-Ziabari, S. M., Lemmin, U., Soulignac, F., **Foroughan, M.**, & Barry, D. A. (2022). Basin-scale gyres and mesoscale eddies in large lakes: a novel procedure for their detection and characterization, assessed in Lake Geneva. https://doi.org/10.5194/gmd-15-8785-2022

Hamze-Ziabari, S. M., Lemmin, U., **Foroughan, M.**, Reiss, R. S. & Barry, D. A. (2022). Chimney-like intense pelagic upwelling in the center of basin-scale cyclonic gyres in large Lake Geneva. https://doi.org/10.22541/essoar.167161029.94177941/v1

Foroughan, M., Riasi, A., & Bahreini, A. (2022). Investigating barotrauma in juvenile salmon passing through a very low head turbine using response surface methodology. Proceedings of the Institution of Mechanical Engineers, Part C: Journal of Mechanical Engineering Science. https://doi.org/10.1177/09544062211050447

CONFERENCES & PRESENTATIONS

Foroughan, M. *et al.* (2022, May 23-27). The effect of natural surfactants on air-water momentum exchange under light wind conditions in Lake Geneva [*Oral presentation*]. EGU General Assembly 2022, Vienna, Austria.

Foroughan, M. *et al.* (2022, May 17-20). Air-water momentum exchange in Lake Geneva under light wind conditions: The effect of natural surfactants [*Poster presentation*]. 8th International Symposium on Gas Transfer at Water Surfaces, Plymouth, UK.

Foroughan, M. *et al.* (2020, November 6-7). Signatures of coherent flow structures in the atmospheric surface layer over Lake Geneva [*Oral presentation*]. 18th Swiss Geoscience Meeting, Zurich, Switzerland.

RESEARCH SKILLS

Pre/post-processing of **in situ measurement observations** (real-time/offline):
- *Water-side:* Temperature moorings, ADCP, ADV, CTD
- *Air-side:* Sonic anemometer, LiDAR, meteorological station

Pre/post-processing of **remotely-sensed data** (real-time/offline):
- *Airborne:* Infrared (IR) and red-green-blue (RGB) time-lapse imagery
- *Satellite:* SENTINEL-1 Synthetic Aperture Radar (SAR)

Post-processing of **numerical simulation results**:
- MIT General Circulation Model (MITgcm) results for Lake Geneva

Data analysis skills:
- Spectral | wavelet | empirical orthogonal function (EOF) analysis for spatio-temporal datasets, Eddy-covariance analysis, Image processing.

Machine learning skills:
- XGBOOST, Random Forest, Decision Tree, Explainable Boosting Machine, SHAP (SHapley Additive exPlanations), CNN (for image processing)

Data analysis/visualization software skills:
- Python [SciPy, Pandas, OpenCV, Mayavi, Cartopy], Matlab, R

TEACHING /SUPERVISING EXPERIENCE	**Teaching assistant**, Limnology (graduate course), EPFL • Supervising exercise sessions. • Assessment and grading of exercises.	2020- 2022
	Teaching assistant, Soil Science (undergraduate course), EPFL • Supervising exercise sessions. • Assessment and grading of exams.	2018- 2023
	Supervising a undergraduate **internship project**, EPFL • Project title: ”*Nighttime convective cooling in Lake Geneva*”	Summer 2023
	Supervising a graduate **internship project**, EPFL • Project title: ”*Kinematics of natural slicks on Lake Geneva*”	Summer 2022
	Supervising a graduate **machine learning course project**, EPFL • Project title: ”*Characterizing vertical migration of zooplankton in Lake Geneva using image processing-based methods*”	Fall 2022
	Supervising a graduate **machine learning course project**, EPFL • Project title: ”*Automatic detection of natural slicks in Lake Geneva from a ground-based optical imagery package*”	Fall 2021
	Supervising a graduate **semester project**, EPFL • Project title: ”*Investigating effects of wind and water currents on the distribution of surface patches on Lake Geneva using image processing.*”	Fall 2019
RELEVANT RESEARCH EXPERIENCE	**Research assistant**, Swiss Federal Laboratories for Materials Science and Technology CFD analyst in EU Horizon 2020 project entitled ” Integrated inter-sector framework to increase the thermal resilience of European workers in the context of global warming ”	May 2017 – Dec 2017
	Persian Gazelle Solar Car III Project Participated in World Solar Challenge 2015, Australia, Cruiser Class *Responsibilities:* • Head of Aerodynamic Engineering Department: Vehicle aerodynamic analysis with numerical simulation and conducting experimental test for energy consumption analysis • Member of Manufacturing Team: Chassis and body manufacturing by composites	Sep 2011 – Oct 2015
AWARDS & HONORS	**Excellent Research Achievement**, For Persian Gazelle Solar Car III, 24th Research Festival, University of Tehran.	2015
	Full Scholarship to study at the University of Tehran for Undergraduate Program	2009
	Ranked 151st among **350,000** participants in the nationwide university entrance examination for Undergraduate Programs.	2009
WORK EXPERIENCE	**Savola Group, Savola Behshahr Company**, Supply chain Mechanical Engineer, Optimizing production processes.	Jan 2014- Oct 2014
	National Organization for Development of Exceptional Talents High School, Physics teacher	Sep 2012- May 2013